

University of Alberta

**Air Injection for River Water Quality
Improvement**

by

Wenming Zhang

A thesis submitted to the Faculty of Graduate Studies and Research
in partial fulfillment of the requirements for the degree of

Doctor of Philosophy

in

Water Resources Engineering

Department of Civil and Environmental Engineering

©Wenming Zhang

Fall 2012

Edmonton, Alberta

Permission is hereby granted to the University of Alberta Libraries to reproduce single copies of this thesis and to lend or sell such copies for private, scholarly or scientific research purposes only. Where the thesis is converted to, or otherwise made available in digital form, the University of Alberta will advise potential users of the thesis of these terms.

The author reserves all other publication and other rights in association with the copyright in the thesis and, except as herein before provided, neither the thesis nor any substantial portion thereof may be printed or otherwise reproduced in any material form whatsoever without the author's prior written permission.

To my family,

Abstract

The problem of low dissolved oxygen (DO) level has been found to be widespread in ice-covered or polluted rivers. This thesis is targeted at providing some fundamental studies on the remediation measure of injecting air/oxygen via existing effluent diffusers to increase river's DO level, with two main focuses: effluent mixing from multiport diffusers and bubbly jets in crossflows.

A comprehensive literature review was first provided on transport of conservative chemicals with jets and plumes in the environment. Effluent mixing in rivers was studied based on a field dye test, and the mixing was further divided into near-field and far-field mixing. In the near-field (within the vertically fully mixed distance), effluent mixing from a multiport diffuser was studied in four zones: free jet zone, jet surface impingement zone, merging zone and river vertical mixing zone. The applicability of prevailing models for multiport diffusers was examined. In the far-field, river transverse mixing dominates further mixing of effluent. A modified streamtube method was proposed to describe transverse mixing. This method can produce a reliable mixing coefficient even with relatively low-quality field data. Effects of river discharge variation and ice cover on dimensional and dimensionless transverse mixing coefficient were investigated in a fixed river reach.

Bubble plumes and bubbly jets produced by injecting air-water mixtures via a nozzle, were studied in crossflows in a large laboratory channel. Their general behaviors, mainly trajectories, were first photographically studied. Air and water discharges at the nozzle and the strength of crossflows were found to

have significant impacts on the general behaviors. Proposed models could well simulate the trajectories of both gas-phase plumes and liquid-phase jets in crossflows. Detailed measurements on bubble properties in bubble plumes and bubbly jets in a crossflow were then conducted with a fiber-optic probe. Distributions of gas void fractions, bubble frequency, bubble velocity, bubble diameter and specific interfacial area were obtained at different crosssections. Centerline properties and spreading rates of bubble plumes were investigated. Relation of bubble slip velocity versus bubble diameter for bubbly jets in crossflow was obtained, and compared with those for single isolated bubbles and bubbly jets in stagnant water.

Acknowledgements

I would like to acknowledge the University of Alberta for providing the F.S. Chia Scholarship and other scholarships for my PhD study. Funding from the Department of Civil and Environmental Engineering and my PhD supervisor, Dr. David Z. Zhu, is also gratefully acknowledged.

I want to express my deepest appreciation to Dr. David Z. Zhu for his invaluable supervision encouragement and friendship. His patient, timely and continuous support guided me to explore the academic field of water resources engineering. Dr. Zhu also helped me a lot in daily life. I am also grateful to Dr. Nallamuthu Rajaratnam for his valuable and kind guidance and suggestions on my research.

I am very grateful for the contributions of the committee members of my PhD candidacy and final exams: Dr. John Gulliver (University of Minnesota), Dr. Brian Fleck (Department of Mechanical Engineering), Dr. Tong Yu, Dr. Mark Loewen, Dr. Nallamuthu Rajaratnam and Dr. David Z. Zhu. I am also grateful to Dr. Robert Doneker for providing the software, CORMIX.

I wish to specially thank Perry Fedun and Chris Krath for their professional technical supports in the lab and field. I am also thankful to Dr. F. Bhuiyan, M.Spafford, T. McKenna, Z. Pan, N. Hall, K. Sharma, J. Cai, A. Camino and B. Liu for their helps with the field work in the Athabasca River. Special thanks are also to Dr. I. E. Lima Neto for kindly sharing his knowledge on the optical probe system, and to Dr. A. Camino for the numerous discussions with her.

I hope to thank my friends and colleagues at the University of Alberta. They are Y. She, A. Camino, M.M. Ali, J. Cai, L. Zhao, J. Xie, X. Chen, J. Guo, A. Azimi, B. Abudul, M. Langford, N. Hall, A. Hall, J. Nafziger, M. Shafieifar. It was a pleasure to meet you and share a wonderful time at our campus.

Finally, my greatest thanks are dedicated to my wife, my parents and my sister for their continuous love, support and encouragement. Their unconditional love makes my life full of sunshine, and their firm support makes me progress further.

Table of Contents

| | |
|--|----|
| Chapter 1 General Introduction..... | 1 |
| 1.1 Research background | 1 |
| 1.2 Thesis outline | 4 |
| References | 6 |
| Chapter 2 Transport with Jets and Plumes of Chemicals in the Environment – a Literature Review * | 8 |
| 2.1 Introduction | 8 |
| 2.2 Turbulent Jets and Plumes in Stagnant Environment..... | 10 |
| 2.2.1 <i>Simple Jets</i> | 10 |
| 2.2.2 <i>Simple Plumes</i> | 12 |
| 2.2.3 <i>Buoyant Jets</i> | 14 |
| 2.3 Effect of Boundaries on Jets and Plumes | 16 |
| 2.3.1 <i>Wall Jets</i> | 16 |
| 2.3.2 <i>Surface Jets</i> | 18 |
| 2.3.3 <i>Jets and Plumes in Coflow</i> | 20 |
| 2.3.4 <i>Jets and Plumes in Crossflow</i> | 23 |
| 2.3.5 <i>Multiple Jets</i> | 27 |
| 2.4 Multiphase Jets and Plumes | 31 |
| 2.4.1 <i>Bubbly Jets and Plumes</i> | 31 |
| 2.4.2 <i>Slurry Jets and Plumes</i> | 35 |
| 2.5 Future directions..... | 38 |
| References | 39 |

| | |
|---|-----|
| Chapter 3 Near-Field Mixing Downstream of a Multiport Diffuser in a Shallow River * | 60 |
| 3.1 Introduction | 60 |
| 3.2 Field Work and Dye Test Results | 63 |
| 3.2.1 Field Work | 63 |
| 3.2.2 Dye Test Results | 66 |
| 3.3 Result Analysis | 68 |
| 3.3.1 Minimum Dilution | 70 |
| 3.3.2 Zone I: Free Jet Zone | 72 |
| 3.3.3 Zone II: Jet Surface Impingement Zone | 73 |
| 3.3.4 Zone III: Merging Zone – Passive Dispersion Analysis | 74 |
| 3.3.5 Zone IV: Vertical Mixing Zone | 77 |
| 3.4 Discussions | 80 |
| 3.5 Summary and Conclusions | 81 |
| Notation | 83 |
| References | 84 |
| Chapter 4 Transverse Mixing in an Unregulated Northern River * | 98 |
| 4.1 Introduction | 98 |
| 4.2 Literature Review | 99 |
| 4.3 Field Work | 104 |
| 4.4 Estimate of Cumulative Discharge and Conservation of Dye Mass Flux | 107 |
| 4.5 A Modified Method for Calculating Transverse Mixing Coefficient | 109 |
| 4.5.1 Modified Method | 109 |
| 4.5.2 Comparison of Methods | 111 |
| 4.5.3 Application of the Modified Method | 113 |

| | |
|---|-----|
| 4.6 Discussions | 115 |
| 4.6.1 <i>Effect of River Discharge</i> | 116 |
| 4.6.2 <i>Effect of Ice Cover</i> | 118 |
| 4.6.3 <i>Mixing Length for 100-times Dilution</i> | 120 |
| 4.7 Summaries and Conclusions | 121 |
| References | 122 |
| Chapter 5 Trajectories of Bubble Plumes and Bubbly Jets in Crossflows* | 141 |
| 5.1 Introduction | 141 |
| 5.2 Experimental apparatus and procedures | 146 |
| 5.3 Trajectory Results and Analysis..... | 148 |
| 5.3.1 <i>Pure Water Jets</i> | 148 |
| 5.3.2 <i>Pure Bubble Plumes</i> | 150 |
| 5.3.3 <i>Bubbly Jets</i> | 152 |
| 5.3.4 <i>Modeling of the Water Jets in Bubbly Jets in Strong Crossflows</i> | 155 |
| 5.3.5 <i>Modeling of the Bubble Plumes in Bubbly Jets in Strong Crossflows</i> | 157 |
| 5.4 Summary and Conclusions..... | 159 |
| References | 161 |
| Chapter 6 Measurements of Bubble Plumes and Bubbly Jets in a Crossflow* . | 182 |
| 6.1 Introduction | 182 |
| 6.2 Literature Review | 183 |
| 6.3 Experimental Setup and Procedure | 192 |
| 6.3.1 <i>Apparatus and Procedure</i> | 192 |
| 6.3.2 <i>Calibration of the Optical Probe System</i> | 196 |
| 6.4 Results and Analysis | 199 |

| | |
|---|-----|
| 6.4.1 Gas Void Fraction | 200 |
| 6.4.2 Bubble Frequency..... | 203 |
| 6.4.3 Bubble Velocity..... | 204 |
| 6.4.4 Bubble Diameter..... | 208 |
| 6.4.5 Specific Interfacial Area | 211 |
| 6.4.6 Cross-sectional Distribution..... | 211 |
| 6.5 Discussions..... | 213 |
| 6.5.1 Properties along the Centerlines of Bubble Plumes and Bubbly Jets | 213 |
| 6.5.2 Spreading Rates of Bubble Plumes and Bubbly Jets | 216 |
| 6.5.3 Conservation of Air Flow Rate | 218 |
| 6.5.4 Bubble Slip Velocity..... | 220 |
| 6.5.5 Aeration Potential and Bubble Size Recommended for Artificial Aeration | 222 |
| 6.6 Summaries and Conclusions | 224 |
| References | 226 |
| Chapter 7 General Conclusions and Recommendations for Future Research .. | 269 |
| 7.1 General Conclusions | 269 |
| 7.2 Recommendations for Future Research | 270 |

List of Tables

| | |
|---|-----|
| Table 2-1. Summary of Mean Properties of Simple Plane Jet and Circular Jet (data sources: Rajaratnam 1976[1]; Fischer et al. 1979 [2]; Rajaratnam 1984 [3]; Lee and Chu 2003 [4]) | 47 |
| Table 2-2. Summary of Mean Properties of Plane Plume and Circular Plume (data sources: Fischer et al. 1979 [1]; Rajaratnam 1984 [2]; Lee and Chu 2003 [3]) | 48 |
| Table 2-3. Summary of Mean Properties of Turbulent Buoyant Jet (data sources: Rajaratnam 1984 [1]; Lee and Chu 2003 [2]) | 49 |
| Table 2-4. Summary of Mean Properties of Plane Wall Jet and Bluff Wall Jet (data sources: Rajaratnam and Subramanya 1967 [1]; Rajaratnam and Pani 1974 [2]; Rajaratnam 1976[3]; Launder and Rodi 1983 [4]) | 50 |
| Table 2-5. Summary of Mean Properties of Non-buoyant Plane Surface Jet and Bluff Surface Jet (data sources: Rajaratnam 1976[1]; Rajaratnam 1984 [2]; Rajaratnam and Humphries 1984 [3]; Gholamreza-kashi et al. 2007 [4]) | 51 |
| Table 2-6. Summary of Mean Properties of Buoyant Plane Surface Jet and Bluff Surface Jet (data sources: Chu and Vanvari 1976 [1]; Pande and Rajaratnam 1977 [2]; Rajaratnam 1984 [3]; Rajaratnam 1985 [4]; Rajaratnam and Subramanyan 1985 [5]) | 52 |
| Table 3-1. Measured Dye Mass Flux Compared to the Injection | 87 |
| Table 3-2. Main Physical Parameters for the Effluent, Ambient and Diffuser | 88 |
| Table 4-1. Studies of Transverse Mixing Coefficients in Ice-covered Rivers | 125 |
| Table 4-2. Basic Hydraulic Parameters in the Study Reach in 2008 Dye Test | 126 |
| Table 4-3. Comparison of Estimated Cumulative Discharges with ADP measurements | 127 |
| Table 4-4. Transverse Mixing Coefficients Calculated by Using the Standard Method of Moments, Beltaos' Generalized Method of Moments, and Modified Method Proposed in this Study | 128 |
| Table 4-5. Basic Hydraulic Parameters in 1994 and 1995 Dye Tests | 129 |
| Table 4-6. Transverse Mixing Coefficients in 1994 and 1995 Dye Tests Calculated by Using Modified Method Proposed in this Study | 130 |
| Table 5-1. Experimental Conditions for Bubble Plumes and Bubbly Jets in Crossflows | 163 |
| Table 6-1. Experimental Conditions for Bubble Plumes and Bubbly Jets in the Crossflow of 0.20 m/s | 231 |
| Table 6-2 Summary of minimum mean bubble diameter in experiments of air-water bubbly jets discharged via nozzles in water | 232 |

List of Figures

| | |
|---|-----|
| Figure 1-1 DO concentrations in the Athabasca River upstream of Grand Rapids in 2003 (modified from Chambers et al. 2006)..... | 7 |
| Figure 2-1. Schematic of a simple plane jet (for circular jet, replace $2b_0$ by d_0 and y by r) | 53 |
| Figure 2-2. Schematic of (a) plane and (b) bluff wall jets..... | 54 |
| Figure 2-3. Schematic of (a) plane and (b) bluff surface jets | 55 |
| Figure 2-4. Schematic of plane jets in coflow (for circular jets, replace $2b_0$ by d_0 and y by r) | 56 |
| Figure 2-5. Schematic of jets in crossflow | 57 |
| Figure 2-6. An example of a unidirectional diffuser | 58 |
| Figure 2-7. (a) Schematic of multiple merging jets, with the indication of (b) jet cross-section deformation (modified from Wang and Davidson 2003) | 59 |
| Figure 3-1. Schematic of the near-field mixing processes for a diffuser with an oblique angle into a shallow river: (a) aerial view; (b) side view..... | 89 |
| Figure 3-2. (a) Arrangement of Al-Pac's diffuser; (b) river bathymetry near the diffuser; (c) dye sampling sites at 4.8 m, 20.0 m, 33.3 m, 60.4 m, and 114.1 m downstream of the diffuser, with indication of cumulative discharge distribution | 90 |
| Figure 3-3. Measured dye concentrations at different sections | 91 |
| Figure 3-4. Water surface concentrations with cumulative discharges at different sections | 92 |
| Figure 3-5. (a) Measured minimum dilutions; (b) comparison with jet theories; (c) comparison with CORMIX and present models | 93 |
| Figure 3-6. Modeling results of two neighboring jets from CORMIX1: (a) vertical trajectories; (b) horizontal trajectories | 94 |
| Figure 3-7. Measured and modeled concentration profiles at the water surface at various sections | 95 |
| Figure 3-8. Measured and modeled vertical concentration profiles at various sections.... | 96 |
| Figure 3-9. Effect of river velocity on lateral concentration distribution at Section 20 m | 97 |
| Figure 4-1. Study reach in the Athabasca River, with the study location indicated in the top right provincial map of Alberta, Canada | 131 |

| | |
|---|-----|
| Figure 4-2. Measured dye concentrations (filled triangle solid line) at different sections with indication of river depths (open circle dashed line)..... | 132 |
| Figure 4-3. Comparisons of measured velocities with indication of standard deviations and cumulative discharges with estimated values across Section 13.73 km..... | 133 |
| Figure 4-4. Measured (open square) and modeled (line) dye concentrations versus cumulative discharges at different sections, where M/M_0 indicates the ratio of measured dye mass flux, by using the measured concentrations, to the initial dye injection rate; $M/M_0 = 100\%$ for the modeled concentration profiles; Points A and B in Fig. 4-4(4) are discussed in this study..... | 134 |
| Figure 4-5. Change of variances of transverse concentration profiles along the river by using (a) standard method of moments; (b) generalized method of moments; and (c) the modified method proposed in this study | 135 |
| Figure 4-6. Modeled and measured dye concentrations at different sections in 1994 dye test where M/M_0 indicates the ratio of measured dye mass flux, by using the measured concentrations, to the initial dye injection rate | 136 |
| Figure 4-7. Change of variances of transverse concentration profiles along the river in (a) 1994 and (b) 1995 dye tests, by using the modified method proposed in this study | 137 |
| Figure 4-8. Modeled and measured dye concentrations at different sections in 1995 dye test in ice-covered condition, where M/M_0 indicates the ratio of measured dye mass flux, by using the measured concentrations, to the initial dye injection rate | 138 |
| Figure 4-9. Effect of river discharge on (a) dimensional; (b) dimensionless transverse mixing coefficient; and (c) dimensional factor of diffusion | 139 |
| Figure 4-10. Mixing lengths for 100-times dilution under varying discharges with and without ice cover..... | 140 |
| Figure 5-1. Schematic of the experimental setup; experiment shown in the photo: Expt. B-3-3 | 164 |
| Figure 5-2. Effect of dye on bubble properties in Expt. B-1-3, (a) without dye; (b) with Rhodamine W.T.; and (c) with a liquid food color..... | 165 |
| Figure 5-3. Photos of pure water jets, bubble plumes and bubbly jets at an ambient velocity of 0.02 m/s; photo size: $73.7 \times 55.0 \text{ cm}^2$ | 166 |
| Figure 5-4. Photos of pure water jets, bubble plumes and bubbly jets at an ambient velocity of 0.20 m/s; photo size: $73.7 \times 55.0 \text{ cm}^2$ | 167 |
| Figure 5-5. Photos of pure water jets, bubble plumes and bubbly jets at an ambient velocity of 0.47 m/s; photo size: $73.7 \times 55.0 \text{ cm}^2$ | 168 |

| | |
|---|-----|
| Figure 5-6. Comparison of measurement results of jet centerlines with previous studies for the case of pure water jets | 169 |
| Figure 5-7. Comparison of the angle of bubble plume centerline from images with that from arccosine (U/U_b) and that from arctangent (U_s/U) in the crossflow of $U = 0.20$ m/s, where U_b is the measured bubble velocity along the centerline and U_s is the bubble slip velocity from Clift et al. (1978); (a) for the cases of pure bubble plumes and bubbly jets with small Q_w and (b) for the case of bubbly jets with large Q_w | 170 |
| Figure 5-8. Comparison of measured bubble plume centerlines with modeled centerlines for the case of pure bubble plumes and the case of bubbly jets with small Q_w in the crossflow of 0.20 m/s..... | 171 |
| Figure 5-9. Comparison of measured bubble plume centerlines with modeled centerlines for the case of pure bubble plumes and the case of bubbly jets with small Q_w in the crossflow of 0.47 m/s..... | 172 |
| Figure 5-10. Comparison of measured bubble plume centerlines with modeled centerlines for the case of pure bubble plumes and the case of bubbly jets with small Q_w in the crossflow of 0.02 m/s..... | 173 |
| Figure 5-11. Division of six zones for the case of bubbly jets: I, bubbly jet zone where bubbles and water jet are well mixed; II, transition zone where bubble start separating from water jet; III, zone of separated bubble plume; IV, zone of separated water jet; V, a zone where rather tiny bubbles can be observed; VI, a zone where possible leakage from bubbly jet or water jet may occur. Definition of separation height, H_s , is also illustrated. Photo shown is for Experiment B-1-5. | 174 |
| Figure 5-12. (a) Effect of the existence of bubbles on the water jet half-thickness W_z along the jet centerline ζ in the bubbly jet experiments with $Q_w = 3$ LPM and $U = 0.20$ m/s; (b) Effect of the strength of crossflow on W_z in the bubbly jet experiments with $Q_a = 1$ LPM and $Q_w = 3$ LPM..... | 175 |
| Figure 5-13. (a) Measurement result of max rise height of bubbly jets and pure water jets; (b) comparison of water velocities at the nozzle exit based on max rise height with theoretical values for the case of pure water jets | 176 |
| Figure 5-14. Comparison of measurement results of water jet centerlines with modeled centerlines for the case of bubbly jets in the crossflow of 0.20 m/s | 177 |
| Figure 5-15. Comparison of measurement results of water jet centerlines with modeled centerlines for the case of bubbly jets in the crossflow of 0.47 m/s | 178 |
| Figure 5-16. Relation of separation height, H_s , with α for bubbly jets | 179 |

| | |
|---|-----|
| Figure 5-17. Comparison of measurement results of bubble plume centerlines with modeled centerlines for the case of bubbly jets in the crossflow of 0.20 m/s..... | 180 |
| Figure 5-18. Comparison of measurement results of bubble plume centerlines with modeled centerlines for the case of bubbly jets in the crossflow of 0.47 m/s..... | 181 |
| Figure 6-1. Schematic of experimental setup in a flume of 25 m × 1.2 m × 0.8 m (L × W × H)..... | 233 |
| Figure 6-2. Cylinder used to calibrate gas void fraction measurement by using the optical probe | 234 |
| Figure 6-3. Calibration of the optical probe on (a) void fraction, (b) bubble diameter, and (c) bubble velocity | 235 |
| Figure 6-4. Photos of bubble plumes or bubbly jets in 12 experimental conditions; side view, photo size: 73.7 × 55.0 cm ² ; the first and second numbers in the experiment scenarios represent the gas and water discharges at the nozzle exit (unit: LPM), respectively, and the same way will be used in all the following figures | 236 |
| Figure 6-5. Typical time series of gas void fraction and bubble velocity obtained from the optical probe system; time series using moving average, with time step of 1 second and averaging window size of 2 seconds; measurement taken near the bubbly jet centerline ($\eta = -0.14$ cm, $y = 0.35$ cm) at Section 80 <i>d</i> in Experiment 3-3..... | 237 |
| Figure 6-6. Typical bubble size distribution measured at the bubble plume centerline at Section 80 <i>d</i> in each experiment; data were directly obtained from the optical probe system, without adjustment for bubble non-sphericity, to exclude the change of size distribution due to the adjustment..... | 238 |
| Figure 6-7. Distribution of gas void fraction in the η direction..... | 239 |
| Figure 6-8. Distribution of gas void fraction in the y direction..... | 240 |
| Figure 6-9. Distribution of dimensionless gas void fraction in the η direction | 241 |
| Figure 6-10. Distribution of dimensionless gas void fraction in the y direction | 242 |
| Figure 6-11. Distribution of bubble frequency in the η direction..... | 243 |
| Figure 6-12. Distribution of bubble frequency in the y direction..... | 244 |
| Figure 6-13. Distribution of bubble velocity in the η direction..... | 245 |
| Figure 6-14. Possible effect of bubble wakes on a single bubble in Expt. 5-0; although tracking the same bubble may not appear direct in part of the images in Fig. (b)-(e), it is more direct by comparing the whole images; bubble velocities are based on the vertical locations of the front of the bubble, i.e. vertical interfacial velocities, and the interfacial | |

| | |
|---|-----|
| velocity is used in the RBI optical probe system (Kiambi et al. 2003); image size in (a): 73.7 × 55.0 cm ² and in (b)-(e): 5.5 × 18.8 cm ² | 246 |
| Figure 6-15. Distribution of bubble velocity in the y direction | 247 |
| Figure 6-16. Distribution of bubble diameter in the η direction | 248 |
| Figure 6-17. Distribution of bubble diameter in the y direction | 249 |
| Figure 6-18. Distribution of specific interfacial area in the η direction | 250 |
| Figure 6-19. Distribution of specific interfacial area in the y direction | 251 |
| Figure 6-20. Distribution of void fraction at Section 80 <i>d</i> in (a) experiment 3-0 and (b) experiment 3-3, with a measurement mesh of 1 × 1.25 cm ² | 252 |
| Figure 6-21. Distribution of bubble frequency at Section 80 <i>d</i> in (a) experiment 3-0 and (b) experiment 3-3, with a measurement mesh of 1 × 1.25 cm ² | 253 |
| Figure 6-22. Distribution of bubble velocity at Section 80 <i>d</i> in (a) experiment 3-0 and (b) experiment 3-3, with a measurement mesh of 1 × 1.25 cm ² | 254 |
| Figure 6-23. Distribution of bubble diameter at Section 80 <i>d</i> in (a) experiment 3-0 and (b) experiment 3-3, with a measurement mesh of 1 × 1.25 cm ² | 255 |
| Figure 6-24. Distribution of bubble specific interfacial area at Section 80 <i>d</i> in (a) experiment 3-0 and (b) experiment 3-3, with a measurement mesh of 1 × 1.25 cm ² | 256 |
| Figure 6-25. Change of (a) dimensional gas void fraction along the centerlines of bubble plumes or bubbly jets; and (b) dimensionless gas void fraction along the centerlines of bubbly jets with $Q_w = 3$ or 5 LPM ($Re > 8,000$) | 257 |
| Figure 6-26. Comparison between the experimental result of Expt. 5-5 and the modeling result from CORMIX1 for a single-phase jet in crossflow that has initial concentration $C_0 = \alpha_0$ and initial velocity $U_0 = U_{w0}$ (using Method III in Table 1) as in Expt. 5-5, (a) dimensionless centerline gas void fraction or concentration and (b) dimensionless centerline bubble velocity or jet velocity | 258 |
| Figure 6-27. Change of bubble velocity along the centerlines of bubble plumes or bubbly jets | 259 |
| Figure 6-28. Change of bubble frequency along the centerlines of bubble plumes or bubbly jets | 260 |
| Figure 6-29. (a) Change of bubble diameter along the centerlines of bubble plumes or bubbly jets; (b) change of bubble diameter at the centerlines at Section 100 <i>d</i> with Reynolds number based on superficial water velocity at the nozzle exit | 261 |
| Figure 6-30. Change of specific interfacial area along the centerlines of bubble plumes or bubbly jet | 262 |

| | |
|--|-----|
| Figure 6-31. Spreads of the bubble plumes or bubbly jets in all the 12 experiments..... | 263 |
| Figure 6-32. Comparison of air flow rates at Sections $80d$ and $100d$ from integration of Eq. (6.7) with their injected rates in the experiments of bubbly jets | 264 |
| Figure 6-33. Relation of bubble slip velocity with bubble diameter for bubble plumes and bubbly jets in crossflow, without the consideration of bubble-induced water velocities inside bubble plumes | 265 |
| Figure 6-34. Dye stripe experiments to show the strengths of bubble-induced water velocities inside bubble plumes | 266 |
| Figure 6-35. Comparison of average difference of bubble slip velocity from the present measurement and that from Clift et al. (1978) in Fig. 6-33, ΔU_s , with bubble induced water velocity in the vertical direction $U_{bw,v}$ estimated from videos of dye stripe experiments..... | 267 |
| Figure 6-36. Aeration potential ($\int_{-\infty}^{+\infty} \int_{-\infty}^{+\infty} K_L ad\eta dy$) at Section $80d$ in each experiment. | 268 |

Chapter 1

General Introduction

1.1 Research background

Dissolved oxygen (DO) is one of the most essential water quality parameters and the maintenance of a certain level of DO is crucial for a healthy river ecosystem. However, severe winter DO depletions have been found wide-spread in rivers throughout the arctic and sub-arctic regions of Russia, Alaska, and northern Canada (Whitfield and McNaughton 1986; Chambers 2000). Low DO levels may severely affect the feeding rate, spawning, hatch and even the survival of fish and benthic macroinvertebrate species (Chambers 2000). The low DO levels in northern rivers are typically caused by the low river discharge in the winter, prevention of surface reaeration by ice cover, industrial and municipal wastewater discharges, and the bottom sediment oxygen demand (Lima Neto et al. 2007).

An example of ice covered rivers with low concentrations of DO is the Athabasca River. The Athabasca River, with an annualized discharge of 661 m³/s, is an important river in northern Alberta, Canada. It supplies water to numerous local communities, Alberta's five pulp and paper mills and Canada's oil sand industry, and receives effluents from them. The river also provides important habitat for more than 30 species of fish. The current guidelines for DO threshold values in Alberta are 5.0 mg/L for acute exposure and 6.5 mg/L for 7-day chronic exposure (Alberta Environment 1999). In the winter, the DO level in the Athabasca River has been reported to drop below the chronic guideline (Chambers et al. 2006; Lima Neto et al. 2007). For

instance, as shown in Fig. 1-1, in 2003, the DO concentration decreased below 6.5 mg/L for a period of 42 days upstream of the Grand Rapids.

In the Athabasca River, a direct and low-cost remediation measure was reported by Lima Neto et al. (2007) to increase the DO level by injecting liquid oxygen via the existing effluent diffusers along the river. Two field oxygen injection tests have been conducted through the diffuser of Alberta-Pacific Forest Industries Inc., with an injection rate of up to 5,000 lb/day. Analysis shows that the absorption rate of injected oxygen into water may reach as high as 50%, suggesting the effectiveness of this method.

In order to better understand and further improve the effect and efficiency of oxygen injection, two important processes must be studied: the bubbly jet process and the river mixing process downstream of a multiport diffuser. The first process transfers the injected air/oxygen into river water through the spread, breakup and diffusion of the air bubbles before they escape into the air, while the second process governs the advection and turbulent diffusion of DO further downstream and across the river. The study on river mixing itself is also important for delineating effluent plume and assessing its environmental impact, as required by the current Environment Canada's Environmental Effects Monitoring Programs (Environment Canada, <http://www.ec.gc.ca/esee-eem/default.asp?lang=En&n=4CDB9968-1>). The river mixing study provides a hydrodynamic mixing basis for the study of air/oxygen injection.

The focus of this thesis is on both the river mixing process and bubbly jet process. A comprehensive literature review on transport of conservative chemicals with turbulent jets and plumes in the environment was first conducted to provide a solid foundation for the following studies. The river mixing was studied based on a field dye test. The river mixing was further divided into near-field and far-field mixing, which are

defined as mixing within and beyond the vertically fully mixed distance, respectively. In the near-field, the challenge is on the performance of a river multiport diffuser on effluent mixing and its interaction with river ambient flow. In the far-field, river geometry and hydraulic characteristics govern the transverse mixing and the difficulty is on the effects of seasonal variation of river discharge and ice cover on transverse mixing coefficient. The bubbly jet process was studied in the laboratory. Bubble plumes were produced by injecting air into water via a nozzle, while bubbly jets were made by injecting a mixture of air and water into water. Bubbly jets have been studied in stagnant water by Lima Neto et al. (2008a,b,c,d), Lima Neto (2011) and others. This study introduced crossflow, which is typically present in rivers. Crossflow significantly complicates bubbly jets, and relevant studies have been rarely reported. The present study contained two parts, with the first one on the general behaviors (e.g., trajectories) of bubbly jets in different crossflows and the second one on the detailed measurement of bubble properties in a single crossflow. All the above mentioned issues are to be addressed in this thesis.

This thesis will improve the knowledge on three aspects: performance of river multiport diffuser; river vertical and transverse mixing; and bubble plumes and bubbly jets in crossflow. This thesis also provide detailed field and laboratory data for the development and calibration of computational dynamics models on multiport diffusers, river mixing, and air-water two-phase jets and plumes. In particular, this thesis is useful in guiding the activities such as effluent mixing and air/oxygen injection for river water quality improvement.

1.2 Thesis outline

This thesis is written in paper format and composed of five contributions on effluent mixing in rivers and bubbly jets in crossflow. Each contribution is presented in a separate chapter, and the following is a brief introduction.

In Chapter 2, a comprehensive literature review is presented on transport with jets and plumes of conservative chemicals in the environment. This chapter includes the review on various types of jets and plumes, including simple jets and plumes, buoyant jets, wall jets, surface jets, jets and plumes in coflow and crossflow, multiple jets, bubbly and slurry jets and plumes. The chapter provides a general foundation for the following studies of effluent near-field mixing from a multiport diffuser and bubbly jets in crossflow.

In Chapter 3, near-field mixing downstream of a multiport diffuser in a shallow river is studied with a field dye test. The near-field mixing is analyzed in four zones: the free jet zone, the jet surface impingement zone, the merging zone and the vertical mixing zone. The field data is also used to examine the applicability of some prevailing models for multiport diffusers. The main objective is to better understand the mixing performance of multiport diffusers in rivers of shallowness and with strong crossflow.

In Chapter 4, far-field transverse mixing in an unregulated northern river is studied based on field dye tests. The main focus is on the effects of river discharge variation and ice cover on transverse mixing in a fixed river reach. A modified streamtube method is also proposed to describe transverse mixing. The method can produce reliable mixing coefficient even with relatively low-quality field data.

In Chapter 5, general behaviors (mainly trajectories) of bubble plumes and bubbly jets in different crossflows are studied in a large laboratory flume. Pure water jets are also included in the experiments for comparison purpose. Effects of air and

water flow rates at the nozzle and strength of crossflow are examined. Models proposed are able to well simulate both the trajectories of gas-phase plumes and liquid phase jets for bubble plumes and bubbly jets in crossflow.

In Chapter 6, bubble properties of bubble plumes and bubbly jets in a crossflow are measured in detail by using a double-tip optical probe system. The distributions of gas void fractions, bubble frequency, bubble velocity, bubble diameter and specific interfacial area are obtained at different cross-sections of bubble plumes and bubbly jets. Air mass flux at each section is integrated and compared with the injection flux. Bubble properties are studied along bubble plume centerlines and compared with the change of centerline concentration and velocity in single-phase jet in crossflow. Spreading rates of bubble plumes are next examined. Bubble induced water velocity in bubble plumes is studied. The relation of bubble slip velocity versus bubble diameter in crossflow is investigated and compared with those for single isolated bubbles and bubbly jets in stagnant water. Finally, aeration potential of each experiment is studied and a bubble diameter is recommended for artificial aeration in practice.

In Chapter 7, some general conclusions are made and recommendations for future research are provided.

References

- Alberta Environment. (1999). "Surface water quality guidelines for use in Alberta." Environmental Assurance Division, Science and Standards Branches, Edmonton, Alberta, 25p.
- Chambers, P. A., Brown, S., Culp, J. M., Lowell, R. B., and Pietroniro, A. (2000). "Dissolved oxygen decline in ice-covered rivers of northern Alberta and its effects on aquatic biota." *J. Aquatic Ecosystem Stress and Recovery*, 8(1), 27-38.
- Chambers, P. A., Culp, J. M., Glozier, N. E., Cash, K. J., Wrona, F. J., and Noton, L. (2006). "Northern rivers ecosystem initiative: nutrients and dissolved oxygen – issues and impacts" *Environ. Monit. Assess.*, 113, 117-141.
- Lima Neto, I. E. (2011). "Modeling the liquid volume flux in bubbly jets using a simple integral approach." *J. Hydraul. Eng.*, doi:10.1061/(ASCE)HY.1943-7900.0000499.
- Lima Neto, I. E., Zhu, D. Z., Rajaratnam, N., Yu T., Spafford, M., and McEachern, P. (2007). "Dissolved oxygen downstream of an effluent outfall in an ice-cover river: natural and artificial aeration." *J. Environ. Eng.*, 133 (11), 1051-1060.
- Lima Neto, I. E., Zhu, D. Z. and Rajaratnam, N. (2008a). "Air injection in water with different nozzles." *J. Environ. Eng.*, 134 (4), 283-294.
- Lima Neto, I. E., Zhu, D. Z. and Rajaratnam, N. (2008b). "Bubbly jets in stagnant water." *Int. J. Multiphase Flow*, 34 (12), 1130-1141.
- Lima Neto, I. E., Zhu, D. Z. and Rajaratnam, N. (2008c). "Effect of tank size and geometry on the flow induced by circular bubble plumes and water jets." *J. Hydraul. Eng.*, 134 (6), 833-842.
- Lima Neto, I. E., Zhu, D. Z. and Rajaratnam, N. (2008d). "Horizontal injection of gas-liquid mixtures in a water tank." *J. Hydraul. Eng.*, 134 (12), 1722-1731.
- Whitfield, P.H., and McNaughton, B. (1986). "Dissolved-oxygen depressions under ice cover in two Yukon rivers." *Water Resour. Res.*, 22 (12), 1675-1679.

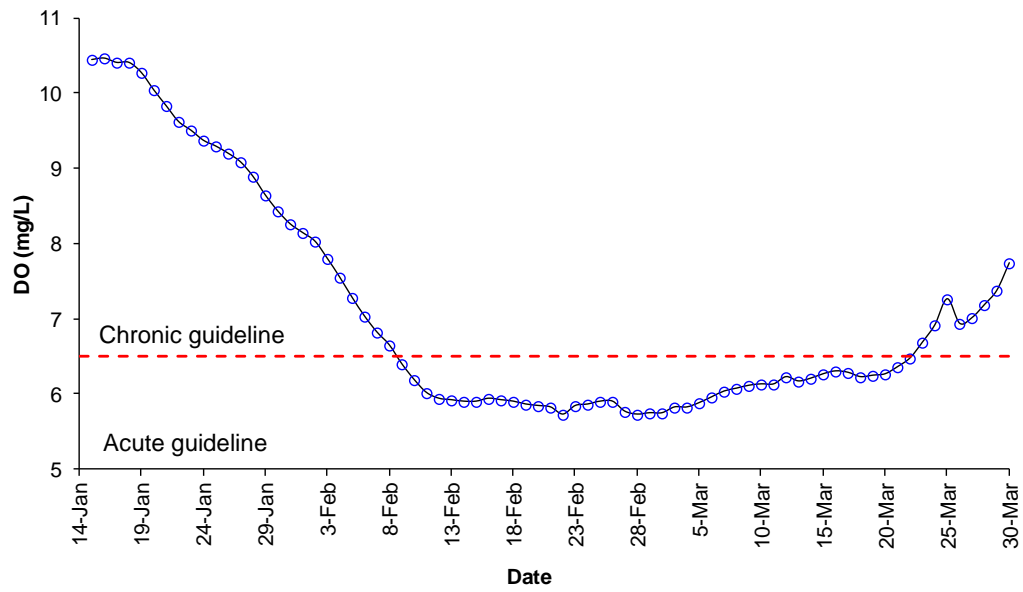


Figure 1-1 DO concentrations in the Athabasca River upstream of Grand Rapids in 2003 (modified from Chambers et al. 2006)

Chapter 2

Transport with Jets and Plumes of Chemicals in the Environment – a Literature Review*

Jets and plumes are common in our environment. Some examples of jets are: wastewater discharged from an outfall; emission from an aircraft or vehicle; and the eruption of volcano. Some examples of plumes are: the smoke from a chimney stack or cigarette; the thermal plumes from a fire; municipal wastewater or hot water discharged in deep water; and oil spill from sea bed. One of the most important features of jets or plumes is their ability of entraining ambient fluid and achieve self-dilution. This greatly triggers our interests to study jets and plumes. This chapter is a review of the studies on turbulent jets and plumes, with a focus on the transport of conservative pollutants.

2.1 Introduction

The earliest experimental study of turbulent jets appears to be the work of Trupel on circular jets in 1915 (Abramovich 1963). Förthman performed an experimental study of plane turbulent jets in 1934 and his work also considered plane turbulent wall jets (Förthman 1936). The results of these investigations showed the similarity of the velocity profiles at different distances from the sources of the jets. These studies were followed by the extensive investigations of Hinze and Zijnen (1949) on circular jets and Albertson et al. (1950) for plane and circular jets. Turbulence characteristics of plane

* The content of this chapter has been published as a book chapter. Zhang, W.M., Rajaratnam, N, and Zhu, D.Z. (2011). “Transport with Jets and Plumes of Chemicals in the Environment”, *Encyclopedia of Sustainability Science and Technology*, Robert A. Meyers (ed.), DOI 10.1007/978-1-4419-0851-3, Springer, 25p.

jets were studied by Heskestad (1965) for plane jets and Wygnanski and Fielder (1969) for circular jets. Theoretical solutions for plane jets were developed by Tollmien in 1926 for plane jets and by Goertler in 1942 for circular jets (Rajaratnam 1976). Numerical studies of turbulent jets followed, starting with the work of Rodi and Spalding (1970). Abramovich (1963), Rajaratnam (1976) and Fischer et al. (1979) provided comprehensive treatment of jets.

Turner (1973) provides an introduction to study turbulent plumes in his book on *Buoyancy Effects in Fluids*. Rouse et al. (1952) performed an experimental study of plane and circular plumes wherein they found that the velocity and density defect profiles were similar if proper scales were chosen for velocity, width and density defect. Morton et al. (1956) published an integral study of plumes, wherein the concept of entrainment coefficient was introduced. Since then numerous studies have been conducted on turbulent plumes and forced turbulent plumes (buoyant jets). These studies have been summarized in Chen and Rodi (1980) and Lee and Chu (2003). Turbulent jets and plumes have been studied extensively not only because these flows are very interesting but also that they are of considerable practical importance in the fields of hydraulic, mechanical, aeronautical, environmental, and chemical engineering and many other fields.

This chapter will first review the most classic and well-established theories on simple jets or plumes in stagnant water, and then consider effects of boundaries including: the bed (wall) and the surface of ambient fluid; coflowing and cross-flowing ambient fluid; and the interaction of neighboring jets in the case of multiple jets. Next, two kind of multiphase jets and plumes – bubbly jets and plumes; and slurry jets and plumes – will be briefly introduced. Multiphase jets and plumes are much more complicated compared to the single-phase ones, but have gained more interest in recent

years because of their wide applications. Finally, some directions for future researches will be highlighted.

2.2 Turbulent Jets and Plumes in Stagnant Environment

In this section, the focus is on the transport of conservative pollutants in a steady-state turbulent jet or plume issuing from a simple (plane or circular) nozzle into stagnant ambient fluid of large extent. Such jets or plumes are called simple jets or simple plumes. Theories in this area have been well established. Close to the nozzle exit, there is a wedge-like or cone-like region termed “potential core” where the width of initial velocity distribution decays to a point. The length of the potential core is very short, about $10.4b_0$ for a plane jet where b_0 is the half slot width, or $6.2d_0$ for a circular jet where d_0 is the nozzle diameter (Lee and Chu 2003). Therefore, for practical purposes, our attention will be limited on the flow beyond the potential core, i.e. in the “fully developed flow” region (see Fig. 2-1). The reader who is interested in flow development region may refer to Rajaratnam (1976).

2.2.1 Simple Jets

The integral method is the most common method for analyzing simple jets or plumes. The following is a brief introduction on this method. For a plane jet as shown in Fig. 2-1, the Reynolds-averaged Navier-Stokes equation in x direction, continuity equation and pollutant conservation equation, respectively, can be simplified as (Rajaratnam 1976):

$$u \frac{\partial u}{\partial x} + v \frac{\partial u}{\partial y} = \frac{1}{\rho} \frac{\partial \tau}{\partial y} \quad (2.1)$$

$$\frac{\partial u}{\partial x} + \frac{\partial v}{\partial y} = 0 \quad (2.2)$$

$$\frac{\partial uC}{\partial x} + \frac{\partial vC}{\partial y} = \varepsilon \frac{\partial^2 C}{\partial y^2} \quad (2.3)$$

where u and v are the time-averaged velocities in x and y directions, respectively; C is the pollutant concentration; ρ is the density of the fluid; τ is the turbulent shear stress; ε is the mean value of turbulent diffusion coefficient.

After multiplying Eq. (2.1) by ρ and then integrating from $y = 0$ to $y = \infty$, Eq. (2.1) becomes:

$$\frac{d}{dx} \int_0^{\infty} \rho u^2 dy = 0 \quad (2.4)$$

Eq. (2.4) states that the jet momentum flux at different x -sections is conserved. Using Eq. (2.2) and integrating the first term of Eq. (2.2) from $y = 0$ to $y = \infty$, we have:

$$\frac{dq_x}{dx} = \frac{d}{dx} \int_0^{\infty} u dy = -v_{y=\infty} \quad (2.5)$$

where q_x is the jet volume flux per unit slot length. The entrainment hypothesis assumes that the entrainment velocity $v_e = v_{y=\infty} = -\alpha_e u_m$, where α_e is called the jet entrainment coefficient; u_m is jet centerline (maximum) velocity; the negative sign indicates the ambient fluid is entrained into the jet. Eq. (2.5) says that the jet volume flux increases with traveling distance x due to the entrainment of ambient fluid, which explains the ability of jet in diluting pollutants. Similarly, integrating Eq. (2.3) from $y = 0$ to $y = \infty$, we have:

$$\frac{d}{dx} \int_0^{\infty} uC dy = 0 \quad (2.6)$$

Eq. (2.6) states that the mass fluxes of pollutants at different x -sections are conserved if the chemical or biological reactions of pollutants are not considered.

Numerous laboratory experiments and numerical simulations have confirmed that: beyond the potential core, the jet velocity or concentration exhibits self-similarity.

The most widely used expression for such similarity is the Gaussian distribution, which represents laboratory data satisfactorily:

$$\frac{u}{u_m} = \exp\left[-k_1 \left(\frac{y}{b}\right)^2\right] \quad (2.7)$$

$$\frac{C}{C_m} = \exp\left[-k_1 \left(\frac{y}{k_2 b}\right)^2\right] \quad (2.8)$$

where C_m is the jet time-averaged centerline (maximum) concentration; b is the jet velocity half-width where the velocity is 50% (if $k_1=0.693$, refer to Fig. 2-1) or 37% (if $k_1=1$) of u_m ; $k_2 b$ defines the jet concentration half-width where the concentration is 50% or 37% of C_m ; k_2 is the ratio of concentration half-width to velocity half-width. Using Eqs. (2.4) - (2.8), the analytical solutions for plane jets can be derived, as shown in Table 2-1. The coefficients of the solutions are mainly determined from experimental results and integrations.

Using the same procedures as above, the equations of momentum flux, volume flux and pollutant mass flux for a circular jet can be derived. These equations suggest that: the jet momentum flux at any x -section is conserved; the jet volume flux across any x -section increases with traveling distance due to the entrainment of ambient fluid; Although the entrainment causes the pollutant get diluted within the jet core, the mass flux of any conservative pollutant at any x -section is conserved. The solutions to these equations for circular jets are summarized in Table 2-1.

2.2.2 Simple Plumes

A plume is produced from a steady discharge of a fluid whose motion is controlled by its buoyancy, with negligible effect of initial momentum. First, a plane plume of density ρ_0 issued into a stagnant unstratified ambient fluid of density ρ_a is considered. It is assumed that $\Delta\rho_0/\rho_a \ll 1$ (true for most practical cases), where the initial density

defect $\Delta\rho_0 = \rho_a - \rho_0$. After some manipulation, the Reynolds-averaged Navier-Stokes equation in x direction becomes:

$$u \frac{\partial u}{\partial x} + v \frac{\partial u}{\partial y} = \frac{1}{\rho_a} \frac{\partial \tau}{\partial y} + g \frac{\Delta\rho}{\rho_a} \quad (2.9)$$

where $\Delta\rho = \rho_a - \rho$; and ρ is the plume density. For a plane plume, the continuity equation and pollutant conservation equation can be simplified in the same form as for a plane jet (Eqs. (2.2) and (2.3)).

Using the integral method, Eq. (2.9) can be reduced to:

$$\frac{d}{dx} \int_0^\infty \rho u^2 dy = \int_0^\infty g \Delta\rho dy \quad (2.10)$$

Eq. (2.10) says that axial momentum flux increases in x direction, and the increase rate is equal to the buoyancy per unit length (in x direction) of the plume. For a plane plume, the continuity equation and pollutant conservation equation can be reduced the same as Eqs. (2.5) and (2.6). Eq. (2.5) states that the volume flux of a plume increases due to the entrainment of ambient fluid, and Eq. (2.6) states that although the concentration of pollutant decreases, its total mass flux is conserved. Note that C in Eq. (2.6) can be also interpreted as $g\Delta\rho$, and then Eq. (2.6) becomes the integral form of buoyancy conservation equation.

Experimental results show that: similarly as for jets, the plume velocity or concentration also exhibit self-similarity and the Gaussian distribution can well describe it. Using the Gaussian profiles (Eqs. (2.7) and (2.8)), the analytical solutions for a plane plume can be derived as shown in Table 2-2. The coefficients differ slightly in different references as they are determined using the results of different experiments. Here, to constitute the solutions, an useful dimensionless parameter is introduced: the densimetric Froude number at the slot exit $F_0 = U_0 / \sqrt{g (\Delta\rho / \rho_a) b_0}$ (for circular plume, $F_0 = U_0 / \sqrt{g (\Delta\rho / \rho_a) d_0}$).

For a circular plume, the Reynolds-averaged Navier-Stokes equations, continuity equation and pollutant conservation equation can be simplified, and the integral method can be used to obtain their integral forms of the equations. These equations indicate that: the momentum flux in the plume increases with axial (x) direction, and the increase rate is equal to the buoyant force per unit axial length; the volume flux in the plume increases due to the entrainment of ambient fluid; the pollutant mass flux (or the flux of density defect) remains invariant in the axial direction. The analytical solutions for a circular plume are also presented in Table 2-2. The constants in these equations change slightly in different references where different experimental results were used.

2.2.3 Buoyant Jets

For a buoyant jet, the initial momentum flux cannot be neglected. Near the nozzle (slot) exit, it is expected that the buoyant flow will be like a jet; after some distance from the exit where the increase of momentum flux is much larger than the initial momentum flux, the buoyant flow will behave like a plume. For a plane buoyant jet, based on dimensional analysis, a characteristic length scale to judge whether the buoyant flow behaves like a jet or plume may be defined as:

$$L_M = \frac{M_0}{B_0^{2/3}} \quad (2.11)$$

where the initial specific momentum flux $M_0 = qU_0$; the initial specific buoyancy flux $B_0 = qg \Delta\rho_0/\rho_a$. If the jet centerline trajectory $l \ll L_M$, the buoyant jet can be treated as a pure jet and the simple jet equations can be used; if $l \gg L_M$, it can be treated as a pure plume and the simple plume equations are valid. Buoyant jets will be plume-like beyond $l/L_M \geq 4\sim 5$ (Kotsovinos and List 1977; Papanicolaou and List 1988).

Characteristic length scale of jet/plume can only roughly help us calculate the evolution of a buoyant jet. The Reynolds equations, continuity equation and pollutant mass conservation equations can be simplified and the integral method can be used to obtain the analytical solutions. For a plane buoyant jet, the integral forms of the momentum, continuity, pollutant mass (or buoyancy) conservation equations are the same as Eqs. (2.10), (2.5) and (2.6), respectively. Here, for a buoyant jet, the integral form of energy equation needs to be introduced (as a result of multiplying Eq. (2.9) by u and integrating from $y = 0$ to $y = \infty$):

$$\frac{d}{dx} \int_0^{\infty} \frac{\rho u^2}{2} u dy = - \int_0^{\infty} \tau \frac{\partial u}{\partial y} dy + \int_0^{\infty} g \Delta \rho u dy \quad (2.12)$$

Eq. (2.12) states that the flux of kinetic energy in the jet plume is decreased by turbulence production (first term in the right hand side of Eq. (2.12)) and increased by the work done by buoyancy (second term in the right hand side).

The Gaussian type self-similarity equations are still valid for plane buoyant jets. Using Eqs. (2.7) and (2.8), as well as the experimental results on the jet spreading rate db/dx and on the ratio of the concentration half-width to the velocity half-width b_C/b , and after some mathematical manipulations, the solutions for a plane buoyant jet can be obtained as shown in Table 2-3. It is interesting to note that: in Table 2-3, the jet centerline concentration or velocity equation is composed of two parts, corresponding to two limits (pure jet-like or pure plume-like conditions).

The characteristic length scale for a buoyant circular jet or plume is:

$$L_M = \frac{M_0^{3/4}}{B_0^{1/2}} \quad (2.13)$$

Similarly, for a buoyant circular jet, the integral equations of the momentum, continuity, pollutant mass (or buoyancy) conservation and kinetic energy can be obtained. Using

the Gaussian distribution for jet velocity or concentration and some experimental data, the analytical solutions for buoyant circular jets are shown in Table 2-3.

2.3 Effect of Boundaries on Jets and Plumes

In this section, the effect of different types of boundaries on jets and plumes will be considered, including the solid bed (wall), the free surface of ambient fluid, the coflowing or crossflowing ambient fluid, and the neighboring jets in the case of multiple jets.

2.3.1 Wall Jets

Wall jets are the jets discharged tangentially or at certain angles to a solid boundary (wall) (see Fig. 2-2). A simple case is first considered: a plane jet discharged tangentially to a smooth flat plate in deep still ambient fluid of the same kind. For turbulent plane wall jets with high Reynolds numbers ($R_0 = U_0 b_0 / \nu = 10^4 \sim 10^5$, where ν is the kinematic viscosity of the fluid) at the slot exit, the length of the potential core will be (6.1~6.7) b_0 (Rajaratnam 1976), which is in the same range as for simple jets. As expected, experiments show that: near the wall, there exists a thin layer (boundary layer) where the jet velocity increases from zero at the wall to a maximum velocity u_m ; above the boundary layer (named free mixing region), the jet velocity decreases from u_m to zero at some large distance y from the wall. Similarly as for simple jets, the jet width may be defined as where the jet velocity is 50% (or 37%) of u_m and $\partial u / \partial y < 0$ (i.e. in the free mixing region). In the boundary layer region, the boundary layer theories may be used to further divide this region into two or three sub-layers: in the sub-layer very close to the wall, the velocity distribution is linear with y ; some distance away from the wall, the velocity distribution can be described by the

logarithmic law (Schlichting and Gersten 2000). For the velocity distributions of the entire wall jet, after some distance (about $20 b_0$) from the slot exit, they exhibit self-similarity (Förthmann 1934; Verhoff 1963). Verhoff (1963) proposed an empirical equation which agreed well with the experimental data:

$$\frac{u}{u_m} = 1.48 \left(\frac{y}{b}\right)^{1/7} \left[1 - \operatorname{erf}\left(0.68 \frac{y}{b}\right)\right] \quad (2.14)$$

Using the equations of motion and the integral method, the following results for plane wall jets are obtained: $u_m \propto x^{-1/2}$; $b \propto x$. The detailed results are listed in Table 2-4. To study the effect of wall roughness on wall jets, readers may refer to Rajaratnam (1967), Tachie et al. (2004), Dey et al. (2010) and Rostamy et al. (2010). To study the jets impinging on walls, readers may refer to Beltaos and Rajaratnam (1972), Rajaratnam (1976) and Chan et al. (2003).

For non-buoyant circular wall jets (herein termed “bluff wall jet” to include semi-circular and rectangular wall jets with aspect ratio not very different from unity; the properties of bluff jets are not very different from those of circular jets), a number of studies have been conducted: square wall jets by Sforza and Herbst (1970), circular wall jets by Newman et al. (1972), bluff (including square, rectangular, circular, elliptic, and equilateral triangular) wall jets by Rajaratnam and Pani (1974), square wall jets by Lübcke et al. (2003) and circular wall jets by Agelin-Chaab (2010). These experiments show that after some distance from the potential core, the velocity distributions both in the vertical central plane and in the horizontal plane (see Fig. 2-2) are self-similar. From similarity analysis on the equations of motion or from dimensional analysis, the following results can be obtained for bluff wall jets: $u_m \propto x^{-1}$; $b_y \propto x$; $b_z \propto x$ (Rajaratnam 1976). Experimental results support these predictions, and the results are listed in Table 2-4.

2.3.2 Surface Jets

A surface jet can be produced by discharging a fluid at the surface of an ambient fluid (see Fig. 2-3). One typical example is the surface discharge of heated water from a power plant through either an open-channel or a pipe into an ocean, a lake or river. Rivers flowing into lakes, reservoirs and oceans and storm water discharges into rivers may be also viewed as surface jets. In this section, our attention will be limited in the region from the end of the jet potential core to the end of the near-field (where the mixing is still dominated by the jet momentum and buoyancy). The length of the near field is in the order of $100\sqrt{A_0}$ (Rajaratnam 1984), where A_0 is the cross-sectional area of the flow at discharge. For the mixing in the far-field (where the turbulence in rivers, lakes or oceans dominates further mixing), readers can refer to Fischer et al. (1979) and Rutherford (1994).

Non-buoyant plane surface jets in stagnant water are now considered. Eqs. (2.1) - (2.8) for plane submerged jets also work for plane surface jets. Using the integral method and some mathematical manipulations, some useful results can be obtained: $u_m \propto x^{-1/2}$; $b \propto x$; $C_m \propto x^{-1/2}$, which are in the same form as those for plane submerged jets (Table 2-1). Experiments on plane surface jets were conducted by Chu and Vanvari (1976), Rajaratnam and Humphries (1984) and others. The experimental results are listed in Table 2-5. The results confirm that essentially a plane surface jet is quite similar to half of the corresponding plane submerged jet, but with slightly different coefficients. For example, the jet spreading rate of plane surface jets $db/dx = 0.07$, smaller than the value of 0.10 for plane submerged jets.

Next, non-buoyant bluff surface jets in stagnant water are considered. From the experiments of Rajaratnam and Humphries (1984), the Gaussian function describes the velocity distributions well both in vertical (half-Gaussian) and transverse directions,

unless there is excess wave generation at the water surface (in this case u_m occurs some distance below the water surface). Using the integral method, it can be shown that: $u_m \propto x^{-1}$; $b_z \propto x$; $b_y \propto x$, which are in the same forms as for circular submerged jets. Rajaratnam and Humphries' experimental results show that: the jet spreading rate in the transverse direction $db_z/dx = 0.09$, twice of that in the vertical direction $db_y/dx = 0.044$. The phenomenon of the several times faster transverse spreading has also been observed in the studies of Anthony and Willmarth (1992), Gholamreza-kashi et al. (2007), and Cuthbertson and Davies (2008). These studies further found that: there exists a thin layer (called "surface current") at the free surface, which exhibits even faster transverse spreading compared to that below the layer. Comparing Table 2-5 with Table 2-4, one may find that surface jets are somehow similar to wall jets, e.g., they both spread faster in the horizontal direction than in the vertical direction due to the boundary constraint in the vertical direction, and they have similar forms of jet equations.

For the surface discharges such as heated water into rivers or wastewater into the oceans, the effect of buoyancy needs to be considered. Experimental results have indicated that the behavior of buoyant surface jets is mainly controlled by three parameters: the Richardson number at the outfall, $Ri_0 = gd_0\Delta\rho_0/(\rho_a U_0^2)$; the depth (thickness) of the surface jet, d_0 (or b_0 for a plane jet); the depth of the surface stratified layer formed at the end of the near-field of the surface jet, $\overline{b_\infty}$. For a buoyant surface jet with a fixed Ri_0 , depending on the value of $d_0/\overline{b_\infty}$, there could be four possible hydraulic phenomena: a surface jet, a surface (density) jump at the outfall, a surface jet followed by a surface jump, or a drowned jump. Rajaratnam and Subramanyan (1985) presented a graph to distinguish which of the four possibilities may happen for a plane buoyant surface jet. For the case of a pure plane buoyant surface jet (without any jump),

the experiments of Rajaratnam and Subramanyan (1985) show that: initially the jet spreading rate db/dx follows the equation of the plane non-buoyant surface jet, but after some longitudinal distance, the spreading rate slows down, and eventually the jet thickness approaches a constant. In other words, generally the buoyancy effect constrains the spreading of a plane surface jet. Their results also indicate that: u/u_m is self-similar at different x sections, however these self-similarities can no longer be described by the Gaussian distribution and seem to be related with Ri_0 . The results of Chu and Vanvari (1976) reveal that: the entrainment coefficient α_e of a plane buoyant surface jet decreases continuously with the increase of bulk Ri (defined as $U_0 d_0 g \Delta \rho_0 / (\rho_a u_m^3)$) with x ; and α_e equals to zero when Ri increases to 0.2.

For bluff buoyant surface jets, a number of experiments have shown that the jet behavior is strongly affected by Ri_0 at the outfall. For convenience, bluff surface jets may be classified into two classes, the small Ri_0 class ($Ri_0 \leq 0.1$) and the large Ri_0 class ($Ri_0 > 0.1$). From a number of experiments, the common findings for the two classes are that: the vertical velocity profile $u(y)$ in the center-plane and the transverse (across the jet) velocity profile $u(z)$ just below the water surface are self-similar; and the self-similarities can be well described by half-Gaussian or Gaussian distribution. Using the similarity analysis of the simplified equations of motion, the following relations can be obtained: for the small Ri_0 class, $u_m \propto x^{-1}$, $C_m \propto x^{-1}$, $b_y \propto x$, $b_z \propto x$; and for the large Ri_0 class, $u_m \propto x^{-1/3}$, $C_m \propto x^{-2/3}$, $b_y = \text{constant}$, $b_z \propto x$. Detailed results are listed in Table 2-6.

2.3.3 Jets and Plumes in Coflow

Similarly as solid bed or free surface of ambient fluid, coflowing or crossflowing ambient fluid itself can be viewed as some sort of boundary affecting jet behavior. Jets

in coflow exist when jets are discharged in the direction of flowing ambient fluids (Fig. 2-4). Extensive experimental or numerical studies show that: beyond the potential core, the jet concentration and the jet excess velocity relative to the ambient velocity exhibit self-similarity. The self-similarity may be described by the Gaussian distribution, exponent function, or cosine expression (Rajaratnam 1976; Lee and Chu 2003). In the following, plane jets and circular jets in uniform coflow will be first briefly introduced.

For coflowing plane jets, the integral form of equation of motion is:

$$\frac{d}{dx} \int_0^{\infty} \rho u \Delta u dy = 0 \quad (2.15)$$

where $\Delta u = u - U_a$, the jet excess velocity. Eq. (2.15) states that the excess momentum flux is conserved in x direction. Using Eq. (2.15) and similarity analysis, Rajaratnam (1976) obtained the following asymptotic relations: for the strong jet region (i.e. $\Delta u_m / U_a \gg 1$), $\Delta u_m \propto x^{-1/2}$ and $b \propto x$; and for the weak jet region (i.e. $\Delta u_m / U_a \ll 1$), $\Delta u_m \propto x^{-1/2}$ and $b \propto x^{1/2}$. Based on the experimental results in the literature, Rajaratnam (1976) derived that:

$$\frac{\Delta u_m}{\sqrt{U_0(U_0 - U_a)}} = \frac{3.41}{\sqrt{x/b_0}} \quad (2.16)$$

$$\frac{b}{b_0} = 0.118 \frac{x}{b_0} \frac{1}{1 + \frac{0.41}{\sqrt{\alpha(\alpha - 1)}} \sqrt{x/b_0}} \quad (2.17)$$

where $\alpha = U_0 / U_a$, the ratio of jet exit velocity to ambient velocity. Note that Rajaratnam (1976) also summarized other more complex forms of equations for Δu_m and b , which were derived by Patel (1971) and Pande and Rajaratnam (1979).

For circular jets in coflow, the integral momentum equation can be derived:

$$\frac{d}{dx} \int_0^{\infty} \rho 2\pi r u \Delta u dr = 0 \quad (2.18)$$

which says that the jet excess momentum is conserved in axial direction. Using Eq. (2.18) and similarity analysis on the equations of motion, Rajaratnam (1976) presented the following asymptotic relations: for the strong jet region (i.e. $\Delta u_m/U_a \gg 1$), $\Delta u_m \propto x^{-1}$ and $b \propto x$; for the weak jet region (i.e. $\Delta u_m/U_a \ll 1$), $\Delta u_m \propto x^{-2/3}$ and $b \propto x^{1/3}$. Pande and Rajaratnam (1979) proposed a complex expression for Δu_m . Lee and Chu (2003) also derived asymptotic solutions for circular jets in coflow: for the strong jet region, the jet solution is assumed to be the same as in stagnant water (see Table 2-1); for the weak jet region,

$$\frac{\Delta u_m}{U_a} = 2.14 \left(\frac{x}{l_m^*} \right)^{-2/3} \quad (2.19)$$

$$\frac{b}{l_m^*} = 0.385 \left(\frac{x}{l_m^*} \right)^{1/3} \quad (2.20)$$

where l_m^* is the excess momentum length scale defined as $M_{e0}^{1/2}/U_a$; $M_{e0} = (U_0 - U_a)U_0\pi d_0^2/4$, the jet specific excess momentum at discharge.

To completely model circular jets in coflow, Lee and Chu (2003) formulated an integral model based on a Lagrangian jet spreading hypothesis:

$$U^{*2} + U^* - \frac{1}{\pi B^{*2}} = 0 \quad (2.21)$$

$$\frac{dB^*}{dx} = \beta_s \frac{U^*}{1 + U^*} \quad (2.22)$$

where $U^* = \Delta U/U_a$; $B^* = B/l_m^*$; ΔU and B are respectively the excess velocity and half of the width of the top-hat profile (instead of the Gaussian profile) of an equivalent jet, which carries the same mass flow and excess momentum flux as the actual jet; $\beta_s = dB/dx$ in stagnant water. It can be proved that $\Delta U = \Delta u_m/2$ and $B = \sqrt{2}b$, where Δu_m and b are respectively the maximum excess velocity and 37% half-width for the Gaussian profile. From Eqs. (2.21) - (2.22), ΔU and B can be solved. The actual jet centerline dilution can be obtained:

$$S_c = \frac{C_0}{C_m} = \frac{\lambda^2 \pi B^2 (U_a + \frac{2}{1 + \lambda^2} \Delta U)}{2Q_0^2} \quad (2.23)$$

where Q_0 and C_0 are the initial jet discharge and concentration, respectively; λ is the ratio of concentration half-width to velocity half-width using the Gaussian profile ($\lambda \approx 1.2$). The modeling results of Lee and Chu (2003) reveal that: the centerline dilution of a circular jet in coflow is only slightly smaller than that in stagnant water; and the centerline excess velocity decays in a similar way as in stagnant water.

2.3.4 Jets and Plumes in Crossflow

Now consider a non-buoyant circular jet discharged at an oblique angle (but not 0 or 180 degree) to a flowing ambient fluid. In fact, most outfalls or diffusers in oceans or rivers discharge effluents as jets in crossflow, as the jet (effluent) dilution can be considerably enhanced even in a weak crossflow (Rajaratnam 1976; Lee and Chu 2003). Jets in crossflow has been studied extensively by Abramovich (1963), Rajaratnam (1976), Fischer et al. (1979), Wright (1977; 1984), Andreopoulos (1985), Hodgson and Rajaratnam (1992), Margason (1993), Smith and Mungal (1998), Lee and Chu (2003), Huang et al. (2005), Kikkert et al. (2009) and others. According to these studies, the evolution of jets in crossflow can be divided into three regions: the potential core region, the maximum deflection region, and the vortex region (see Fig. 2-5). The length of the potential core has been found to be mostly controlled by the relative strength of the jet compared to the crossflow ($\alpha = U_0/U_a$), and typically in the range of $2d_0$ to $6d_0$ which is smaller than that of a free jet (Pratte and Baines 1967).

Beyond the potential core region, the jet would be largely deflected due to the stagnation pressure exerted by the free stream and the entrainment of ambient fluid (and thus horizontal momentum). Jet deflection probably is the most distinct feature in

crossflow. After the maximum deflection region, the jet would be gradually parallel to the direction of ambient flow. Laboratory experiments (Abramovich 1963; Hodgson and Rajaratnam 1992; Lee and Chu 2003) and numerical simulations (Lee and Chu 2003) have found that: after some distance beyond the potential core, the jet cross-section would be like a kidney shape with a pair of two counter-rotating vortices (see Fig. 2-5). The vortex pair significantly entrains ambient fluid in the form of tornado vortices into the jet (Lee and Chu 2003), which explains the considerable enhancement of jet dilution in crossflow. The concentrations at the centers of the two vortices have been found to be about 1.1-1.6 times of the jet centerline concentration (Hodgson and Rajaratnam 1992; Lee and Chu 2003).

For non-buoyant jets in crossflow, it is common to analyze them in three regions: the momentum dominated near field (MDNF), the momentum dominated far field (MDFF) and the transition between MDNF and MDFF. If the jet trajectory $\xi \ll l_m$, where l_m is defined as:

$$l_m = \frac{M_{v0}^{1/2}}{U_a} \quad (2.24)$$

and M_{v0} is the vertical momentum at the exit, then the jet is in MDNF, where the effect of jet momentum is much stronger than that of the ambient crossflow. In MDNF, the classic equations for jets in stagnant ambient fluid are approximately valid. If $\xi \gg l_m$, the jet is in MDFF, where the effect of ambient crossflow is dominant over the jet momentum. In MDFF, the jet properties can be studied with physical and numerical models. Fischer et al. (1979) used dimensional analysis to find the asymptotic formulas for MDNF and MDFF. Lee and Chu (2003) studied the jets in MDFF based on the analogy to advected line puffs. Using length scale analysis and numerical models, they proposed the formulas which can represent satisfactorily experimental results:

$$\frac{y_c}{l_m} = 1.56\left(\frac{x}{l_m}\right)^{1/3} \quad (2.25)$$

$$b_{vc} = 0.28y_c \quad (2.26)$$

$$S_c = 0.46 \frac{U_a y_c^2}{Q_0} \quad (2.27)$$

where y_c is the vertical location of the centerline concentration; b_{vc} is the vertical centerline half-width defined by 37% of the centerline concentration; S_c is the centerline dilution.

The most common jet discharge angle in crossflow is 90 degree, i.e. jets are discharged at right angle to the ambient crossflow. Rajaratnam (1976) summarized the early studies in 1950s to 1970s that mostly focused on jet trajectories. Hodgson and Rajaratnam (1992) conducted detailed laboratory experiments on circular jets at right angle to crossflow and proposed the following equations:

$$S_c = 1.09(\alpha x/d_0)^{0.56} \quad (2.28)$$

$$\frac{y_c}{\alpha d_0} = 1.46\left(\frac{x}{\alpha d_0}\right)^{0.26} \quad (2.29)$$

$$\frac{W_z}{\alpha d_0} = 1.20\left(\frac{x}{\alpha d_0}\right)^{0.29} \quad (2.30)$$

$$\frac{W_y}{\alpha d_0} = 0.78\left(\frac{x}{\alpha d_0}\right)^{0.37} \quad (2.31)$$

where W_z and W_y are the jet width and thickness (see Fig. 2-5). Eqs. (2.28) - (2.31) have also been validated by a field experiment in the Lesser Slave River, Canada. Hodgson and Rajaratnam's equations are mainly derived based on the experiments conducted in the range of $x/\alpha d_0 = 1 \sim 1000$. It is interesting to note that Hodgson and Rajaratnam's expressions fit the experimental data satisfactorily both in MDNF, MDFF and the transition between the two.

Now consider a circular plume in crossflow. Similarly as l_m , a length scale l_b needs to be defined to compare the relative strength of plume buoyancy with crossflow:

$$l_b = \frac{B_0}{U_a^3} \quad (2.32)$$

If the jet trajectory $\xi \ll l_b$, then the plume is in the buoyancy dominated near field (BDNF) where the effect of buoyancy is dominant over crossflow; if $\xi \gg l_b$, then plume is in the buoyancy dominated far field (BDFF) where the effect of crossflow is more pronounced than the buoyancy. In BDNF, the plume is essentially vertical and only slightly advected, thus the equations for plumes in stagnant fluid are approximately valid. Similarly as jets in crossflow, after some distance from the nozzle, the plume cross-section will become a kidney shape that is made up of a vortex pair, and the concentration at the centers of the vortices have been found to be 1.4-1.7 times of the plume centerline concentration. In BDFF, the plume bends over and finally approaches the ambient flow direction. The analysis on the plume properties in BDFF relies on experiments or numerical models. Based on the equations of motion and the use of similarity solutions, Fischer et al. (1979) derived asymptotic formulas for the BDNF and BDFF. As the plume in BDFF behaves similarly as the advected line thermal, Lee and Chu (2003) used numerical models to obtain the plume characteristics. The predictions are comparable to experimental results. The formulas Lee and Chu derived are:

$$\frac{y_c}{l_b} = 1.3 \left(\frac{x}{l_b} \right)^{2/3} \quad (2.33)$$

$$b_{vc} = 0.4y_c \quad (2.34)$$

$$S_c = 0.46 \frac{U_a y_c^2}{Q_0} \quad (2.35)$$

Note Eq. (2.35) for BDFF is exactly in the same form as the equation for MDFF.

Now consider the case of a circular buoyant jet in crossflow. In this case, the relative strengths of buoyancy, momentum and crossflow need to be considered. If

$l_b \ll l_m$, then the jet would in sequence experience MDNF, MDFF and BDFF; if $l_b \gg l_m$, then the sequence would be MDNF, BDNF and BDFF (Fischer et al. 1979; Lee and Chu 2003; Lam et al. 2006). Equations should be selected carefully according to the studied location of the jet (e.g., in MDNF or MDFF or BDNF or BDFF). The transitions between MDNF and MDFF and between BDNF and BDFF are better treated using numerical models (Lee and Chu 2003).

For jets directed at an oblique angle to crossflow, the reader may refer to Platten and Keffer (1971) and Kikkert et al. (2009). For plane jets and plume in crossflow, the reader may refer to Girshovich (1966), Jones and Wille (1996), Kalita et al. (2002) and Huang et al. (2005).

2.3.5 Multiple Jets

Effluents may be discharged via single port outfalls or multiport diffusers. Multiport diffusers are commonly used given their fast mixing and diluting ability and thus less adverse impacts on the environment. The jets issuing from the ports of a multiport diffuser are usually viewed as multiple jets. The characteristics of multiple jets are primarily determined by the arrangements of multiport diffusers. Generally, multiport diffusers can be classified into three categories: unidirectional diffuser (where net horizontal momentum flux is imparted perpendicular to diffuser line), staged diffuser (where net horizontal momentum flux is imparted parallel to the diffuser line), and alternating diffuser (where no net horizontal momentum flux is imparted) (Doneker and Jirka 2007). Fig. 2-6 illustrates one typical example of a unidirectional diffuser. It can be expected that different types of diffusers have significantly different jet mixing and spreading properties.

Studies on multiple jets (or diffusers) have been reported extensively in the past decades (Knystautas 1964; Jirka and Harleman 1973; Fischer et al. 1979; Lee and Jirka 1980; Adams 1982; Jirka and Akar 1991; Huang et al. 1996; Kim and Seo 2000; Lee and Chu 2003; Wang and Davidson 2003; Tian et al. 2004; Tang et al. 2008; Zhang and Zhu 2011; and others). Most of these studies focused on the deep water ambient condition (e.g., in oceans and lakes), and limited studies dealt with the shallow water condition (e.g., in rivers). In this section, only the deep water condition is considered. Theoretically, multiple jets in sequence experience: the individual free jet zone (where jets has no effect on each other), the jet merging zone (where the interaction between jets are strong), and the 2-dimentional zone thereafter (Parr and Sayre 1979; Zhang and Zhu 2011) (see Fig. 2-7). In practice, multiple jets are usually simplified as one line momentum source, neglecting the interactions between individual jets that are complex and not well understood (Jirka and Harleman 1973; Lee 1980).

Previously, some basic characteristics of three-dimensional free jets and two-dimensional (plane) jets have been introduced; hence, in the following, the studies on the merging process of unidirectional non-buoyant circular jets will be briefly summarized. As yet, only limited studies on jet merging have been reported (Knystautas 1964; Hodgson et al. 1999; Pun et al. 2000; Wang and Davidson 2003; Pani et al. 2009). To calculate the concentration or velocity field in the jet merging process, the most widely-used method is superposition. However, as the momentum equation is nonlinear, simple superposition of individual jets would overestimate the jet velocity. Knystautas (1964) studied the velocity field of merging jets in still ambient fluid and showed that the jet velocity can be modeled by superposing the momentum (u^2) of individual jets (based on Reichardt's hypothesis). Hodgson et al. (1999) proposed the following equation for the velocity field of the merging jets in still water:

$$u^2 = \sum_{i=-n}^{i=+n} u_i^2 = u_m^2 \sum_{i=-n}^{i=+n} \exp \left[-150 \left(\frac{z - iL}{x} \right)^2 \right] \quad (2.36)$$

where $(2n+1)$ is the number of jets; the centerline velocity of each individual jet $u_m = 6.13U_0d_0/x$; L is the distance between the centers of neighboring jets; z is the transverse distance from the central jet axis. Hodgson et al. (1999) extended the Reichardt's hypothesis on lateral transport of momentum to the lateral transport of pollutant, and showed that uC is additive. After solving the velocity field from Eq. (2.36), the pollutant concentration field can be obtained from Eq. (2.37):

$$uC = \sum_{i=-n}^{i=+n} u_i C_i = u_m C_m \sum_{i=-n}^{i=+n} \exp \left[-130 \left(\frac{z - iL}{x} \right)^2 \right] \quad (2.37)$$

where the centerline concentration of each individual jet $C_m = 5.34C_0d_0/x$. Hodgson's experimental results validated the use of Eqs. (2.36) - (2.37).

Hodgson et al. (1999) revealed some basic physics in the jet merging, where the jet spreading rate db/dx and the ratio of the jet concentration half-width to the velocity half-width b_C/b are both assumed to be constant during merging. Wang and Davidson (2003) developed a similar model for jet merging in stagnant ambient fluid, but allows the change of db/dx and b_C/b during merging, as well as the change of these parameters in horizontal (the jet merging) plane and vertical (the free entrainment) plane. Theoretical analysis and experimental data indicate that: the jet merging in stagnant ambient fluid occurs at $4.5 < x/L < 12$. Note that in Wang and Davidson (2003), the start of merging refers to the location where the jet interaction begins to influence the bulk properties of the central jet, which is beyond the location where the physical jet boundaries start intersecting. By studying their experimental data and that of Knystautas (1964), Wang and Davidson (2003) found that: during the jet merging, the jet spreading rate db/dx (or db_C/dx) increases by 30% in the vertical plane, while it

decreases by a similar amount in the horizontal plane; the ratio of velocity half-width in the vertical plane to that in the horizontal plane $b_{vertical}/b_{horizontal}$ increase from 1 to 1.5 during merging; the ratio of concentration half-widths $b_{C,vertical}/b_{C,horizontal}$ increase from 1 to 1.8. Obviously, the jet merging process constrains the jet spreading and thus dilution in the jet merging plane, while accelerates them in the free entrainment plane. This phenomenon is similar to the boundary effects found in wall jets or surface jets.

In recent years, researchers started to study the jet merging in coflow (Pun et al. 2000; Pani et al. 2009). Pun et al. (2000) developed a multiple-point hybrid model for merging jets in coflow, which combines a length-scale model and an Eulerian-integral model. The model allows multiple transition points for each parameter (jet velocity, spread and dilution), instead of a single transition point for all these parameters. The multiple-point hybrid model is shown to be able to significantly reduce transition errors during merging compared to the single-point model, and predicts favorable results compared to the integral solution. Pani et al. (2009) developed a model based on Reichardt's hypothesis for multiple coflowing jets. Instead of momentum (u^2) is additive in stagnant water, Pani et al. showed that the excess momentum ($u\Delta u$) is additive in coflow and follows Gaussian distribution. Using the method of superposition and a generalized spreading hypothesis, Pani et al. presented the equations for predicting the velocity field and centerline dilution downstream of multiple circular jets in coflow, which appeared to agree with the experimental data.

2.4 Multiphase Jets and Plumes

In this section, two kind of multiphase jets and plumes will be introduced: bubbly jets and plumes and slurry jets and plumes. Both of them have wide engineering applications.

2.4.1 Bubbly Jets and Plumes

Bubbly jets are produced by injecting gas-liquid mixtures into liquids, while bubble plumes are produced by injecting gases into liquids. Bubble plumes and bubbly jets are widely used to achieve artificial aeration, circulation and mixing in confined reactors, aeration tanks, polluted water bodies, ice-covered rivers, and deep stratified lakes and reservoirs (Whipple and Yu 1970; Wüest et al. 1992; Schierholz et al. 2006; Lima Neto et al. 2007). Such kind of gas-liquid two phase flow is also common in hydraulic structures, e.g., the gas super-saturation downstream of hydro-power dams. So far, most of the early studies were conducted in confined setups, where the sizes and geometry of the setup further complicates the characteristics of bubbly jets and plumes (Lima Neto et al. 2008c). In this section, studies in stagnant water of relatively large scale will be first briefly introduced and then flowing ambient fluid will be considered.

For two-phase flows, the dissolving of the gas phase into the liquid phase can be derived from Fick's law of diffusion as (Mueller et al. 2002):

$$\frac{dC}{dt} = K_L a (C_s - C) \quad (2.38)$$

where C is the dissolved gas (e.g., oxygen) concentration in the liquid; C_s is the dissolved gas concentration at saturation; t is the time; K_L is the gas transfer coefficient; a is the gas-liquid interfacial area per unit liquid volume (also named the specific interfacial area). From Eq. (2.38), the gas transfer rate is mainly controlled by K_L and a ,

which differ significantly in different setups. Previous studies (Barnhart 1969; Motarjemi and Jameson 1978) have shown that these two parameters are greatly influenced by bubble size. Bubble size depends on a number of factors: nozzle sizes and types, initial gas volume fractions, the solubility and mass transfer ability of the gas, turbulence intensity and flow structure of the ambient liquid, impurities and surfactants in the ambient liquid, and etc. (Clift et al. 1978; Lima Neto et al. 2008a,b,c,d). Lima Neto et al. (2008b) proposed a criterion to judge the sizes and shapes of the bubbles produced by injecting a mixture of air and water into water: if the nozzle Reynolds number $Re = U_{w0}d_0/\nu_w < 8000$ (where U_{w0} is the superficial water velocity based on the water discharge at the nozzle and nozzle diameter d_0), then large and irregular bubbles will be produced; if $Re \geq 8000$, smaller and uniform bubbles will be produced. A decrease in gas discharge or an increase in liquid discharge will decrease the bubble size (Varley 1995; Lima Neto 2008b,d).

Now consider the vertical injection of a pure gas into a pure stagnant liquid. The bubbles produced at the orifice will coalesce/breakup and rise, inducing ambient liquid entrained into the bubble core and the dissolving of the gas into the ambient. Lima Neto et al. (2008a) studied air injection into still water with six different nozzles (single orifice, multiple orifices and airstone), and found that the water entrained into the bubble core under different initial air discharges Q_a and nozzle types can be described as a function of Q_a and vertical distance from the nozzles.

For a vertical bubbly jet in stagnant liquid, Milgram (1983), Brevik and Kristainsen (2002), and Lima Neto et al. (2008b) reported that: the bubble area typically only occupies 50-90% of the bubbly jet in the radial direction. Lima Neto et al. (2008b) studied bubbly jets produced by injecting a mixture of air-water into stagnant water and found that: the more uniform and smaller the bubble sizes, the wider the bubble core can

spread in the radial direction; within the bubbly jets, the radial distributions of the time averaged bubble concentration (void fraction) and water velocity of the mean flow can be well described by Gaussian distributions, similarly as for single-phase jets or plumes; db/dx of the bubbly jets is close to that of the pure water jet.

Although the existence of bubbles seems not to change the Gaussian profiles, the entrainment of the ambient into the bubbly jets is enhanced. Milgram (1983), Socolofsky and Adams (2002), Brevik and Kristainsen (2002), and Lima Neto et al. (2008b) reported an entrainment coefficient of bubbly jets in the range of 0.03-0.15, much larger than the values of pure jets or plumes. The additional entrainment probably associates with the bubble wakes (Leitch and Baines 1989) and additional liquid turbulence caused by interactions of the bubbles and their wakes (Lima Neto et al. 2008b). At a specific height of the centerline of a bubbly jet, Lima Neto et al. (2008b) compared the liquid volume flux Q_w of the bubbly jet with that of a pure water jet with the same nozzle diameter and water flow rate:

$$\frac{Q_w}{Q_{w(C_0=0)}} = 1 + 6.426 \times 10^6 \left(\frac{C_0}{Re}\right)^{3/2} \quad (2.39)$$

where the initial gas volume fraction $C_0 = Q_{a0}/(Q_{a0} + Q_{w0})$; Q_{a0} and Q_{w0} are the initial volumetric flow rates of air and water, respectively. It can be expected that the average dilution for a bubbly jet is larger than that of a pure jet due to the additional entrainment of ambient water as shown in the right hand side of Eq. (2.39).

For a bubbly jet injected horizontally into a stagnant liquid, there are only limited experimental studies (Varley 1995; Morchain et al. 2000; Fonade et al. 2001; Lima Neto et al. 2008d). Lima Neto et al. (2008d) studied the injection of air-water mixtures into a water tank of relatively large and reported that: first, the bubbly jet come out of the nozzle as a whole quasi-horizontal bubbly jet where bubble breakup/coalescence occurs and only a few bubbles escape from the bubbly jet and rise

vertically due to buoyancy; then, there follows a separation zone where the quasi-vertical bubble plume partially separates from the water jet (when the initial gas volume fraction $C_0 < 0.15$, the bubble plume completely separates from the water jet); finally, the bubble plume continues rising and the water jet impinges the water surface and becomes surface jet. In Lima Neto et al. (2008d), the length and width of the bubble plume, as well as the centerline trajectories of the bubble plume and water jet were also proposed in dimensionless forms.

Bubble properties and mean liquid flow of bubbly jets could be non-dimensionalized as functions of the initial gas volume fraction and nozzle Reynolds number for the vertical injection or as functions of the initial gas volume fraction and nozzle densimetric Froude number for the horizontal injection (Lima Neto et al. 2008b,d). The variation of bubble properties and mean liquid flow along the jet centerline and across the jet needs further study. For bubble plume modeling, the reader may refer to Bravo et al. (2007).

Crossflow will exert substantial effects on bubbly jets or bubble plumes, of which the most distinguishing is the separation of bubble plumes (named generally as dispersed phases) from the entrained ambient fluids (continuous phases) (Scolofsky and Adam 2002). So far, limited studies exist on bubbly jets or bubble plumes in crossflow. Socolofsky and Adams (2002) conducted laboratory experiments on bubble plumes produced by injecting air, air and oil, as well as air and alcohol in uniform crossflow. In weak crossflow, the separation between the bubble plumes and the entrained fluid does not occur before the plumes reach the surface. While in strong crossflow, the separation is significant and the separation height h_s can be given by an empirical relation:

$$h_s = \frac{5.1B_0}{(U_a u_s^{2.4})^{0.88}} \quad (2.40)$$

where U_a is the horizontal crossflow velocity; u_s is the bubble slip (terminal rise) velocity; $B_0 = Q_0 g'$; Q_0 is the discharge of the plume fluid; $g' = (\rho_a - \rho_p)g/\rho_a$; ρ_a is the ambient density of water; ρ_p is the density of the plume fluid. Socolofsky and Adams also reported that: before h_s , the plumes can be treated as single-phase plumes; after h_s , the bubble plumes follow the trajectory of the vector sum of u_s and U_a (i.e. the bubble plumes rise in a linear line), and the separated entrained fluid behaves like a momentum jet (the momentum is gained by the acceleration of bubbles before the separation).

2.4.2 Slurry Jets and Plumes

Slurry jets are produced by injecting a mixture of liquid phase and solid phase (such as sand or clay particles). Slurry jets have wide applications in pumping industrial (e.g., mining or petroleum) tailings into settling tanks, dredging and land reclamation, discharging storm water and industrial waters that have solid particles, and etc. A number of experimental and numerical studies in this area have been reported (Brush 1962; Singanetti 1966; Awaya et al. 1985; Parthasarathy and Faeth 1987; Mazurek et al. 2002; Jiang et al. 2005; Hall et al. 2010). Usually, two injection ways were used, vertically upward and vertically downward. In the following, the main focus will be on the vertically downward injection of slurry jets into stagnant ambient fluids. Compared to single-phase jets, the adding of the solid phase will change the properties of the flow (Sheen et al. 1994).

Previous experiments have indicated that the velocity and concentration of the solid phase across slurry jets follow self similar Gaussian distributions (Singanetti 1966; Jiang et al. 2005; Hall et al. 2010). In the slurry jets with dilute solid particles, Jiang et al. (2005) reported that the velocity and concentration of the liquid phase also

exhibit self similar Gaussian profiles. However, this may not be valid for the slurry jets with solid particles of high concentration.

The spreading of the solid phase has been found to increase linearly along the axial direction (Brush 1962; Mazurek et al. 2002; Hall et al. 2010). Brush (1962) reported that the spreading rate of the velocity of the solid phase db_s/dx depended on the particle size. Mazurek et al. (2002) confirmed this by photographic measurements on sand jets, and further generalized the spreading as a function of the initial densimetric Froude number of the solid particle. Recently, Hall et al. (2010) conducted detailed experiments on pure sand jets and sand-water slurry jets in stagnant water. With the densimetric Froude number at the nozzle exit ($F_0 = U_0/\sqrt{gd_0(\rho_s - \rho_w)/\rho_w}$ where U_0 is the initial velocity of the sand particle from a nozzle of diameter d_0 and ρ_s is sand density) in the range of 2 ~ 6, db_s/dx measured 0.087~0.109, not very different from that of single-phase jets in stagnant fluids. The difference lies in the ratio of concentration to velocity spreading rates of the solid phase ($b_{s,c}/b_s$). Hall et al. (2010) reported that, for sand jets and slurry jets with high F_0 ($F_0 \approx 6$), $b_{s,c}/b_s = 0.86 \sim 0.92$, which means the sand concentration spreads slower than the velocity; and for slurry jets with low F_0 ($F_0 \approx 2$), $b_{s,c}/b_s \approx 1.0$ which means they have almost equal spreading rates. This finding is contrary to the classic single-phase jet theory, which states that the concentration scale spreads faster than the velocity scale ($b_c/b \approx 1.2$).

Similar as single-phase jets, along the axial direction of slurry jets, the velocity and concentration of both solid phase and liquid phase decay rapidly. According to Hall et al. (2010), beyond the potential core (about $2.9d_0F_0^{2/5}$), the axial concentration of the solid phase can be well described by:

$$\frac{C_m}{C_0} = \frac{17.12}{\left(\frac{x}{d_0F_0^{2/5}}\right)^{5/3} + 11.39} \quad (2.41)$$

In Eq. (41), the $-5/3$ power relation is very similar to that of single-phase plume (Table 2-2), as Eq. (2.41) was established in the region at $x > 5L_M$ where the buoyant slurry jet behaved like a slurry plume (Papanicolaou and List 1988). Similar $-5/3$ power relation was also built for the sand concentration in sand jets. For both sand jets and slurry jets, the axial velocity of the solid phase was found to decrease rapidly and then reach a final plateau region. Generally, before the plateau region, the axial velocity of the solid phase in slurry jets can be well represented by:

$$\frac{u_m F_0}{U_0} = \frac{1.63}{\left(\frac{x}{d_0 F_0}\right)^{1/3} + 0.56} \quad (2.42)$$

Similar as Eq. (2.42), for sand jets, before reaching the velocity plateau region, the axial sand velocity was also found to follow the $-1/3$ power relation, which is very similar to that of single-phase plumes (Table 2-2). The terminal (settling) centerline velocity of the solid phase was found in the range of $0.32 \sim 0.43$ m/s, which is larger than the settling velocity of 0.033 m/s for individual solid particles. The larger terminal velocity probably can be attributed to the interactions between solid particles, i.e. the wake of previous solid particles tends to decrease the drag forces for the following particles.

For the studies dealing with particle interactions, the reader may refer to Lain and Garcia (2006), Tamburello and Amitay (2008), and Yan et al. (2008). For the effect of solid particle size on velocity distribution, concentration profile and turbulent properties, the reader may refer to Azimi et al. (2011). For vertically upward slurry jets, the reader may refer to Jiang et al. (2005).

2.5 Future directions

Some of the basic characteristics of a variety of jets and plumes have been reviewed, including simple jets and plumes, buoyant jets, surface jets, wall jets, jets and plumes in coflow and crossflow, multiple jets, bubbly jets and plumes, and slurry jets and plumes. The turbulence and turbulence structures in these flows have not been discussed. Interested readers may refer to the works of Heskestad (1965), Wygnanski and Fielder (1969), and Launder and Rodi (1983). Also, the behaviors of jets and plumes in stratified environment have not been covered. The readers may refer to the works of Morton et al. (1956), Turner (1973), and Roberts et al. (1989 a, b). To facilitate the applications of jets and plumes theories, software packages have been developed. The USEPA-supported CORMIX is perhaps the most commonly-used expert system for dealing with environmental problems involving jets and plumes. Other models are VISJET and Visual Plume.

In addition to the simple jets and plumes, all the other varieties of jets and plumes still require research studies. This constitutes the general tone for the future research. Herein, some of key areas are listed as follows:

- Physics and models of bubbly jets, and their application in aeration and mixing of ponds, lakes, and wastewater treatment plants;
- Physics and models of slurry jets, and their industrial applications;
- Physics and models of three phase jets and plumes, especially oil-water-gas plumes produced by oil spills in oceans;
- Physics and models of jets and plumes in stratified environment;
- Development, improvement and validation of computational fluid dynamics (CFD) modeling (such as direct numerical modeling (DNS), large eddy simulation (LES), k-epsilon modeling and others).

References

- Abramovich, G.N. (1963). *The Theory of Turbulent Jets*. English translation published by M.I.T. Press, Massachusetts, 671 p.
- Adams, E.E. (1982). "Dilution analysis for unidirectional diffusers." *ASCE J. Hydr. Div.*, 108(HY3), 327-342.
- Agelin-Chaab, M. (2010). "Experimental study of three-dimensional offset jets and wall jets." Ph.D. Thesis, Department of Mechanical and Manufacturing Engineering, University of Manitoba, Winnipeg.
- Albertson, M.L., Dai, Y.B., Jensen, R.A., and Rouse, H. (1950). "Diffusion of submerged jets." *Trans. ASCE.*, 115, 639-697.
- Andreopoulos, J. (1985), "On the structure of jets in a crossflow," *J. Fluid Mech.*, 157, 163 – 197.
- Anthony, D. G., and Willmarth, W. W. (1992). "Turbulence measurements in a round jet beneath a free surface." *J. Fluid Mech.*, 243, 699-720.
- Awaya, Y., Fujisaki, K., and Matsunaga, K. (1985). "Transition in the behavior of sediment laden vertical buoyant jet." *J. Hydrosoci. Hydr. Eng.*, 3(1), 63-74.
- Azimi, A.H., Zhu, D.Z., and Rajaratnam, N. (2011). "Effect of particle size on the characteristics of sand jets in water." *J. Eng. Mech.*, 137(12), 822-834.
- Barnhart, E.L. (1969). "Transfer of oxygen in aqueous solutions." *J. Sanit. Eng. Div.*, 95(3), 645-661.
- Beltaos, S., and Rajaratnam, N. (1972). "Plane turbulent impinging jets." *J. Hydr. Res.*, 11, 29-59.
- Bravo, H.R, Gulliver, J.S., and Hondzo, M. (2007). "Development of a commercial code-based two-fluid model for bubble plumes." *Env. Modell. Software*, 22 (4), 536-547
- Brevik, I., Kristiansen, Ø. (2002). "The flow in and around air bubble plumes." *Int. J. Multiphase Flow*, 28, 617-634.
- Brush, L. M. J. (1962). "Exploratory study of sediment diffusion." *J. Geophys. Res.*, 67(4), 1427-1433.
- Chan, T., Zhou, Y., Liu, M., and Leung, C. (2003). "Mean flow and turbulent measurements of the impingement wall jet on a semi-circular convex surface." *Exp. Fluids*, 34(1), 140-149.

- Chen, C.J., and Rodi, W. (1980). *Vertical Turbulent Buoyant Jets - A Review of Experimental Data*. Pergamon Press, Oxford, 83 p.
- Chu, V.H., and Vanvari, M.R. (1976). "Experimental study of turbulent stratified shearing flow." *J. Hydr. Div., ASCE*, 102(6), 691-706.
- Clift, R., Grace, J.R., and Weber, M.E. (1978). *Bubbles, Drops, and Particles*. Academic Press, New York, 380 p.
- Cuthbertson, A. J. S., and Davies, P. A. (2008). "Deposition from particle-laden, round, turbulent, horizontal, buoyant jets in stationary and coflowing receiving fluids." *J. Hydr. Eng.*, 134(4), 390-402.
- Dey, S., Nath, T.K., and Bose, S.K. (2010). "Fully rough submerged plane wall-jets." *J. Hydro-Env. Res.*, 4(4), 301-316.
- Doneker, R.L., and Jirka, G.H. (2007). "CORMIX user manual – A hydrodynamic mixing zone model and decision support system for pollutant discharges into surface waters." U.S. EPA-823-K-07-001, 1-236.
- Fischer, H.B., List E.J., Imberger, J., Brooks, N.H. (1979). *Mixing in Inland and Coastal Waters*. Academic Press, New York, 483 p.
- Fonade, C., Doubrovine, N., Maranges, C., and Morchain, J. (2001). "Influence of a transverse flowrate on the oxygen transfer performance in heterogeneous aeration: Case of hydro-ejectors." *Water Res.*, 35(14), 3429-3435.
- Förthmann, E. (1936). "Turbulent jet expansion." English translation N.A.C.A. TM-789. (Original paper in German, 1934. Ing. Archiv., 5)
- Gholamreza-kashi, S., Martinuzzi, R.J., and Baddour, R.E. (2007). "Mean flow field of a nonbuoyant rectangular surface jet." *J. Hydr. Eng.*, 133(2), 234-239.
- Girshovich, T.A. (1966). "Theoretical and experimental study of a plane turbulent jet in a crossflow." *Fluid Dyn.*, 9, 84-86.
- Hall, N., Elenany, M., Zhu, D.Z., and Rajaratnam, N. (2010). "Experimental study of sand and slurry jets in water." *J. Hydr. Eng.*, 136(10), 727-738.
- Heskestad, G. (1965). "Hot-wire measurements in a plane turbulent jet." *Trans. ASME J. Appl. Mech.*, 1-14.
- Hinze, J.O., and Zijnen, B.G. Van Der Hegge (1949). "Transfer of heat and matter in the turbulent mixing zone of an axially symmetrical jet." *Appl. Sci. Res.*, A1, 435-461.
- Hodgson, J.E., and Rajaratnam, N. (1992). "An experimental study of jet dilution in crossflows." *Can. J. Civ. Eng.*, 19, 733-743.

- Hodgson, J.E., Moawad, A.K., and Rajaratnam, N. (1999). "Concentration field of multiple circular turbulent jets." *J. Hydr. Res.*, 37(2):249-256.
- Huang, J.F., Davidson, M.J., and Nokes, R.I. (2005). "Two-dimensional and line jets in a weak cross-flow." *J. Hydr. Res.*, 43(4), 390-398.
- Huang, H., Fergen, R.E., Rroni, J.R., and Tsai, J.J. (1996). "Probabilistic analysis of ocean outfall mixing zones." *J. Env. Eng.*, 122 (5), 359-367.
- Jiang, J. S., Law, A. W. K., and Cheng, N. S. (2005). "Two-phase analysis of vertical sediment-laden jets." *J. Eng. Mech.*, 131(3), 308-318.
- Jirka, G.H., and Akar, P.J. (1991). "Hydrodynamic classification of submerged multiport-diffuser discharges." *J. Hydr. Eng.*, 117(9), 1113-1128.
- Jirka, G.H., and Harleman, D.R.F. (1973). "The mechanics of submerged multiport diffuser for buoyant discharges in shallow water." *R.M. Parsons Laboratory Report*, Massachusetts Institute of Technology, Boston.
- Jones, W.P., and Wille, M. (1996). "Large-eddy simulation of a plane jet in a cross-flow." *Int. J. Heat and Fluid Flow*, 17, 296-306.
- Kalita, K., Dewan, A., and Dass, A.K. (2002). "Prediction of turbulent plane jet in crossflow." *Numer. Heat Transfer, Part A*, 41, 101-111.
- Kikkert, G. A., Davidson, M. J., and Nokes, R. I. (2009). "A jet at an oblique angle to a cross-flow." *J. Hydro-Env. Res.*, 3(2), 69-76.
- Kim, D.G., and Seo, I.W. (2000). "Modeling the mixing of heated water discharged from a submerged multiport diffuser." *J. Hydraul. Res.*, 38(4), 259-269.
- Knystautas, R. (1964). "The turbulent jet from a series of holes in Line." *Aeronaut. Q.*, 15, 1-28.
- Kotsovinos, N.E., and List, E.J. (1977). "Plane turbulent buoyant jet. Part I. Integral properties." *J. Fluid Mech.*, 81, 25-44.
- Lain, S., and Garcia, J. (2006). "Study of four-way coupling on turbulent particle-laden jet flows." *Chem. Eng. Sci.*, 61, 6775-6785.
- Lam, K.M., Lee, W.Y., Chan, C.H.C., and Lee, J.H.W. (2006). "Global behaviors of a round buoyant jet in a counterflow." *J. Hydr. Eng.*, 132(6), 589-604.
- Launder, B.E., and Rodi, W. (1983). "The turbulent wall jet - measurement and modeling." *Ann. Rev. Fluid Mech.*, 15, 429-459.
- Lee, J.H.W., and Chu, V.H. (2003). *Turbulent Jets and Plumes – A Lagrangian Approach*. Kluwer Academic Publishers, 390 p.

- Lee, J.H. W, Jirka, G.H. (1980). "Multiport diffuser as line source of momentum in shallow water." *Water Resour. Res.*, 16(4), 695-708.
- Leitch, A.M., Baines, W.D. (1989). "Liquid volume flux in a weak bubble plume." *J. Fluid Mech.*, 205, 77-98.
- Lima Neto, I.E., Zhu, D.Z., Rajaratnam, N., Yu T., Spafford., M., and McEachern, P. (2007). "Dissolved oxygen downstream of an effluent outfall in an ice-cover river: natural and artificial aeration." *J. Env. Eng.*, 133 (11), 1051-1060.
- Lima Neto, I.E., Zhu, D.Z. and Rajaratnam, N. (2008a). "Air injection in water with different nozzles." *J. Env. Eng.*, 134 (4), 283-294.
- Lima Neto, I.E., Zhu, D.Z. and Rajaratnam, N. (2008b). "Bubbly jets in stagnant water." *Int. J. Multiphase Flow*, 34 (12), 1130-1141.
- Lima Neto, I.E., Zhu, D.Z. and Rajaratnam, N. (2008c). "Effect of tank size and geometry on the flow induced by circular bubble plumes and water jets." *J. Hydr. Eng.*, 134 (6), 833-842.
- Lima Neto, I.E., Zhu, D.Z. and Rajaratnam, N. (2008d). "Horizontal injection of gas-liquid mixtures in a water tank." *J. Hydr. Eng.*, 134 (12), 1722-1731.
- Lübcke, H.M., Rung, Th., and Thiele, F. (2003). "Predication of the spreading mechanism of 3D turbulent wall jets with explicit Reynolds-stress closures." *Int. J. Heat Fluid Flow*, 24, 434-443.
- Margason, R.J. (1993). "Fifty years of jet in cross flow research." Computational and experimental assessment of jets in cross flow, AGARD, report CP-534.
- Mazurek, K.A., Christison, K., and Rajaratnam, N. (2002). "Turbulent sand jet in water." *J. Hydr. Res.*, 40(4), 527-530.
- Milgram, H. (1983). "Mean flow in round bubble plumes." *J. Fluid Mech.*, 133, 345-376.
- Morchain, J., Moranges, C., and Fonade, C. (2000). "CFD modeling of a two-phase jet aerator under influence of a crossflow." *Water Res.*, 34(13), 3460-3472.
- Morton, B.R., Taylor, G.I., and Turner, J.S. (1956). "Turbulent gravitational convection from maintained and instantaneous sources." *Proc. R. Soc. London, Series A*, 234, 1-23.
- Motarjemi, M., and Jameson, G. J. (1978). "Mass transfer from very small bubbles – the optimum bubble size for aeration." *Chem. Eng. Sci.*, 33(11), 1415-1423.
- Mueller, J. A., Boyle, W. C., and Pöpel, H. J. (2002). *Aeration: Principles and practice*, CRC, New York.

- Newman, B.G., Patel, R.P., Savage, S.B., and Tjio, H.K. (1972). "Three-dimensional wall jet originating from a circular orifice." *Aeronaut. Quart.*, 23, 188-200.
- Pande, B.B.L and Rajaratnam, N. (1979) Turbulent jets in co-flowing streams. ASCE Journal of Engineering Mechanics, Vol. 105, pp. 1025-1038.
- Pande, B.B.L., and Rajaratnam, N. (1977). "An experimental study of bluff buoyant turbulent surface jets." *J. Hydr. Res.*, 15(3): 261-275.
- Pani, B. S., Lee, J. H. W., and Lai, A. C. H. (2009). "Application of Reichardt's hypothesis for multiple coflowing jets." *Journal of Hydro-environment Research*, 3(3), 121-128.
- Papanicolaou, P.N., and List, E.J. (1988). "Investigations of round vertical turbulent buoyant jets." *J. Fluid Mech.*, 195, 341-391.
- Parr, A.D., and Sayre, W.W. (1979). "Multiple jets in shallow flowing receiving waters." *ASCE J. Hydraul. Div.*, 105(HY11), 1357-1374.
- Parthasarathy, R.N., and Faeth, G.M. (1987). "Structure of particle laden turbulent water jets in still water." *Int. J. Multiphase Flow*, 13(5), 699-716.
- Patel, R.P. (1971) "Turbulent jets and wall jets in uniform streaming flow." *Aeronaut Quarterly*, 22, 311- 326.
- Platten, J.L., and Keffer, J.F. (1971). "Deflected Turbulent Jet Flows." *Transactions ASME J. Applied Mech.*, 38E(4): 756-758.
- Pratte, B.D., and Baines, W.D. (1967). "Profiles of the round turbulent jets in a cross flow." *J. Hydr. Div. ASCE*, 92, 53-64.
- Pun, K.L., Davidson, M.J., and Wang, H.J. (2000). "Merging jets in a co-flowing ambient Fluid – A hybrid approach." *J. Hydraul. Res.*, 38(2): 105-114.
- Rajaratnam, N. (1967). "Plane turbulent wall jets on rough boundaries." *Water Power*, 149-242.
- Rajaratnam, N. (1976). *Turbulent Jets*, Elsevier Scientific, Amsterdam, The Netherlands, 304 p.
- Rajaratnam, N. (1984). *Turbulent Jets and Plumes*, Lecture Notes, University of Alberta, Edmonton, Canada, 213p.
- Rajaratnam, N. (1985). "An experimental study of bluff surface discharges with small Richardson number." *J. Hydr. Res.*, 23(1): 47-55.
- Rajaratnam, N., and Humphries, J.A. (1984). "Turbulent non-buoyant surface jets." *J. Hydr. Res.*, 22(2), 103-105.

- Rajaratnam, N., and Pani, B.S. (1974). "Three-dimensional turbulent wall jets." *Proc. ASCE J. Hydr. Div.*, 100, 69-83.
- Rajaratnam, N., and Subramanya, K. (1967). "Diffusion of rectangular wall jets in wide channels." *J. Hydr. Res.*, 5, 281-294.
- Rajaratnam, N., and Subramanyan, S. (1985). "Plane turbulent buoyant surface jets and jumps." *J. Hydr. Res.*, 23(2), 131-146.
- Roberts, P.J.W., Snyder, W.H., and Baumgartner, D.J. (1989a). "Ocean outfalls I: Submerged waste field formation." *J. Hydr. Eng.* 115(HY1), 1-25.
- Roberts, P.J.W., Snyder, W.H., and Baumgartner, D.J. (1989b). "Ocean outfalls II: Spatial evolution of submerged waste field." *J. Hydr. Eng.* 115(HY1), 26-48.
- Rodi, W., and Spalding, D.B. (1970). "A two-parameter model of turbulence and its application to free jets." *Wärme Stoffübertragung*, 3, 85-95.
- Rostamy, N., Bergstrom, D., and Sumner, D. (2010). "An experimental study of a turbulent wall jet on smooth and rough surfaces." Nickels, T.B. (ed.). IUTAM symposium on the physics of wall-bounded turbulent flows on rough walls.
- Rouse, H., Yih, C.S., and Humphreys, H.W. (1952). "Gravitational convection from a boundary source." *Tellus*, 4, 201-210.
- Rutherford, J. C. (1994). *River Mixing*. John Wiley & Sons, West Sussex, England, 347p.
- Schierholz, E.L., Gulliver, J.S., Wilhelms, S.C., and Henneman, H.E. (2006). "Gas transfer from air diffusers." *Water Res.*, 40(5), 1018-1026.
- Schlichting, H., and Gersten, K. (2000). *Boundary Layer Theory*. Springer-Verlag Berlin Heidelberg, 801p.
- Sforza, P.M., and Herbst, G. (1970). "A study of three-dimensional incompressible turbulent wall jets." *AIAA J.*, 8, 276-283.
- Sheen, H.J., Jou, B.H., and Lee, Y.T. (1994). "Effect of particle size on a two-phase turbulent jet." *Exp. Therm. Fluid Sci.*, 8, 315-327.
- Singansetti, S. R. (1966). "Diffusion of sediment in submerged jet." *J. Hydr. Div.*, 92(2), 153-168.
- Smith, S.H. and Mungal, M.G. (1998), "Mixing, structure and scaling of the jet in crossflow," *J. Fluid Mech.*, 357, 83 - 122.
- Socolofsky, S.A., and Adams, E. E. (2002). "Multi-phase plumes in uniform and stratified crossflow." *J. Hydr. Res.*, 40(6), 661-672.

- Tamburello, D.A., and Amitay, M. (2008). "Active manipulation of a particle laden jet." *Int. J. Multiphase Flow*, 34, 829-851.
- Tang, H.S., Paik, J., Sotiropoulos, F., and Khangaonkar, T. (2008). "Three-dimensional numerical modeling of initial mixing of thermal discharges at real-life configurations." *J. Hydr. Eng.*, 134(9), 1210-1224.
- Tachie, M.F., Balachandar, R., and Bergstrom, D.J. (2004). "Roughness effects on turbulent plane wall jets in an open channel." *Exp. Fluid*, 37(2), 281-292.
- Tian, X., Roberts, P.J.W., and Daviero, G.J. (2004). "Marine wastewater discharges from multiport diffuser. II: Unstratified flowing water." *J. Hydr. Eng.*, 130(12), 1147-1155.
- Turner, J.S. (1973). *Buoyancy Effects in Fluids*. Cambridge University Press, Cambridge, 367 p.
- Varley, J. (1995). "Submerged gas-liquid jets: Bubble size prediction." *Chem. Eng. Sci.*, 50(5), 901-905.
- Verhoff, A. (1963). "The two-dimensional turbulent wall jet with and without an external stream." Rep. 626, Princeton University.
- Wang, H.J., and Davidson M.J. (2003). "Jet interaction in a still ambient fluid." *J. Hydr. Eng.*, 129(5), 349-357.
- Whipple, W. J., and Yu, S. L. (1970). "Instream aerators for polluted rivers." *J. Sanit. Eng. Div.*, 96(5), 1153-1165.
- Wright, S.J. (1977). "Mean behavior of buoyant jet in a crossflow." *J. Hydr. Div., ASCE*, 103(HY5), 499-513.
- Wright, S.J. (1984). "Buoyant jets in density-stratified crossflow" *J. Hydr. Eng., ASCE*, 110(5), 643-656.
- Wüest, A., Brooks, N. H., and Imboden, D. M. (1992). "Bubble plume modeling for lake restoration." *Water Res. Res.*, 28(12), 3235-3250.
- Wynanski, I., and Fielder, H. (1969). "Some measurements in the self-preserving jet." *J. Fluid Mech.*, 38, 577-612.
- Yan, J., Luo, K., Fan, J., Tsuji, Y., and Cen, K. (2008). "Direct numerical simulation of particle dispersion in a turbulent jet considering inter-particle collisions." *Int. J. Multiphase Flow*, 34, 723-733.
- Zhang, W., and Zhu, D.Z. (2011). "Near-field mixing downstream of a multiport diffuser in a shallow river." *J. Env. Eng.*, 137(4), 230-240.

Books and reviews not cited in this chapter, but important:

- Cheremisinoff, N.P. (ed.) (1986). *Encyclopedia of Fluid Mechanics, Volume 2: Dynamics of Single-Fluid Flow and Mixing*. Gulf Publishing, Houston, 1505 p.
- Cheremisinoff, N.P. (ed.) (1986). *Encyclopedia of Fluid Mechanics, Volume 3: Gas-Liquid Flow*. Gulf Publishing, Houston, 1535 p.
- Cheremisinoff, N.P. (ed.) (1993). *Encyclopedia of Fluid Mechanics, Supplement 2: Advances in Multiphase Flow*. Gulf Publishing, Houston, 674 p.
- Davies, P.A., and Valente Neves, M.J. (ed.) (1994). *Recent Research Advances in the Fluid Mechanics of Turbulent Jets and Plumes*. Kluwer Academic Publishers, Dordrecht, 514 p.
- Fay, J.A. (1973). "Buoyant plumes and wakes." *Ann. Rev. Fluid Mech.*, 5, 151-160.
- Jirka, G.H. (2004). "Integral model for turbulent buoyant jets in unbounded stratified flow. Part 1: Single round jet." *Env. Fluid Mech.*, 4, 1-56.
- Jirka, G.H. (2006). "Integral model for turbulent buoyant jets in unbounded stratified flow. Part 2: Plane Jet Dynamics Resulting from Multiport Diffuser Jets." *Env. Fluid Mech.*, 6, 43-100.
- List, E.J. (1982). "Turbulent jets and plumes." *Ann. Rev. Fluid Mech.*, 14, 189-212.
- Philip, A.A. (1997). *Earth Surface Processes, Chapter 7: Jets, Plumes and Mixing at the Coast*. Blackwell Science Ltd, Oxford, 241-266 pp.
- Rodi, W. (1982). *Turbulent Buoyant Jets and Plumes*. Pergamon Press, Oxford, 184 p.
- Rubin, H., and Atkinson, J. (2001). *Environmental fluid mechanics*. Marcel Dekker, New York, 728 p.
- Shen, H.H., Cheng, A.H.D., Wang, K.H., Teng, M.H., and Liu, C.C.K. (ed.) (2002). *Environmental Fluid Mechanics Theories and Applications*. ASCE, Reston, Virginia, 467 p.
- Wood, A.W. (2010). "Turbulent plumes in nature." *Ann. Rev. Fluid Mech.*, 42, 391-412.
- Wood, I.R., Bell, R.G., and Wilkinson, D.L. (ed.) (1993). *Ocean Disposal of Wastewater*. World Scientific, Singapore, 425 p.

Table 2-1. Summary of Mean Properties of Simple Plane Jet and Circular Jet (data sources: Rajaratnam 1976[1]; Fischer et al. 1979 [2]; Rajaratnam 1984 [3]; Lee and Chu 2003 [4])

| Parameter | Plane Jet | Circular Jet |
|---|--|--|
| Maximum (centerline) concentration C_m | $\frac{C_m}{C_0} = \frac{\alpha_1}{\sqrt{x/b_0}}$ where $\alpha_1 = 3.37$ in [2], 3.45 in [3], 3.21 in [4], | $\frac{C_m}{C_0} = \frac{\alpha_1}{x/d_0}$ where $\alpha_1 = 4.96$ in [2], 5.34 in [3], 5.26 in [4] |
| Cross-sectional average concentration C_{avg} | $\frac{C_m}{C_{avg}} = \alpha_2$, where $\alpha_2 = 1.2$ in [2], 1.25 in [4] | $\frac{C_m}{C_{avg}} = \alpha_2$ where $\alpha_2 = 1.4$ in [2], 1.76 in [3], 1.68 in [4] |
| Maximum (centerline) velocity u_m | $\frac{u_m}{U_0} = \frac{\alpha_3}{\sqrt{x/b_0}}$ where $\alpha_3 = 3.50$ in [1], 3.41 in [2], 3.65 in [4] | $\frac{u_m}{U_0} = \frac{\alpha_3}{x/d_0}$ where $\alpha_3 = 6.3$ in [1], 6.2 in [2] and [4], 6.13 in [3] |
| Velocity half-width b^* | $b = \alpha_4 x$, where $\alpha_4 = 0.10$ in [1], 0.116 in [2], 0.097 in [3], 0.12 in [4] | $b = \alpha_4 x$, where $\alpha_4 = 0.10$ in [1], 0.107 in [2], 0.096 in [3], 0.114 in [4] |
| Concentration half-width b_C^* | $b_C/b = \alpha_5$, where $\alpha_5 = 1.35$ in [2] and [4], 1.17 in [3] | $b_C/b = \alpha_5$, where $\alpha_5 = 1.19$ in [2], 1.17 in [3], 1.2 in [4] |
| Entrainment coefficient α_e | $\alpha_e = 0.053$ in [1] and [4] | $\alpha_e = 0.026$ in [1], 0.028 in [3], 0.057 in [4] |

Note: * in [2] & [4], b (or b_C) is defined as where the velocity (or concentration) is 37% of u_m (or C_m); while in others, defined as 50% of u_m (or C_m).

Table 2-2. Summary of Mean Properties of Plane Plume and Circular Plume (data sources: Fischer et al. 1979 [1]; Rajaratnam 1984 [2]; Lee and Chu 2003 [3])

| Parameter | Plane Plume | Circular Plume |
|---|--|---|
| Maximum (centerline) concentration C_m or density defect $\Delta\rho_m$ | $\frac{C_m}{C_0} = \frac{\Delta\rho_m}{\Delta\rho_0} = \frac{\alpha_1 F_0^{2/3}}{x/b_0}$ where $F_0 = \frac{U_0}{\sqrt{g \frac{\Delta\rho}{\rho_a} b_0}}$ $\alpha_1 = 3.78$ in [1], 3.84 in [2], 4.25 in [3] | $\frac{C_m}{C_0} = \frac{\Delta\rho_m}{\Delta\rho_0} = \frac{\alpha_1 F_0^{2/3}}{(x/d_0)^{5/3}}$ where $F_0 = \frac{U_0}{\sqrt{g \frac{\Delta\rho}{\rho_a} d_0}}$ $\alpha_1 = 7.75$ in [1], 7.83 or 9.37 in [2], 8.90 in [3], |
| Cross-sectional average concentration C_{avg} | $\frac{C_m}{C_{avg}} = \alpha_2$, where $\alpha_2 = 1.32$ in [2], 1.25 in [3] | $\frac{C_m}{C_{avg}} = \alpha_2$, where $\alpha_2 = 1.40$ in [1], 1.70 in [3] |
| Maximum (centerline) velocity u_m | $\frac{u_m}{U_0} = \frac{\alpha_3}{F_0^{2/3}}$ where $\alpha_3 = 2.09$ in [1], 2.52 in [2], 2.85 in [3], | $\frac{u_m}{U_0} = \frac{\alpha_3}{F_0^{2/3} (x/d_0)^{1/3}}$ where $\alpha_3 = 4.34$ in [1], 4.00 or 4.33 in [2], 4.35 in [3], |
| Velocity half-width b^* | $b = \alpha_4 x$, where $\alpha_4 = 0.116$ in [1] and [3], 0.128 in [2] | $b = \alpha_4 x$, where $\alpha_4 = 0.100$ in [1], 0.085 in [2], 0.105 in [3], |
| Concentration half-width b_C^* | $b_C/b = \alpha_5$, where $\alpha_5 = 1.35$ in [1] and [3], 1.17 in [2] | $b_C/b = \alpha_5$, where $\alpha_5 = 1.20$ in [1], 1.16 in [2], 1.19 in [3] |
| Entrainment Coefficient α_e | $\alpha_e = 0.136$ in [2], 0.103 in [3] | $\alpha_e = 0.047$ in [2], 0.088 in [3] |

Note: * in [1] & [3], b (or b_C) is defined as where the velocity (or concentration) is 37% of u_m (or C_m); while in others, defined as 50% of u_m (or C_m).

Table 2-3. Summary of Mean Properties of Turbulent Buoyant Jet (data sources: Rajaratnam 1984 [1]; Lee and Chu 2003 [2])

| Parameter | Plane Buoyant Jet | Circular Buoyant Jet |
|---|--|--|
| Characteristic length for jet/plume L_M | $L_M = \frac{M_0}{B_0^{2/3}}$ | $L_M = \frac{M_0^{3/4}}{B_0^{1/2}}$ |
| Maximum (centerline) concentration C_m or density defect $\Delta\rho_m$ | $\frac{C_m}{C_0} = \frac{\Delta\rho_m}{\Delta\rho_0} = \frac{\alpha_{11}}{\left[\frac{\alpha_{12}}{F_0^2} + \frac{\alpha_{13}}{(x/b_0)^{3/2}}\right]^{1/3}} \frac{1}{(x/b_0)}$ <p>where $F_0 = \frac{U_0}{\sqrt{g\frac{\Delta\rho}{\rho_a}b_0}}$, $\alpha_{11}=12.75$, $\alpha_{12}=21.19$, $\alpha_{13}=50.0$ in [1]</p> | $\frac{C_m}{C_0} = \frac{\Delta\rho_m}{\Delta\rho_0} = \frac{\alpha_{11}}{\left[\frac{\alpha_{12}}{F_0^2} \left(\frac{x}{d_0}\right)^5 + \alpha_{13} \left(\frac{x}{d_0}\right)^3\right]^{1/3}}$ <p>where $\alpha_{11}=100$, $\alpha_{12}=1920$, $\alpha_{13}=6720$ in [1]</p> |
| Cross-sectional average concentration C_{avg} | $\frac{C_m}{C_{avg}} = \sqrt{1 + \frac{1}{k_2^2}} = 1.24$ <p>where $k_2 = b_C/b = 1.35$ in [2]</p> | $\frac{C_m}{C_{avg}} = 1.80$ in [1] $\frac{C_m}{C_{avg}} = 1 + \frac{1}{k_2^2} = 1.69$ <p>where $k_2 = b_C/b = 1.2$ in [2]</p> |
| Maximum (centerline) velocity u_m | $\frac{u_m}{U_0} = \left[\frac{\alpha_{31}}{F_0^2} + \frac{\alpha_{32}}{(x/b_0)^{3/2}}\right]^{1/3}$ <p>where $\alpha_{31}=21.2$, $\alpha_{32}=50.7$ in [1]</p> | $\frac{u_m}{U_0} = \left[\frac{\alpha_{31}}{F_0^2} \left(\frac{x}{d_0}\right) + \frac{\alpha_{32}}{(x/d_0)^3}\right]^{1/3}$ <p>where $\alpha_{31}=64.75$, $\alpha_{32}=223.25$ in [1]</p> |
| Velocity half-width b | $b = \alpha_4 x$ <p>where $\alpha_4=0.097$ in [1]</p> | $b = \alpha_4 x$ <p>where $\alpha_4=0.097$ in [1]</p> |
| Concentration half-width b_C | $b_C/b = \alpha_5$ <p>where $\alpha_5=1.18$ in [1]</p> | $b_C/b = \alpha_5$ <p>where $\alpha_5=1.16$ in [1]</p> |
| Entrainment Coefficient α_e | $\alpha_e = \alpha_{ej} + \frac{\alpha_{61}(\alpha_{ep} - \alpha_{ej})}{\alpha_{61} + \frac{\alpha_{62}F_0^2}{(x/b_0)^{3/2}}}$ <p>where α_{ej} and α_{ep} is the entrainment coefficients for the plane jet and plume respectively, $\alpha_{61}=17.1$, $\alpha_{62}=41.4$ in [1]</p> | $\alpha_e = \alpha_{ej} + \frac{\alpha_{61}}{\alpha_{62} + \frac{\alpha_{63}F_0^3}{(x/d_0)^3}}$ <p>where $\alpha_{61}=0.44$, $\alpha_{62}=20.74$, $\alpha_{63}=2.38$ in [1]</p> |

Table 2-4. Summary of Mean Properties of Plane Wall Jet and Bluff Wall Jet (data sources: Rajaratnam and Subramanya 1967 [1]; Rajaratnam and Pani 1974 [2]; Rajaratnam 1976[3]; Launder and Rodi 1983 [4])

| Parameter | Plane Wall Jet | Bluff Wall Jet |
|---|---|--|
| Maximum (centerline) concentration C_m | | |
| Cross-sectional average concentration C_{avg} | $\frac{C_{avg}}{C_0} = \frac{\alpha_1}{x/b_0}$ where $\alpha_1 = 4.032$ in [3] | |
| Maximum (centerline) velocity u_m | $\frac{u_m}{U_0} = \frac{\alpha_3}{\sqrt{x/b_0}}$ where $\alpha_3 = 3.50$ in [1] & [3] | |
| Velocity half-width b | $b = \alpha_4 x$ where $\alpha_4 = 0.068$ in [3]; $db/dx = 0.073$ in [4] | $\frac{b_y}{d_0} = 0.90 + \alpha_{41} \frac{x}{h}$ $\frac{b_z}{B} = \alpha_{42} \frac{x}{B} - 1.25$ where $\alpha_{41} = 0.045$, $\alpha_{42} = 0.20$, B is the nozzle (horizontal) width in [2] & [3]; $db_y/dx = 0.048$ and $db_z/dx = 0.26$ in [4] |
| Concentration half-width b_C | | |
| Entrainment Coefficient α_e | $\alpha_e = 0.035$ in [3] | |

Table 2-5. Summary of Mean Properties of Non-buoyant Plane Surface Jet and Bluff Surface Jet (data sources: Rajaratnam 1976[1]; Rajaratnam 1984 [2]; Rajaratnam and Humphries 1984 [3]; Gholamreza-kashi et al. 2007 [4])

| Parameter | Non-buoyant Plane Surface Jet | Non-buoyant Bluff Surface Jet |
|---|--|--|
| Maximum (centerline) concentration C_m | | |
| Cross-sectional average concentration C_{avg} | | |
| Maximum (centerline) velocity u_m | $\frac{u_m}{u_0} = \frac{\alpha_3}{\sqrt{x/b_0}},$ where $\alpha_3 = 3.1$ in [3] | $\frac{u_m}{u_0} = \frac{\alpha_3}{x/d_0},$ where $\alpha_3 = 13$ in [4] |
| Velocity half-width b | $db/dx = \alpha_4$ where $\alpha_4 = 0.07$ in [2] & [3] | In transverse direction: $db_z/dx = \alpha_{41},$ In vertical direction: $db_y/dx = \alpha_{42},$ where $\alpha_{41} = 0.09$ in [2] & [3], 0.12 (below the free surface) and 0.22 (at the free surface) in [4]; and $\alpha_{42} = 0.044$ in [2] & [3], 0.025 in [4] |
| Concentration half-width b_c | $b_c/b = \alpha_5$ where $\alpha_5 = 1.15$ in [2] | |
| Entrainment Coefficient α_e | $\alpha_e = 0.037$ in [2] | |

Table 2-6. Summary of Mean Properties of Buoyant Plane Surface Jet and Bluff Surface Jet (data sources: Chu and Vanvari 1976 [1]; Pande and Rajaratnam 1977 [2]; Rajaratnam 1984 [3]; Rajaratnam 1985 [4]; Rajaratnam and Subramanyan 1985 [5])

| Parameter | Buoyant Plane Surface Jet | Buoyant Bluff Surface Jet with $Ri_0 \leq 0.1$ | Buoyant Bluff Surface Jet with $Ri_0 > 0.1$ |
|---|--|--|---|
| Maximum (centerline) concentration C_m | | | $\frac{C_m}{C_0} = \frac{\alpha_1}{(x/\sqrt{A_0})^{2/3}}$, where $\alpha_1 = 2.83$ in [3] |
| Cross-sectional average concentration C_{avg} | | | |
| Maximum (centerline) velocity u_m | u/u_m exhibits self-similarity, but cannot be well described by Gaussian profile, as $u/u_m \approx 0$ at $y/b \approx 1.4$ [5] | $\frac{u_m}{U_0} = \frac{\alpha_3 Ri_0^{1/10}}{\sqrt{x/A_0}}$, where $\alpha_3 = 15.3$ in [3] & [4] | $\frac{u_m}{U_0} = \frac{\alpha_3}{(x/\sqrt{A_0}-5.0)^{1/3}}$ where $\alpha_3 = 1.25$ in [3] |
| Velocity half-width b | First b/b_0 increases linearly as non-buoyant surface jet to some point x/b_0 (the location depends on Ri_0); then the increase rate db/dx decreases non-linearly; finally approaches asymptotically a horizontal line [5]. | $db_y/dx = \alpha_{41}$ $db_z/dx = \alpha_{42}$ where α_{41} decreases with Ri_0 ($\alpha_{41} = 0.044$ for $Ri_0 = 0$, 0.02 for $Ri_0 = 0.038$, 0 for $Ri_0 = 0.09$); α_{42} increases with Ri_0 in [3] & [4] | $\frac{b_{y*}}{d_0} = \frac{\alpha_{41}}{Ri_0^{1/8}}$ $\frac{b_z}{\sqrt{A_0}} = \alpha_{42} \left(\frac{x}{\sqrt{A_0}} + 2.0 \right)$ where b_{y*} is the average of b_y which changes slightly with y ; $\alpha_{41} = 0.29$ in [2], 0.26 in [3]; $\alpha_{42} = 0.54$ in [3] |
| Concentration half-width b_C | | $b_{yC}/b_y = \alpha_{51}$ $b_{zC}/b_z = \alpha_{52}$ where $\alpha_{51} = 1.0$ in [3] & [4] and $\alpha_{52} = 1.15$ in [3] | $b_{yC}/b_y = \alpha_{51}$ $b_{zC}/b_z = \alpha_{52}$ where $\alpha_{51} = 1.12$ in [2] & [3]; and $\alpha_{52} = 1.9$ in [2], 1.6 in [3] |
| Entrainment Coefficient α_e | α_e decreases from about 0.04 to 0 when Ri increases from 0 (non-buoyant plane surface jet) to 0.2 [1] | | |

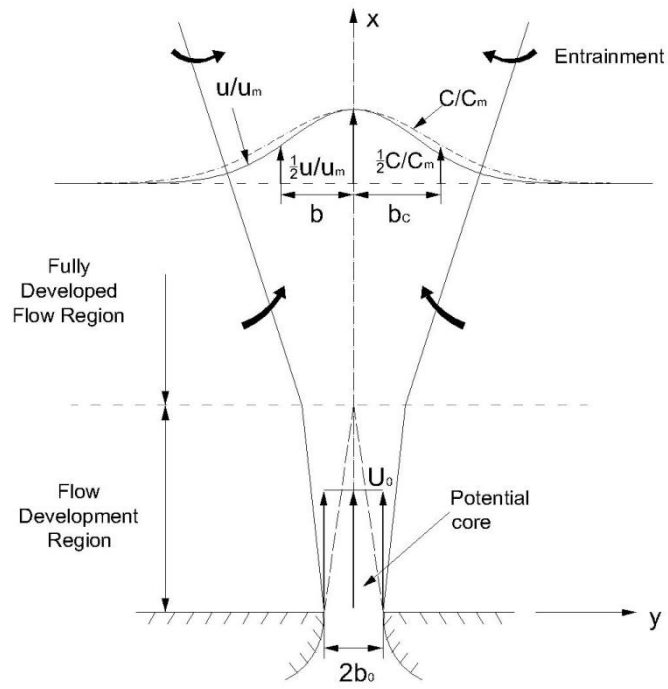


Figure 2-1. Schematic of a simple plane jet (for circular jet, replace $2b_0$ by d_0 and y by r)

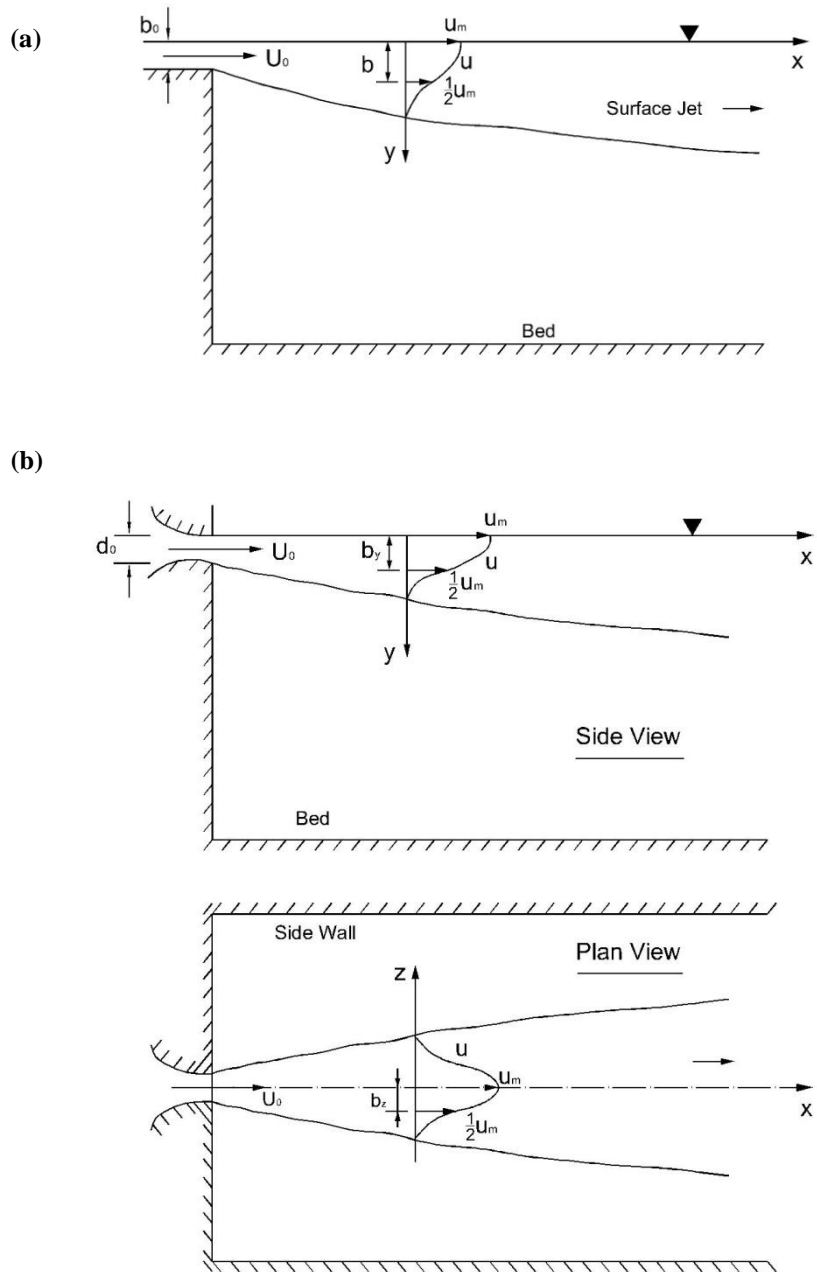


Figure 2-3. Schematic of (a) plane and (b) bluff surface jets

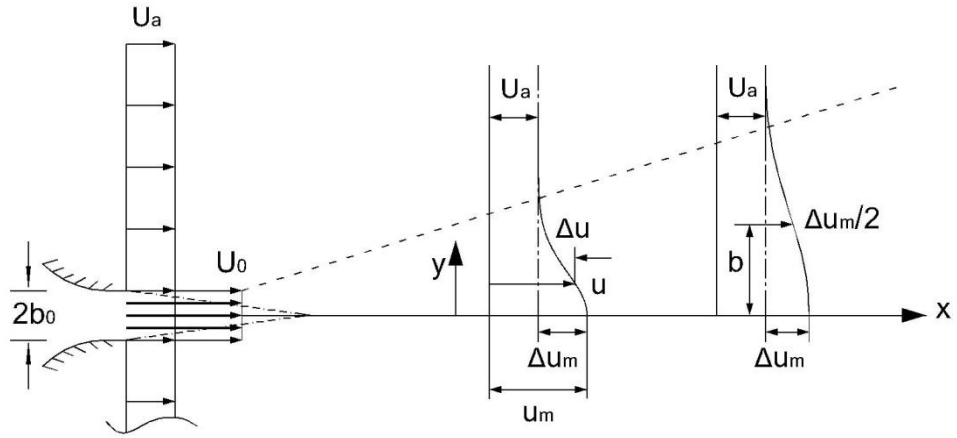


Figure 2-4. Schematic of plane jets in coflow (for circular jets, replace $2b_0$ by d_0 and y by r)

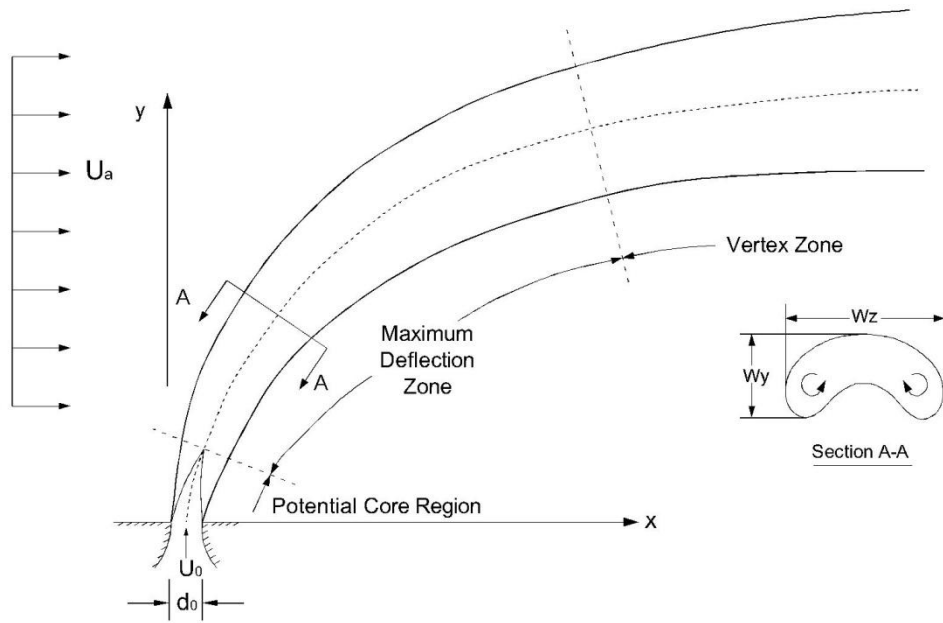


Figure 2-5. Schematic of jets in crossflow

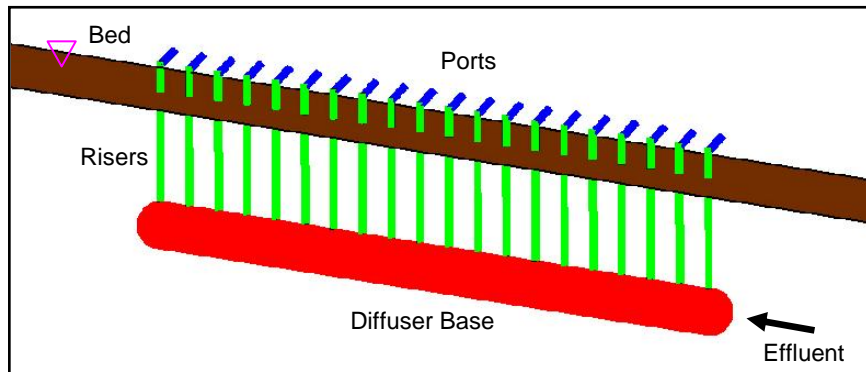


Figure 2-6. An example of a unidirectional diffuser

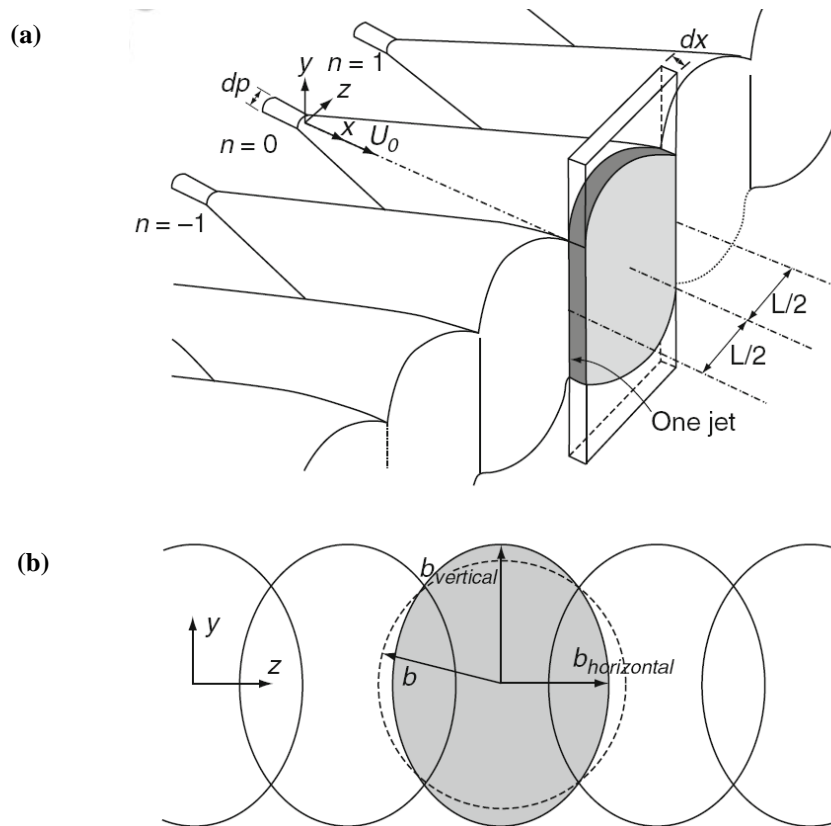


Figure 2-7. (a) Schematic of multiple merging jets, with the indication of (b) jet cross-section deformation (modified from Wang and Davidson 2003)

Chapter 3

Near-Field Mixing Downstream of a Multiport Diffuser in a Shallow River*

3.1 Introduction

Multiport diffusers are commonly used to quickly mix effluents to reduce their environmental impact. Their performances have been investigated intensively in the past few decades (e.g., Knystautas 1964; Jirka and Harleman 1973; Fischer et al. 1979; Lee and Jirka 1980; Adams 1982; Huang et al. 1996; Kim and Seo 2000; Lee and Chu 2003; Wang and Davidson 2003; Jirka 2004; Tian et al. 2004; Tang et al. 2008). Most of these studies, however, focused on ocean diffusers, and limited studies dealt with river diffusers. River conditions are significantly different than oceanic conditions due to their relative shallowness and strong crossflow (i.e., river velocities). Despite the wide use of river diffusers, there have been virtually no reported field studies on the near-field mixing downstream of such diffusers. It is important to gain a better understanding of river diffusers to properly assess the environmental impact of effluent discharge and to improve their design.

In this study, we will examine the performance of a river diffuser in the Athabasca River located in Northern Alberta, Canada. The Athabasca River is a large river (with an annual discharge of 661 m³/s) and receives effluents from Alberta's five pulp mills through multiport diffusers. The river experiences low dissolved oxygen

* The content of this chapter has been published as: Zhang, W.M., and Zhu, D.Z. (2011). "Near-field mixing downstream of a multiport diffuser in a shallow river." *J. Environ. Eng.*, ASCE, 137(4), 230-240.

levels during the winter due to the thick ice covering the surface (which prevents surface re-aeration) and low winter river discharge. To remediate this, Lima Neto et al. (2007) proposed injecting oxygen into the river through existing effluent diffusers. However, to increase the oxygen transfer efficiency from gas to dissolved form in the river, a better understanding of mixing downstream of diffusers is critical. Moreover, the mixing study is also required by current Environment Canada's regulations that the effluent plumes be delineated and their impact assessed.

Parr and Sayre (1979) studied the near-field mixing of multiple jets in shallow flowing water and divided the mixing region into three zones: an individual jet zone, a merging zone (where the individual jets merge in transverse direction), and 2-dimensional zone thereafter. Parr and Melville (1981) and Adams (1982) proposed analytical models to predict the bulk dilution for river diffusers without giving the locations where the prediction takes place. Lee (1985) found little difference between these two models.

Many experiments on individual jets have been conducted, and relations for jets in stagnant water, coflow, and crossflow have been built (Rajaratnam 1976; Fischer et al. 1979; Lee and Chu 2003). However, for a jet with an arbitrary discharge angle, our knowledge is still limited, and we must rely on numerical models such as the integral model (Jirka 2004). Of the limited experimental studies performed, Platten and Keffer (1971) examined the trajectories of jets directed at 60-135 ° from the ambient velocity. More recently, Kikkert et al. (2009) studied the trajectories, spreads, and dilutions of jets discharged at 0-90 ° from the ambient velocity.

The jet merging process is usually neglected for multiport diffusers. For example, the concept of "equivalent slot diffuser" treats the whole diffuser as one line source (Jirka and Harleman 1973). In engineering design, sufficient distance should be

provided between the diffuser's ports to adequately use the diluting ability of each port (Wang and Davidson 2003). Otherwise, individual jets will interact with each other. Hodgson (1991) showed that simple superposition of individual jets would overestimate the jet velocity and concentration. Literature on jet merging has been scarce, and most studies were conducted in still ambient fluids (Knystautas 1964; Hodgson et al. 1999; Wang and Davidson 2003). Recently a few studies in coflow have also been reported (Pun et al. 2000; Pani et al. 2009).

Given the shallowness of rivers, mixing could be greatly affected by the water surface or the river bed. Only a few studies have been reported in this area. Rajaratnam (1976) summarized some earlier studies on the effect of the river bed on mixing. Hodgson (1991) reported the complex surface impingement by circular jets in crossflow. Doneker and Jirka (2007) also presented some results on bottom attachments and surface impingements of jets. Cuthbertson and Davies (2008) reported that the water surface significantly enlarges the lateral spread of jets in still water. Such phenomenon has also been confirmed by velocity measurement and flow visualization for surface jets (Anthony and Willmarth 1992).

A number of software has been developed to model the performance of multiport diffusers including CORMIX, Visual Plume, and VISJET. CORMIX and Visual Plume are among the US Environmental Protection Agency's approved software for effluent disposal in bounded and unbounded surface water, respectively, and VISJET is recently developed software for effluent discharge in unbounded water. Although these models have shown consistent results compared to some laboratory and field data from oceans and lakes (Tsanis et al. 1994; Jirka 2004), there are no reported studies on their applications for river diffusers. Recently Tang et al. (2008) used a computational fluid dynamics model to simulate the three-dimensional features of

thermal discharge in a natural river. However, the model was only calibrated within a distance of 1.5 m downstream of two ports of a diffuser.

This chapter studied the near-field mixing downstream of a river diffuser before vertical mixing was complete. The fieldwork included a dye test, bathymetry surveys and flow measurements. Water samples were collected at different vertical and transverse locations at various sections. The near-field mixing was analyzed in four zones (Fig. 3-1): free jet zone, jet surface impingement zone, merging zone, and vertical mixing zone. Analytical models were proposed after the jets impinged the water surface. The field data was also used to evaluate some existing models for diffusers.

3.2 Field Work and Dye Test Results

3.2.1 Field Work

A field dye test was conducted within a 32-km reach to study the mixing of effluent from Alberta Pacific Forest Inc.'s (Al-Pac's) diffuser in the Athabasca River. The diffuser, located in the thalweg near the right bank, has 25 ports, of which 20 are currently used (Fig. 3-2(a)). The ports, 15 cm in diameter and 2 m apart, are unidirectional and approximately 1 m above the river bed. The angle between the ports and the bed is 45°, and the projection of the ports on the horizontal plane is parallel to the river velocity. The end of diffuser's base is sealed.

The fieldwork was conducted from September 22 to October 3, 2008, when the river discharge was low before the formation of ice in the river. In the first 3.5 km sub-reach, the bathymetry was surveyed in detail using a Trimble R8 Real Time Kinematic (RTK) GPS simultaneously with a SonarLite Echo sounder. The RTK GPS records positions with an accuracy of 1-2 cm, and the echo sounder measures depths with an accuracy of ± 2.5 cm. The bathymetry survey results near Al-Pac's diffuser are shown in

Fig. 3-2(b). Under the conditions investigated, the river width was approximately 260 m, the cross-sectional average depth was 1.6 m, and the average depth in the effluent region was 2.4 m. Due to the river's shallowness and the 45° port angle, surface impingement by the jets were visually observed approximately 4 m downstream of the diffuser, and the impingement lasted 1-2.5 m.

Velocities and discharges were measured at six sections using a SonTek 3.0 MHz Acoustic Doppler Profiler (ADP). Each section was measured at least three times, and the ADP gave quite stable river discharges. The ADP also gave depth-average velocities and cumulative discharges across each section. At the time of the dye test, the river discharge measured $224.2 \pm 0.3 \text{ m}^3/\text{s}$, the cross-sectional average velocity was 0.54 m/s, and the averaged velocity in the effluent region was 0.64 m/s. Measurement data on bathymetry, river discharge, and water surface elevation was used to build a two-dimensional (depth-averaged) hydrodynamic model using River 2D. The model was then calibrated with average errors of 0.02 m/s for velocity and $1.83 \text{ m}^3/\text{s}$ for cumulative discharge. The distribution of cumulative discharge from the calibrated model is shown in Fig. 3-2(c).

In the dye test, Rhodamine WT ($80.63 \pm 2.30 \text{ g/L}$) was injected at $14.17 \pm 0.16 \text{ mL/min}$ continuously for 45 hours by a peristaltic pump into the effluent pipeline, which was located at 5 km upstream of the diffuser. The effluent discharge and temperature were monitored by Al-Pac and averaged $956.6 \pm 6.3 \text{ L/s}$ and $27.2 \pm 0.1 \text{ }^\circ\text{C}$, respectively, during the dye test. The average river water temperature was $11.6 \text{ }^\circ\text{C}$. Water samples were taken at five sections (4.8 m, 20.0 m, 33.3 m, 60.4 m, and 114.1 m) downstream of the diffuser. At each section, 20 sampling sites were selected covering a width of about 80 m (Fig. 3-2(c)). For the first four sections, at each sampling site, samples (250 mL each) were collected simultaneously at four depths from the water

surface (0, 0.5 m, 1 m and 1.5 m). Thus a total of 80 samples were collected at each section. Three sampling sites were chosen exactly at the impingement locations at Section 4.8 m. In the last section (where the vertical mixing was expected to be complete), samples were only taken at a depth of 0.5 m. Although the horizontal sampling positions were recorded by RTK GPS, the actual error for these positions was approximately 1 m, which arose from the moving of the boat, thus creating the distance lag between the sampling site and GPS recorded site.

Samples were kept in fridge before dye concentrations were measured using a Turner Quantech Fluorometer. The fluorometer was calibrated between 0 and 5,000 parts per trillion (ppt), with an average relative error of 1%. Each sample was measured at least three times with a standard deviation of about 3 ppt. Recovery ratios (defined as the fluorescence of the tested water standard over the background fluorescence divided by the fluorescence of the distilled water standard) were $98.8 \pm 2.1\%$ and $96.3 \pm 3.3\%$ for the river water and the effluent, respectively. This suggests that the physical and chemical properties of the tested waters do not interfere the reading of fluorescence. Background concentrations of the effluent and the river water were 610.87 ± 2.79 ppt and 31.63 ± 1.21 ppt, respectively. These values were within the normal background range of pure water (20 ppt) and raw sewage (1,000 ppt), and were caused by the fluorescence of extraneous materials in the water and a small emission from water itself (Turner Designs 2001). The river background value has been removed from the concentration values in this study.

The conservation of dye mass flux is important for evaluating a dye test. As the concentration field is rather three-dimensional in the near field, it is difficult to directly calculate the conservation ratio. Thus the dye mass flux was calculated after vertical mixing was complete (starting from Section 114 m). For six far-field sections, the

average value of this ratio was $96.7 \pm 8.4\%$ (Table 3-1). The conservation of dye mass flux in the far field was quite encouraging for the analysis in the near field.

3.2.2 Dye Test Results

The dye test results are shown in Figs. 3-3 and 3-4. From Fig. 3-3, the peak concentration drops quickly as the effluent travels downstream. The concentration decreased from 20,522 ppt (C_0) inside the diffuser to 1,638 ppt ($C/C_0 = 0.080$) at Section 4.8 m and further to 409 ppt ($C/C_0 = 0.020$) at Section 114 m. This reflects the fast diluting ability of the multiport diffuser. It is interesting to notice the wave-shape lateral concentration distributions, and usually three peaks were detected at each section. The three peaks at Section 4.8 m corresponded to the sampling locations specially selected at the three jet impingement locations at the water surface. Given there were 20 sampling sites at each section, many other peaks would have been missed.

The concentrations near the diffuser, especially at Section 4.8 m, strongly depended on their sampling positions. At Sites A, B and C of Section 4.8 m (Fig. 3-3(a)), the concentrations at all depths were small, suggesting that these sites were in the middle of two neighboring jets, which had not merged yet. Examination of their GPS positions and the concentrations at the neighboring sites further shows that these sites were approximately 1 m upstream of the impingement locations. For example, at Site A, the water surface concentration was 0, however, at Site E (almost the same transverse location as A), the water surface concentration was as high as 1,579 ppt ($C/C_0 = 0.077$). The same concentration jump also occurred at Sites C and F (Fig. 3-3(a)). At Site D, the concentration at the water surface was lower than the concentrations found at depths of 0.5 m and 1.0 m, which suggests that the jet was approaching but had not reached the water surface there (i.e., Site D was a little upstream of the impingement location).

The concentrations at the downstream sections were expected to be much less sensitive to the sampling positions than at Section 4.8 m. With the merging of jets, the lateral concentration difference became smaller (Fig. 3-4). At Section 114 m, the lateral concentration distribution began to evolve into a (skewed) Gaussian distribution and finally was so at 516 m downstream of the diffuser (Zhang and Zhu 2011).

Note that in addition to the sampling positions, river turbulence could also contribute to the wave-shape (peak-trough) lateral concentration distribution. In this study, because of the constraint of the moving boat for sampling, each sample was taken within approximately 1.5-2 seconds, which was close to the estimated integral time scale (less than 1.7 seconds) of the river turbulence. Longer sampling time would better eliminate the effect of river turbulence on the concentration fluctuation of samples and produce a smoother lateral concentration distribution. However, this was not employed in the field because not only it would greatly complex the sampling setup and procedure, but more importantly, the influence of river turbulence on the lateral concentration distribution was expected to be small compared to that of the sampling positions.

Indeed, river turbulence would induce some uncertainty in the concentration measurement near the jet edges, but such influence was limited at the jet centerline where the focus of this study was. The jet exit velocity from the ports of the diffuser was 2.7 m/s, much larger than the river velocity. Therefore, near the diffuser, the peak concentrations were not affected by river turbulence. On the other hand, if river turbulence was dominant, the concentration fluctuations at the downstream sections should be as large as that at Section 4.8 m; on the contrary, Fig. 3-4 shows much smaller fluctuations at the downstream sections. Moreover, according to the analysis with CORMIX, the jets of the diffuser completed merging with each other shortly after the

diffuser, and then the lateral range of uniform dye concentration was wide (over 40 m). Thus, the effect of river turbulence (including secondary flows) should be limited on the lateral concentration distribution after the merging. Furthermore, the limited effect of river turbulence on the samples can be double checked from the conservation ratio of dye mass flux measured at each section (see Table 3-1).

Generally concentrations at the water surface were highest and dropped with depth, but the vertical concentration differences decreased with longitudinal distance. At Section 4.8 m, the concentration difference at the water surface and the depth of 1.5 m was as high as 1,500 ppt ($\Delta C/C_0 = 0.073$), while the difference was only 170 ppt ($\Delta C/C_0 = 0.008$) at Section 60.4 m. This suggests the dye at Section 60.4 m approached, but had not yet reached complete vertical mixing. As shown in Fig. 3-3, after the jets impinged the water surface, the dye diffused from the water surface toward the river bed.

Peak concentrations were noticed at the off-shore end of the effluent region (Figs. 3-3 and 3-4). The locations of these peaks were consistent with cumulative discharges at different sections (Fig. 3-4). Initially the effluent was distributed within a width of 38 m (20 ports) along the diffuser. This width did not increase much at the downstream sections (with an average of 41.2 m as shown in Fig. 3-3), indicating that the advection was much stronger than the jet spread and transverse turbulent diffusion. In Fig. 3-4, the cumulative discharges at different sections were consistent in the effluent region; within this region, the river discharge measured $59.7 \pm 1.1 \text{ m}^3/\text{s}$ (26.6% of the total).

3.3 Result Analysis

Some length scales are examined here to obtain an overall understanding of the turbulent buoyant jets from the diffuser. The ratio of jet exit velocity (U_0) to ambient

river velocity (u) is 4.3, and the initial density difference ($\Delta\rho_0/\rho_a$) is 3.1‰, where ρ_a is the density of the ambient water. The initial densimetric Froude number ($U_0/\sqrt{g_0' d_0}$) is 40.2, where d_0 is the port diameter; $g_0' = g\Delta\rho_0/\rho$; and g is the acceleration due to gravity. The buoyancy length scale for a buoyant jet in crossflow is $l_b = B_0/u^3 = 0.01$ m, where the initial specific buoyancy flux $B_0 = g_0' Q_0$; and Q_0 is the jet discharge at one port. The momentum length scale for a buoyant jet in crossflow is $l_m = M_0^{1/2}/u = 0.57$ m, where the initial specific momentum flux $M_0 = U_0 Q_0$. The characteristic length for jet/plume in still water is $L_M = M_0^{3/4}/B_0^{1/2} = 5.67$ m.

According to Fischer et al. (1979) and Lam et al. (2006), with $l_b \ll l_m$, the jets in our study can be described as weakly buoyant jets in strong crossflow, which experience in sequence momentum dominated near field, momentum dominated far field, and buoyancy dominated far field. In other words, the jets are first momentum dominated within 0.57 m, and beyond that, the ambient flow becomes dominant. Given $L_M = 5.67$ m, the buoyancy is not important compared to the momentum when the effluent impinges on the water surface as the water depth above the diffuser's ports (1.4 m) is small than L_M . At the surface impingement location (near Section 4.8 m), the minimum dilution was 13.3 times, and thus, the maximum temperature difference there was only 1.2 °C or $\Delta\rho/\rho_a = 0.23$ ‰. Due to the weak buoyancy at the impingement location, according to Doneker and Jirka (1990), buoyant surface spreading will not happen, and the further mixing can be characterized as passive dispersion induced by river turbulence.

In the following analysis, the minimum dilution will be compared with jet theories to further understand the general behavior of jets from the diffuser. Mixing will be analyzed in four zones, and CORMIX will be used for comparison. Furthermore,

analytical models will be built after the jets impinge the water surface. The buoyancy effect will be considered in the CORMIX models, but not in the analytical models.

3.3.1 Minimum Dilution

Minimum dilution, the key parameter to assess an effluent discharge, is defined as C_0/C_m , where C_m is the maximum concentration at a downstream section. To assess the whole diffuser, C_m was considered to be the average of the three peak concentrations detected at each section (Fig. 3-3). As it was difficult to obtain more peaks in the field, the average of the three peaks, to a large extent, represent the minimum diluting ability of the whole diffuser.

The measurement of C_0/C_m is shown in Fig. 3-5. In Fig. 3-5(a), the length of the potential core was estimated to be $2d_0$. According to Rajaratnam (1976), the potential core length of a circular jet in crossflow depends on U_0/u , and in our study, the length was calculated to be $3d_0$. This length further reduced to about $2d_0$ on the x (longitudinal) axis due to the 45° discharge angle. In Fig. 3-5(a), the entire 114 m can be divided into two parts, each fitted with a power law relation. From Fig. 3-5(b), the slope of C_0/C_m decreases dramatically with the downstream distance as the jet entrainment is more effective in mixing compared to the river turbulence.

The measurement of C_0/C_m may be compared with jet theories to indicate whether the jets behave more like circular (or plane jets) in crossflow or coflow. The equations currently available are:

Circular Jet in Crossflow (Hodgson and Rajaratnam 1992)

$$C_0/C_m = 1.09(\alpha x / d_0)^{0.56} \quad (2.1)$$

Circular Jet in Coflow (Lee and Chu 2003)

$$C_0/C_m = 0.174(xM_{e0}^{0.5} / Q_0) \quad (2.2)$$

Plane Jet in Coflow (Pun et al. 2000)

$$C_0/C_m = (\alpha - 1)I_{c2}(2k/I_{q2})^{0.5}(l_p x)^{0.5}/(M_{e0}^{0.5}/u) \quad (2.3)$$

where M_{e0} is the jet excess momentum; l_p is the distance between ports; I_{c2} and I_{q2} are constants of 2.3 and 1.8; and k , the jet spread rate, is about 0.11. Note that Eq. (2.1) was selected for the momentum dominated far field, which started from $x = 0.57$ m (l_m) in our study. Lee and Chu (2003) also proposed a comparable equation to Eq. (2.1). Eq. (2.3) was selected for weak plane jet since the plane jet was calculated to become weak after $x = 1.3$ m in our study (according to Pun et al. 2000).

Eqs. (2.1) - (2.3) are plotted in Fig. 3-5(b). Generally, Eqs (2.1) - (2.2) over-predict C_0/C_m , as these equations were built for one port of a diffuser. However, Eq. (2.3) gives more favorable results, which suggests that the jets with $U_0/u = 4.3$ and a 45° discharge angle will bend and merge quickly, and behave more like a weak plane jet in coflow afterwards. This general behavior originates from the measured $C_0/C_m \sim x^{0.5}$ (Fig. 3-5(a)), which is similar to Eq. (2.3). Some discrepancies exist between Eq. (2.3) and the measurement at the start ($x = 0 - 4.8$ m) and end ($x = 60.4 - 114.1$ m) of the study reach. This is because initially the jets are independent circular jets, and as jets travel greater distances, the water surface and the river bed limits the further dilution of jets, whereas Eq. (2.3) assumes the infinity of the ambient.

As shown in Fig. 3-5(a), between the potential core ($2d_0$) and Section 4.8 m ($32d_0$), the measured $C_0/C_m \sim x^{0.93}$ is similar to Eq. (2.2). However, Eq. (2.2) underestimates C_0/C_m at Section 4.8 m, since crossflow is more favorable for jet dilution than coflow (Lee and Chu 2003). For a jet discharged at 45° to an infinitely large ambient, C_0/C_m is expected to have a smaller exponent for x (i.e., 0.5-1, where 0.5 and 1 are from the relations for a circular jet in crossflow and coflow, respectively).

The present results are also comparable with the laboratory results in a study of multiple nonbuoyant circular jets in crossflow (Moawad and Rajaratnam 1998). Parr and Sayre (1979) developed an equation for C_0/C_m based on experiments of multiple jets in shallow flowing water:

$$C_0/C_m = 0.28(x/d_0 + 2.5) \quad \text{for } x \leq 2d_0(q_a + q_j)/q_j \quad (2.4)$$

where q_a is the average ambient discharge per unit width assigned to a diffuser's port; and q_j is the diffuser discharge per unit length. In the valid range for Eq. (2.4), the predicted C_0/C_m for our study are 9.7 and 38.0 at $x = 4.8$ m and 20 m, respectively, which are close to the corresponding field values of 13.2 and 31.4. Note that when x increases, Eq. (2.4) tends to over-predict C_0/C_m , even when compared to Parr and Sayre's own data.

3.3.2 Zone I: Free Jet Zone

Free jet means that the jet does not contact the water surface, river bed, or neighboring jets. Current theories mainly apply for jets in stagnant fluids, although some studies have also been reported in coflow and crossflow (Lee and Chu 2003; Jirka 2004). For jets with an arbitrary discharge angle, numerical models need to be relied on. In this study, the most widely used software, CORMIX 5.0GT, will be used. CORMIX incorporates several independent models such as CORMIX1 for single-port discharge and CORMIX2 for multiport discharge. The average velocity and depth in the effluent region (Table 3-2) were used for modeling.

The results for jet trajectories from CORMIX1 are shown in Fig. 3-6. CORMIX defines the jet width as the location where the concentration is 37% or 46% of the local centerline concentration. For consistency, these are adjusted to the more commonly used "jet half-width" where the concentration is 50% of the centerline. As shown in Fig. 3-

6(a), the free jet zone is short: only 3.3 m ($22d_0$) downstream of the diffuser. The angle between the jet and ambient velocity decreases quickly from the initial 45° to 15° at $x = 1$ m, and further to 8° at $x = 3.3$ m, suggesting the general behavior of a jet with a 45° angle and $U_0/u = 4.3$ would be more like a jet in coflow instead of crossflow. The same conclusion was drawn from the comparison of C_0/C_m with jet theories.

In Fig. 3-6(b), the jet half-width appears to increase linearly in the aerial view, and the jet spread rate is about 0.08 for the 50% jet half-width, or about 0.10 for the 37% jet half-width. This is close to the value of 0.11 for the 37% jet half-width of a circular jet in stagnant water (Lee and Chu 2003). The jet centerline excess velocity was predicted to decrease quickly from the initial 2.3 m/s to 0.7 m/s at $x = 1$ m, and further to 0.2 m/s at $x = 3.3$ m.

3.3.3 Zone II: Jet Surface Impingement Zone

Surface impingement by jets is rather complex as it is strongly dynamic and three-dimensional. In Fig. 3-6(a), the jet thickness of this zone seems stable. However, in the transverse direction, the jet half-width suddenly increases from 0.3 m ($2d_0$) to 0.75 m ($5d_0$) at $x = 3.3 - 4.5$ m ($22d_0 - 30d_0$). This results in a jet spread rate of 0.38, approximately 4.7 times of that in the free jet zone (Fig. 3-6(b)). This sudden lateral increase is caused by the vertical restriction of jet spread exerted by the water surface. The sudden increase in jet width and the stableness in jet thickness indicate that surface impingement can enhance dilution. In a study of vertical buoyant jets in stagnant shallow water, Kuang and Lee (2006) reported that the dilution can increase 3-6 times near surface impingement due to an internal hydraulic jump. The predicted location and length of the surface impingement zone was consistent with field observations.

So far, no other jet model has been found to be capable of dealing with surface impingement, and the literature has also been quite limited. Hodgson (1991) used photography to study the effect of finite depth on circular jets in crossflow and found that the jets would eventually rise to a stable terminal layer near the water surface (before vertical dispersion). For our study, the terminal layer was calculated to be from the water surface to a depth of 0.62 m ($4.1d_0$), which is comparable to a depth of 0.79 m ($5.3d_0$) from CORMIX1.

Hodgson (1991) also studied the effect of surface impingement on the lateral enlargement of jet spread and found that the enlargement was related to $U_0d_0/(uH_0)$, where H_0 is the depth at jet discharge. Using his experimental data, the lateral jet spread rate with impingement was estimated to be 7.2 times the value without impingement for our study. This is close to the 4.7 times from CORMIX1. Similar phenomena have also been observed for surface jets, and the ratio of jet lateral spread rates with and without surface effect was 3.9 - 6.3 (Anthony and Willmarth 1992). Three-dimensional computational fluid dynamics models will be needed to study the details of this problem.

3.3.4 Zone III: Merging Zone – Passive Dispersion Analysis

Due to the energy dissipation during surface impingement, the jet centerline excess velocity would greatly decay from 0.2 m/s at $x = 3.3$ m. Thus beyond the surface impingement, i.e., from $x = 4.5$ m ($30d_0$), further mixing can be treated as passive dispersion. CORMIX1 and superposition can be used to simulate the concentration field induced by all the ports. In Fig. 3-6(b), the 50% jet half-widths would interact at $x = 6$ m ($40d_0$), indicating that the jet merging approaches completion there. Using the concept of “equivalent slot diffuser”, CORMIX2 neglects the individual jet spreading and

merging processes. As the predictions from CORMIX were not quite satisfactory for our study (Figs. 3-7 and 3-8), analytical dispersion models were developed using the measurement results at Section 4.8 m ($32d_0$ or $2H$, where H is river depth) as initial conditions.

The analytical models are based on assuming 20 steady-state point sources 2 m apart from each other at the water surface some distance upstream of Section 4.8 m. For each source, the advection-diffusion equation is:

$$u \frac{\partial C}{\partial x'} = D_{x'} \frac{\partial^2 C}{\partial x'^2} + D_y \frac{\partial^2 C}{\partial y^2} + D_z \frac{\partial^2 C}{\partial z^2} \quad (2.5)$$

where x' is the longitudinal coordinate from the virtual origin of a point source (note x starts from the diffuser); y is the transverse coordinate; z is the vertical coordinate from the water surface; and D is the turbulent diffusion coefficient. Neglecting the diffusion in the x' direction as it is small than the advection, the analytical solution to the concentration field induced by all 20 sources is:

$$C(x', y, z) = \sum_{i=1}^{20} \frac{2\dot{M}_0/20}{4\pi\sqrt{D_y D_z x'}} \exp\left[-\frac{(y-y_i)^2}{4D_y t} - \frac{z^2}{4D_z t}\right] + \text{Images} \quad (2.6)$$

where y_i is the lateral position of the i th source; \dot{M}_0 is the dye injection rate for the whole diffuser; $t = x'/u$ is the time for the dye to travel from the virtual origin to x' ; the coefficient value of 2 expresses the reflecting effect at the water surface; and the image term is introduced to account for the river bed.

Beyond the surface impingement, the concentrations at the water surface were greater than at any other depths. Thus the merging process was focused at the water surface ($z = 0$). From Eq. (2.6),

$$C(x', y, 0) = \sum_{i=1}^{20} \frac{2\dot{M}_0/20}{4\pi\sqrt{D_y D_z x'}} \exp\left[-\frac{(y-y_i)^2}{4D_y t}\right] + \text{Images}$$

$$= \sum_{i=1}^{20} C_{m1} \exp \left[-0.693 \frac{(y-y_i)^2}{b^2} \right] + \text{Images} \quad (2.7)$$

where $C_{m1} = \dot{M}_0 / (40\pi\sqrt{D_y D_z} x')$ is the maximum concentration induced by one point source; and b is Gaussian 50% half-width. From Eq. (2.7), it can be easily shown:

$$t = b^2 / (2.772 D_y) \text{ or } b = \sqrt{2.772 D_y t} \quad (2.8)$$

The initial conditions at Section 4.8 m are: $C_{m1,4.8} = 1,549$ ppt ($C/C_0 = 0.075$); and $b_{4.8} = 0.9$ m. The value of $b_{4.8}$ was determined by matching the modeled concentration profile with the measurement points excluding Points A-D as stated before (Fig. 3-7(a)). The transverse diffusion coefficient is $D_y = 0.30u^*H = 0.044$ m²/s, where u^* is the shear velocity. The coefficient 0.30 was calculated using the method of moment based on the dye test results within the entire 32-km reach (Zhang and Zhu 2009). In Eq. (2.8), the time for the dye to arrive at Section 4.8 m is $t_{4.8} = 6.6$ s, which means the virtual origin of a point source is 4.2 m upstream of Section 4.8 m, close to the diffuser's location. The time for the dye to arrive at any location x can be calculated by $t = t_{4.8} + (x - 4.8)/u$; thus, the value of b at x can be calculated using Eq. (2.8). The maximum concentration at x can be calculated using $C_{m1} = C_{m1,4.8} t_{4.8}/t$. The concentration field induced by all the sources can be calculated using Eq. (2.7).

Modeled and measured concentration profiles at the water surface are shown in Fig. 3-7. It is clear that, within a short distance, the effluent would complete merging (defined as where the lateral variation of concentration is less than 5% of the mean concentration). The complete merging location was calculated to be $x = 6.0$ m ($40d_0$ or $3l_p$) (i.e., only 1.5 m after surface impingement). Wang and Davidson (2003) proposed a merging zone of $4.5l_p < x < 12l_p$ for circular jets in still water. Their merging distance is longer than our result, as there is no surface impingement in their study, and the impingement accelerates the merging (Fig. 3-6(b)). Pani et al. (2009) presented an

example of applying Reichardt's hypothesis for multiple jets in coflow and reported that the jets completed merging at $x \approx 7l_p$. Surface impingement was also not considered in Pani's study.

3.3.5 Zone IV: Vertical Mixing Zone

For $x > 6$ m ($40d_0$ or $2.5H$), the following mixing can be referred as vertical mixing. In this zone, the predicted concentration profiles at the water surface will be first examined. In Fig. 3-7, generally the present model and CORMIX1 are better than CORMIX2. CORMIX1 under-predicts the concentrations at Section 4.8 m. For CORMIX2, as the prediction is either flux-averaged or depth-averaged, its prediction is much smaller than the measurement. With the increase of x , the CORMIX2 prediction is more accurate (Fig. 3-7(d)-(e)) as the vertical mixing is more approached completion.

Vertical concentration profiles in this zone will be next examined. Three methods were used to test the sensitivity of the modeling results to different initial conditions. Method 1 assumes 20 point sources (as stated above) with Gaussian concentration distribution in the lateral direction and half Gaussian in the vertical direction for each point source. Method 2 assumes a lateral uniform source with half Gaussian in the vertical direction. Method 3 assumes a uniform source both in the lateral and vertical directions.

Method 1: This method is based on three-dimensional dispersion. Eq. (2.6) can be rewritten as:

$$C(x', y, z) = C_{w/o}(x', y, 0) \left[\exp\left(-\frac{z^2}{4D_z t}\right) + \exp\left(-\frac{(2H-z)^2}{4D_z t}\right) \right] \quad (2.9)$$

where $C_{w/o}(x', y, 0)$ is the water surface concentration without the river bed effect as expressed in the superposition term of Eq. (2.7), and it has already been calculated

during the water surface concentration profile modeling. The second term with the square bracket accounts for the river bed. The vertical diffusion coefficient can be calculated from C_{m1} as $D_z = \dot{M}_0^2 / (40\pi\sqrt{D_y}C_{m1}x')^2$. By using the initial conditions at Section 4.8 m and the known injection rate, D_z was derived to be 0.013 m²/s. This value approximates the 0.011 m²/s value derived from the classical formula of $D_z = 0.067u^*H$ (Fischer et al. 1979).

Method 2: As lateral merging completes at $x = 6$ m, this method is based on two-dimensional dispersion:

$$C(x', z) = \frac{2\dot{M}_0}{Lu\sqrt{4\pi D_z t}} \exp\left(-\frac{z^2}{4D_z t}\right) + \text{Image} = C_m \exp\left[-0.693\left(\frac{z}{b}\right)^2\right] + \text{Image} \quad (3.10)$$

where $t = (x'/u)$ and b can be related as in Eq. (2.8); x' is the virtual origin of line source; L is the effluent width; and the image term can be written similarly as in Eq. (2.9). The only initial condition needed for this method is $C_{m,4.8} = 1,549$ ppt. The Gaussian 50% half-thickness b can be calculated from C_m as $b = \dot{M}_0 / (C_m Lu\sqrt{\pi/2.772})$. Using $L = 41.2$ m (Fig. 3-3), $b_{4.8}$ was 0.45 m, which can be further examined by fitting the half Gaussian profile with the measurement points (Fig. 3-8(a)). At x , $C_m = C_{m,4.8}\sqrt{t_{4.8}/t}$, and b can be calculated using Eq. (2.8). In Eq. (2.10), $C_m \sim x'^{-0.5}$ arises from the lateral merging of 20 sources, each having $C_m \sim x'^{-1}$ as seen in Eq. (2.7). The measurement of $C_m \sim x'^{-0.5}$ in Fig. 3-5(a) confirms the use of Eq. (2.10).

Method 3: As the jets impinged the water surface, it is possible to further simplify the initial vertical concentration profile as a top-hat with a thickness of h . Then the concentration field becomes:

$$C(x', z) = \int_{-h}^h \frac{C_{m,4.8}}{\sqrt{4\pi D_z t}} \exp\left(-\frac{(z-\xi)^2}{4D_z t}\right) d\xi + \text{Image} \quad (3.11)$$

where ξ has the same meaning as z ; and h can be calculated as $h = HC_f/C_{m,4.8}$, where C_f is the concentration for complete vertical mixing. The solution is:

$$C(x', z) = \frac{C_{m,4.8}}{2} \left[\operatorname{erf} \left(\frac{z+h}{\sqrt{4D_z t}} \right) - \operatorname{erf} \left(\frac{z-h}{\sqrt{4D_z t}} \right) \right] + \text{Image} \quad (3.12)$$

where erf is the error function. The image term expressing the river bed effect can be easily written.

The modeled vertical concentration profiles are shown in Fig. 3-8. Generally, the analytical models give satisfactory predictions, CORMIX1 predicts faster vertical mixing, and CORMIX2 gives an unsatisfying results. There are little differences among the present three methods, suggesting the initial conditions are not very important for the vertical mixing. However, the measurement does show that the half Gaussian vertical profile is more reasonable than the top-hat after surface impingement. At Section 4.8 m, CORMIX2 gives flux averaged concentrations, but obviously the location is not properly predicted. With the increase of x , the present methods give better predictions.

The length for complete vertical mixing (x_v) is defined as the distance where the vertical variation of concentrations is less than 5% of the depth-averaged concentration. CORMIX1 and CORMIX2 predict x_v to be 50 m ($21.7H$) and 19 m ($7.9H$), respectively. However the field data show that x_v is beyond 60.4 m (Fig. 3-8(d)). CORMIX1 underestimates the value because it uses a large vertical diffusion coefficient ($D_z = 0.03 \text{ m}^2/\text{s}$), three times the value from the well-known $D_z = 0.067u^*H$. For CORMIX2, the underestimation is caused by assuming that x_v happens at “about five layer depths from the diffuser”. This assumption seems doubtful from our data. The present models predicted x_v as 94 m ($38.9H$). According to Fischer et al. (1979), x_v can be also roughly

estimated using $0.4uH^2/D_z = 114 \text{ m } (47.2H)$, where 0.4 was selected for the effluent discharged at the water surface.

3.4 Discussions

The performances of CORMIX and the present models on minimum dilutions are shown in Fig. 3-5(c). Note in CORMIX2, C_0/C_m has a discrete point at $x = 19 \text{ m } (7.9H)$, which is caused by the use of different modules before (plane jet module) and after (dispersion module) 19 m. Before $x = 19 \text{ m}$, CORMIX2 only predicts flux averaged dilutions, and the plane jet centerline dilutions can be estimated through dividing by a coefficient of 1.3 (Doneker and Jirka 2007). For CORMIX1, superposition was only used in the passive dispersion zone. The predictions from the present models with and without the river bed effect are both shown in Fig. 3-5(c).

In Fig. 3-5(c), generally CORMIX over-predicts C_0/C_m , and the analytical models match the measurements well. From CORMIX1, the predicted C_0/C_m increases quickly from 8.8 to 16.3 in the surface impingement zone. And at Section 4.8 m, C_0/C_m reaches 17.0, which is a little higher than the measurement of 13.2 since CORMIX1 models the vertical mixing faster (Fig. 3-8 (a)). The analytical models with and without the river bed effect only differ slightly beyond $x = 60 \text{ m } (24.9H)$ since the effect of the river bed on the water surface concentrations is small.

Two other widely used software for multiport diffusers were also examined: VISJET 2.0 and Visual Plume 1.0. These two software, mainly developed for deep water discharges, stop running when the jets impinge the water surface. However, their predictions before the impingement can be used to calibrate CORMIX. The comparison shows that VISJET and Visual Plume predict similar jet trajectories and dilutions in the

free jet zone as CORMIX. This suggests the reliability of the CORMIX modeling results in the free jet zone, even though we do not have field data in this zone.

In all the above models, the river velocity is assumed to be constant. However, the ambient velocity changes in the transverse direction, which may affect the lateral concentration distribution. The off-shore end of Al-Pac's diffuser extends near the end of the thalweg (Fig. 3-2); thus, the velocity there is lower than the velocity near the center of the diffuser. As an example, the ADP measurement at Section 20 m, together with the lateral concentration distribution, are shown in Fig. 3-9. The high concentrations at the off-shore end are related with the corresponding lower ambient velocities. Our results show that, on average, if the ambient velocity decreased by 29%, the concentration would increase by 38%. Moawad and Rajaratnam (1998) also reported in laboratory study that: if the ambient velocity decreased by 42% while keeping other conditions the same, the concentration would increase on average by 57%. Similar results can be also obtained using CORMIX1.

3.5 Summary and Conclusions

In Chapter 3, near-field effluent mixing downstream of a multiport diffuser was studied in a wide shallow river. Concentration was measured both in vertical and transverse locations at five sections in a reach of 114 m ($761d_0$ or $47.3H$). Near-field mixing was analyzed in four zones: the free jet zone, the jet surface impingement zone, the merging zone, and the vertical mixing zone. Analytical models were proposed for the three-dimensional concentration field after the jets impinged the water surface. Some existing models for multiport diffusers were also examined. The main conclusions are:

- (1) Dilution was found to occur much quicker near the diffuser than far away from it. Dilution for complete vertical mixing was mainly controlled by the portion of the river discharge that was occupied by the diffuser.
- (2) In the free jet zone, various computer models gave consistent results on trajectories and dilutions. This zone was modeled within a downstream distance of 3.3 m ($22d_0$).
- (3) Surface impingement would cause a sudden increase of jet width in the lateral direction and enhance dilution. Most existing models were unable to deal with this complex problem, and only CORMIX1 was able to model this to some degree. The result shows that the impingement lasted from $x = 3.3$ to 4.5 m ($22 - 30d_0$), which is consistent to field observation.
- (4) Beyond surface impingement, further mixing could be treated as passive dispersion. Analytical models give satisfactory predictions of the three-dimensional concentration field. The lateral jet merging was accelerated by the surface impingement, and the merging completed at $x = 6.0$ m ($3l_p$).
- (5) The vertical mixing zone was identified as $x = 6.0 - 91.4$ m ($2.5 - 37.9H$), and the mixing was found to be insensitive to initial condition using a half Gaussian or top-hat distribution. The vertical mixing coefficient was found to be $0.013 \text{ m}^2/\text{s}$, close to the value of $0.011 \text{ m}^2/\text{s}$ derived from the classic formula of $D_z = 0.067u^*H$.

For similar studies in the future, we recommend conducting detailed measurements at a section downstream of the impingement location and using the models presented in this study. If no field measurements have been conducted, we

recommend using CORMIX1 to obtain the minimum dilution after surface impingement and Method 2 (Eq. 2.10) to model the near-field dispersion. CORMIX2 is only recommended after vertical mixing is complete.

Notation

The following symbols are used in this chapter:

- B_0 = initial (specific) buoyancy flux (m^4/s^3);
- b = half-width for Gaussian concentration profile (m);
- C = dye concentration (ppt);
- C_0 = dye concentration inside the diffuser (ppt);
- C_f = concentration for complete vertical mixing (ppt);
- C_m = maximum concentration at a certain section (ppt);
- C_{m1} = maximum concentration induced by one point source (ppt);
- D = turbulent diffusion coefficient (m^2/s);
- d_0 = port diameter (m);
- H = river depth (m);
- h = initial top-hat thickness (m);
- L = lateral width of dye distribution (m);
- l_b = buoyancy length scale for a jet in crossflow (m);
- l_M = characteristic length for jet/plume (m);
- l_m = momentum length scale for a jet in crossflow (m);
- l_p = distance between ports (m);
- \dot{M}_0 = dye injection rate ($\mu\text{g}/\text{s}$);
- M_0 = initial (specific) momentum flux (m^4/s^2);
- M_{e0} = jet excess momentum;
- Q = total river discharge (m^3/s);
- Q_0 = jet discharge for a diffuser's port (m^3/s);
- t = time (s);
- U_0 = jet exit velocity (m/s);
- u = river velocity (m/s);
- u^* = shear velocity (m/s);

x = longitudinal distance downstream of the diffuser;
 x' = longitudinal distance downstream of the virtual origin of a point source (m);
 x_v = length for vertically complete mixing (m)
 y = transverse coordinate (m);
 y_i = lateral position of the i th point source (m);
 z, ξ = vertical coordinate (m);

References

- Adams, E.E. (1982). "Dilution analysis for unidirectional diffusers." *J. Hydraul. Div.*, 108(HY3), 327-342.
- Anthony, D. G., and Willmarth, W. W. (1992). "Turbulence measurements in a round jet beneath a free surface." *J. Fluid Mech.*, 243, 699-720.
- CORMIX 5.0GT* [Computer software]. MixZon, Portland, OR.
- Cuthbertson, A. J. S., and Davies, P. A. (2008). "Deposition from particle-laden, round, turbulent, horizontal, buoyant jets in stationary and coflowing receiving fluids." *J. Hydraul. Eng.*, 134(4), 390-402.
- Doneker, R.L., and Jirka, G.H. (1990). "Expert system for hydrodynamic mixing zone analysis of conventional and toxic submerged single port discharges (CORMIX1)." *EPA/600/3-90/012*, Environmental Research Laboratory of U.S. Environmental Protection Agency (USEPA), Athens, GA, 1-250.
- Doneker, R.L., and Jirka, G.H. (2007). "CORMIX user manual – A hydrodynamic mixing zone model and decision support system for pollutant discharges into surface waters." *EPA-823-K-07-001*, USEPA, Washington, D.C., 206.
- Fischer, H.B., List, E.J., Koh, R.C.Y., Imberger, J., Brooks, N.H. (1979). *Mixing in Inland and Coastal Waters*, Academic Press, San Diego.
- Hodgson, J.E. (1991). "Turbulent jet discharges in rivers." Ph.D. Thesis, Department of Civil Engineering, University of Alberta, Edmonton, AB, Canada.
- Hodgson, J.E., Rajaratnam, N. (1992). "An experimental study of jet dilution in crossflows." *Can. J. Civ. Eng.*, 19, 733-743.
- Hodgson, J.E., Moawad, A.K., and Rajaratnam, N. (1999). "Concentration field of multiple circular turbulent jets." *J. Hydraul. Res.*, 37(2):249-256.

- Huang, H., Fergen, R.E., Rroni, J.R., and Tsai, J.J. (1996). "Probabilistic analysis of ocean outfall mixing zones." *J. Environ. Eng.*, 122 (5), 359-367.
- Jirka, G.H. (2004). "Integral model for turbulent buoyant jets in unbounded stratified flow. Part I: Single round jet." *Environ. Fluid Mech.*, 4, 1-56.
- Jirka, G.H., and Harleman, D.R.F. (1973). "The mechanics of submerged multiport diffuser for buoyant discharges in shallow water." *R.M. Parsons Laboratory Report*, Massachusetts Institute of Technology, Boston, MA.
- Kikkert, G. A., Davidson, M. J., and Nokes, R. I. (2009). "A jet at an oblique angle to a cross-flow." *J. Hydro-environ. Res.*, 3(2), 69-76.
- Kim, D.G., and Seo, I.W. (2000). "Modeling the mixing of heated water discharged from a submerged multiport diffuser." *J. Hydraul. Res.*, 38(4), 259-269.
- Knystautas, R. (1964). "The turbulent jet from a series of holes in Line." *Aeronaut. Q.*, 15, 1-28.
- Kuang, C.P., and Lee, J.H.W. (2006). "Stability and mixing of a vertical axisymmetric buoyant jet in shallow water." *Environ. Fluid Mech.*, 6, 153-180.
- Lam, K.M., Lee, W.Y., Chan, C.H.C., and Lee, J.H.W. (2006). "Global behaviors of a round buoyant jet in a counterflow." *J. Hydraul. Eng.*, 132(6), 589-604.
- Lee, J.H.W. (1985). "Comparison of two river diffuser models." *J. Hydraul. Eng.*, 111(7), 1069-1078.
- Lee, J.H.W., and Chu, V.H. (2003). "Turbulent jets and plumes, a Lagrangian approach." Kluwer Academic, Boston.
- Lee, J.H. W, Jirka, G.H. (1980). "Multiport diffuser as line source of momentum in shallow water." *Water Resour. Res.*, 16(4), 695-708.
- Lima Neto, I.E., Zhu, D.Z., Rajaratnam, N., Yu T., Spafford., M., and McEachern, P. (2007). "Dissolved oxygen downstream of an effluent outfall in an ice-covered river: natural and artificial aeration." *J. Environ. Eng.*, 133 (11), 1051-1060.
- Moawad, A.K., and Rajaratnam, N.(1998). "Dilution of multiple nonbuoyant circular jets in crossflows." *J. Environ. Eng.*,124(1), 51-58.
- Pani, B. S., Lee, J. H. W., and Lai, A. C. H. (2009). "Application of Reichardt's hypothesis for multiple coflowing jets." *J. Hydro-environ. Res.*, 3(3), 121-128.
- Parr, A.D., and Melville, J.G. (1981). "Nearfield performance of river diffusers." *J. Environ. Eng.*, 107(5), 995-1008.
- Parr, A.D., and Sayre, W.W. (1979). "Multiple jets in shallow flowing receiving waters." *ASCE J. Hydraul. Div.*, 105(11), 1357-1374.

- Platten, J.L., and Keffer, J.F. (1971). "Deflected Turbulent Jet Flows." *J. Applied Mech.*, 38E(4): 756-758.
- Pun, K.L., Davidson, M.J., and Wang, H.J. (2000). "Merging jets in a co-flowing ambient fluid - A hybrid approach." *J. Hydraul. Res.*, 38(2): 105-114.
- Rajaratnam, N. 1976. *Turbulent jets*, Elsevier Scientific, Amsterdam, The Netherlands.
- River2D* [Computer software]. Univ. of Alberta, Edmonton, AB, Canada.
- Tang, H.S., Paik, J., Sotiropoulos, F., and Khangaonkar, T. (2008). "Three-dimensional numerical modeling of initial mixing of thermal discharges at real-life configurations." *J. Hydraul. Eng.*, 134(9), 1210-1224.
- Tian, X., Roberts, P.J.W., and Daviero, G.J. (2004). "Marine wastewater discharges from multiport diffuser. II: Unstratified flowing water." *J. Hydraul. Eng.*, 130(12), 1147-1155.
- Tsanis, I.K., Valeo, C., and Diao, Y. (1994). "Comparison of near-field mixing zone models for multiport diffusers in the Great Lake." *Can. J. Civ. Eng.*, 21, 141-155.
- Turner Designs. (2001). "A practical guide to flow measurement." Turner Quantech fluorometer: Turner design guide, Waltham, MA.
- VISJET 2.0* [Computer software]. Univ. of Hong Kong, Hong Kong.
- Visual Plume 1.0* [Computer software]. USEPA, Washington, DC.
- Wang, H.J., and Davidson M.J. (2003). "Jet interaction in a still ambient fluid." *J. Hydraul. Eng.*, 129(5), 349-357.
- Zhang, W.M., Zhu, D.Z. (2011). "Transverse mixing in an unregulated natural river." *J. Hydraul. Eng.*, 137(11), 1426-1440.

Table 3-1. Measured Dye Mass Flux Compared to the Injection

| Section (km) | \dot{M} / \dot{M}_0 (%) |
|--------------|---------------------------|
| 0.114 | 90.93 |
| 0.260 | 89.82 |
| 0.516 | 91.42 |
| 1.282 | 111.76 |
| 2.260 | 101.08 |
| 4.131 | 95.48 |
| Average | 96.75 |

Table 3-2. Main Physical Parameters for the Effluent, Ambient and Diffuser

| | Parameters | Values |
|----------|--|--------|
| | Flow rate (m ³ /s) | 0.957 |
| Effluent | Effluent temperature (°C) | 27.2 |
| | Discharge concentration (ppt) | 20522 |
| | River discharge (m ³ /s) | 224.2 |
| Ambient* | Avg. river depth in effluent region (m) | 2.41 |
| | Avg. river velocity in effluent region (m/s) | 0.64 |
| | Water temperature (°C) | 11.6 |
| | Angle between diffuser and river velocity (°) | 90 |
| | Number of ports | 20 |
| | Distance between ports (m) | 2 |
| Diffuser | Nearest port to right bank (m) | 32.4 |
| | Avg. height of ports above river bed (m) | 1 |
| | Port diameter (m) | 0.15 |
| | Vertical angle between ports and river velocity (°) | 45 |
| | Horizontal angle between ports and river velocity (°) | 0 |

* Manning's n was 0.033 based on the velocity, water surface slope, and bathymetry field data.

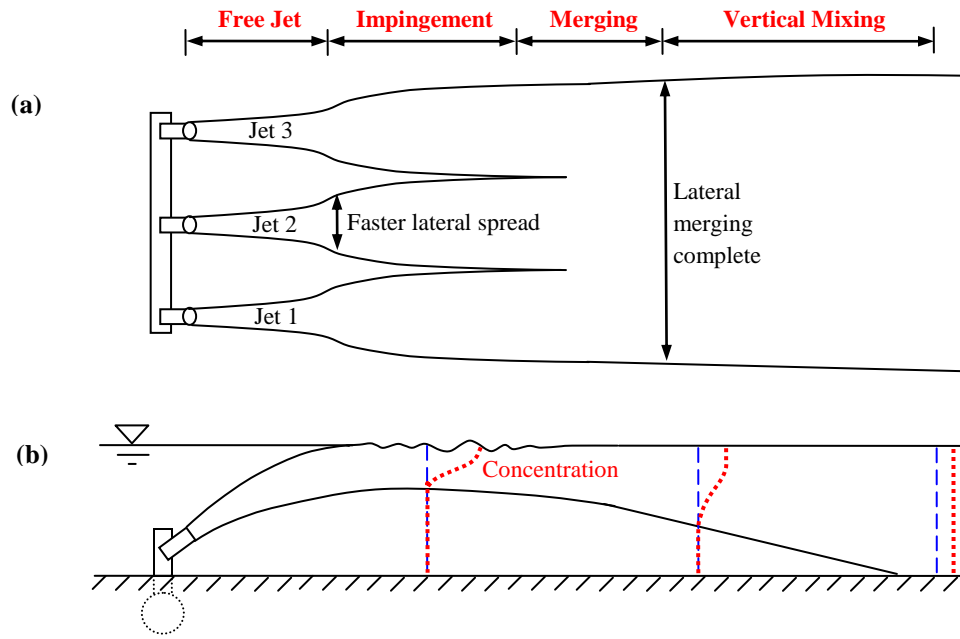


Figure 3-1. Schematic of the near-field mixing processes for a diffuser with an oblique angle into a shallow river: (a) aerial view; (b) side view

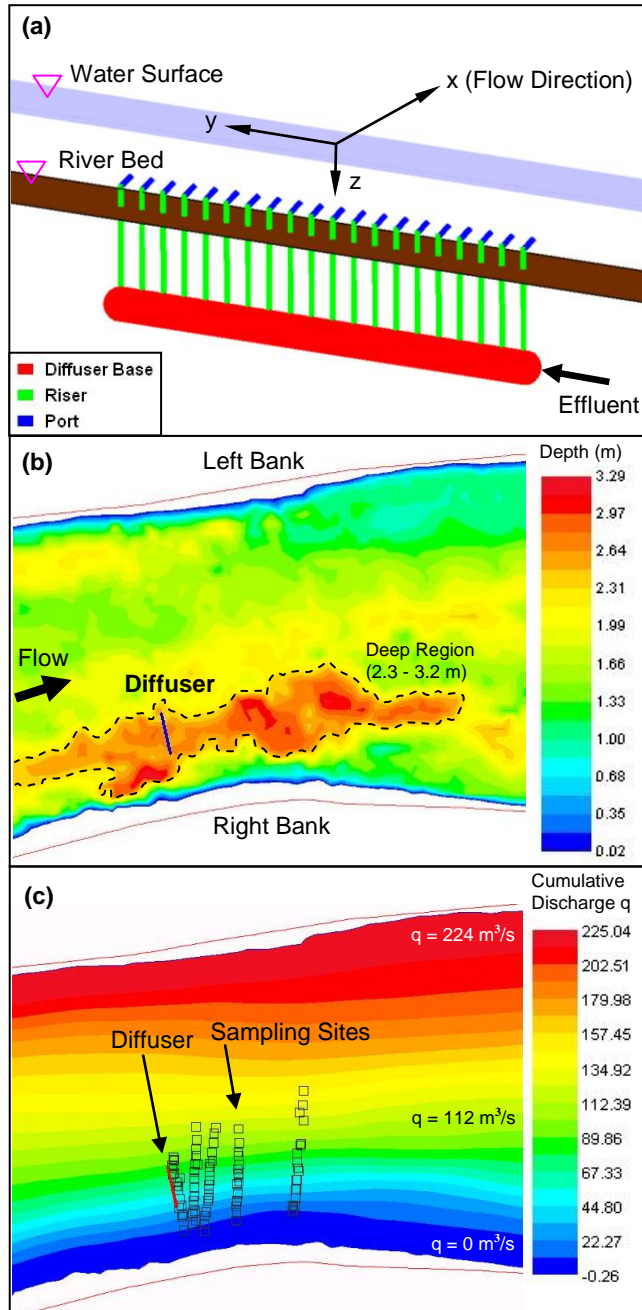


Figure 3-2. (a) Arrangement of Al-Pac's diffuser; (b) river bathymetry near the diffuser; (c) dye sampling sites at 4.8 m, 20.0 m, 33.3 m, 60.4 m, and 114.1 m downstream of the diffuser, with indication of cumulative discharge distribution

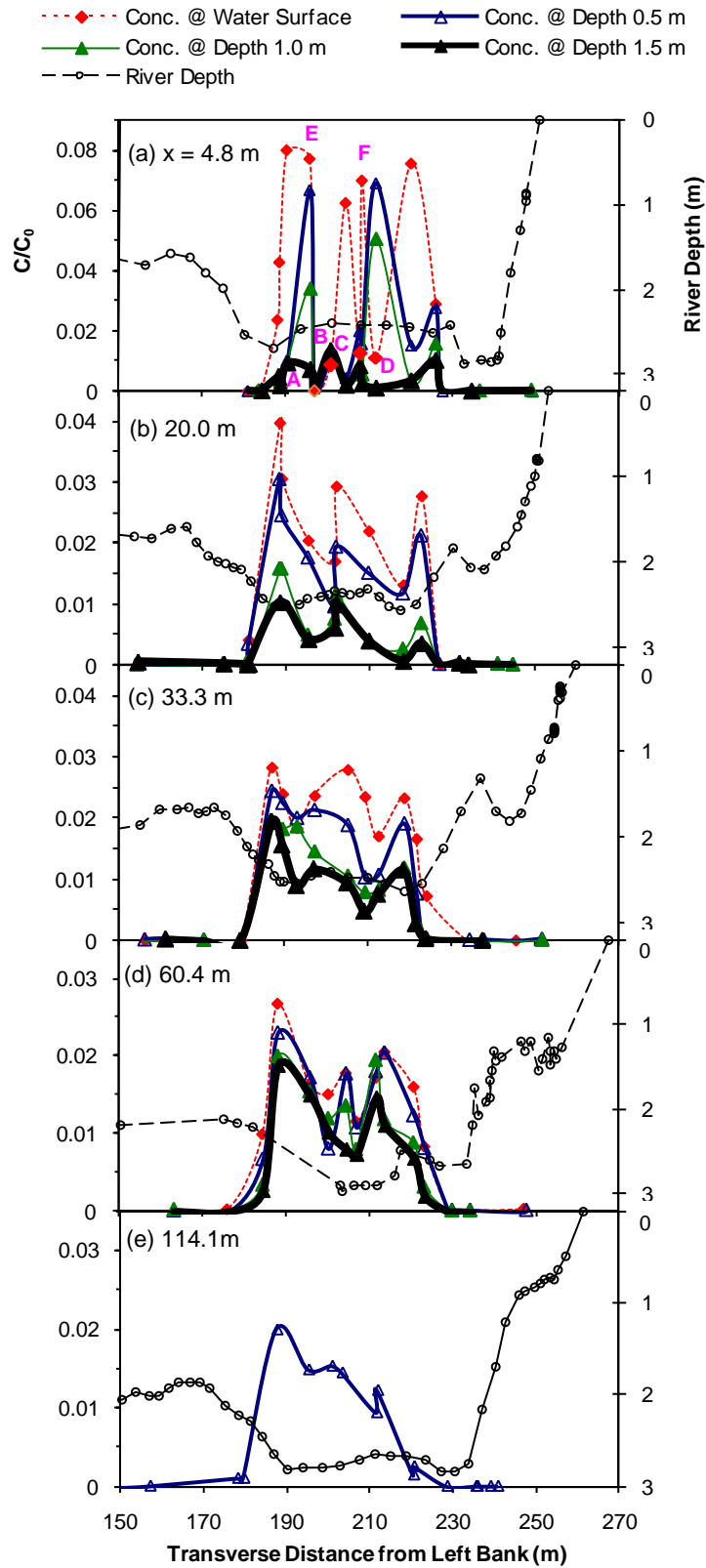


Figure 3-3. Measured dye concentrations at different sections

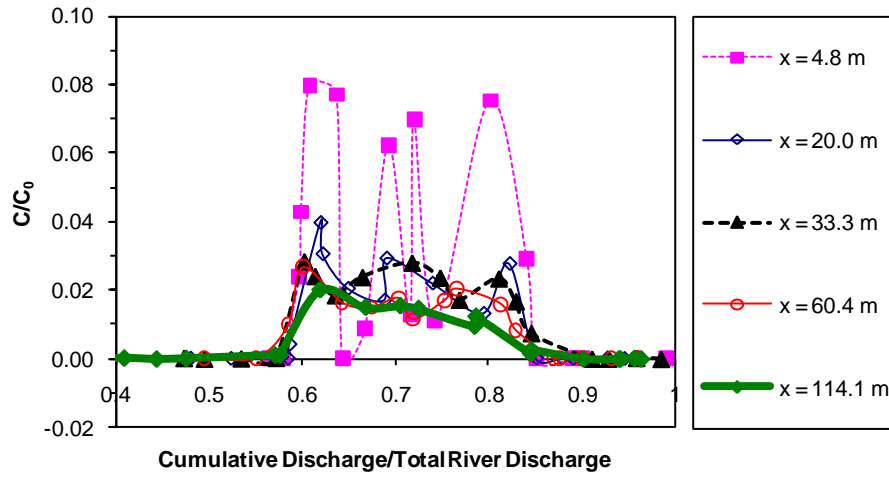


Figure 3-4. Water surface concentrations with cumulative discharges at different sections

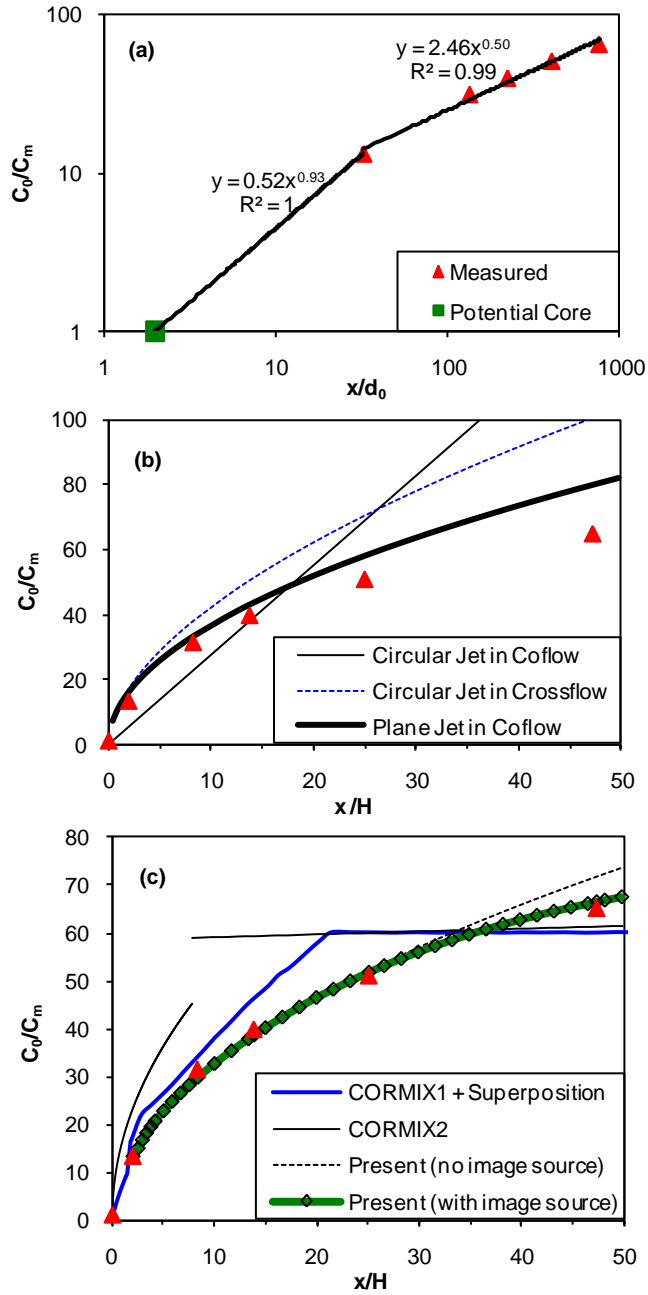


Figure 3-5. (a) Measured minimum dilutions; (b) comparison with jet theories; (c) comparison with CORMIX and present models

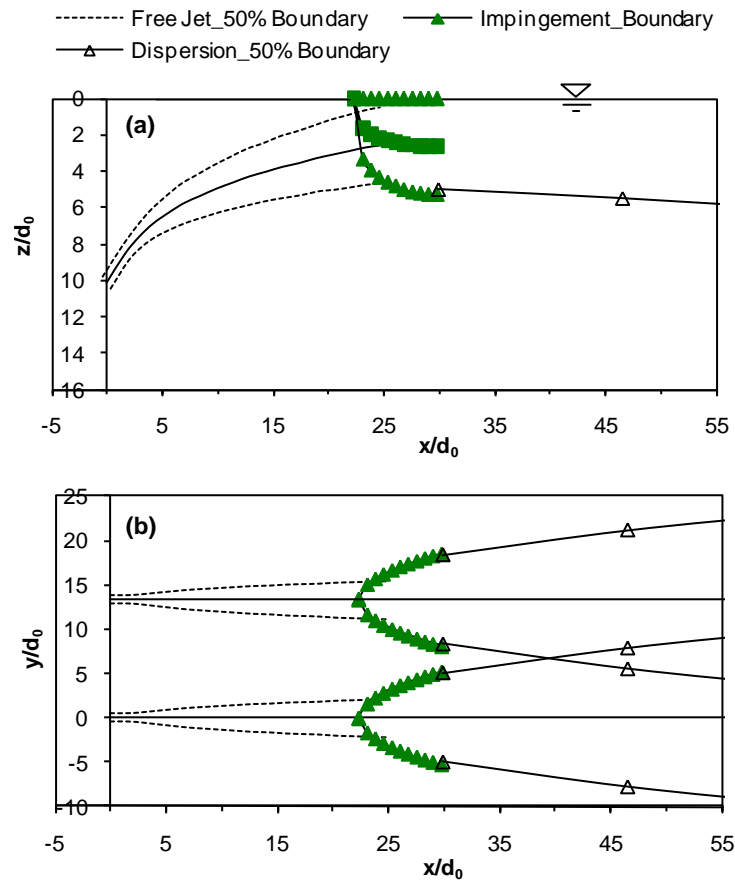


Figure 3-6. Modeling results of two neighboring jets from CORMIX1: (a) vertical trajectories; (b) horizontal trajectories

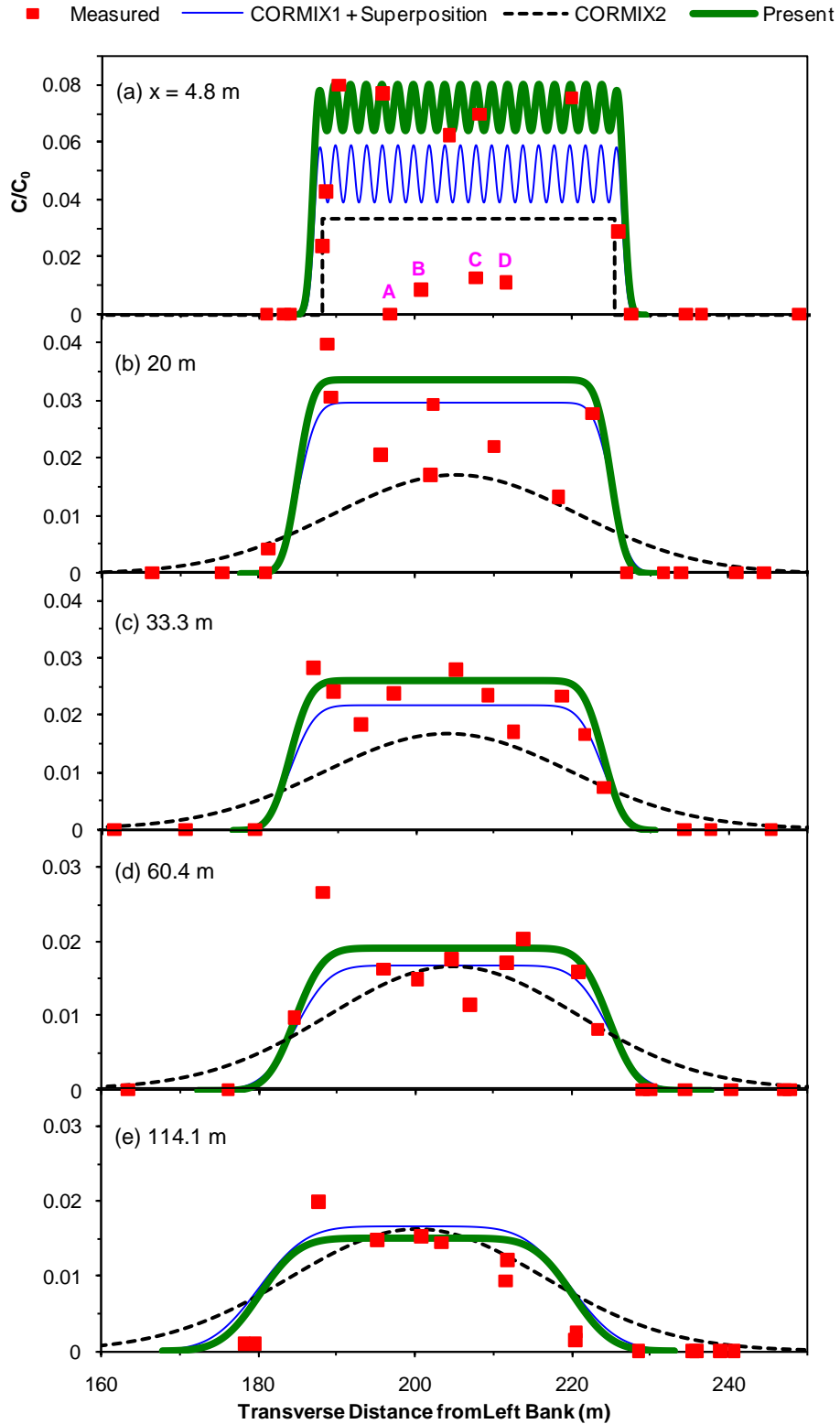


Figure 3-7. Measured and modeled concentration profiles at the water surface at various sections

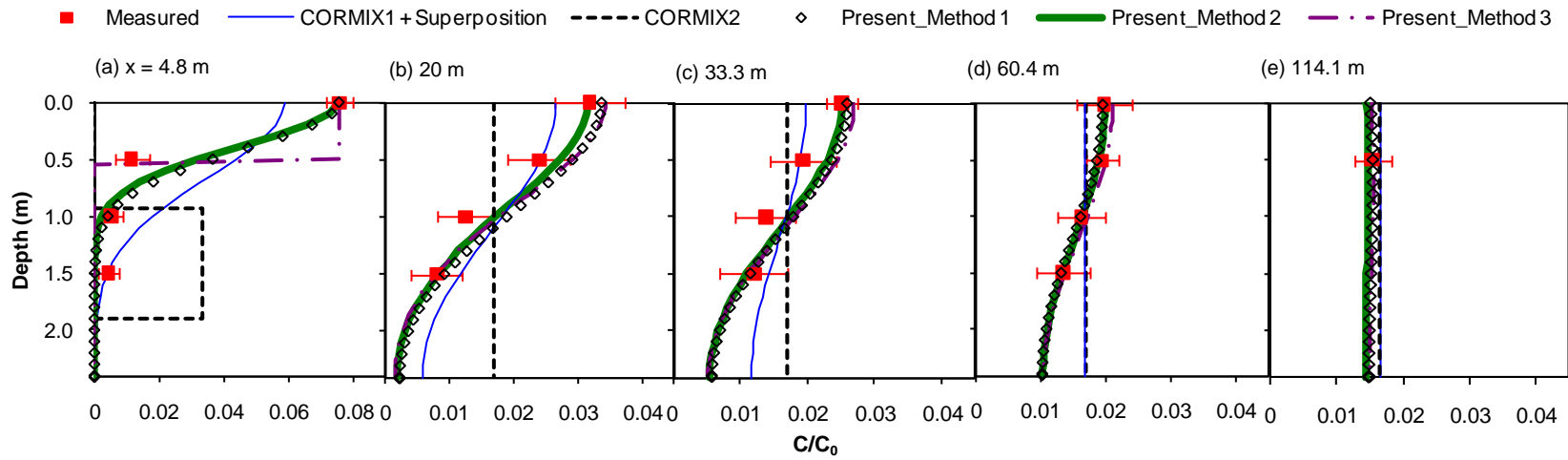


Figure 3-8. Measured and modeled vertical concentration profiles at various sections

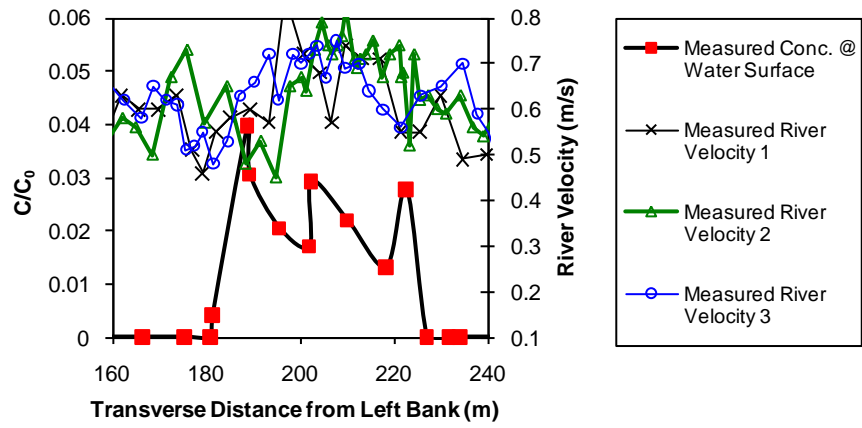


Figure 3-9. Effect of river velocity on lateral concentration distribution at Section 20 m

Chapter 4

Transverse Mixing in an Unregulated Northern River^{*}

4.1 Introduction

The Athabasca River in Alberta, Canada is a northern unregulated natural river (Fig. 4-1). Its discharge varies from about 1500 m³/s in the summer to less than 100 m³/s in the winter. The river receives effluents from five of Alberta's pulp and paper mills and supplies water to Canada's oil sands industry. In the winter, the river discharge is low and ice cover prevents surface re-aeration. The river's dissolved oxygen may drop below the critical level for fish and benthic macroinvertebrate species due to the wastewater discharges and the bottom sediment oxygen demand (Lima Neto et al. 2007). In Alberta, it is required that effluent plumes are delineated and the distances for 100-times dilution are reported in order to assess the environmental impact (Beak 1995).

Given that natural rivers are usually much wider compared to their depth, transverse mixing dominates the effluent mixing process. The transverse mixing coefficient, E_y , is commonly used to describe this process. Fischer et al. (1979) and Rutherford (1994) provided some general guidelines for the selection of E_y values in natural rivers. For northern unregulated rivers such as the Athabasca River, however, the highly seasonal variation of river discharge and the existence of ice cover in the winter, pose challenges to predict E_y . Some limited studies on the effects of river discharge and ice cover on E_y often give contradicting results (Elhadi et al. 1984; Rutherford 1994).

^{*} The content of this chapter has been published as: Zhang, W.M., and Zhu, D.Z. (2011). "Transverse mixing in an unregulated natural river." *J. Hydraul. Eng.*, ASCE, 137(11), 1426-1440.

In this study, a field dye test was conducted to study the effluent mixing characteristics downstream of the diffuser of Alberta Pacific Forest Inc. (Al-Pac) in the Athabasca River. The near-field mixing characteristics (within the first 114 m, before the completion of vertical mixing) were analyzed in Chapter 3. Chapter 4 focuses on the transverse mixing from 114 m to 32.6 km downstream of the diffuser. The distribution of cumulative discharge is constructed based on the river cross-sectional shapes, and a modified method is proposed to calculate the transverse mixing coefficient. Effects of river discharge and ice cover on transverse mixing are discussed. The mixing length for 100-times dilution is then examined under varying river discharges with and without ice cover. Chapter 4 will improve our understanding on transverse mixing in unregulated northern rivers. In particular, this study will provide a hydrodynamic mixing basis for the proposed oxygen injections through the existing effluent diffusers to improve the level of dissolved oxygen in the ice-covered Athabasca River.

4.2 Literature Review

Transverse mixing in rivers has been actively studied since the middle of the 20th century. Early studies were summarized by Fischer et al. (1979), Elhadi et al. (1984) and Rutherford (1994), while more recent studies were reported by Boxall and Guymer (2003), Baek et al. (2006), Seo et al. (2006), Albers and Steffler (2007), Jeon et al. (2007), Dow et al. (2009) and others. Transverse mixing coefficient, E_y , is commonly non-dimensionalized as E_y/U^*H , where H is the average river depth; and the average river shear velocity $U^* = \sqrt{gRS}$, where g is the gravitational acceleration, R is the hydraulic radius, and S is the water surface slope. Fischer et al. (1979) and Rutherford (1994) summarized that: $E_y/U^*H = 0.1 - 0.3$ for relatively straight channels, $0.3 - 0.9$ for gently meandering channels, and $1 - 3$ for sharp curved channels. The large variations in

E_y/U^*H is probably due to the site-specific nature of transverse mixing (Dow et al. 2009) as well as the differences in the field work designs and data analyses (Rutherford 1994).

A number of factors may affect the value of E_y , for example, river sinuosity, local curvature, river width, depth, discharge, river shear velocity, and ice cover. Of these factors, river sinuosity has been identified to have a significant effect on E_y . An increase in river sinuosity will greatly increase the value of E_y (Jeon et al. 2007). Rutherford (1994) summarized that downstream of some river bends, E_y could increase by 2 - 6 times. Boxall and Guymer (2003) studied a laboratory meandering channel and found that E_y increased around the bends and then decreased in the straight reaches after the bends. Similar phenomenon was also reported in Dow et al. (2009) in the North Saskatchewan River. Boxall and Guymer (2003) also developed an integrated approach to predict E_y along a meandering channel. Albers and Steffler (2007) proposed an analytical equation to quantify the change of E_y along a bend. The increase of E_y at bends is mainly caused by the helical motion of secondary currents. There have been a few recent attempts in measuring the three-dimensional flow structures at bends in laboratory models and river channels (Boxall and Guymer 2003; Szupiany et al. 2007) in an effort to link them to transverse mixing.

Jeon et al. (2007) summarized previous studies, and developed an empirical equation for E_y/U^*H which increased with river sinuosity, the ratio of river velocity to shear velocity, and river aspect ratio. However, these parameters as well as a few others, such as the ratio of river depth (or width) to the radius of river bend as reported by Fischer et al. (1979), have not been widely verified and adopted. No confirmed conclusion has been drawn on the effect of river discharge on transverse mixing coefficients in natural rivers. Based on studies in 23 rivers, Rutherford (1994) summarized that generally E_y increased with river discharge while E_y/U^*H remained

constant. Sayre (1979) noted that E_y decreased by 3 times around a bend in the Missouri River when the river discharge increased. Putz et al. (2000) reported that E_y/U^*H decreased slightly from 0.48 to 0.34 when the river discharge increased from 84 to 960 m^3/s .

Ice cover significantly increases the difficulty in conducting dye tests, and its effect on the transverse mixing coefficient has not been well understood (Elhadi et al. 1984). Previous studies in ice-covered rivers are listed in Table 4-1. Engmann (1974) used a wood cover to simulate the ice cover in a straight laboratory flume and found that wood cover reduced E_y and E_y/U^*H by approximately half, but it had little effect on E_y/U^*R . Notice that with ice cover, the hydraulic radius R is about $0.5H$. Engman and Kellerhals (1974) reported in the Lesser Slave River that with ice cover and a discharge decreased by 56% in the winter, E_y , E_y/U^*H and E_y/U^*R were reduced by 87%, 75% and 48%, respectively, compared to their open-water values. Beltaos (1980) found in the Athabasca River that with a discharge reduction of 69 - 81% under the ice-cover, E_y and E_y/U^*H were reduced by 57 - 85% and 23 - 32%, respectively, whereas E_y/U^*R was increased by 37 - 55%, compared to their open-water values. However, in the ice-covered Beaver River, Beltaos (1980) reported an increase of 26% in E_y/U^*H , which is contrary to the finding from the Athabasca River, and an increase of 151% in E_y/U^*R , which is much larger than that from the Athabasca River. Lau (1985) reported in the Nith River and Grand River that E_y was reduced by half; E_y/U^*H almost remained constant; and E_y/U^*R was increased significantly under the ice cover. Neill et al. (1995) reported in the ice-covered Peace River that $E_y/U^*H = 0.21$, which appears smaller than the common open-water value for such a meandering river reach. From Table 4-1, the effect of ice cover is usually compounded with the effect of discharge variation.

A number of field mixing studies have been reported for the Athabasca River near Al-Pac. Beltaos (1980) conducted two dye tests in 1974 (open-water condition) and 1975 (ice-covered condition). Van Der Vinne (1993) conducted a dye test in 1992 (ice-covered condition). Beak (1995) conducted two dye tests in 1994 (open-water condition) and 1995 (ice-covered condition), but the mixing coefficients were not calculated. Putz and Smith (2001) conducted two dye tests in 1997 (open-water condition). The results of these field studies will be discussed in this study.

Several methods have been reported for analyzing dye test results to obtain E_y . The most classic method is the standard “method of moments” (Fischer et al. 1979), which is based on the change of the variance of transverse concentration profiles with longitudinal distance. However, this method is only valid before the plume reaches any bank. Holly et al. (1972) derived the “generalized method of moments” to account for the bank effect. But Holly’s method is based on Cartesian coordinates and requires information about the transverse velocities that are typically difficult to measure. Beltaos (1980) and Rutherford (1994) further developed the generalized method of moments by using the concept of “cumulative discharge” to include the effect of non-zero transverse velocities in natural rivers. Another common method to determine E_y is based on finding the best-fit simulation with the measurement (Lau and Krishnappan 1981; Putz and Smith 2001). Note that the above methods can be directly applied to analyze results from steady dye injection. For slug dye tests (i.e. with transient dye injection), the “routing procedure” has been widely used (Fischer et al. 1979; Baek et al. 2006; Seo et al. 2006). The following is a brief introduction on the methods of moments, as steady dye injection is more commonly used than transient injection.

Standard Method of Moments: By using the concept of cumulative discharge, the depth-averaged, steady-state mixing equation becomes (Yotsukura and Sayre 1976):

$$\frac{\partial C}{\partial x} = D \frac{\partial^2 C}{\partial q^2} \quad (4.1)$$

where C is the tracer (e.g. dye) concentration; x is the longitudinal distance; D is the factor of diffusion; and q is the cumulative discharge. In Eq. (4.1), D is the cross-sectional average of $m_x h^2 u e_y$, where m_x is a metric coefficient and close to 1; h is the local river depth; u is the local river velocity in the x direction; and e_y is the local transverse mixing coefficient. q is defined as $\int_0^y u h dy$, with y being the transverse distance from one bank to the other. To derive Eq. (4.1), D is assumed to be constant across the river.

Based on $C - q$ profiles at different cross-sections, the method of moments is the most widely accepted method (thus this method is termed “standard”) to calculate D :

$$D = \frac{1}{2} \frac{d\sigma_q^2}{dx} \quad (4.2)$$

where σ_q^2 is the variance of a $C - q$ profile. Eq. (4.2) is only valid before the plume impinges the nearest bank, as beyond that the plume no longer follows a Gaussian distribution. σ_q^2 is defined as:

$$\sigma_q^2 = \frac{\int_0^Q (q - q_0)^2 C dq}{\int_0^Q C dq} \quad (4.3)$$

where q_0 is the centroid of the $C - q$ profile; and Q is the river discharge. The reach averaged transverse mixing coefficient, E_y , can then be calculated (Beltaos 1980):

$$E_y = \frac{D}{\psi U H^2} \quad (4.4)$$

where U is the average river velocity; ψ is the dimensionless shape-velocity factor, expressed as:

$$\psi = \frac{1}{UH^2Q} \int_0^Q m_x u h^2 dq \quad (4.5)$$

Rutherford (1994) summarized that ψ is normally between 1.0 and 3.6 for natural rivers.

Generalized Method of Moments: Beltaos (1980) and Rutherford (1994) derived a generalized method of moments to account for the bank effect, respectively. The general form is:

$$\sigma_q^2 = 2D \int_0^x f(x) dx \quad (4.6)$$

Beltaos (1980) used the plume concentrations at the banks to calculate $f(x)$:

$$f(x) = 1 - \left(1 - \frac{q_0}{Q}\right) \frac{C_{RB}}{C_\infty} - \frac{q_0}{Q} \frac{C_{LB}}{C_\infty} \quad (4.7)$$

where C_{RB} and C_{LB} are the concentrations at the right and left banks, respectively; C_∞ is the concentration of complete transverse mixing. Before the plume reaches either bank, $f(x) = 1$, and Eq. (4.6) reduces to Eq. (4.2). Rutherford (1994) used the whole concentration profile across a section to calculate $f(x)$:

$$f(x) = - \int_0^Q q \varphi(q) \frac{\partial C}{\partial q} dq \bigg/ \int_0^Q C dq \quad (4.8)$$

where φ is used to describe the change of D across the section. If $\varphi = 1$ (i.e. D is uniform across the section) and the plume does not reach either bank, integrating Eq. (4.8) by parts results in $f(x) = 1$, and Eq. (4.6) reduces to Eq. (4.2). From Eq. (4.6), when σ_q^2 is plotted with $\int_0^x f(x) dx$, half of the slope of the fitted straight line will be the value of D .

E_y can then be calculated by using Eqs. (4.4) - (4.5).

4.3 Field Work

The field work was conducted from September 22 to October 3, 2008 when the discharge was low before ice formation in the river. The location of the 32.58 km study

reach is shown in Fig. 4-1. In the first 3.5 km sub-reach, the bathymetry was surveyed in detail by using simultaneously a Trimble R8 real time kinematic global positioning system (RTK GPS) and a SonarLite echosounder. The RTK GPS records position with an accuracy of 1 - 2 cm, and the echosounder records depth with an accuracy of ± 2.5 cm. Bathymetry data were used to build a two-dimensional (depth-averaged) hydrodynamic model. Beyond the bathymetry survey region, the river cross-sectional shapes were measured with a survey rod and a hand-held GPS. The accuracy of the handheld GPS is in the order of 1-2 m.

A SonTek 3.0 MHz acoustic Doppler profiler (ADP) was used to measure the river velocities and discharges. The blanking distance from the ADP transducer to the first measurement cell was 0.2 m where no measurements can be made. For the reason of acoustic reflection from the river bed, ADP also does not measure the area close to the bed. The 1/6 power law velocity profile was used by the ADP to extrapolate velocities above (near water surface) and below (near the bed) the measurement area (SonTek/YSI 2005). Each section was measured three times, and the ADP gave quite stable river discharge values. The ADP also gave local depth-average velocities and cumulative discharges across the sections. Note that in this study, the ADP was mainly designed to measure the river discharge in the moving vessel measurement mode, and thus the ADP was not able to give accurate values for transverse and vertical velocity components (typically only a few percent of the longitudinal velocity). At the time of the dye test, the measured river discharge was between 224 - 251 m³/s and velocities 0.44 - 0.69 m/s (Table 4-2). The increase of river discharge along the study reach arose from the inflows of La Biche River (Fig. 4-1) and a number of small creeks at the banks.

Rhodamine WT of 80.63 ± 2.30 g/L was injected by a peristaltic pump into the effluent pipeline located 5 km upstream of the diffuser at a rate of 14.17 ± 0.16 mL/min

continuously for 45 hrs. The diffuser, located in the right (looking downstream) half of the river, was using 20 ports, spaced 2 m apart. The effluent discharge and temperature averaged 977.1 ± 23.7 L/s and 27.5 ± 0.3 °C, respectively. A total of 12 dye sections were selected (see Fig. 4-1 and Table 4-2). At each section, about 20 water samples were collected at a depth of 0.5 m. The sampling positions were recorded by the RTK GPS within the first 4 km downstream of the diffuser and by the handheld GPS beyond that.

Dye concentrations in water samples were measured by using a Turner Quantech fluorometer, which was calibrated between 0 to 5000 parts per trillion (ppt) with an average relative error of 1%. Each sample was measured at least three times with a standard deviation of approximately 3 ppt. Measurements show that the chemical and physical properties of the river water or the effluent does not interfere with the reading of fluorescence (see the recovery ratios in Zhang and Zhu 2011). Background concentrations of the effluent and the river water were 610.87 ± 2.79 ppt and 31.63 ± 1.21 ppt, respectively, which were within the normal background range of pure water (20 ppt) and raw sewage (1,000 ppt) (Turner Designs 2001). The river background value has been removed from the concentration values in this study.

The dye test results and the cross-sectional shapes are shown in Fig. 4-2. At Section 4.13 km, there is an island in the river (Fig. 4-1), and only the bathymetry of the main (right) channel is presented, because the left channel is rather shallow and dye concentrations were measured at zero. From Fig. 4-2, the cross-sectional shapes are highly irregular, and the plume gradually mixes across the river. The dye concentration was 20,104 ppt inside the diffuser. According to the analysis in the near-field, complete vertical mixing was already achieved at Section 114 m (Zhang and Zhu 2011). The maximum concentration at this location was 409 ppt, about 50 times (minimum)

dilution. This rapid dilution was mainly due to the use of the multiport diffuser. At Section 32.6 km, the maximum dye concentration was 125 ppt, about 161 times dilution from Al-Pac's diffuser or 3.2 times dilution from Section 114 m due to the river transverse mixing.

Fig. 4-2 also shows that the plume contracted from about 150 m at Section 4.13 km to about 100 m at Section 6.63 km. This highlights the necessity to use the concept of cumulative discharge. There are two out-of-trend points at Sections 13.7 km and 24.5 km. Re-examination excluded human errors. Evidence shows that this section of the river has significant groundwater discharge (P. McEachern, Alberta Environment, private communication, Aug. 28, 2009). These two points were excluded from the following analysis.

4.4 Estimate of Cumulative Discharge and Conservation of Dye Mass Flux

From the 12 dye sections, 4 sections (114 m, 2.26 km, 13.73 km, and 32.58 km) were measured with the ADP, which calculated the cumulative discharge directly. For the other 8 sections, cumulative discharge needed to be estimated. It will be useful to have a reliable method to predict the distribution of cumulative discharge across a river, as velocity measurement is usually time-consuming. In addition, there is always a need to adjust the velocity measurement results for different river discharge conditions.

Several methods to predict the cumulative discharge have been reported. They essentially divide a cross-section into sub-sections and assume that at each sub-section velocity follows the same relation as that for the whole cross-section. Beltaos (1980) and Rutherford (1994) proposed the use of Manning or Chezy equations to estimate the local depth-averaged velocity, but their methods have not been examined against measurements. Smith (1983) suggested an untested expression similar to the Chezy

equation, and Boxall and Guymer (2003) found this expression provided good estimation for cumulative discharge across a laboratory channel.

In this study, the Manning equation was applied to each sub-section. The river discharge can be written as:

$$Q = \int_0^B \frac{1}{n} R^{\frac{2}{3}} S^{\frac{1}{2}} h dy = \frac{S^{\frac{1}{2}}}{n} \int_0^B h^{\frac{5}{3}} dy \quad (4.9)$$

where B is the river width; and n is the Manning's coefficient. At each cross-section, if Q and local depth $h(y)$ are known, the coefficient $S^{\frac{1}{2}}/n$ can be easily determined to be $Q / \int_0^B h^{\frac{5}{3}} dy$. Then the local depth-averaged velocity, u , and cumulative discharge, q , can be calculated as:

$$u = \frac{S^{\frac{1}{2}}}{n} h^{\frac{2}{3}} ; q(y) = \int_0^y u h dy \quad (4.10)$$

As an example, the estimated u and q were compared with the field measurements at Section 13.73 km in Fig. 4-3. The u estimation is satisfactory, and the q estimation is quite good as q is an integral property not particularly sensitive to the variation of velocity. Comparisons of the estimated q with the measured q at eight sections are listed in Table 4-3. Within approximately one boat length from the start or end of an ADP track, the standard deviations of the velocity measurements were high (see Fig. 4-3). Thus, comparisons were only made beyond these distances to exclude the boat influence on the measurements. Generally, the absolute values of relative error for u estimation averaged 15.81 ± 2.07 % (similar to Table 4-3, not shown here). The absolute values of relative error for q estimation averaged 5.42 ± 2.84 %, which is on the same error level as reported by Boxall and Guymer (2003) in a laboratory channel.

The measured dye concentrations were plotted with measured (at Sections 114 m, 2.26 km, 13.73 km and 32.58 km) or estimated (at all the other sections) cumulative

discharges in Fig. 4-4. Dye mass flux, M , at each section was calculated and compared with the initial dye mass injection rate, M_0 :

$$M/M_0 = \int_0^Q Cdq / M_0 \times 100\% \quad (4.11)$$

where C is the measured dye concentration. The calculation results are also shown in Fig. 4-4, where the average $M/M_0 = 97.0 \pm 7.8\%$.

There are two sections where the dye mass fluxes were not well conserved. At Section 1.28 km, the dye mass flux was over-estimated by 12%. The error mainly originated from the insufficient samples that were collected between points A and B in Fig. 4-4(4), and a straight line was used to interpolate the concentrations between A and B. At Section 6.63 km, the dye mass flux was underestimated by 15%, which is probably due to the error in the q estimation. From Fig. 4-1, Section 6.63 km is located at the apex of a bend, where the flow structure is rather complex.

4.5 A Modified Method for Calculating Transverse Mixing Coefficient

4.5.1 Modified Method

All the existing methods for calculating transverse mixing coefficient, E_y , use raw field data directly, thus, the results depend strongly on the data quality, especially on the $C - q$ profiles. However, it is usually difficult to control the quality of field data; for example, dye mass flux may not be well conserved; water samples may not be sufficient within the plume at certain sections; some samples may have excessively high or low concentrations (due to human errors, background value of other effluent sources, or dilution by groundwater). These will directly affect the calculation results. Thus, the raw data should be first adjusted or pre-processed. For this reason, a modified method is

proposed to best-fit the raw field data by using analytical solutions on the concentration profiles, and the best-fitted profiles are used to calculate E_y .

Assuming the factor of diffusion, D , is constant from the dye injection location to any specified section x , the analytical solution to Eq. (4.1) follows the Gaussian distribution for a steady-state point source (Fischer et al. 1979):

$$C(x, q) = \frac{M_0}{\sqrt{4\pi Dx}} \exp\left[-\frac{(q - q_1)^2}{4Dx}\right] + \text{Images} \quad (4.12)$$

where q_1 is the cumulative discharge at the dye injection location and image sources are introduced to account for the reflection at the banks. When the injection occurs over a range of cumulative discharge from $q = a$ to $q = b$ (i.e. a line source such as from a diffuser), Eq. (4.12) can be integrated:

$$C(x, q) = \int_a^b \frac{M_0}{(b-a)\sqrt{4\pi Dx}} \exp\left[-\frac{(q - q')^2}{4Dx}\right] dq' + \text{Images} \quad (4.13)$$

Let $\eta = (q - q')/\sqrt{4Dx}$ and use the definition of the error function $erf(x) = 2\int_0^x \exp(-\eta^2) d\eta/\sqrt{\pi}$, the solution to Eq. (4.13) is:

$$C(x, q) = \frac{M_0}{2(b-a)} \left[erf\left(\frac{q-a}{\sqrt{4\pi Dx}}\right) - erf\left(\frac{q-b}{\sqrt{4\pi Dx}}\right) \right] + \text{Images} \quad (4.14)$$

In Eq. (4.12) or (4.14), D is the only variable, and is determined by the method of least squares to best fit the measurement data.

Based on the best-fitted $C - q$ profiles (not the raw field data), Beltaos' or Rutherford's generalized method of moments is used to calculate D . Although D values can be also obtained in best-fitting the measured concentration profiles by using Eq. (4.12) or (4.14), these D values are the average between the location of the source ($x = 0$) and the studied section x . Thus they are unable to reflect the change of D values from section to section, which is the most concerned in river mixing studies. From D , E_y can be calculated according to Eqs. (4.4) - (4.5).

4.5.2 Comparison of Methods

Based on the 2008 (present) dye test results, the modified method is compared with the standard and generalized method of moments. Basic hydraulic parameters at the 12 dye sections are listed in Table 4-2. In Table 4-2, the resulting shape-velocity factors, ψ , confirms the summary by Rutherford (1994) that ψ is normally in the range of 1.0 - 3.6 for natural rivers. At Section 8.48 km, $\psi = 5.11$, which is caused by the highly irregular cross-sectional shape (see Fig. 4-2(8)). Following Eq. (4.2) or (4.6), transverse variance σ_q^2 is plotted versus x or $\int_0^x f(x)dx$ for the three methods in Fig. 4-5.

Note that in Figs. 4-5(b) and 4-5(c), Beltaos' generalized method of moments was used. Although Rutherford's generalized method of moments (Eq. (4.8)) were successfully used by Rutherford (1994) and Boxall and Guymer (2003), in this study, negative values of $f(x)$ were obtained at Sections 24.49 km and 32.58 km, where the values of $\partial C/\partial q$ were positive (see Fig. 4-4(11) and 4-4(12)). This resulted in a negative value of D between the two sections, which is physically impossible. For the modified method in Fig. 4-5(c), σ_q^2 was calculated based on the best-fitted $C - q$ profiles in Fig. 4-4, where it shows that the Gaussian type distribution works well to delineate the plume across a natural river.

From the slopes of the fitted lines in Fig. 4-5, transverse mixing coefficients were calculated and shown in Table 4-4. From the standard method of moments in Fig. 4-5(a), it appears the whole reach can be divided into 3 sub-reaches, with $E_y/U^*H = 0.30$ in the first 13.73 km. The results for the other two sub-reaches are unreliable, as the dye already contacted the banks there. From Beltaos' generalized method of moments in Fig. 4-5(b), the total study reach can be divided into 2 sub-reaches, with $E_y/U^*H = 0.33$ in the first 13.73 km and 0.43 in the following 18.85 km. Similarly, from the modified

method in Fig. 4-5(c), $E_y/U^*H = 0.34$ in the first 13.73 km and 0.51 in the following 18.85 km. It appears that the sharp bend near 13.73 km divides the whole study reach into two sub-reaches. The second sub-reach has a larger river sinuosity than the first sub-reach and thus has a larger value of E_y/U^*H (Jeon et al. 2007).

Beltaos' generalized method of moments takes into account the bank effect, and thus is superior to the standard method of moments (Table 4-4). With increasing bank effects, the standard method of moments increasingly underestimates D or E_y/U^*H from 40% in the sub-reach 13.73 - 24.49 km to 75% in the sub-reach 24.49 - 32.58 km. The modified method gives similar results as Beltaos' generalized method of moments because the variances σ_q^2 calculated from the best-fitted $C - q$ profiles are, overall, close to those from the unprocessed $C - q$ profiles (Fig. 4-5). The modified method has clear advantages when the quality of field data is relatively low. For instance, at Section 1.28 km, insufficient samples were taken between Points A and B in Fig. 4-4(4) (e.g., sparse data points). If the raw data are used directly with a linear interpolation between A and B, the variance σ_q^2 (and thus D and E_y) would be overestimated by 109% compared to using the curved line based on Eq. (4.14) in Fig. 4-4(4). It is clear that the sparseness of raw field data will have less impact on the accuracy of the results if the modified method is used, because this method only uses the raw field data to calibrate the modeled concentration profiles.

As shown in Figs. 4-5(b) and 4-5(c), the modified method significantly improves the correlation of data sets. The generalized method of moments can only show some general trends of D along the study reach (i.e. its local changes are unreliable). For instance, σ_q^2 decreases obviously at three sections in Fig. 4-5(b), resulting in negative local values of D that are physically impossible. Negative local values of D were also frequently encountered in many previous studies, as the quality

control over field data was difficult. In contrast, the modified method allows the examination of D (and thus E_y) all along the river. Note that in Fig. 4-5(c), σ_q^2 slightly decreases (6%) at one section (6.63 km), which is mainly caused by the error in the q estimation at this section as stated before. Overall, through pre-processing the field data, the modified method is able to improve or ensure the data reliability, as illustrated at Section 1.28 km.

4.5.3 Application of the Modified Method

The modified method is now further examined by applying it to two other field dye tests in both open-water and ice-covered conditions. Beak (1995) conducted two dye tests via Al-Pac's diffuser in 1994 (open-water) and 1995 (ice-covered), but the mixing coefficients were not calculated.

Beak's 1994 dye test: Dye concentrations were measured with transverse distances at nine sections (Table 4-5), and river velocities were measured at four of these sections. For the sections without velocity measurements, Eqs. (4.9) - (4.10) were used to estimate q . The $C - q$ profiles are shown in Fig. 4-6, where the concentrations are in parts per billion (ppb). The average dye mass flux, $M/M_0 = 90.2 \pm 9.5$ %. In Fig. 4-6, the locations of peak concentrations change slightly at different sections, mainly because of the inconsistency in the measurement results of river discharge (see Table 4-5). The modeled results according to Eq. (4.14) are also shown in Fig. 4-6, and are in good agreement with the measurements. The variances σ_q^2 from the $C - q$ profiles are plotted in Fig. 4-7(a). Similarly, the study reach can be divided into two subreaches, and their mixing coefficients are listed in Table 4-6.

Comparing Table 4-6 with Table 4-4, the values of D , E_y and E_y/U^*H in the first sub-reach were respectively 21%, 33%, and 44% higher in the 1994 dye test than those

in the 2008 dye test. The higher values of E_y and E_y/U^*H in the 1994 test mainly originate from the higher value of D , which is further because of the high value of σ_q^2 at Section 16 km in the 1994 test (Fig. 4-7(a)). The faster lateral spread of the plume at Section 16 km is caused by the sharp bend near 13.7 km (Fig. 4-1). If one more cross-section had been measured near the sharp bend in the 1994 test, the values of D , E_y and E_y/U^*H would be close to the values in the 2008 test. This suggests the importance of correctly selecting measurement sections. In the second sub-reach, the differences between the 1994 and 2008 dye tests for the values of D , E_y and E_y/U^*H were 6%, 7% and 13%, respectively. The reason for the small differences is that the sub-reach 16 - 32 km in the 1994 test is actually located within the sub-reach 13.73 - 32.58 km in the 2008 test. From the above analysis, although essentially the same, the 2008 test gives more reliable results than the 1994 test (which would overestimate E_y/U^*H by 22% for the whole 32 km reach).

Beak's 1995 dye test: Six to ten holes were drilled through an ice cover of 0.5 m thickness to take water samples at each of the 5 sections listed in Table 4-5. Since no velocity measurements were conducted, the river velocity and cumulative discharge needed to be estimated. No estimating method has been reported specifically for ice-covered rivers. With the ice cover, the Manning equation is still valid (Ashton 1986), and thus Eq. (4.9) is still reasonable. But Manning's n should be interpreted as composite Manning's n induced by the river bed and ice cover, and the coefficient in Eqs. (4.9) - (4.10) becomes to be $2^{-2/3}S^{1/2}/n$. Moreover, the accuracies of Eqs. (4.9) - (4.10) are expected to be lower for ice-covered rivers, because the roughness of ice cover is site- and time-specific (Engman 1974; Ashton 1986). For the Feb. 1995 dye test, the cross-sectional average velocity was estimated in this study to be 0.26 - 0.35

m/s at $Q = 84 \text{ m}^3/\text{s}$, close to the measurement of 0.23 and 0.32 m/s at two sections at $Q = 92 \text{ m}^3/\text{s}$ in the same reach in Feb. 1992 (Van Der Vinne 1993).

The $C - q$ profiles are shown in Fig. 4-8, with average dye mass flux $M/M_0 = 94.6 \pm 10.2 \%$. In Fig. 4-8, the modeled results by using Eq. (4.14) are also shown. Note that at Section 8 km, the measured concentration near the right bank is lower than the modeled value probably due to the tributary creek flows; at Section 64 km, the low M/M_0 value indicates the inaccuracy in either the measured concentration and/or the river discharge. The overall good match with the measurements indicates the suitability of Eq. (4.14) for ice-covered rivers. More importantly, from Fig. 4-8, six water samples at each section appear to be sufficient to calibrate Eq. (4.14), indicating that the number of water samples for a field dye test may be reduced by more than 50%. The variance σ_q^2 was plotted in Fig. 4-7(b), and the resulting mixing coefficients are listed in Table 4-6. Here, the 32 km reach can be treated as a whole, with $E_y/U^*H = 0.33$. The 1994 and 1995 dye tests confirm that the modified method applies for steady-state mixing problems in both open-water and ice-covered conditions.

4.6 Discussions

Five other dye tests have also been reported in or close to the present study reach, in addition to the 2008 (present) dye test and Beak's 1995 dye test. A total of seven dye tests provide a rare and valuable opportunity to examine the effects of river discharge and ice cover on transverse mixing coefficients in a fixed reach. Note that in this discussion, Beak's 1994 dye test is not included because it would overestimate E_y/U^*H by 22% as analyzed before.

Beltaos (1980) conducted two dye tests in a 17.6 km reach downstream of the Athabasca Town (see Fig. 4-1) in the Athabasca River in 1974 (open-water) and 1975

(ice-covered) when $Q = 566$ and $105 \text{ m}^3/\text{s}$, respectively. Although Beltaos' study reach is about 23 km upstream of the present, the channel characteristics are quite similar (Putz et al. 2000), e.g., the channel width, cross-sectional shape, sinuosity, bed and bank materials. This suggests that the mixing coefficients in these two reaches should be close. Van Der Vinne (1993) conducted a dye test from the Athabasca Town to the Calling River (see Fig. 4-1) in ice-covered condition in 1992 when $Q = 166 \text{ m}^3/\text{s}$. His study reach was 76.9 km, which included the 32.6 km present reach. Putz and Smith (2001) conducted two dye tests under $Q = 960$ and $876 \text{ m}^3/\text{s}$ in 1997 (open-water). Their study reach was also 32 km, but started from 1 km upstream of Al-Pac's diffuser.

All the mixing coefficients from the above seven dye tests are plotted versus Q in Fig. 4-9. Note that in Putz and Smith (2001), only E_y/U^*H was reported. E_y was calculated by using the widely-accepted rule that river shear velocity is about 1/10 of the mean velocity (Roberts and Webster 2002). The 1/10 rule can be checked in Table 4-3 and some other studies such as Engmann and Kellerhals (1974). The factor of diffusion D was calculated by using Eq. (4.4), where the shape-velocity factor ψ was estimated to be 1.30 and 1.33 for $Q = 960$ and $876 \text{ m}^3/\text{s}$, respectively, based on Eq. (4.5).

4.6.1 Effect of River Discharge

Fig. 4-9 indicates that the variation of Q significantly affects E_y and D , but it has limited effect on E_y/U^*H . For $Q = 84 - 960 \text{ m}^3/\text{s}$, the average value of $E_y/U^*H = 0.36 \pm 0.05$, with a standard deviation of about 14% of its mean value. As it is expected that all the data points can be subject to an uncertainty of up to 20%, it is reasonable to conclude that the variation of Q has limited influence on E_y/U^*H .

In Fig. 4-9(a), the relationship of E_y vs. Q can be well fitted with a straight line: $E_y = \alpha Q$, where $\alpha = 1.3 \times 10^{-4}$. At $Q = 0$, E_y should be 0, meaning the straight line must start from the origin. By using the Manning equation for Q , one obtains:

$$\frac{E_y}{U^*H} = \frac{\alpha B}{n\sqrt{g}} R^{\frac{1}{6}} \quad (4.15)$$

Eq. (4.15) may be approximated as: $E_y/U^*H \propto R^{\frac{1}{6}} \approx R^0 = 1$, which explains the approximate constant value of E_y/U^*H in Fig. 4-9(b). By using $\alpha = 1.3 \times 10^{-4}$, the river width $B = 274$ m, $g = 9.81$ m/s², and Manning's $n = 0.033$ (Zhang and Zhu 2011), $\alpha B/n\sqrt{g}$ is calculated to be 0.34, quite close to $E_y/U^*H = 0.36$ in Fig. 4-9(b).

Fig. 4-9(b) appears to show that E_y/U^*H decreases slightly with the increase of Q in open-water conditions. However, by relating R with Q through the Manning equation, Eq. (4.15) shows that E_y/U^*H will be proportional to $Q^{1/10}$, i.e., it will increase slightly with the increase of Q . The difference in the E_y/U^*H vs. Q relation is likely due to many of the simplifications involved in the above derivations. In addition, a slight change in the E_y vs. Q relation will also change this trend. For instance, if a power law relation such as $E_y = 4.3 \times 10^{-4} Q^{0.81}$ (with correlation coefficient $R^2 = 0.988$) is used to fit the data sets in Fig. 4-9(a), then E_y/U^*H will be proportional to $Q^{-0.09}$, which can reflect the slightly decreasing trend of E_y/U^*H with Q .

In Fig. 4-9(c), the relationship of D vs. Q may be well fitted by a power law: $D = \varepsilon Q^2$, where $\varepsilon = 1.67 \times 10^{-6}$. If D is non-dimensionalized in the form of DB/Q^2 (Gowda 1984), then

$$DB/Q^2 = \varepsilon B \quad (4.16)$$

By using $\varepsilon = 1.67 \times 10^{-6}$ and $B = 274$ m, DB/Q^2 is calculated to be 4.6×10^{-4} , close to the value of $DB/Q^2 = (4.4 \pm 1.2) \times 10^{-4}$, which is obtained from plotting DB/Q^2 with Q (similar to Fig. 4-9(b), not shown here).

These results are compared with limited previous studies. Rutherford (1994) summarized 53 studies in 23 rivers, and found that overall, E_y increased with Q , whereas E_y/U^*H remained constant. However, Rutherford (1994) questioned the suitability of this general trend for a fixed river or river reach. Putz et al. (2000) studied the same reach as in the present study, and reported that E_y/U^*H decreased from 0.48 to 0.34 when Q increased. From Figs. 4-9(a) and 4-9(b), it is reasonable to conclude that E_y/U^*H is overall (considering both open-water and ice-covered conditions) a constant for varying Q in the fixed reach, and there appears to be a trend that E_y/U^*H slightly decreases with the increase of Q in open-water conditions.

4.6.2 Effect of Ice Cover

The effect of ice cover was first examined through the comparison of the 2008 dye test (open-water) with the 1995 dye test (ice-covered). From Figs. 4-5(c) and 4-7(b), the study reach can be treated as a whole in ice-covered condition, without the need to divide it into several sub-reaches as in open-water condition. This is likely due to the fact that the additional friction induced by the ice cover may reduce the secondary circulations at river bends (Engmann and Kellerhals 1974).

In ice-covered condition, the lateral spread of the plume (indicated by σ_q^2) was only about 1/10 of their open-water values. Thus, the values of D reduced to 1/4 - 1/16 and E_y to 1/2 - 1/4 in the winter (see Tables 4-4 and 4-6). From Table 4-1, the present result of the E_y value being reduced on average by 68% in ice-covered condition is comparable to the 50 - 88% reductions reported by Engmann (1974), Engmann and Kellerhals (1974), Beltaos (1980), and Lau (1985). From Fig. 4-9(a), the decrease of E_y is mainly caused by the reduction of Q in the winter.

From Fig. 4-9(b), with ice cover, $E_y/U^*H = 0.31 \pm 0.03$, about 21% smaller than the open-water value of 0.39 ± 0.05 ; and DB/Q^2 is about 35% smaller (similar to Fig. 4-9(b), not shown here). This finding, i.e., smaller values of E_y/U^*H obtained in ice-covered condition, agrees with all the previous results listed in Table 4-1, with the exception of Beltaos (1980) who reported a 26% increase of E_y/U^*H in the Beaver River. The present 21% reduction of E_y/U^*H in ice-covered condition is different from the 50 - 75% reductions in the studies of Engmann (1974) and Engmann and Kellerhals (1974), and the 4 - 5% reductions in the study of Lau (1985), but quite comparable to the reductions of 23% and 32% at two reaches of the Athabasca River in the study of Beltaos (1980). As Beltaos' and the present study are both in the Athabasca River, it is possible that the reduction amount of E_y/U^*H is river-specific due to different ice cover and flow conditions. Further research will be needed to fully understand this.

The following physical processes may explain the reduction of E_y/U^*H in ice-covered condition. With the introduction of ice cover, the additional friction will generate more river turbulence and thus E_y increases; meanwhile, the typical one large circulation eddy spanning the cross-section at bends (Chow 1959; Fischer et al. 1979) in open-water condition will break into two smaller counter-rotating circulation eddies in ice-covered condition (as measured by Demers et al. 2010), and thus, E_y decreases. Since the secondary flow typically has more pronounced effect on E_y than the ice cover induced river turbulence (Fischer et al. 1979), the general result is that E_y/U^*H decreases in ice-covered condition. Recently, Dow (2009) measured the flow field below a floating ice cover in a laboratory straight flume and showed that the effect of ice cover on the longitudinal velocity is limited within a small region close to the ice cover.

4.6.3 Mixing Length for 100-times Dilution

As an application of the above discussion, the mixing length for 100-times dilution was examined for Al-Pac's effluent under varying river discharges with and without ice cover. The dilution here refers to minimum dilution. The effluent discharge was assumed to be the same as that during the 2008 dye test ($0.977 \text{ m}^3/\text{s}$). For simplification, the river width was assumed constant for different Q because it only increases by 2 - 8% at high Q . The water surface level during the 2008 dye test serves as a base; the water levels at other Q were estimated by using the Manning equation; and the distributions of q were estimated based on Eqs. (4.9) - (4.10). The plume was modeled with Eq. (4.14), where the value of $D = 1.67 \times 10^{-6} Q^2$ as shown in Fig. 4-9(c). To examine the sensitivity of the mixing length to D , a 15% increase (or decrease) of the D value was tested. The results are shown in Fig. 4-10.

From Fig. 4-10, river discharge has a significant influence on the mixing length. For the range of $Q = 100 - 500 \text{ m}^3/\text{s}$, with the decrease of Q , the mixing length increases dramatically, e.g., when Q drops from 400 to $100 \text{ m}^3/\text{s}$, the mixing length increases from 1 to 216 km. For $Q < 97.7 \text{ m}^3/\text{s}$ (100 times of the effluent discharge), the river is incapable of diluting the effluent 100 times, i.e. the mixing length is infinity. For $Q \geq 426 \text{ m}^3/\text{s}$, the river discharge that Al-Pac's diffuser spans over, $(b - a) \geq 97.7 \text{ m}^3/\text{s}$, means the mixing length is 0 since Eq. (4.14) assumes immediate mixing of the effluent with the river flow between $q = a$ and $q = b$. In this case, the near-field mixing should be studied. According to Zhang and Zhu (2011), the near-field mixing length is about 100 m. If the value of D increases (or decreases) 15%, the mixing length will decrease 13% (or increase 18%). At the Q during the 2008 dye test, the mixing length was calculated to be 6.2 - 8.4 km, a little smaller than the measurement of 8.5 - 13.7 km. The

underestimation is mainly because of the simplification that only one D value was used in the whole reach without the consideration of its local variation.

4.7 Summaries and Conclusions

A field dye test was conducted to study the transverse mixing in a 32.58 km reach of the Athabasca River in northern Canada. A method for estimating cumulative discharge was developed by using the river bathymetry and the Manning equation across a river section. This method was shown to be accurate, with relative error of 5.42 ± 2.84 %. A modified method was proposed for calculating transverse mixing coefficient, E_y , which first uses raw field data to calibrate analytical concentration profiles and then uses the calibrated profiles to calculate E_y . The major advantage of this modified method is that it can produce reliable mixing coefficients in both open-water and ice-covered conditions even with relatively poor quality field data (e.g., sparse measurement points or some erroneous data points). The modified method, together with the method for estimating cumulative discharge, can greatly reduce the workload of a field dye test, as velocity measurements are not required at each section and less water samples are needed.

The effects of river discharge and ice cover on transverse mixing were examined. In the present study reach, E_y and D (factor of diffusion) were found to follow approximately linear and quadratic relations, respectively, with Q (from 84 to 960 m^3/s). However, overall E_y/U^*H appeared unaffected (14%) by the variation of Q in both open-water and ice-covered conditions. In open-water condition, with increase of Q (from 238 to 960 m^3/s), E_y/U^*H appeared to decrease slightly (22%). In ice-covered condition, E_y/U^*H was found to be 21% smaller than the average open-water value. The 50 - 88% reductions in E_y in ice-covered condition reported previously and in the

present study were caused by the reduction of the winter Q . The effect of river discharge on transverse mixing was then demonstrated in an analysis of mixing length for 100-times dilution. When Q decreases, the mixing length would increase greatly from approximately 100 m to hundreds of kilometers. If the D value increases (or decreases) by 15%, the mixing length will decrease by 13% (or increase by 18%).

As a note for further research on transverse mixing in rivers, it will be important to obtain three-dimensional velocity measurement in the field, relate these results to the river hydrodynamic and morphodynamic features, and finally elucidate how these parameters control transverse mixing.

References

- Albers, C., and Steffler, P. (2007). "Estimating transverse mixing in open channels due to secondary current-induced shear dispersion." *J. Hydraul. Eng.*, 133(2), 186-196.
- Ashton, G.D. (1986). "*River Lake Ice Engineering*." Water Resources Publications, LLC., Highlands Ranch, CO.
- Baek, K.O., Seo, I.W., and Jeong, S.J. (2006). "Evaluation of dispersion coefficients in meandering channels from transient tracer tests." *J. Hydraul. Eng.*, 132(10), 1021-1032.
- Beak Consultants Ltd. (1995). "Effluent plume delineation study for Alberta Pacific Forest Industries Inc." *Rep. No. 7.10610.1*, Brampton, Ontario.
- Beltaos, S. (1980). "Transverse mixing tests in natural streams." *J. Hydraul. Div.*, 106(10), 1607-1625.
- Boxall, J. B., and Guymer, I. (2003). "Analysis and prediction of transverse mixing coefficients in natural channels." *J. Hydraul. Eng.*, 129(2), 129-139.
- Chow, V.T. (1959). *Open-Channel Hydraulics*. McGraw-Hill, New York.
- Demers, S., Buffin-Belanger, T., and Roy, A.G. (2010). "Helical cell motions in a small ice-covered meander river reach." *River Res. Applic.*, DOI: 10.1002/rra.
- Dow, K. E. (2009). "Experimental investigation of ice floe stability." Ph.D. Thesis, Dept. of Civil and Environmental Engineering, University of Alberta, Edmonton, Canada.

- Dow, K. E., Steffler, P. M., and Zhu, D. Z. (2009). "Case study: Intermediate field mixing for a bank discharge in a natural river." *J. Hydraul. Eng.*, 135(1), 1-12.
- Elhadi, N., Harrington, A., Hill, I., Lau, Y. L., and Krishnappan, B. G. (1984). "River mixing - a state-of-the-art report." *Can. J. Civ. Eng.*, 11(3), 585-609.
- Engmann, J.E.O. (1974). "Transverse mixing characteristics of open and ice-covered channel flows." Ph.D. thesis, Department of Civil Engineering, University of Alberta, Edmonton, Alberta.
- Engmann, J.E.O., and Kellerhals, R. (1974). "Transverse mixing in an ice-covered river." *Water Resour. Res.*, 10(4), 775-784.
- Fischer, H.B., List E.J., Imberger, J., Brooks, N.H. (1979). *Mixing in Inland and Coastal Waters*, A Division of Harcourt Brace and Company, San Diego, California.
- Gowda, T.P.H. (1984). "Water Quality prediction in mixing zones of rivers." *J. Environ. Eng.*, 110(4), 751-769.
- Holley, E.R., Siemons, J. and Abraham, G. (1972). "Some aspects of analyzing transverse diffusion in rivers." *J. Hydraul. Res.*, 10, 27-57.
- Jeon, T. M., Baek, K. O., and Seo, I. W. (2007). "Development of an empirical equation for the transverse dispersion coefficient in natural streams." *Environ. Fluid Mech.*, 7(4), 317-329.
- Lau, Y. L. (1985). "Mixing coefficient for ice-covered and free-surface flows." *Can. J. Civ. Eng.*, 12(3), 521-526.
- Lau, Y. L., and Krishnappan, B. G. (1981). "Modeling transverse mixing in natural streams." *J. Hydraul. Div.*, 107 (2), 209-226.
- Lima Neto, I.E., Zhu, D.Z., Rajaratnam, N., Yu T., Spafford., M., and McEachern, P. (2007). "Dissolved oxygen downstream of an effluent outfall in an ice-cover river: natural and artificial aeration." *J. Environ. Eng.*, 133 (11), 1051-1060.
- Neill, C. R., Yaremko, E.K., Van der Vinne, P.G., Andres, D.D.. (1995). "Under-ice hydraulics and mixing in regulated Peace River." *Proc., 8th Workshop on the Hydraulics of Ice Covered Rivers*, D.D. Andres, ed., Committee on River Ice Processes and the Environment (CRIPE), Hydrology Section, Canadian Geophysical Union, 159–185.
- Putz, G., and Smith, D. W. (2001). "Field measurement and modeling of two-dimensional river mixing." *Water Sci. Tech.: Water Sup.*, 57-64.

- Putz, G., Odigboh, I., and Smith, D. W. (2000). "Two-dimensional modeling of effluent mixing in the Athabasca River downstream of Alberta Pacific Forest Industries, Inc." Sustainable forest management network, *Proj. Rep. 2000-2*, Univ. of Alberta, Edmonton, Canada.
- Roberts, P.J.W., and Webster, D.R. (2002). "Turbulent Diffusion." *Environmental Fluid Mechanics Theories and Application*, Shen et al. (ed.), ASCE, Reston, Virginia, pp7-45.
- Rutherford, J.C. (1994). *River Mixing*. John Wiley & Sons, West Sussex, England.
- Sayre, W.W. (1979). "Shore attached thermal plumes in rivers." *Environmental Impact on Rivers*, Shen, H.W. (ed.), Wiley-Interscience, London, 15.1-15.44.
- Seo, I.W., Baek, K.O., and Jeon, T.M. (2006). "Analysis of transverse mixing in natural streams under slug tests." *J. Hydraul. Res.*, 44(3), 350-362.
- Smith, R. (1983). "Longitudinal dispersion coefficients for varying channels." *J. Fluid Mech.*, 130, 299-314.
- SonTek/YSI (2005). "RiverSurveyor system manual software version 4.30." San Diego, California.
- Szupiany, R. N., Amsler, M. L., Best, J. L., and Parsons, D. R. (2007). "Comparison of fixed- and moving-vessel flow measurements with an ADP in a large River." *J. Hydraul. Eng.*, 133(12), 1299-1309.
- Turner Designs (2001). "A practical guide to flow measurement." Sunnyvale, California.
- Van Der Vinne, D. (1993). "Winter Low Flow Tracer Dye Studies, Athabasca River, Athabasca to Bitumount, February and March, 1992, Part II: Mixing Characteristics." Published by Northern River Basin Study, Edmonton, Alberta.
- Yotsukura, N., and Sayre, W. W. (1976). "Transverse mixing in natural channels." *Water Resour. Res.*, 12(4), 695-704.
- Zhang, W.M. and Zhu, D.Z. (2011). "Near-field mixing downstream of a multiport diffuser in a shallow river." *J. Environ. Eng.*, 137(4), 230-240.

Table 4-1. Studies of Transverse Mixing Coefficients in Ice-covered Rivers

| Study | Reach | Surface condition | Q (m ³ /s) | U (m/s) | B (m) | H (m) | E _y (m ² /s) | $\frac{E_y}{U^*H}$ ⁴ | $\frac{E_y}{UR}$ |
|-----------------------------|---|-------------------|-----------------------|---------|-------|-------|------------------------------------|---------------------------------|------------------|
| Engmann (1974) ¹ | Straight lab. flume | Open-water | 0.007 | 0.12 | 1.22 | 0.05 | 0.85×10 ⁻⁴ | 0.16 | 0.17 |
| | | Ice-covered | 0.007 | 0.12 | 1.22 | 0.05 | 0.46×10 ⁻⁴ | 0.08 | -50% |
| Engman & Kellerhals (1974) | Lesser Slave River, d/s Lesser Slave Lake | Open-water | 59.7 | 0.62 | 42.5 | 2.29 | 0.040 | 0.36 | 0.33 |
| | | Ice-covered | 26.1 | 0.37 | 35.3 | 1.99 | 0.005 | 0.09 | -75% |
| Beltaos (1980) | Athabasca River, d/s Ft. MacMurray | Open-water | 776 | 0.95 | 373 | 2.20 | 0.092 | 0.75 | 0.75 |
| | | Ice-covered | 240 | 0.49 | 252 | 1.92 | 0.040 | 0.58 | -23% |
| Beltaos (1980) | Athabasca River, d/s Athabasca | Open-water | 566 | 0.86 | 320 | 2.05 | 0.066 | 0.41 | 0.41 |
| | | Ice-covered | 105 | 0.40 | 276 | 0.96 | 0.010 | 0.28 | -32% |
| Beltaos (1980) | Beaver River, d/s Beaver Crossing | Open-water | 20.5 | 0.50 | 42.7 | 0.96 | 0.043 | 1.01 | 1.01 |
| | | Ice-covered | 6.5 | 0.28 | 38.7 | 0.61 | 0.019 | 1.27 | +26% |
| Lau (1985) ² | Nith River, near Canning | Open-water | 3.1 | 0.16 | 36.0 | 0.54 | 0.028 | 0.66 | 0.69 |
| | | Ice-covered | 3.8 | 0.23 | 37.5 | 0.44 | 0.014 | 0.63 | -5% |
| Lau (1985) | Grand River, near West Montrose | Open-water | 7.9 | 0.40 | 48.0 | 0.41 | 0.007 | 0.24 | 0.25 |
| | | Ice-covered | 5.2 | 0.34 | 50.8 | 0.30 | 0.003 | 0.23 | -4% |
| Present ³ | Athabasca River, d/s Al-Pac | Open-water | 238.4 | 0.56 | 274 | 1.58 | 0.037 | 0.44 | 0.44 |
| | | Ice-covered | 84.0 | 0.28 | 261 | 1.17 | 0.012 | 0.33 | -25% |

¹Only one data set is included in this table; other data sets have similar results;

²Only the data set near Canning is included in this table; the data sets near the other two locations (Philipsburg and Plattsville) have similar results;

³The data sets are calculated on the basis of the 2008 dye test (open-water) and the 1995 dye test (ice-covered); the 1994 dye test (open-water) essentially has similar results as the 2008 test, but slightly overestimates E_y (for details, see the application of the modified method);

⁴The positive or negative sign indicates the increase or decrease in the value of E_y/U*H compared to the open-water value.

Table 4-2. Basic Hydraulic Parameters in the Study Reach in 2008 Dye Test

| Section (m) | Q (m³/s) | U (m/s) | B (m) | H (m) | S₀ (×10⁻⁴) | U* (m/s) | Ψ |
|------------------------|--------------------------------|--------------------|------------------|------------------|---|---------------------|-------------------|
| 114.1* | 223.95 | 0.51 | 261.50 | 1.70 | | 0.051 | 1.91 |
| 260 | 223.95 | 0.44 | 309.49 | 1.65 | | 0.050 | 1.59 |
| 516 | 223.95 | 0.46 | 339.82 | 1.45 | | 0.047 | 1.44 |
| 1,282 | 223.95 | 0.46 | 335.99 | 1.46 | | 0.047 | 2.48 |
| 2,260* | 224.42 | 0.53 | 284.70 | 1.48 | | 0.048 | 1.45 |
| 4,131 | 224.42 ¹ | 0.64 | 221.45 | 1.27 | 1.566 | 0.044 | 1.41 |
| 6,631 | 224.42 | 0.60 | 214.12 | 1.76 | | 0.052 | 1.32 |
| 8,484 | 224.42 | 0.48 | 398.22 | 1.18 | | 0.043 | 5.11 ² |
| 13,729* | 231.38 | 0.63 | 250.30 | 1.46 | | 0.047 | 1.56 |
| 15,922 | 245.01 | 0.69 | 193.50 | 1.84 | | 0.053 | 2.64 |
| 24,493 | 251.45 | 0.67 | 222.02 | 1.69 | | 0.051 | 1.47 |
| 32,579* | 251.45 | 0.62 | 207.40 | 1.97 | | 0.055 | 2.03 |

*ADP measurement sections; for other sections, Q is estimated on the basis of the ADP measurement and the inflows of tributaries and creeks along the river.

¹Total river discharge, while other values at this section were in the primary (right) channel;

² Value not used for calculating reach-average value;

Table 4-3. Comparison of Estimated Cumulative Discharges with ADP measurements

| Section (m) | Absolute value of relative error ¹ for cumulative discharge (%) | | | | | | | |
|----------------|--|-------------------|-----------------|------|-------------------|-------------------|---------|------|
| | 1st Measurement ² | | 2nd Measurement | | 3rd Measurement | | Section | |
| | Avg. ³ | S.D. ³ | Avg. | S.D. | Avg. | S.D. | Avg. | S.D. |
| -496* | 2.83 | 4.40 | 2.26 | 3.35 | 2.62 | 3.70 | | |
| 4.8* | 12.66 | 16.13 | 6.78 | 8.80 | 8.92 | 10.39 | | |
| 20.0* | 6.63 | 5.59 | 4.04 | 3.20 | 4.96 | 4.00 | | |
| 33.3* | 1.97 | 2.61 | 3.30 | 4.36 | 4.11 | 3.83 | 5.42 | 2.84 |
| 114.1 | 7.53 | 5.73 | 8.93 | 6.94 | 9.65 | 7.92 | | |
| 2,260 | 3.82 | 8.44 | 3.68 | 3.73 | 9.16 | 12.36 | | |
| 13,729 | 4.02 | 3.24 | 3.80 | 3.75 | 3.33 ⁴ | 2.91 ⁴ | | |
| 32,579 | 5.68 | 5.68 | 4.02 | 3.25 | / | / | | |

¹ Absolute value of relative error =

$$|\text{Estimated value} - \text{Measured value}| / \text{Measured value} \times 100\% ;$$

² Compare with the first ADP measurement at a section;

³ Avg. and S.D. stand for average and standard deviation, respectively;

⁴ For details, see Fig. 4-3.

*Used for the near-field mixing analysis (see Zhang and Zhu 2011), and listed herein to further examine the accuracy of the estimating method.

Table 4-4. Transverse Mixing Coefficients Calculated by Using the Standard Method of Moments, Beltaos' Generalized Method of Moments, and Modified Method Proposed in this Study

| Method | Sub-reach (km) | D (m ⁵ /s ²) | U _{avg} (m/s) | H _{avg} (m) | ψ _{avg} | U* _{avg} (m/s) | E _y (m ² /s) | $\frac{E_y}{U'H}$ | $(\frac{E_y}{U'H})_{avg}$ |
|---------------------|----------------|-------------------------------------|------------------------|----------------------|------------------|-------------------------|------------------------------------|--------------------------|---------------------------|
| Standard Moments | 0.114 - 13.73 | 0.0427 | 0.53 | 1.49 | 1.64 | 0.050 | 0.022 | 0.30 | |
| | 13.73 - 24.49 | 0.0802 | 0.66 | 1.67 | 1.89 | 0.051 | 0.023 | 0.27 [*] | / |
| | 24.49 - 32.58 | 0.0420 | 0.64 | 1.83 | 1.75 | 0.053 | 0.011 | 0.11 [*] | |
| Generalized Moments | 0.114 - 13.73 | 0.0447 | 0.53 | 1.49 | 1.64 | 0.048 | 0.023 | 0.33 | 0.39 |
| | 13.73 - 32.58 | 0.1487 | 0.65 | 1.74 | 1.92 | 0.052 | 0.039 | 0.43 | |
| Modified | 0.114 - 13.73 | 0.0465 | 0.53 | 1.49 | 1.64 | 0.048 | 0.024 | 0.34 | 0.44 |
| | 13.73 - 32.58 | 0.1745 | 0.65 | 1.74 | 1.92 | 0.052 | 0.046 | 0.51 | |

^{*} where method is invalid, but listed here for comparison purpose.

Table 4-5. Basic Hydraulic Parameters in 1994 and 1995 Dye Tests

| Section (km) | H_{ice}^1 (m) | Q (m ³ /s) | U (m/s) | B (m) | H ¹ (m) | U* (m/s) | Ψ |
|------------------------------|--------------------|--------------------------|------------|----------|-----------------------|-------------|--------|
| Oct. 1994² | | | | | | | |
| 0.05 | | 258.2 | 0.58 | 257 | 1.72 | 0.051 | 1.47 |
| 0.5 | | 250.4 | 0.64 | 325 | 1.20 | 0.043 | 1.59 |
| 1 | | 276.7 | 0.63 | 337 | 1.30 | 0.045 | 1.49 |
| 2 | | 269.8 | 0.60 | 350 | 1.29 | 0.045 | 1.53 |
| 4 | 0 | 269.8 ³ | 0.81 | 212 | 1.23 | 0.043 | 1.51 |
| 8 | | 283.5 | 0.57 | 334 | 1.48 | 0.048 | 1.30 |
| 16 | | 255.4 | 0.73 | 251 | 1.39 | 0.046 | 1.35 |
| 32 | | 285.8 | 0.72 | 203 | 1.95 | 0.055 | 1.97 |
| 64 | | 274.3 | 0.92 | 215 | 1.39 | 0.046 | 1.43 |
| Feb. 1995⁴ | | | | | | | |
| 0.05 | 0.55 | | 0.29 | 257 | 1.13 | 0.029 | 3.53 |
| 8 | 0.41 | | 0.26 | 334 | 0.95 | 0.027 | 1.99 |
| 16 | 0.50 | 84 | 0.28 | 251 | 1.19 | 0.030 | 1.43 |
| 32 | 0.50 | | 0.29 | 203 | 1.42 | 0.033 | 2.76 |
| 64 | 0.54 | | 0.35 | 215 | 1.13 | 0.029 | 1.66 |

¹ H_{ice} and H are the cross-sectional average ice thickness and the free water depth, respectively;

²Water surface slope was not measured and expected to be the same as in this study because the discharges were close to each other;

³Total river discharge, whereas other values at this section were in the primary (right) channel;

⁴Water surface slope was not measured and should be close to the slope before the formation of ice cover in Oct. 1994 (Engmann and Kellerhals 1974; Ashton 1986).

Table 4-6. Transverse Mixing Coefficients in 1994 and 1995 Dye Tests Calculated by Using Modified Method Proposed in this Study

| Sub-reach (km) | D (m⁵/s²) | U_{avg} (m/s) | H_{avg} (m) | Ψ_{avg} | U*_{avg} (m/s) | E_y (m²/s) | $\frac{E_y}{U^*H}$ | $(\frac{E_y}{U^*H})_{avg}$ |
|--------------------------------------|--|----------------------------------|--------------------------------|------------------------|-----------------------------------|--|--------------------------------------|--|
| Oct. 1994 | | | | | | | | |
| 0.05 - 16 | 0.0563 | 0.62 | 1.40 | 1.45 | 0.046 | 0.032 | 0.49 | 0.53 |
| 16 - 32 ¹ | 0.1637 | 0.72 | 1.67 | 1.66 | 0.050 | 0.049 | 0.58 | |
| Feb. 1995 (Ice-covered River) | | | | | | | | |
| 0.05 - 32 ¹ | 0.0109 | 0.28 | 1.17 | 2.43 | 0.030 | 0.012 | 0.33 | 0.33 |

¹To compare with the 2008 dye test, the study reach was chosen as the first 32 km.

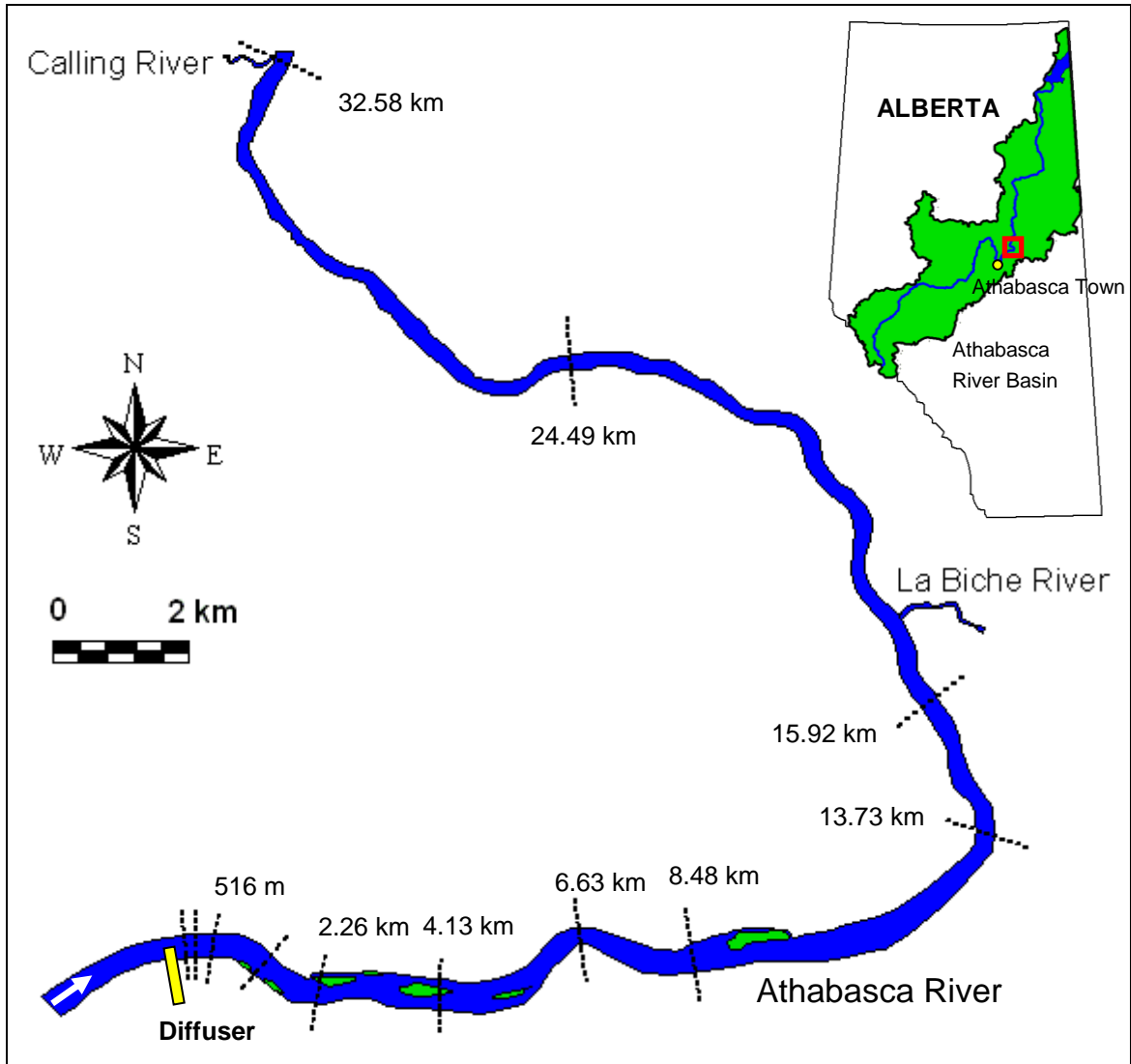


Figure 4-1. Study reach in the Athabasca River, with the study location indicated in the top right provincial map of Alberta, Canada

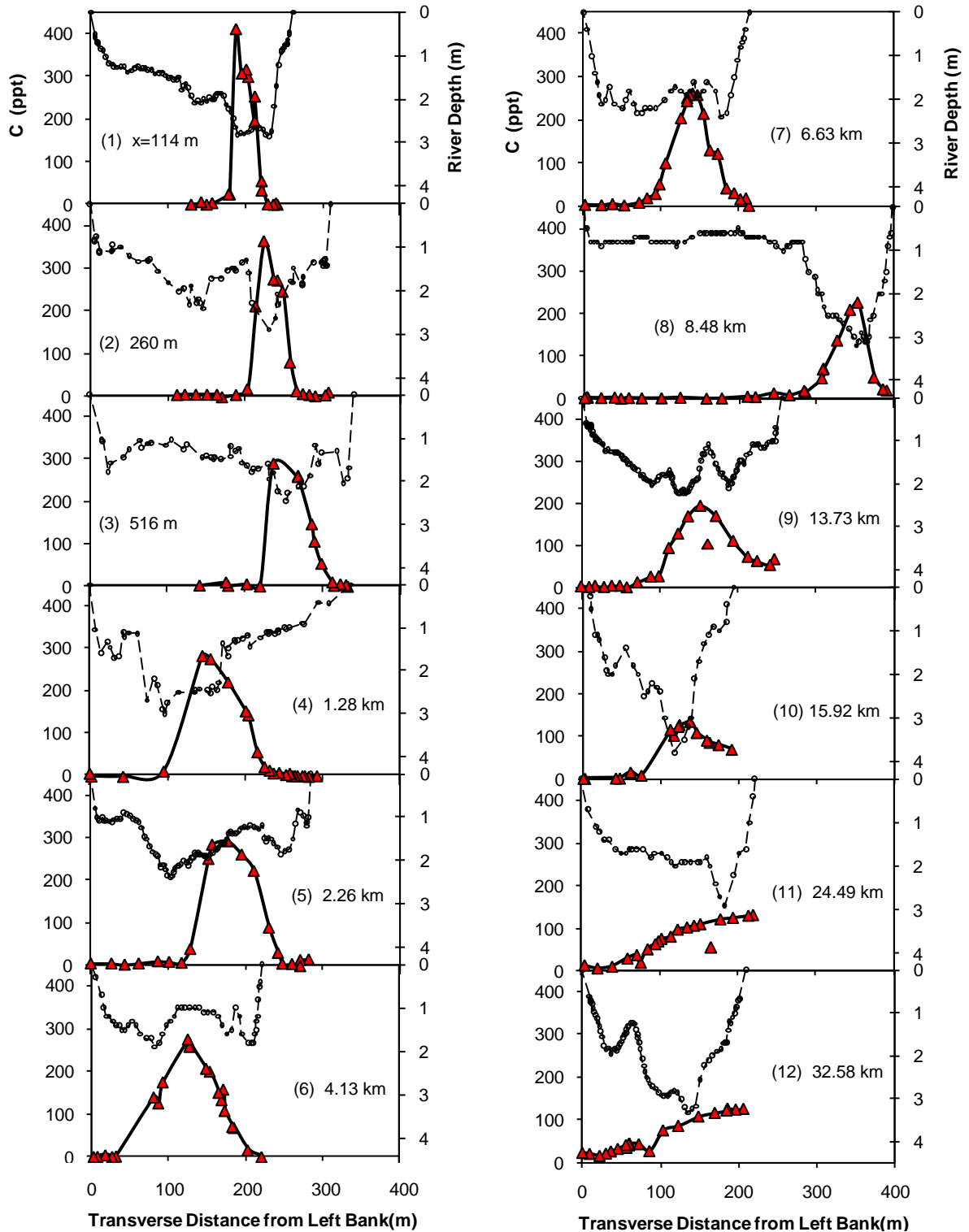


Figure 4-2. Measured dye concentrations (filled triangle solid line) at different sections with indication of river depths (open circle dashed line)

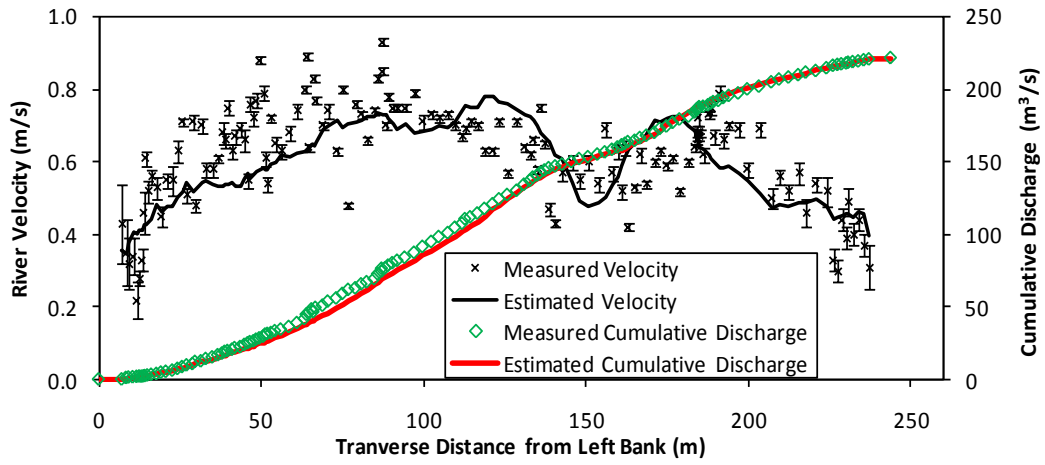


Figure 4-3. Comparisons of measured velocities with indication of standard deviations and cumulative discharges with estimated values across Section 13.73 km

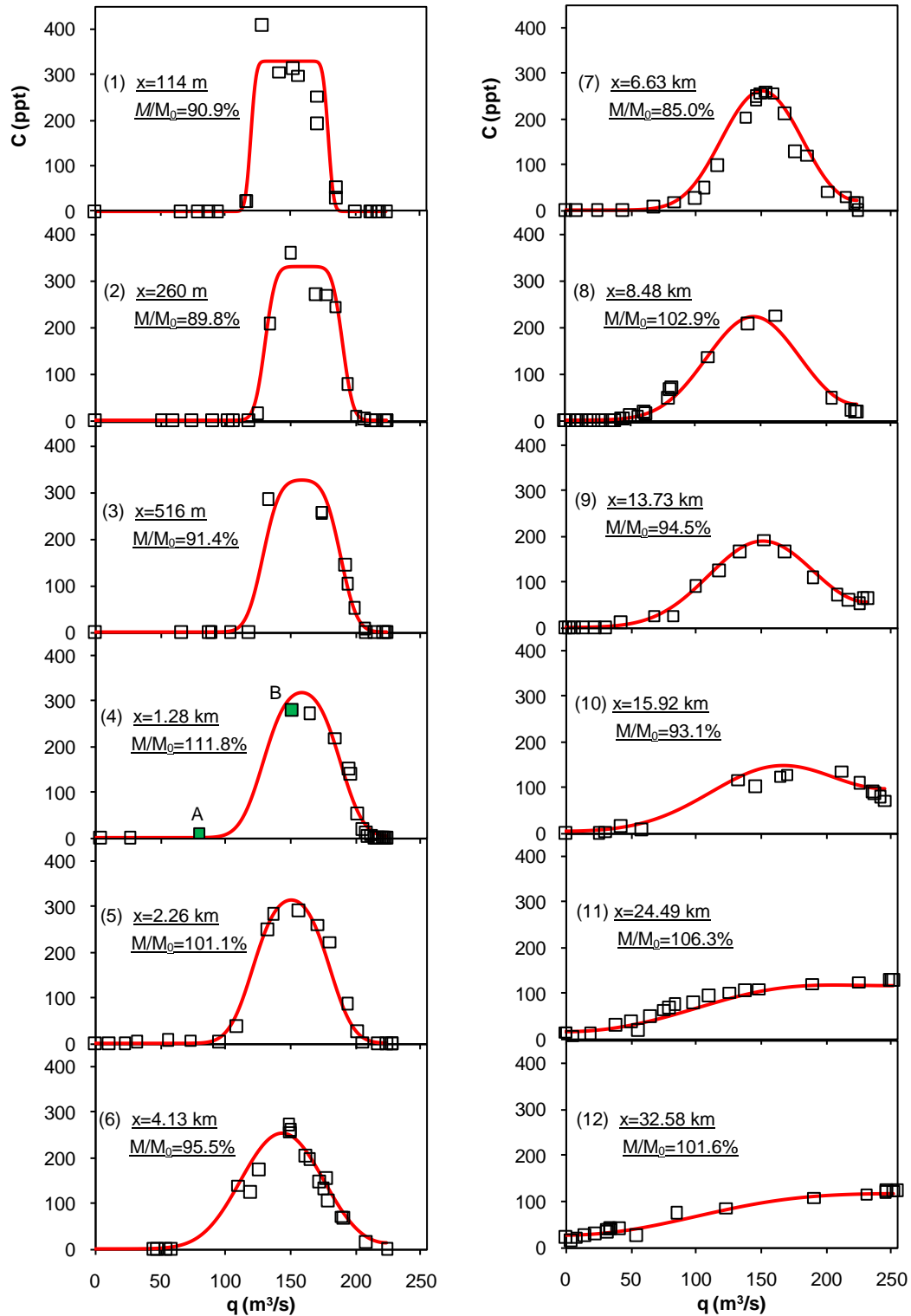


Figure 4-4. Measured (open square) and modeled (line) dye concentrations versus cumulative discharges at different sections, where M/M_0 indicates the ratio of measured dye mass flux, by using the measured concentrations, to the initial dye injection rate; $M/M_0 = 100\%$ for the modeled concentration profiles; Points A and B in Fig. 4-4(4) are discussed in this study

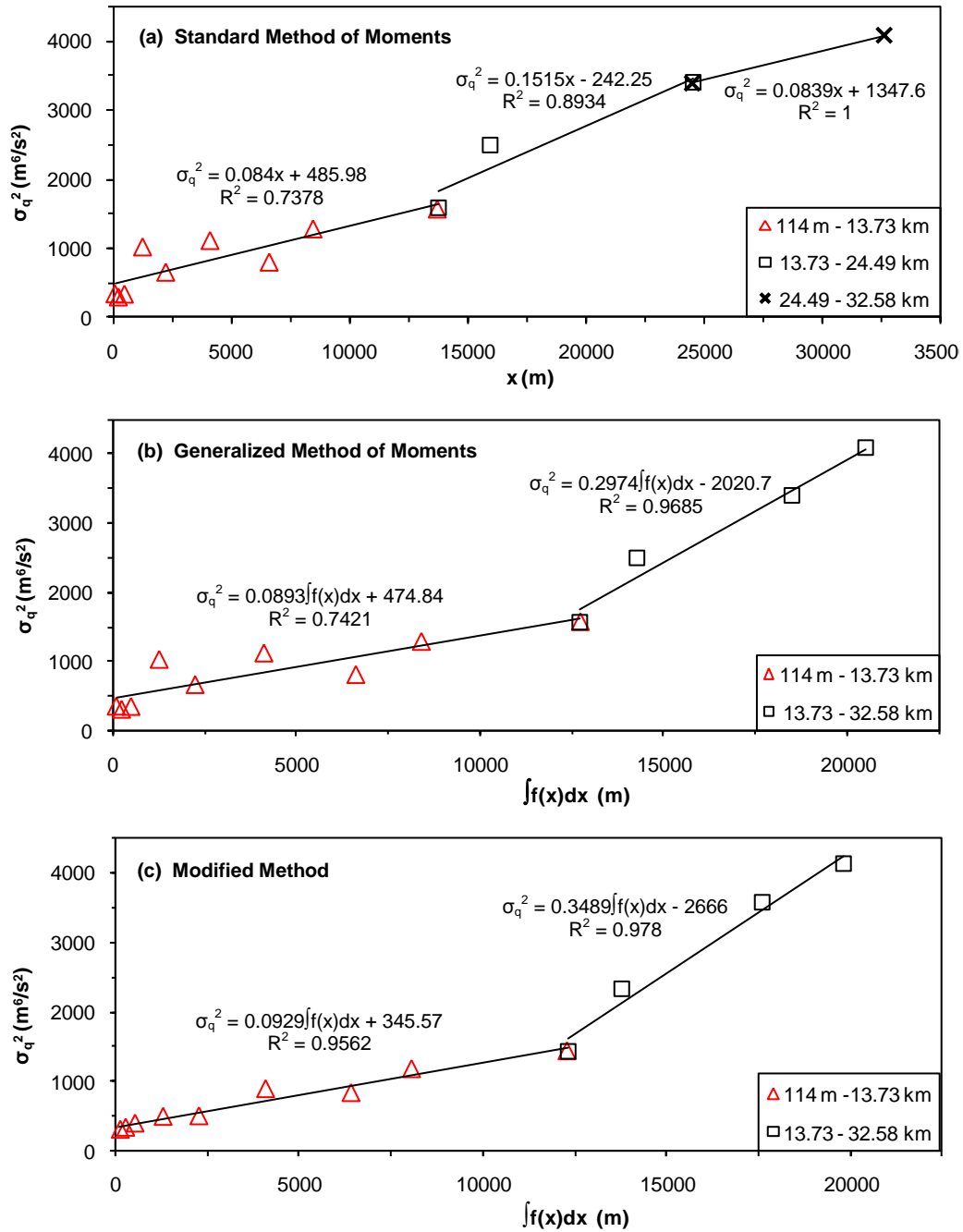


Figure 4-5. Change of variances of transverse concentration profiles along the river by using (a) standard method of moments; (b) generalized method of moments; and (c) the modified method proposed in this study

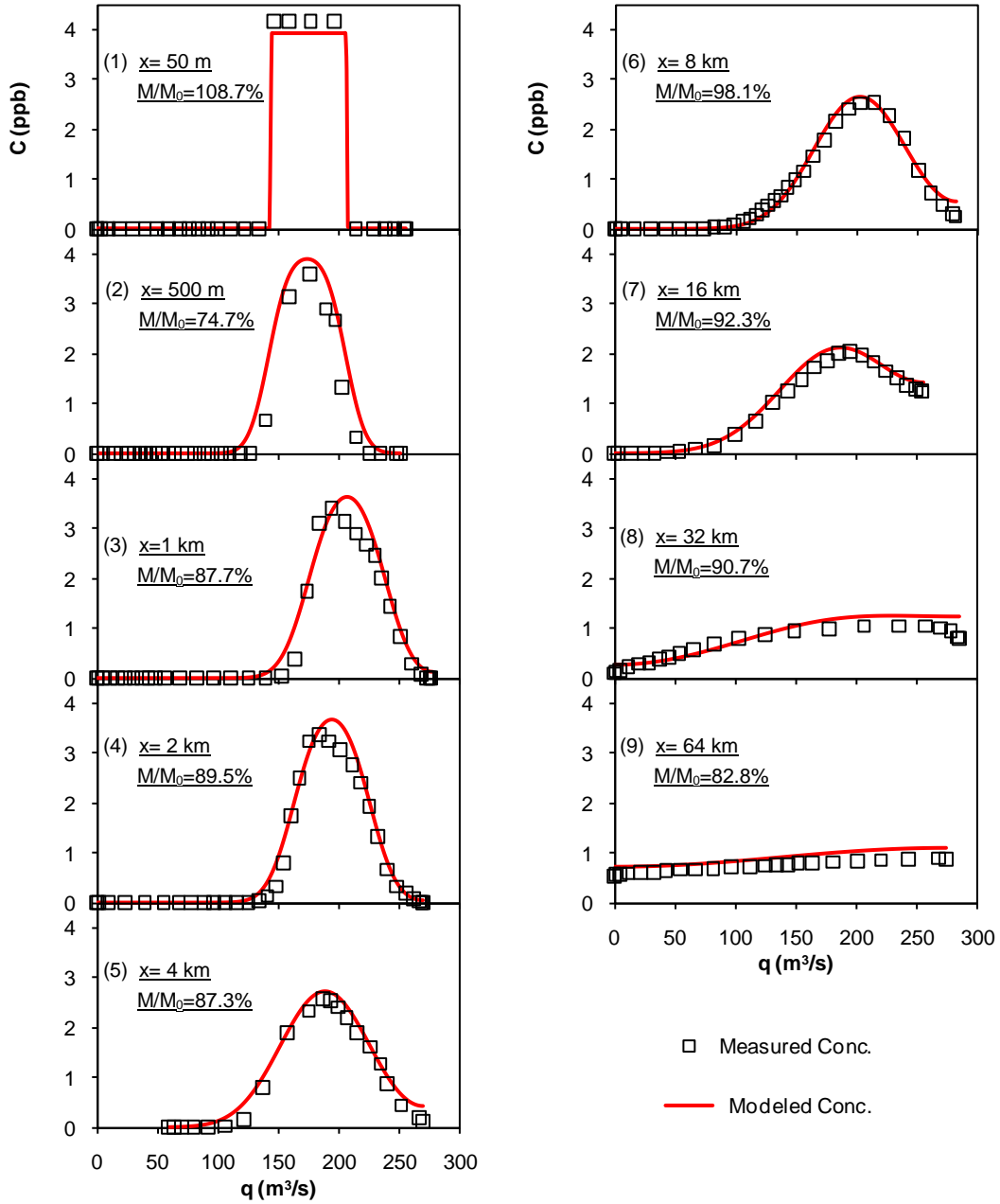


Figure 4-6. Modeled and measured dye concentrations at different sections in 1994 dye test where M/M_0 indicates the ratio of measured dye mass flux, by using the measured concentrations, to the initial dye injection rate

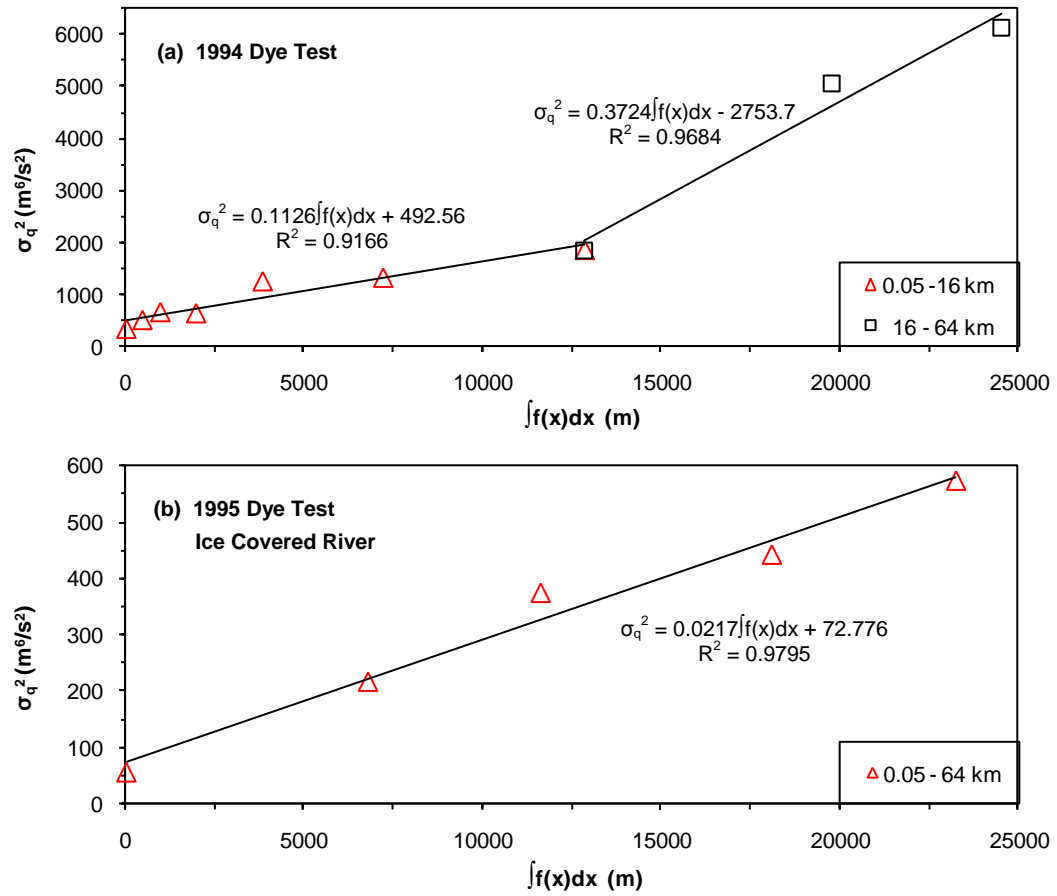


Figure 4-7. Change of variances of transverse concentration profiles along the river in (a) 1994 and (b) 1995 dye tests, by using the modified method proposed in this study

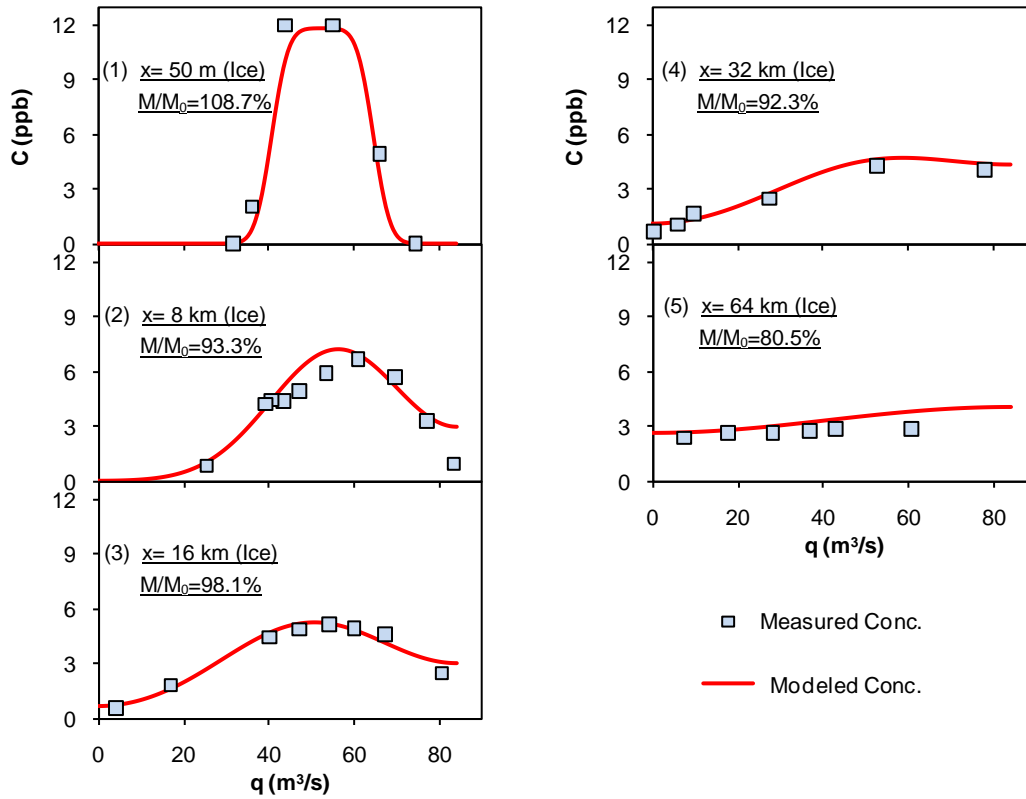


Figure 4-8. Modeled and measured dye concentrations at different sections in 1995 dye test in ice-covered condition, where M/M_0 indicates the ratio of measured dye mass flux, by using the measured concentrations, to the initial dye injection rate

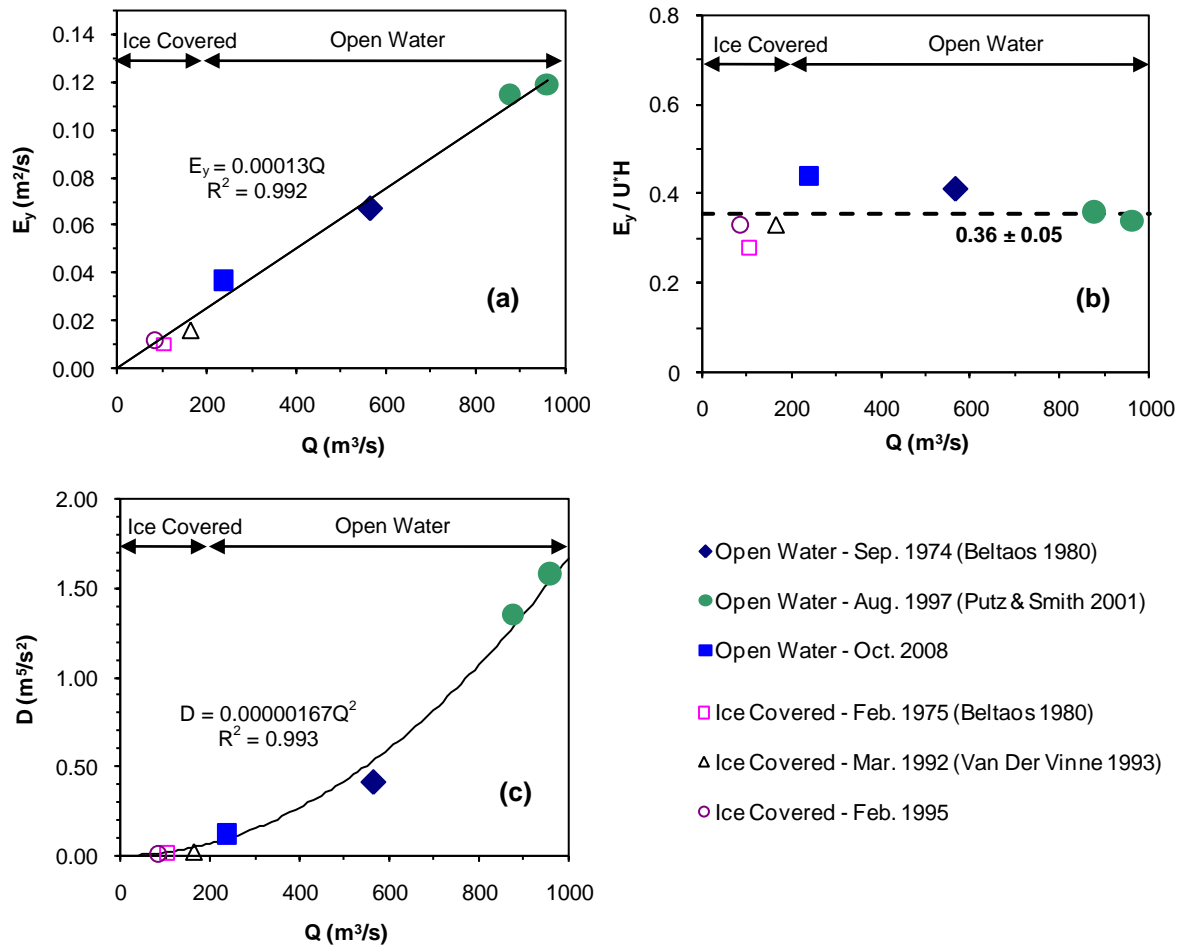


Figure 4-9. Effect of river discharge on (a) dimensional; (b) dimensionless transverse mixing coefficient; and (c) dimensional factor of diffusion

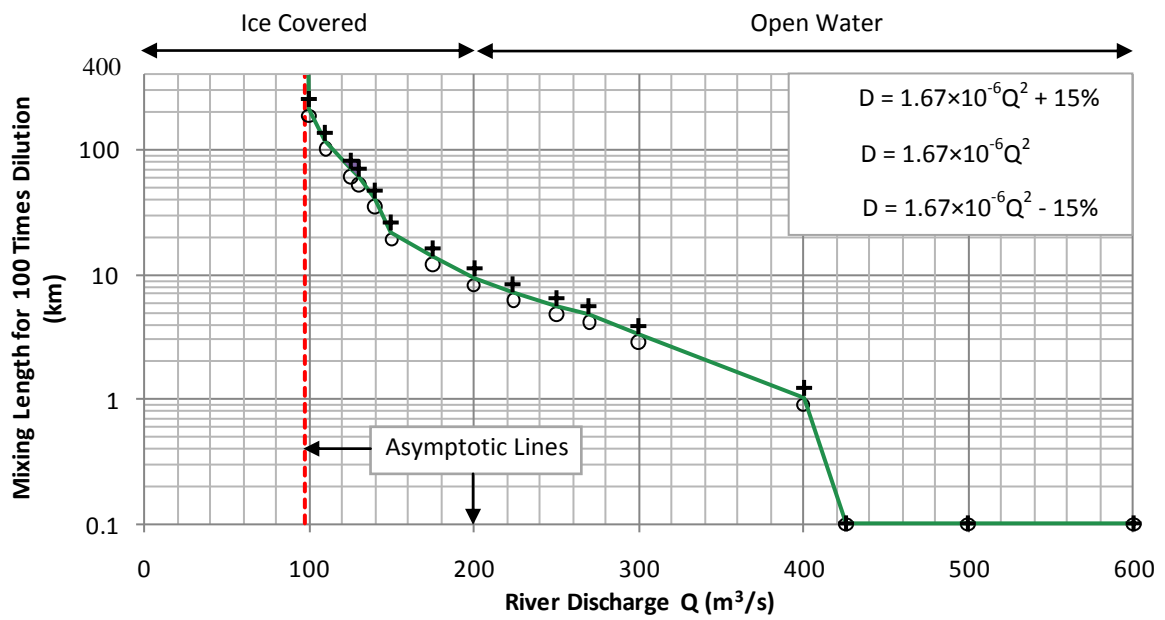


Figure 4-10. Mixing lengths for 100-times dilution under varying discharges with and without ice cover

Chapter 5

Trajectories of Bubble Plumes and Bubbly Jets in Crossflows^{*}

5.1 Introduction

A bubble plume is generated by the injection of a gas (e.g., air) into a liquid (e.g., water) usually via a nozzle or slot, while a bubbly jet is produced by the injection of a pre-mixed gas-liquid mixture into a liquid. Bubble plumes and bubbly jets have wide applications in: providing artificial aeration and mixing in natural water bodies, wastewater treatment plants and chemical reactors; de-stratifying lakes or reservoirs; preventing ice formation in harbors; assessing the impact of accidental blowout of sub-sea oil and gas wells and confining the spills; and etc. Studies on bubble plumes and bubbly jets have been reported in various areas of application (Clift et al. 1978; Milgram 1983; Sun and Faeth 1986a, b; Wüest et al. 1992; Socolofsky and Adams 2002; Sahoo and Luketina 2003, 2006; Seol et al. 2007; Lima Neto et al. 2008a, b, c, d; Norman and Revankar 2011; Lima Neto 2012; many others).

Almost all the studies focus on the case of stagnant ambient fluids (typically, water), and rarely on the case of cross-flowing ambient fluids. However, crossflows are present in many of the above-mentioned applications (Socolofsky and Adams 2002), especially in artificial aeration in rivers as reported by Lima Neto et al. (2007). The necessity to understand bubble plumes and bubbly jets in crossflows and their scarcity

^{*} The content of this chapter is currently being prepared as a journal manuscript: Zhang, W.M., and Zhu, D.Z. (2012). "Trajectories of bubble plumes and bubbly jets in crossflows." *Int. J. Multiphase Flow*, to be submitted.

in the literature stimulate the current research. As a start, Chapter 5 focuses on the general behavior of bubble plumes and bubbly jets in crossflows, i.e., their trajectories. Detailed measurements on the distributions of bubble properties at different sections from the nozzle, including bubble velocity, bubble size, bubble frequency, specific interfacial area and gas void fraction, are provided in Chapter 6.

To the authors' knowledge, only two studies in the literature (i.e., Mannasseh et al. 1998; Socolofsky and Adams 2002) reported bubble plumes or bubbly jets in crossflows, with a focus both on the plume or jet trajectories. Mannasseh et al. (1998) experimentally studied the trajectories of bubble plumes with an air discharge of approximately 0.08 liters per minute (LPM) and bubble diameter of approximately 4 mm in cross-flowing water of 0.14 - 0.22 m/s. From a plan view, they observed that the trajectories of bubble plumes, depending on the crossflow velocities, could be furcated into a pair of or multiple sinusoidal paths with amplitudes and wave lengths of magnitude of 1 cm and 3 cm, respectively. From a side view, their images showed that the trajectories of bubble plumes could be well approximated as linear lines with different angles to the crossflow.

Socolofsky and Adams (2002) studied the trajectories of air bubble plumes, and air-oil and air-alcohol multiphase plumes in cross-flowing water of 0.02 - 0.2 m/s. The air was discharged via an aquarium airstone at a rate of 0.2 - 2.5 LPM; the oil and alcohol were discharged through diffusers at a rate of 0.3 - 1 LPM and 0.2 - 0.4 LPM, respectively. In weak crossflows, they found that the bubbles stayed with the entrained ambient water (visualized with dye) or other dispersed phase (oil or alcohol) till to the water surface of 0.6 m height. However, in strong crossflows, within a short distance, the bubble column separated from the entrained ambient water or other dispersed phase (oil or alcohol) due to the buoyancy of bubbles. But further separation of other dispersed

phase from the entrained ambient water was not observed. An empirical equation was proposed for the separation height of the bubble column, h_s , as a function of crossflow velocity, bubble slip velocity and total kinematic buoyancy flux of the mixed plume. From trajectory modeling, Socolofsky and Adams found that: below h_s , multi-phase plumes behaved like well-mixed single-phase plumes. Above h_s , the separated bubble columns exhibited linear trajectories, which were determined by the vector sum of crossflow velocity and bubble slip velocity; and the separated continuous phase behaved as a momentum jet where the momentum was inherited from the entrainment and acceleration of the multi-phase plume before the separation.

A few studies have reported the trajectories of bubble plumes or bubbly jets in stagnant water. Lima Neto et al. (2008b) observed a linear spread of bubbly jets, with a spreading rate of 0.11-0.14 for the jet half-width (where the water velocity was 37% of the jet centerline velocity) and a rate of 0.18 for the jet visual boundary. Their results were close to the spreading rate of approximately 0.10 for the half-width of pure water jets (Rajaratnam 1976; Lee and Chu 2003), and thus appeared to suggest that bubbles that existed within 60 - 70% of the radius of bubbly jet had little impact on the water jet spreading in bubbly jets. Others studies have reported the ratio of bubble core radius to liquid jet radius for bubble plumes or bubbly jets in the range of 40 - 100% and spreading rate in the range of 0.10-0.20, as summarized in Milgram (1983), Lima Neto et al. (2008b, c) and Lima Neto (2012).

To study bubbly jet trajectory, it is crucial to know the liquid (water) velocity at the nozzle exit, U_{w0} . However, the compressibility of the gas (air) at the nozzle exit complicates this problem, and as yet, no method has been reported to accurately determine it. The concept of superficial water velocity has been used (Lima Neto et al.

2008b, d), which assumes that the area occupied by the gas phase at the nozzle exit is negligible:

$$U_{w0} = \frac{4Q_w}{\pi d^2} \quad (5.1)$$

where Q_w is the injected water flow rate; and d is the nozzle diameter. Lima Neto (2012) calculated the water velocity assuming that the area ratio occupied by the gas phase at the nozzle exit was equal to the volumetric fraction of injected gas (i.e., gas is totally incompressible):

$$U_{w0} = \frac{4Q_w}{(1-C_0)\pi d^2} \quad C_0 = \frac{Q_a}{Q_a + Q_w} \quad (5.2)$$

where C_0 is the gas volume fraction; Q_a is the injected air flow rate. The real value of U_{w0} should be between the two extremes of Eqs. (5.1) and (5.2).

Compared to bubble plumes and bubbly jets in crossflows, theories of single-phase jets in crossflows are more advanced. Single-phase jets in crossflow can be well simulated with commercial software such as CORMIX, Visual Plume and VISJET, or with empirical relations established on experimental results. The case of pure water jets can be used as the control for the study of bubbly jets in crossflows. Numerous studies have been reported on single-phase jet trajectories in crossflows (Pratte and Baines 1967; Rajaratnam 1976; Wright 1977a, b; Fischer et al. 1979; Hodgson and Rajaratnam 1992; Davidson and Pun 1999; Hodgson et al. 1999; Lee and Chu 2003; many others). Wright (1977 a, b) conducted both photographic and concentration measurements for water jets in crossflows. Based on photographic experiments, Wright proposed the following equation for jet centerline in the momentum dominated near field (MDNF) and momentum dominated far field (MDFF), respectively:

$$\text{In MDNF } (z \leq L_m), \quad \frac{z_c}{\alpha d} = C_1 \left(\frac{x}{\alpha d}\right)^{1/2} \quad C_1 = 1.88 - \frac{2.07}{\alpha^{2/3}} \quad (5.3)$$

$$\text{In MDFF } (z > L_m), \quad \frac{z_c}{\alpha d} = C_2 \left(\frac{x}{\alpha d}\right)^{1/3} \quad C_2 = 0.82\alpha^{1/6} \quad (5.4)$$

where x and z_c are the longitudinal and vertical distances from the nozzle, respectively; α is the ratio of jet exit velocity at the nozzle to the crossflow velocity, U_0/U ; L_m is a length scale, defined as $M_0^{1/2}/U$, where M_0 is the specific momentum flux at the nozzle exit. Wright also proposed similar equations based on concentration measurements, with slightly different values of C_1 and C_2 . Wright's results showed that the concentration centerline could be 20% higher than that determined from photographs (the middle of upper and lower jet visual boundaries). Hodgson and Rajaratnam (1992) conducted both laboratory and field experiments for jet concentration and proposed the following equation for jet centerline:

$$\frac{z_c}{\alpha d} = 1.46 \left(\frac{x}{\alpha d}\right)^{0.26} \quad (5.5)$$

Based on numerical models of advected line puff and experimental results of jet concentration, Lee and Chu (2003) proposed that:

$$\text{In MDNF } (z \leq L_m), \quad \frac{z_c}{L_m} = 2.65 \left(\frac{x}{L_m}\right)^{1/2} \quad (5.6)$$

$$\text{In MDFF } (z > L_m), \quad \frac{z_c}{L_m} = 1.56 \left(\frac{x}{L_m}\right)^{1/3} \quad (5.7)$$

One can see that Eqs. (5.3) - (5.7) are all in similar forms, but with different coefficients and exponents.

This chapter presents a study on the general behaviors of bubble plumes and bubbly jets in crossflows, with a focus on their trajectories. Fifteen combinations of air-water mixture were injected through a single orifice nozzle into three crossflows, i.e., a total of 45 experimental conditions were studied. The trajectories of bubble columns and water jets were studied with photographic techniques and image processing. The locations where the bubbles separate from the water jets were investigated, and an

empirical relation was proposed for the separation height. The case of pure water jets was also examined and used as the basis to understand the effect of bubbles on the water jets in bubbly jets. This study is probably the first one that systematically studies the trajectories of air bubble plumes and air-water bubbly jets in cross-flowing ambient water. This study will contribute the understanding of general behaviors of bubble plumes and bubbly jets in crossflow, and advance their applications such as in artificial aeration and mixing in the environment in rivers and oil-gas blowouts in oceans.

5.2 Experimental apparatus and procedures

The experiments were conducted in a large tilting flume of 25 m × 1.2 m × 0.8 m (L×W×H) in the T. Blench Hydraulics Laboratory at the University of Alberta. The side walls and flume bed are made of fiberglass and glass. The water is recirculated by a pump between the flume and an underground sump. A honeycomb flow straightener in the feed plenum is used to uniformly distribute the water before entering the flume, and a tailgate is used to control the water depth. The experimental apparatus was built at 14 m from the flume entrance. In all experiments, the flume was kept horizontal and the water depth was controlled at a constant 65 cm. Three water discharges were used, 15.7±0.5, 155.4±0.4 and 366.4±0.7 L/s, which corresponded to the cross-sectional average velocity of 0.02, 0.20, and 0.47 m/s, respectively (see Table 5-1).

Fig. 5-1 shows the schematic of the experimental setup. A single-orifice nozzle was built vertically in the middle of the flume. The nozzle exit with a diameter of 6 mm, was 12 cm above the flume bed. This distance was determined from a preliminary Acoustic Doppler Velocimeter (ADV) test (Wang 2011), and was set to have a more uniform distribution of ambient velocity in the vertical direction and to exclude the Coanda effect exerted by the flume bed on the water jets. The ADV test also showed

that the side walls of the flume only had a significant effect on the transverse distribution of ambient velocity within 20 cm from the walls, which is far beyond the diffusion zone of bubbly jets. Air-water mixtures were injected via the nozzle into the crossflows. Air and water were pre-mixed inside a Venturi injector (Model 384, Mazzei Injector Corp.) before the nozzle exit. The air was provided from a gas line of the laboratory. A pressure-regulating valve was used to keep the air at 1 atm and constant flow rate. The air flow rate was controlled by an air rotameter. The water was supplied by a pump and its flow rate was controlled by a valve. The air and water flow rates were read directly from their rotameters. The fluctuations of the air and water flow rates were estimated to be less than 2% of their mean values. In this study, fifteen combinations of air and water flow rates were selected with three ambient crossflows (i.e., a total of 45 cases), including the cases of pure water jets, pure bubble plumes, and bubbly jets (see Table 5-1).

To visualize the trajectories of bubbly jets and water jets, dye was injected into the water pipeline before the water pump (see Fig. 5-1). Images of the jet trajectories were captured with a high resolution (1392×1040 pixels) charge coupled device (CCD) camera (TM-1040 CL, Pulnix America Inc.) at one side of the flume. The camera was controlled by a computer frame grabber system (Streams 5, IO Industries Inc.), with a frame rate of 30 frames per second and an exposure time of 1/2000 seconds. Background light was provided by 2×1000 watts halogen lamps diffused in a softbox of 1.2 m × 0.9 m (L×H) at the other side of the flume. The images were set to cover an area of 73.7×55.0 cm², with a resolution of 18.9 pixels/cm. For each of the 45 experimental cases, images were taken for a period of 30 - 40 seconds, and 10 images that were evenly distributed within such period were selected for image processing. In each image, upper and lower boundaries of a bubbly jet or a water jet were determined, and the jet

centerline was defined as the middle of the upper and lower bounds. The average from the 10 images was used as the jet boundary or centerline in each experiment. The standard deviation from 10 images was 0.2-1.1 cm and not shown in the figures for clarity.

Two commonly used dyes, Rhodamine W.T. (Keystone Aniline Corp.) and a brilliant red liquid food color (Dawn Food Products Inc.), were tested before the experiments. Fig. 5-2 shows that Rhodamine W.T. has an enormous impact on bubbles: it makes bubbles much smaller and spread much wider, which may be because surface tension of the water is changed due to the addition of the dye; while the effect of the food color is negligible. Therefore, it is important to point out that Rhodamine W.T. is not suitable for visualization of bubble plumes or bubbly jets. In this study, the food color was selected. The density of the raw food color measured 1012.9 kg/m^3 at $20 \text{ }^\circ\text{C}$. As the food color was mixed with water in the pipeline (see Fig. 5-1), the density of the water-dye mixture at the nozzle exit was estimated to be at most 998.6 kg/m^3 , very close to that of pure water (998.2 kg/m^3). Thus the density increase due to use of the food color was neglected.

5.3 Trajectory Results and Analysis

5.3.1 Pure Water Jets

Photos of pure water jets, bubble plumes and bubbly jets in crossflows of 0.02, 0.20 and 0.47 m/s are shown in Fig. 5-3 - Fig.5-5. Pure water jets in this study were used as references to examine the effect of bubbles in the case of bubbly jets. The results of pure water jets were also used to validate the relations proposed by Wright (1977a), Hodgson and Rajaratnam (1992) and Lee and Chu (2003) for single-phase jets in crossflows (Eqs. 5.3-5.7). Based on the validation, one of the three relations was selected for the

separated water jets in bubbly jets. Note that Experiment C-0-1 was not included for the validation because the lower jet boundary was below the camera window as shown in Fig. 5-5.

The measurement results of water jet centerlines and modeled jet centerlines are shown in Fig. 5-6. Overall, the modeling results are satisfactory. The modeled centerlines by using the equations of Wright (1977a) and Lee and Chu (2003) may not appear continuous at some points because two equations were used in MDNF and MDFF. As can be seen in Fig. 5-6, Lee and Chu's equation best fits the measurements in the crossflow of 0.02 m/s, while Wright's and Hodgson and Rajaratnam's equations better agree the measurements in the crossflow of 0.20 and 0.47 m/s. It is interesting to note that for relatively weak jets in strong crossflow as shown in Experiments B-0-1 and C-0-3 (also see C-0-1 in Fig. 5-5), the measurements at the end of jet centerlines are 2-4 cm below the predictions from Wright's and Hodgson and Rajaratnam's equations. This is possible because that the water jets are near the flume bed and the entrainment of ambient water into the jets causes a pressure drop in the ambient that sucks the jets to move close to or attach the flume bed (Coanada effect). In addition, preliminary ADV tests showed a downward velocity of 2.6% of the cross-sectional average velocity near the nozzle exit location (i.e., 0.52 and 1.3 cm/s for the crossflows of 0.20 and 0.47 m/s, respectively) (Wang 2011), which might be another reason for the centerlines being below Wright's and Hodgson and Rajaratnam's predictions. For bubbly jets, since the water jets only become separated from bubbles in the strong crossflows (0.20 and 0.47 m/s), the equations of Wright (1977a) or Hodgson and Rajaratnam (1992) can be used for separated water jets. In this study, the equations of Wright (1977a) were selected simply because they were based on photographic techniques, same as in this study.

5.3.2 Pure Bubble Plumes

As shown in Fig. 5-3 - Fig. 5-5, a pure bubble plume approximately follows a straight line downstream of the injection location. Similar straight-line bubble plume trajectories were reported in Manasseh et al. (1998) and Socolofsky and Adams (2002). The angle of the straight line mainly depends on the strength of the crossflow: a stronger crossflow corresponds to a smaller angle from the horizontal plane, as expected. On the other hand, the angle is not sensitive to the air discharge at the nozzle exit or bubble size: an increase of Q_a only slightly increases the plume angle. Fig. 5-3 - Fig. 5-5 also show that at a small value of Q_a (1 LPM), bubble size is more uniform; with the increase of Q_a (3 or 5 LPM), bubble size increases obviously, and smaller bubbles appear due to the breakup of large bubbles. Observation on bubble size distributions in strong crossflow (0.20 or 0.5 m/s) shows that larger bubbles tend to be at the upstream side of a bubble plume and smaller bubbles tend to be at the downstream side. This “fractionation” effect cannot be observed in weak crossflow (0.02 m/s). Moreover, in strong crossflow, bubbles appear to be more flattened because of the shear stress exerted by the crossflow on the bubble surface.

Since pure bubble plumes follow the trajectories of straight lines, the modeling becomes simple as long as the angles of the straight lines, θ , are determined. In the experiments with the crossflow of 0.20 m/s, bubble velocities in the direction of bubble plume centerlines, U_b , were measured across Section 100d from the nozzle exit by using an optical probe system (for details, see Chapter 6). If the value of U_b is assumed to be only composed of the crossflow velocity U and bubble slip (or terminal rise) velocity U_s , that is, the water velocity induced by bubble passage and bubble wakes along the bubble plume centerline U_{water} is negligible ($U = (U_b - U_{water}) \times \cos(\theta) \approx U_b \times \cos(\theta)$), then the angle of bubble plume centerline can be calculated to be $\theta = \arccosine(U/U_b)$. The

calculation results are shown in Fig. 5-7(a), and they are obviously larger than the angles directly measured from images. This indicates that the above assumption is invalid, i.e., U_b is also composed of the bubble-induced water velocity along the bubble plume centerline U_{water} in addition to U and U_S .

Socolofsky and Adams (2002) reported that bubble plume centerline followed the trajectory of vector sum of bubble slip velocity U_S and crossflow velocity U . The method of using $\arctangent(U_S/U)$ is tried next to determine the angle of a bubble plume centerline, and the key is to obtain the value of U_S . Direct measurement of U_S is rather challenging because of the difficulty in accurate measurement of bubble-induced water velocity in a bubble plume ($U_S = (U_b - U_{water}) \times \sin(\theta)$). For single isolated bubbles in pure water at 20 °C, Clift et al. (1978) reported the classic graph of U_S versus bubble diameter of volume-equivalent sphere, d_b . For $d_b > 1.3$ mm, as in this study (see Table 5-1), they reported that:

$$U_S = \sqrt{2.14\sigma/\rho d_b + 0.505gd_b^2} \quad (5.8)$$

where σ is the surface tension of air-water interface; ρ is the density of water; and g is the gravitational acceleration. Based on the bubble sizes measured in the crossflow of 0.20 m/s (see Chapter 6), the angles by using the method of $\arctangent(U_S/U)$ are also shown in Fig. 5-7(a). The calculation agrees well with the angles from images. Different bubble plumes containing bubbles of different sizes have similar plume angles because U_S is not very sensitive to the change of d_b (as can be shown in Eq. (5.8)). From the comparison of the angles from $\arccosine(U/U_b)$ and $\arctangent(U_S/U)$ with those from images, it may be concluded that: U_b in the direction of bubble plume angle is composed of bubble slip velocity U_S , crossflow velocity U and bubble-induced water velocity U_{water} ; and U_{water} is also in the direction of bubble plume angle (otherwise, bubble plume trajectory will not be at the angle determined by U_S and U).

The modeled bubble plume centerlines by using the method of $\arctangent(U_S/U)$ for the crossflow of 0.20 m/s are shown in Fig. 5-8, together with the direct measurements from images. Fig. 5-8 shows that the modeled centerlines are in good agreement with the measurements. Assuming that bubble sizes are not substantially different in different crossflows (as can be observed in Fig. 5-3 - Fig. 5-5), the measurement results of d_b at the crossflow of 0.20 m/s and thus U_S were used for the modeling in the other two crossflows. The modeling results are present in Figs. 5-9 and 5-10 with good agreement, which is partially because of the insensitiveness of U_S to d_b .

5.3.3 Bubbly Jets

As can be seen in Fig. 5-3 - Fig. 5-5, properties of bubbly jets depend strongly on the water flow rates at the nozzle Q_w . An increase in Q_w breaks large bubbles into small ones due to the shear forces on the bubble surface exerted by the mean flow and turbulence of the water jets. However, if Q_w is small, the forces are not large enough to break all the large bubbles, resulting a mixture of both large and small bubbles (see the experiments with $Q_w = 1$ LPM in Fig. 5-3 - Fig. 5-5). On the other hand, if Q_w is large enough, bubble sizes are small and more uniform (see the experiments with $Q_w = 3$ or 5 LPM). Lima Neto et al. (2008b) conducted experiments of bubbly jets in stagnant water and proposed that the nozzle Reynolds number based on the superficial water velocity at the nozzle (Eq. (5.1)) and nozzle diameter should be large than 8,000 to cause large bubbles broken into small ones of uniform size. This criterion in stagnant water has been checked in this study: it is still valid for bubbly jets in crossflow. From Fig. 5-3 - Fig. 5-5, crossflow has negligible effect on the breakup of bubbles because the breakup mainly occurs near the nozzle where the jet momentum is more important. For the experiments with small Q_w (1 LPM), the bubble plumes in bubbly jets are more close to

pure bubble plumes, and straight lines can well describe the bubble plume centerline trajectories. Similarly as for pure bubble plume, these centerlines can be modeled by using the method of arctangent(U_s/U) (see Fig. 5-7(a)), where U_s is calculated from Eq. (5.8) based on the measurements of bubble size. The modeling results of centerline trajectories agree well with the measurements, as shown in Fig. 5-8 - Fig. 5-10.

Properties of bubbly jets also strongly rely on the strength of crossflows. In weak crossflows, as seen in Fig. 5-3, bubbles are mixed with (not separated from) the water jet. In stagnant water, Lima Neto et al. (2008b) reported that the bubble core radius occupied 55-70% of the water jet radius, and the spreading rate of the water jet's visual edge was approximately 0.18. In the weak crossflow of 0.02 m/s, the present experiments show that the ratio of bubble core radius to water jet radius is the range of 57-82%, and the spreading rate of water jet's visual boundary is in the range of 0.19-0.20, close to the results in the stagnant water. This suggests that weak crossflow does not significantly change the general properties of bubbly jets, compared to those in stagnant water. However, one thing that weak crossflow does change is the leakage of dye from the water jet into the downstream ambient. The images in Fig. 5-3 were taken at the beginning of jet injection. After a few seconds, leakages could be more clearly observed.

In strong crossflows, the most distinct feature of bubbly jets is the separation of bubble plumes from water jets after some distance away from the injection location. From Figs. 5-4 and 5-5, an increase in crossflow strength accelerates the separation, while an increase in Q_a or Q_w delays the separation. Fig. 5-11 presents a typical example of a bubbly jet of in strong crossflow. Six zones may be defined to better describe the relevant phenomenon. Zone I is the bubbly jet zone, where bubbles are well-mixed with the water jet because of the strong momentum of the water jet near the nozzle. Zone II is

the transition zone, where bubbles start to rise and accumulate near the upper boundary of the water jet due to the buoyancy of the bubbles and due to the momentum decay of the water jet along the jet centerline. Zone III is the separated bubble plume zone, where bubbles have completely separated from the water jet. Note that for a bubbly jet in strong crossflows, the whole trajectory of bubble plume from Zone I to III can no longer be simply approximated as a straight line from the nozzle, which is different from that of a pure bubble plume. Zone IV is the separated water jet zone, where bubbles no longer exist inside the water jet. Zone V is the fine bubble zone, where rather tiny bubbles (with diameters in the order of 0.1 mm) can be observed downstream of the bubble plume. Tiny bubbles behind a larger bubble plume present another example of the fractioning ability of crossflow. Zone VI is the possible leakage zone and the leakage occurs when eddies at the jet lower boundary can no longer be entrained back to the jet and thus are flushed downstream (see Experiments. B-3-5 and B-5-5 in Fig. 5-4). Similar leakage phenomenon of jets or plumes in crossflow has also been observed by Davidson and Pun (1999) and Socolofsky and Adams (2002). From this study, the leakage appears to occur more easily in a weak crossflow, as a strong crossflow tend to suppress rising of the water jet and thus the leakage.

It is interesting to note the effect of bubbles in bubbly jets. First, the existence of bubbles tends to lift up the water jets due to the buoyancy of bubbles. This can be observed both in a weak crossflow (see Experiments A-1-1 and A-0-1 in Fig. 5-3) and a strong crossflow (see in Figs. 5-4 and 5-5). Such lifting effect can be more easily observed in a strong crossflow (see the lift of water jet centerlines) and in the experiments with large bubbles. Second, the existence of bubbles enhances jet mixing, especially with large bubbles. For instance, in the Experiments B-1-1, dye in the water jet is diffused in the range of 1/2 of the water depth, and in the experiments of B-3-1 and

B-5-1 (see Fig. 5-4), dye exists almost the whole range of the water depth. Significant enhancement of jet mixing due to the bubbles can be also observed in Experiments C-1-1, C-3-1 and C-5-1 in Fig. 5-5. This suggests that large bubbles are more preferable than small bubbles for the purpose of artificial mixing, as recommended by Wüest et al. (1992). Small bubbles, of course, are preferred for artificial aeration due to the large air-water interfacial area, as suggested by Wüest et al. (1992) and Sahoo and Luketina (2003). Small bubbles are also able to enhance jet mixing to a certain degree (see Fig. 5-12). Fig. 5-12 presents the water jet's visual half-thickness W_z along the jet centerline ζ with $Q_a = 0 - 5$ LPM and $Q_w = 3$ LPM, where the existence of small bubbles is seen to help the jet diffusion and thus the jet mixing.

It is also important to summarize the effect of crossflow on bubbly jets. First, crossflow bends bubbly jets as it bends pure water jets. Second, crossflow causes fractionation of bubbly jets. The fractionation effect can be observed in the experiments with small Q_w (1 LPM) where large bubbles appear in the upstream side and small bubbles in the downstream side. The separation of the bubble plumes from the water jets in bubbly jets also essentially reflects the fractionation effect. Third, with the increase of crossflow strength, the centerlines of both bubble plume and water jets are suppressed downwards, and the thicknesses of water jets are decreased, as clearly shown in Fig. 5-12(b).

5.3.4 Modeling of the Water Jets in Bubbly Jets in Strong Crossflows

In the following, the centerlines of bubbly jets in strong crossflows are modeled, including the centerlines of water jets and bubble plumes both before and after the separation. To model the water jet centerline, it is crucial to determine the water velocity at the nozzle exit U_{w0} , although this is challenging for bubbly jets as stated

earlier. In this study, bubbly jets were ejected into the air, and the jet maximum rise heights, H_{max} , were recorded. This provides a simple way to estimate U_{w0} , assuming no energy loss during the rise of jets:

$$U_{w0} = \sqrt{2gH_{max}} \quad (5.9)$$

Note that Eq. (5.9) is an estimate of U_{w0} and it is assumed that the value of U_{w0} is not significantly affected with or without the additional pressure exerted by the ambient water above the nozzle (0.53 m in this study). Eq. (5.9) is first examined for the case of pure water jets. Fig. 5-13(a) presents the measurement results of maximum rise heights, and Fig. 5-13(b) shows the comparison U_{w0} by comparing Eq. (5.9) with its theoretical values (Eq. (5.1)) for the case of pure water jets. As seen in Fig. 5-13(b), the differences are 14.4%, 2.4% and 3.4% for $Q_w = 1, 3$ and 5 LPM, respectively. The larger difference for $Q_w = 1$ is mainly because that H_{max} measured only 2.35 cm and a small reading error in H_{max} would cause large difference in U_{w0} . Fig. 5-13(b) verifies the use of Eq. (5.9) for pure water jets.

For bubbly jets, the measurements of H_{max} for nine combinations of Q_a and Q_w are also shown in Fig. 5-13(a), and the calculated values of U_{w0} are listed in Table 5-1. Fig. 5-13(a) shows the substantial impact of Q_a on H_{max} , and thus on U_{w0} . Eq. (5.1) ignores the impact of gas-phase and will significantly underestimate U_{w0} . On the other hand, Eq. (5.2) assumes that the gas-phase is totally incompressible, and will overestimate U_{w0} . As seen from Table 5-1, the values of U_{w0} from Eq. (5.9) are between the two extreme values from Eqs. (5.1) and (5.2), and are more physically reasonable. The values of U_{w0} from Eq. (5.9) might be used to speculate the area ratios occupied by the liquid phase at the nozzle exit, and the result show that they are $18.7 \pm 12.2\%$ larger than the liquid volume fraction, i.e., $(1-C_0)$. This suggests that the compressibility of

gas-phase at the nozzle exit is important. The compressibility appears to relate with both Q_a and Q_w .

The values of U_{w0} from Eq. (5.9) and the validated equations of Wright (1977a) (Eqs. (5.3) - (5.4)) were used to model the water jet centerlines in bubbly jets. The modeling results are shown in Figs. 5-14 and 5-15. Generally, the modeled centerlines are desirable, especially for the experiments in the crossflow of 0.47 m/s in Fig. 5-15. In the crossflow of 0.20 m/s, as seen from Fig. 5-14, the modeled centerlines are located slightly below the measured centerlines, contrary to the finding that the modeled centerlines are slightly higher in the case of pure water jets as shown in Fig. 5-6. The comparison between Figs 5-14 and 5-6 reflects the lift of water jets due to the bubbles. Such lift is more obvious with the increase of Q_a (see Experiments B-3-3 and B-5-3 in Fig. 5-14), but less obvious with the increase of Q_w (see Experiments B-5-3 and B-5-5). The fact that the water jets in bubbly jets are higher than pure water jets as shown in Fig. 5-4 is attributed to two important reasons: the increase of U_{w0} and thus jet momentum in bubbly jets (the primary reason); and the lift forces due to the bubbles, which cannot be ignored for large Q_a . A similar conclusion on the lift of water jets by bubbles in bubbly jets can be made in the crossflow of 0.47 m/s by comparing Fig. 5-15 with Fig. 5-6. But, in stronger crossflow, such lift is insensitive to the change of Q_a or Q_w .

5.3.5 Modeling of the Bubble Plumes in Bubbly Jets in Strong Crossflows

To model the bubble plume centerline in a bubbly jet, it is important to first know the location where bubbles separate from the water jet. Similar to Socolofsky and Adams (2002), the separation location in this study is defined as the intersection point of the water jet centerline and the bubble plume centerline (see Fig. 5-11). Below the separation height, H_s , the bubble plume centerline can be modeled the same way as the

water jet centerline as bubbles are well mixed with the water jet. Above H_S , the bubble plume centerline can be modeled as a straight line, as seen in Figs. 5-4, 5-5, and 5-11.

From Figs. 5-4 and 5-5, the value of H_S appears to increase with the increase of air discharge Q_a or water discharge Q_w , while it decreases with the increase of ambient velocity U . As the increase of Q_a or Q_w means the increase of U_{w0} (see Fig. 5-13 and Table 5-1), H_S is plotted versus $U_{w0}/U = \alpha$ in Fig. 5-16. In addition, if $\alpha = 0$, then in theory, $H_S = 0$. As shown in Fig. 5-16, H_S follows a simple linear relation with α for both crossflow conditions:

$$H_S = 0.896\alpha \quad \text{with } R^2 = 0.95 \quad (5.10)$$

where R is the correlation coefficient. Note that in Fig. 5-16, H_S is not non-dimensionalized because both the nozzle diameter and ambient water depth, which are normally used as the length scales for non-dimensionalization of jets in crossflow, are constant in this study.

In the experiments in the crossflow of 0.20 m/s, as shown in Chapter 6, bubble-induced water velocity along the bubble plume centerline is negligible for the case of bubbly jets with large Q_w (3 or 5 LPM), thus U_b can be treated as vector sum of U_S and U . Therefore, the angle of the bubble plume centerline θ in a bubbly jet can be calculated to be $\arccosine(U/U_b)$. Fig. 5-7(b) shows that the calculated centerline angles are close to those directly measured from images. Note that, as explained earlier, the method of using $\arccosine(U/U_b)$ does not apply for the cases of pure bubble plumes and bubbly jets with small Q_w (1 LPM), because it overestimates the centerline angles, as shown in Fig. 5-7(a). In this study, the method of $\arccosine(U/U_b)$ is used for modeling bubble plume centerlines after the separation in bubbly jets. If no measurement is conducted on U_b , then the angle of a bubble plume centerline θ can be calculated to be $\arctangent(U_S/U)$, where U_S can be estimated based on the U_S versus d_b relation

provided by Clift et al. (1978). The values of angle θ based on $\arctangent(U_s/U)$ and Clift et al. (1978) were examined to be rather close to (2 degrees difference) those from the method of $\arccosine(U/U_b)$ (see Fig. 5-7(b)).

The modeling results of the bubble plume centerlines in bubbly jets in the crossflow of 0.20 m/s are present in Fig. 5-17. In general, the modeling agrees with the measurements. Below the separation height H_s obtained from Eq. (5.10), the bubble plume (to be exact, bubbly jet) centerlines are the same as that of water jets (see Fig. 5-14). Above H_s , the modeled centerlines are slightly lower than the measured ones, because of the underestimation of the jet centerlines before the separation and because of the error in Eq. (5.10) to estimate H_s . From the images, bubble sizes are similar in the crossflows of 0.20 m/s and 0.47 m/s, hence it is reasonable to assume that bubble slip velocity $U_s = U_b \times \sin(\theta)$ in the crossflow of 0.20 m/s is close to that in the crossflow of 0.47 m/s. Similarly, the modeling results in the crossflow of 0.47 m/s are shown in Fig. 5-18, and the modeling is satisfactory.

5.4 Summary and Conclusions

In Chapter 5, bubble plumes and bubbly jets, as well as pure water jets, were photographically studied in three crossflows. The focus is on the centerline trajectories of bubble plumes and bubbly jets, and the cases of water jets were used as references. Bubble plumes and bubbly jets were produced by injecting different combinations of air and water flows via a single-orifice nozzle. In total, 45 cases of bubble plumes, bubbly jets and pure water jets were studied. Effect of air or water discharge at the nozzle on the properties of bubble plumes and bubbly jets were examined. Effect of crossflow strength was also studied. Centerline trajectories of bubble plumes and bubbly jets were modeled. Because literatures on bubbly jets in crossflow are rare, this study will provide

scientific basis for the activities such as artificial mixing and aeration in rivers and oil-gas blowout in oceans. The main conclusions are as follows:

- (1) Properties of bubble plumes and bubbly jets depend strongly on the air and water flow rates at the nozzle exit (Q_a and Q_w). A nozzle Reynolds number of $Re = 8,000$ based on the superficial water velocity at the nozzle is required to breakup large bubbles into small bubbles of uniform size. This criterion, proposed by Lima Neto et al. (2008b) in stagnant water, still hold true for bubbly jets in crossflow. Both large and small bubbles lift up water jets in bubbly jets and enhance water jet mixing.
- (2) Properties of bubble plumes and bubbly jets also rely on the strength of crossflow. In weak crossflows, bubble plumes are mixed with water jets in bubbly jets; while in strong crossflows, bubble plumes separate from water jets in bubbly jets. The separation height H_S was found to be proportional to the ratio of water velocity at the nozzle exit U_{w0} to crossflow velocity U (Eq. (5.10)).
- (3) For pure bubble plumes and bubbly jets with small Q_w (1 LPM or $Re < 8,000$), the bubble plume centerline can be well modeled with a straight line. The angle of the straight line can be well predicted from $\arctangent(U_S/U)$, but are overestimated from $\arccosine(U/U_b)$, where U_S is the bubble slip velocity for single isolated bubbles reported by Clift et al. (1978) and U_b is the bubble velocity measured along a bubble plume centerline. For bubbly jets with large Q_w (3 or 5 LPM, or $Re \geq 8,000$), the angle of straight bubble plume centerlines after separation can be well predicted by both methods. This indicates that bubble-induced water velocity along the bubble plume centerline exists for the

case of pure bubble plumes and bubbly jets with small Q_w , but it is negligible in bubbly jets with large Q_w .

- (4) The case of pure water jets were used to validate the equations of jets in crossflow proposed in literature, and the equations of Wright (1977a) were selected for modeling the water jets in bubbly jets. The water velocity at the nozzle exit U_{w0} is required for the modeling. For bubbly jets, U_{w0} based on the maximum rise height of bubbly jets in air appears to be reasonable, and the modeling agrees well with the measurements.

References

- Clift, R., Grace, J. R., and Weber, M. E. (1978). *Bubbles, drops and particles*, Academic, New York.
- Davidson, M. J., and Pun, K. L. (1999), "Weakly advected jets in crossflow", *J. Hydraul. Eng.* 125(1), 47-58.
- Fischer, H. B., List, E. J., Koh, R. C. Y., Imberger, J., and Brooks, N. H. (1979). *Mixing in inland and coastal waters*, Academic Press, San Diego.
- Hodgson, J. E., Rajaratnam, N. (1992). "An experimental study of jet dilution in crossflows. *Can. J. Civ. Eng.*, 19,733-743.
- Hodgson, J. E., Rajaratnam, N., and Moawad, A. K. (1999). "Circular jets in crossflows of finite depth." *Proc. Instn Civ. Engrs Wat., Marit. Energy*, 136, 35-42.
- Lee, J. H. W., and Chu, V. H. (2003). *Turbulent jets and plumes – a Lagrangian approach*, Kluwer Academic publisher, Norwell, Massachusetts, USA.
- Lima Neto, I. E. (2012). "Modeling the liquid volume flux in bubbly jets using a simple integral approach." *J. Hydraul. Eng.*, 138(2), 210-215.
- Lima Neto, I. E., Zhu, D. Z., Rajaratnam, N., Yu T., Spafford., M., and McEachern, P. (2007). "Dissolved oxygen downstream of an effluent outfall in an ice-cover river: natural and artificial aeration." *J. Environ. Eng.*, 133 (11), 1051-1060.
- Lima Neto, I. E., Zhu, D. Z. and Rajaratnam, N. (2008a). "Air injection in water with different nozzles." *J. Environ. Eng.*, 134 (4), 283-294.
- Lima Neto, I. E., Zhu, D. Z. and Rajaratnam, N. (2008b). "Bubbly jets in stagnant water." *Int. J. Multiphase Flow*, 34 (12), 1130-1141.

- Lima Neto, I. E., Zhu, D. Z. and Rajaratnam, N. (2008c). "Effect of tank size and geometry on the flow induced by circular bubble plumes and water jets." *J. Hydraul. Eng.*, 134 (6), 833-842.
- Lima Neto, I. E., Zhu, D. Z. and Rajaratnam, N. (2008d). "Horizontal injection of gas-liquid mixtures in a water tank." *J. Hydraul. Eng.*, 134 (12), 1722-1731.
- Manasseh, R., Yoshida, S., and Kajio, N. (1998). "Bubble Trajectory Bifurcations in Crossflow." 13th Australasian Fluid Mechanics Conference, Monash University, Melbourne, Australia.
- Milgram, J.H. (1983). "Mean flow in round bubble plumes." *J. Fluid Mech.*, 133, 345-376.
- Norman, T. L., and Revankar, S. T. (2011). "Buoyant jet and two-phase jet-plume modeling for application to large water pools." *Nucl. Eng. Des.*, 241(5), 1667-1700.
- Rajaratnam, N. 1976. *Turbulent jets*, Elsevier Scientific, Amsterdam, the Netherlands.
- Sahoo, G. B., and Luketina, D. (2003). "Modeling of bubble plume design and oxygen transfer for reservoir restoration." *Water Res.*, 37(2), 393-401.
- Sahoo, G. B., and Luketina, D. (2006). "Response of a tropical reservoir to bubbler destratification." *J. Environ. Eng.*, 132(7), 736-746.
- Seol, D. G., Bhaumik, T., Bergmann, C., and Socolofsky, S. A. (2007). "Particle image velocimetry measurements of the mean flow characteristics in a bubble plume." *J. Eng. Mech.*, 133(6), 665-676.
- Socolofsky, S. A., and Adams, E. E. (2002). "Multi-phase plumes in uniform and stratified crossflow." *J. Hydraul. Res.*, 40(6), 661-672.
- Sun, T. Y., and Faeth, G. M. (1986a). "Structure of turbulent bubbly jets. I: Methods and centerline properties." *Int. J. Multiphase Flow*, 12(1), 99-114.
- Sun, T. Y., and Faeth, G. M. (1986b). "Structure of turbulent bubbly jets. II: Phase property profiles." *Int. J. Multiphase Flow*, 12(1), 115-126.
- Wang, X.Y. (2011). "Calibration and testing of a newly constructed hydraulic flume." M. Eng. report, Department of Civil and Environmental Engineering, University of Alberta, Edmonton, Canada.
- Wright, S. J. (1977a). "Effects of ambient crossflows and density stratification on the characteristic behaviour of round turbulent buoyant jets. Ph.D. thesis, Report No. KH-R-36, California Institute of Technology, Pasadena, CA.
- Wright, S. J. (1977b). "Mean behavior of buoyant jet in a crossflow." *J. Hydraul. Div.*, 103(HY5), 499-513.
- Wüest, A., Brooks, N. H., and Imboden, D. M. (1992). "Bubble plume modeling for lake restoration." *Water Resour. Res.*, 28(12), 3235-3250.

Table 5-1. Experimental Conditions for Bubble Plumes and Bubbly Jets in Crossflows

| Ambient | Experiments | Q_a | Q_w | C_0 | d_b^2 | U_{w0} (m/s) ³ | | |
|---------------------------------|-------------------|-------|-------|-------|---------|-----------------------------|-----------|------------|
| | I.D. ¹ | (LPM) | (LPM) | | (mm) | Method I | Method II | Method III |
| | A/B/C-0-1 | 0 | 1 | 0 | / | 0.59 | 0.59 | 0.68 |
| | A/B/C-0-3 | 0 | 3 | 0 | / | 1.78 | 1.78 | 1.82 |
| | A/B/C-0-5 | 0 | 5 | 0 | / | 2.97 | 2.97 | 3.07 |
| Condition A: $U = 0.02$ m/s; | A/B/C-1-0 | 1 | 0 | 1.00 | 8.47 | / | / | / |
| | A/B/C-1-1 | 1 | 1 | 0.50 | 7.81 | 0.59 | 1.19 | 1.01 |
| | A/B/C-1-3 | 1 | 3 | 0.25 | 1.96 | 1.78 | 2.37 | 1.98 |
| Condition B: $U = 0.20$ m/s; | A/B/C-1-5 | 1 | 5 | 0.17 | 1.73 | 2.97 | 3.56 | 3.31 |
| | | | | | | | | |
| Condition C: $U = 0.47$ m/s | A/B/C-3-0 | 3 | 0 | 1.00 | 9.84 | / | / | / |
| | A/B/C-3-1 | 3 | 1 | 0.75 | 8.68 | 0.59 | 2.37 | 1.95 |
| | A/B/C-3-3 | 3 | 3 | 0.50 | 2.46 | 1.78 | 3.56 | 3.13 |
| | A/B/C-3-5 | 3 | 5 | 0.38 | 2.10 | 2.97 | 4.75 | 4.60 |
| | | | | | | | | |
| | A/B/C-5-0 | 5 | 0 | 1.00 | 10.87 | / | / | / |
| | A/B/C-5-1 | 5 | 1 | 0.83 | 8.91 | 0.59 | 3.56 | 2.50 |
| | A/B/C-5-3 | 5 | 3 | 0.63 | 2.93 | 1.78 | 4.75 | 3.60 |
| | A/B/C-5-5 | 5 | 5 | 0.50 | 2.22 | 2.97 | 5.93 | 5.31 |

Notes: ¹ The first character stands for ambient condition, A or B or C; the numbers are injected air and water flow rates in the nozzle, respectively;

² Average bubble diameters were measured at Section $100d$ from the nozzle by using an optical probe system in the crossflow of 0.20 m/s (for details, see Zhang and Zhu 2012);

³ Methods I, II and III are based on Eqs. (5.1), (5.2) and (5.9), respectively.

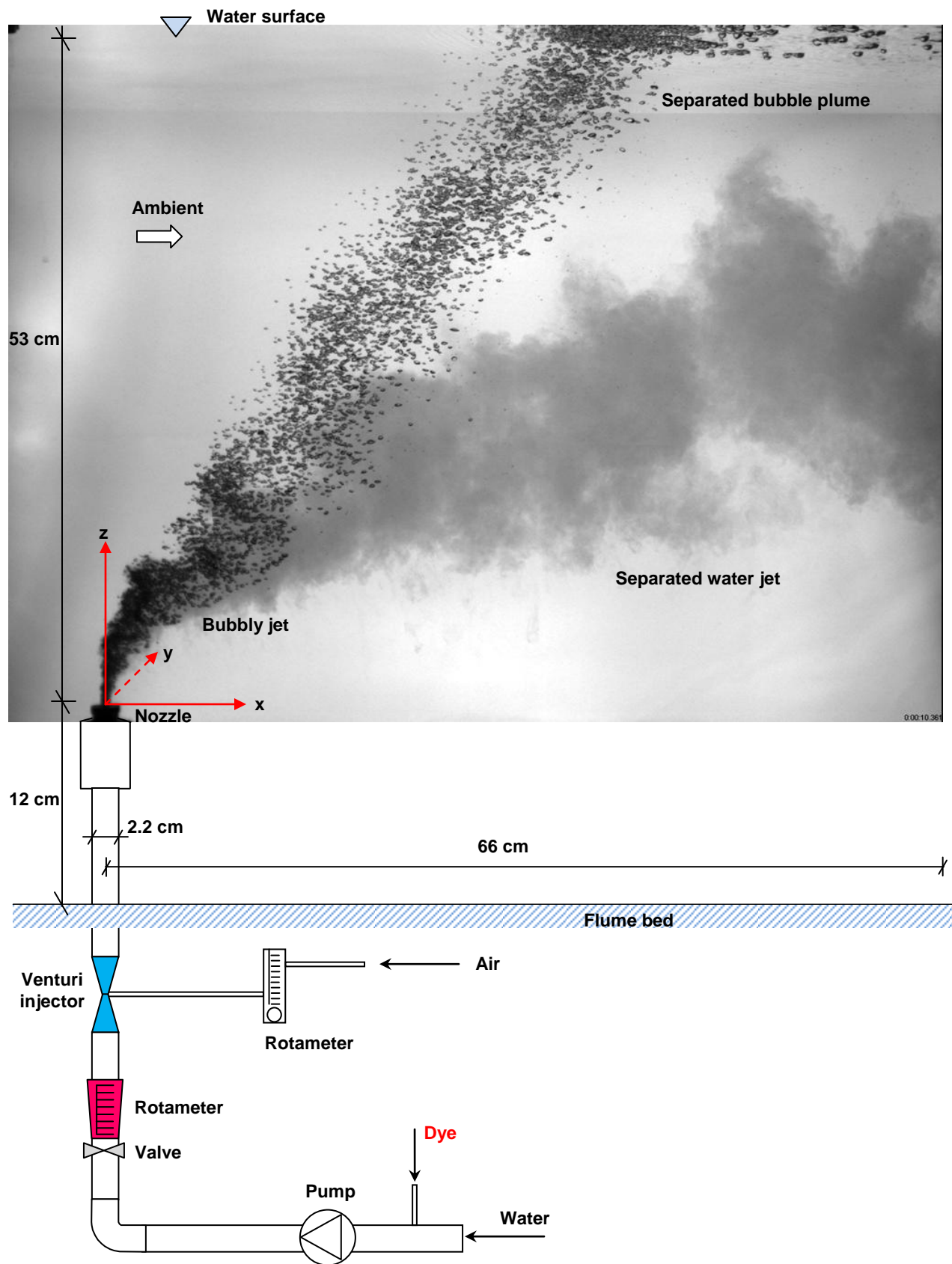


Figure 5-1. Schematic of the experimental setup; experiment shown in the photo: Expt. B-3-3

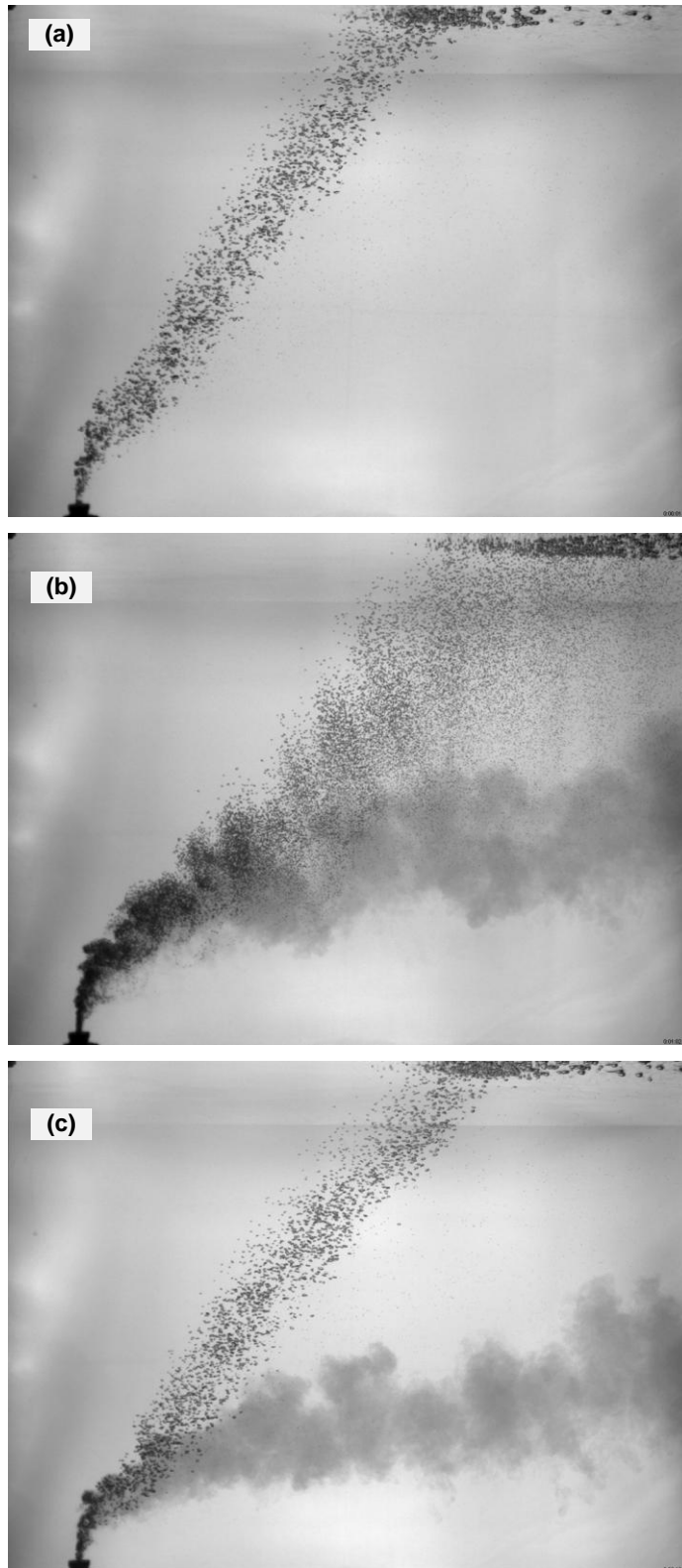


Figure 5-2. Effect of dye on bubble properties in Expt. B-1-3, (a) without dye; (b) with Rhodamine W.T.; and (c) with a liquid food color

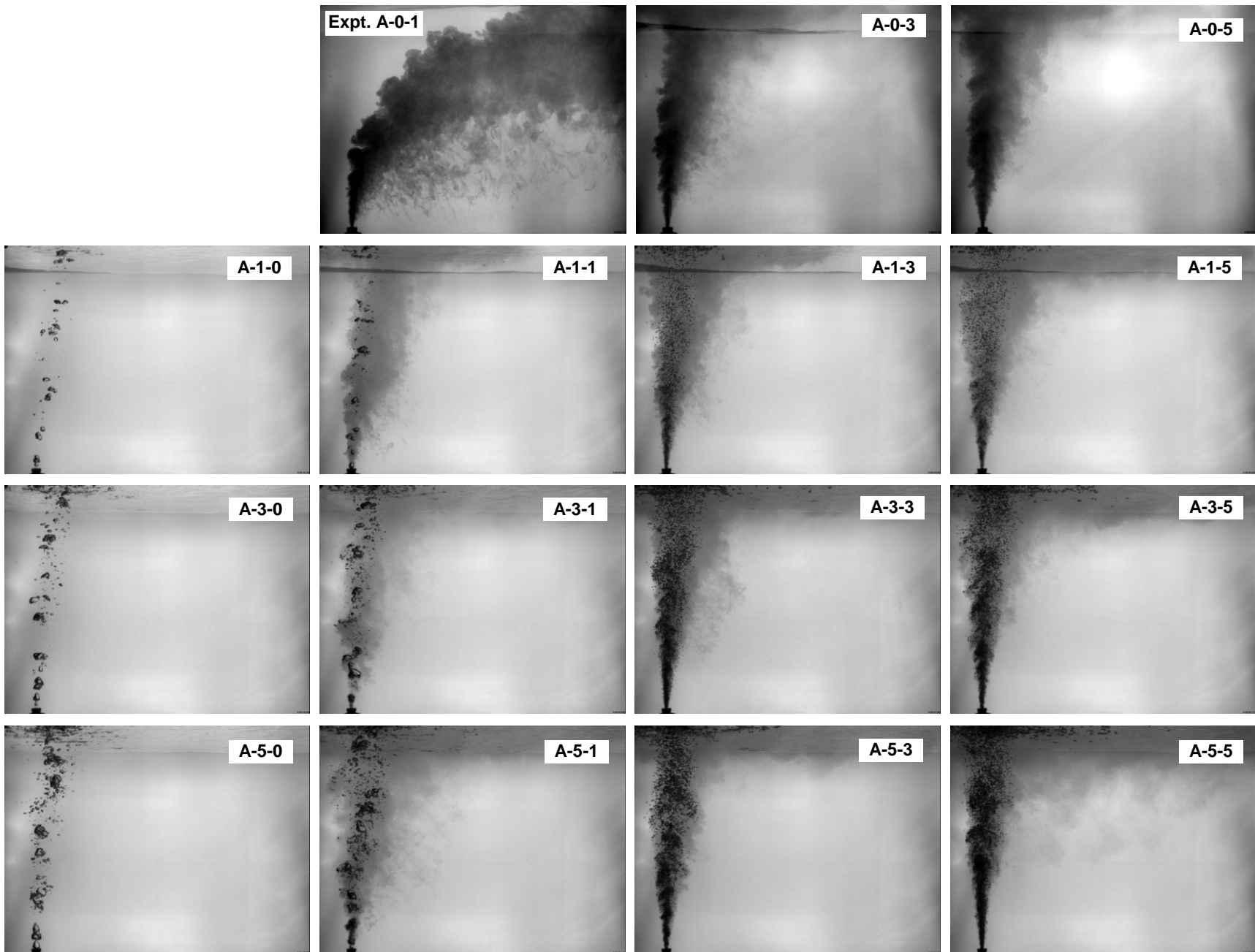


Figure 5-3. Photos of pure water jets, bubble plumes and bubbly jets at an ambient velocity of 0.02 m/s; photo size: $73.7 \times 55.0 \text{ cm}^2$

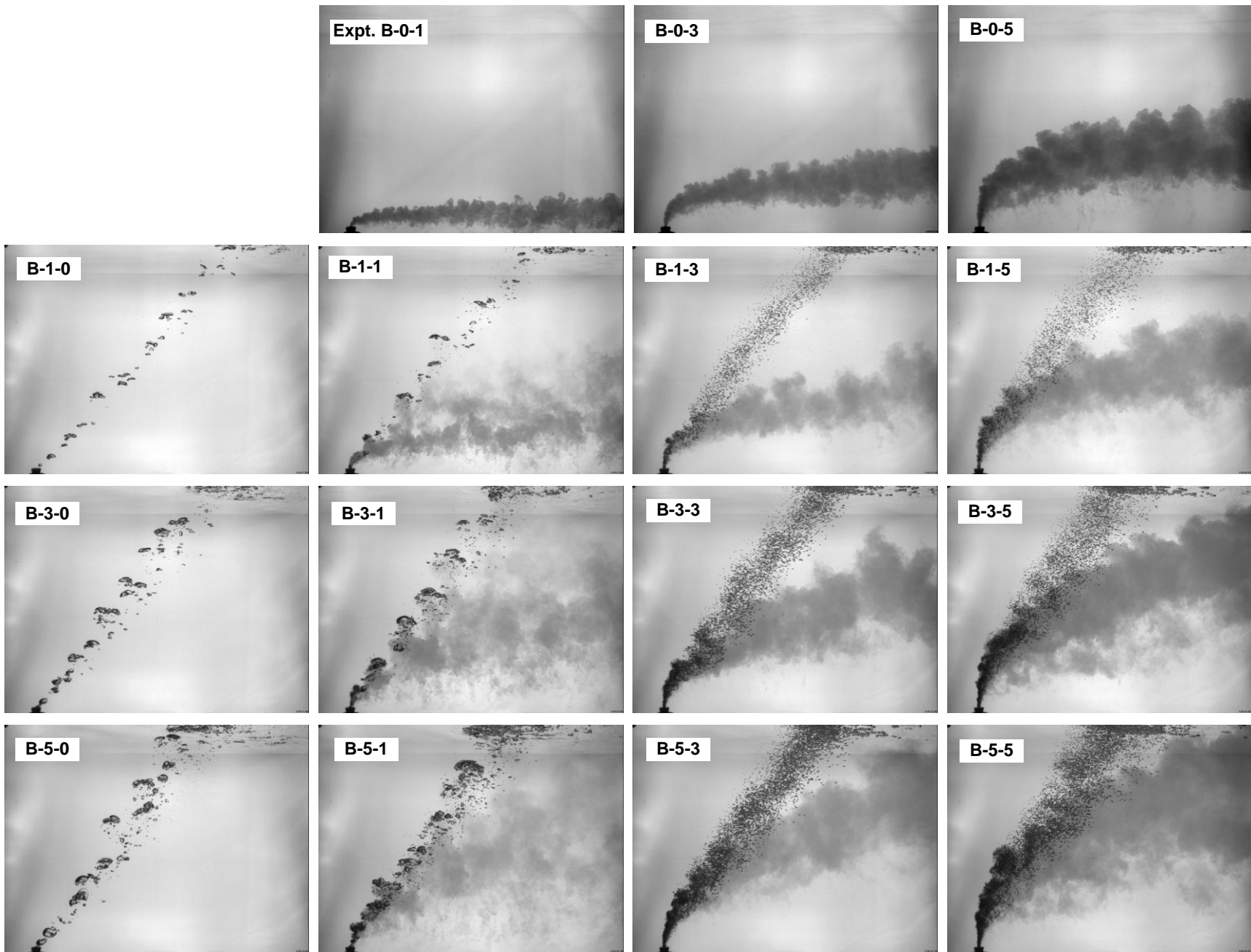


Figure 5-4. Photos of pure water jets, bubble plumes and bubbly jets at an ambient velocity of 0.20 m/s; photo size: $73.7 \times 55.0 \text{ cm}^2$

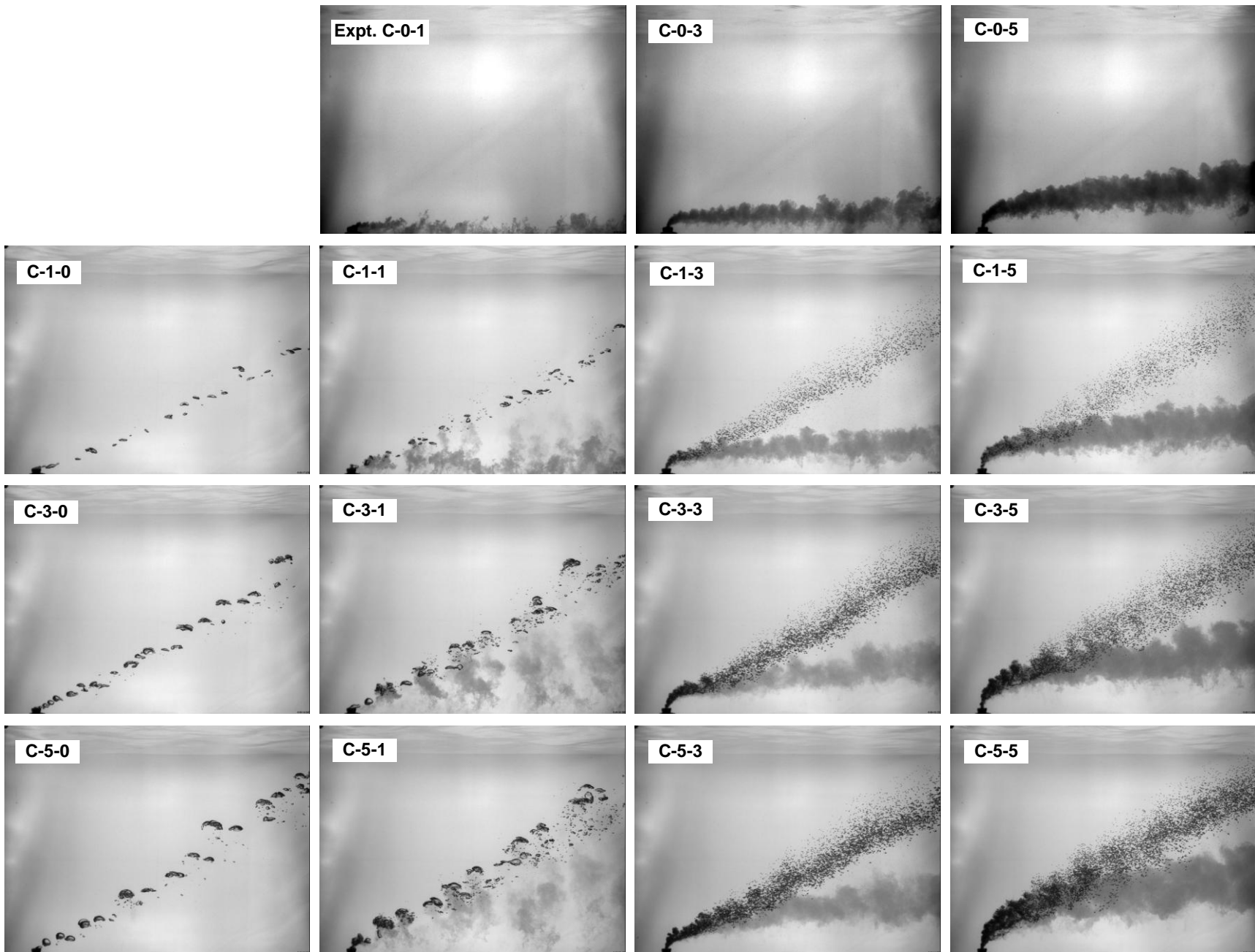


Figure 5-5. Photos of pure water jets, bubble plumes and bubbly jets at an ambient velocity of 0.47 m/s; photo size: $73.7 \times 55.0 \text{ cm}^2$

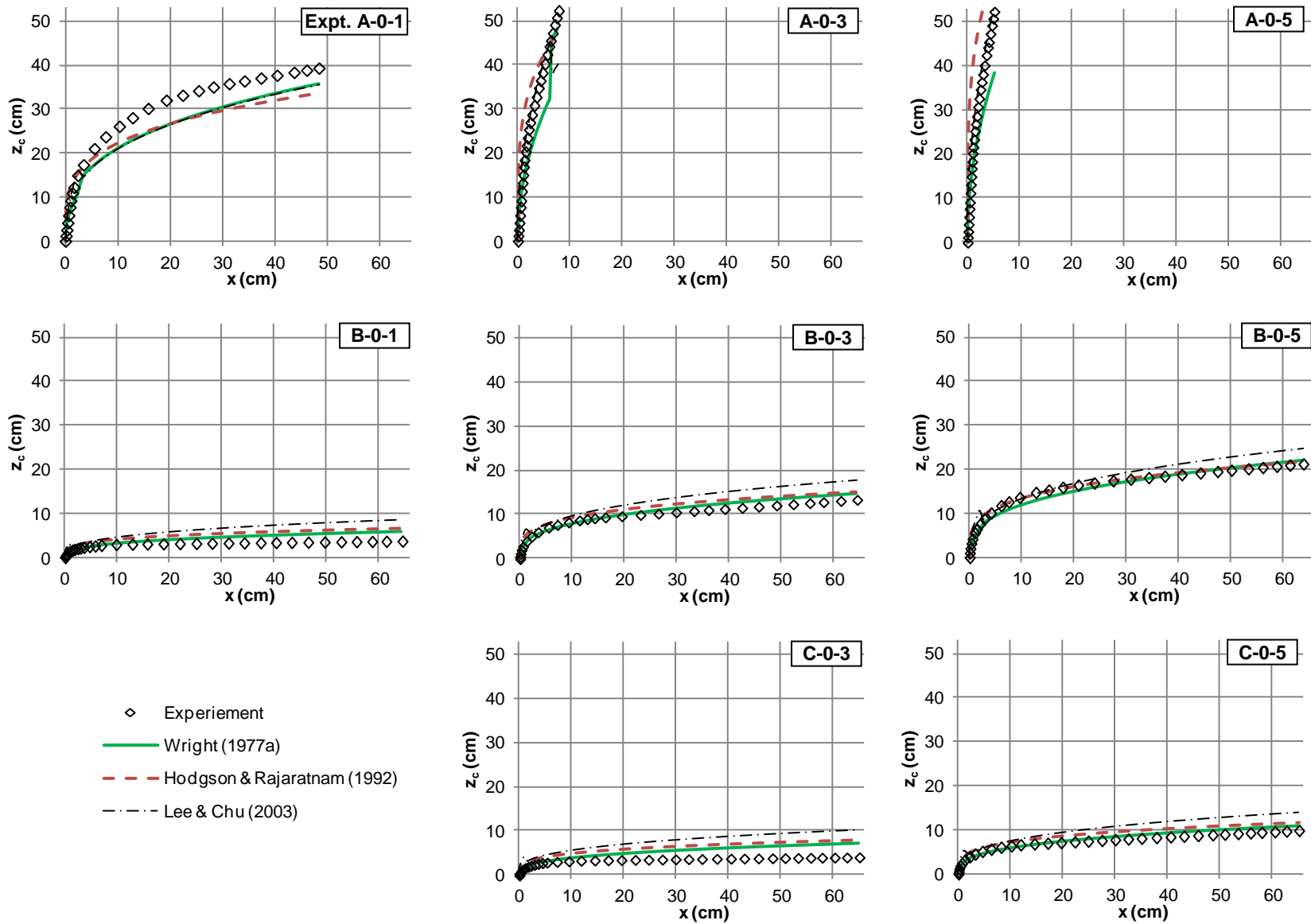


Figure 5-6. Comparison of measurement results of jet centerlines with previous studies for the case of pure water jets

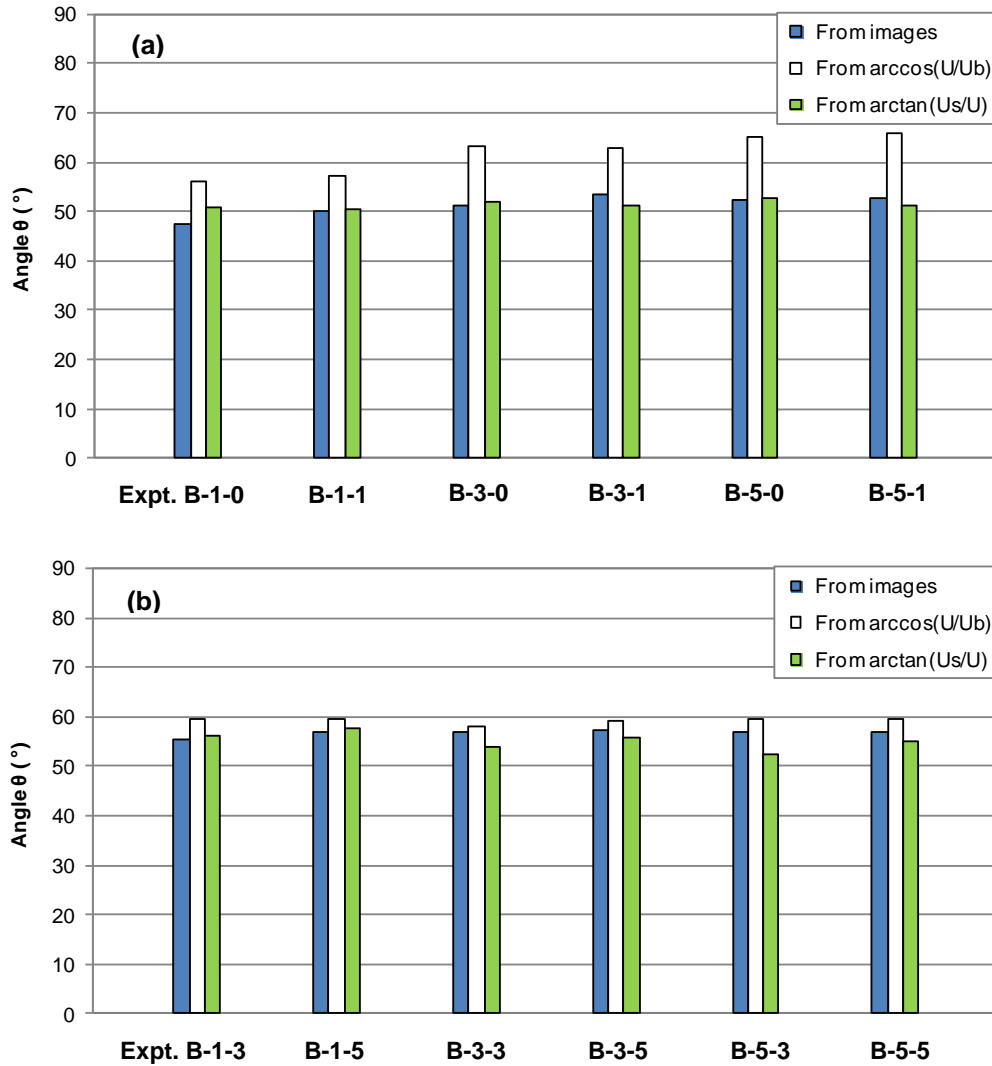


Figure 5-7. Comparison of the angle of bubble plume centerline from images with that from arccosine (U/U_b) and that from arctangent (U_s/U) in the crossflow of $U = 0.20$ m/s, where U_b is the measured bubble velocity along the centerline and U_s is the bubble slip velocity from Clift et al. (1978); (a) for the cases of pure bubble plumes and bubbly jets with small Q_w and (b) for the case of bubbly jets with large Q_w

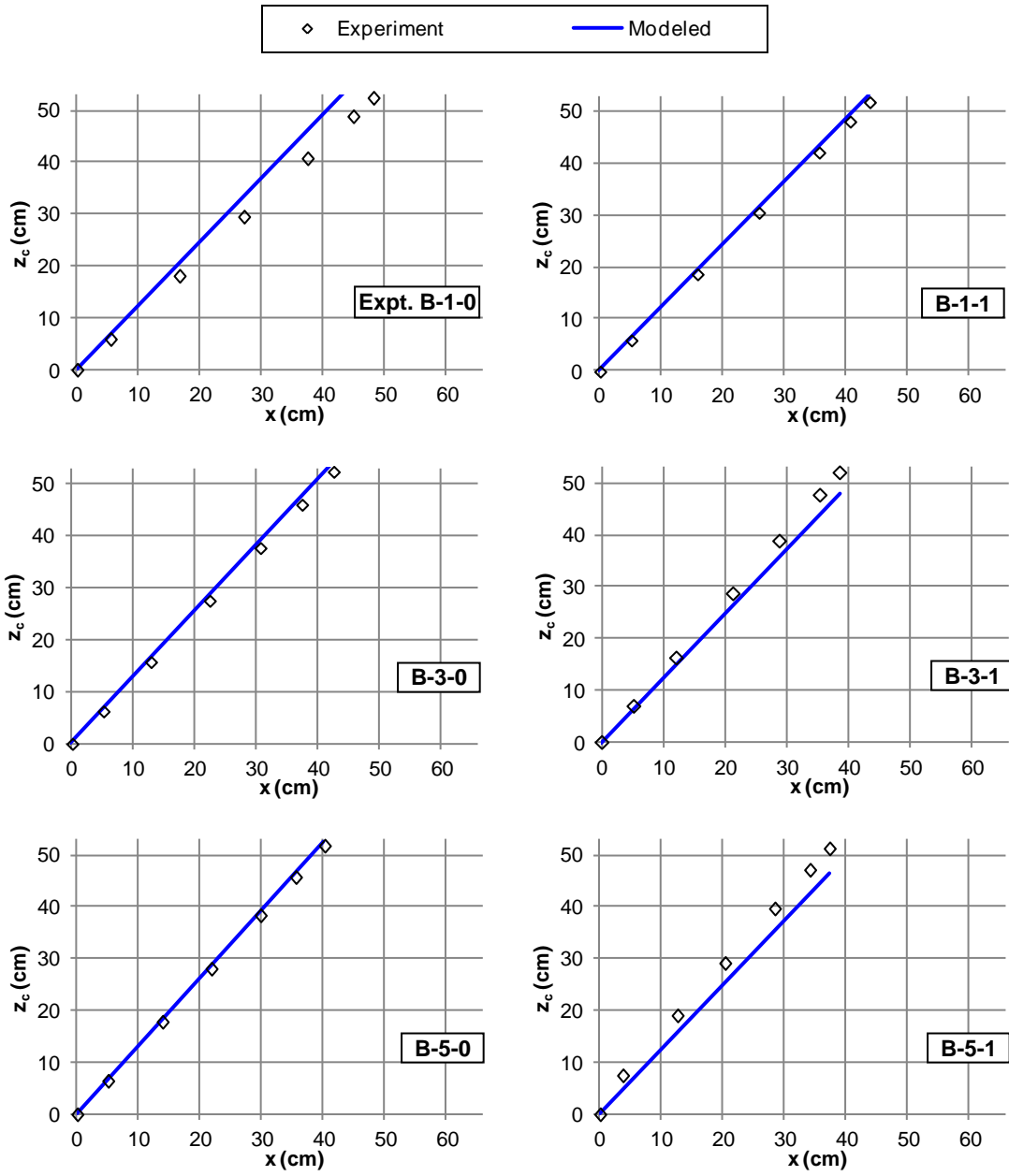


Figure 5-8. Comparison of measured bubble plume centerlines with modeled centerlines for the case of pure bubble plumes and the case of bubbly jets with small Q_w in the crossflow of 0.20 m/s

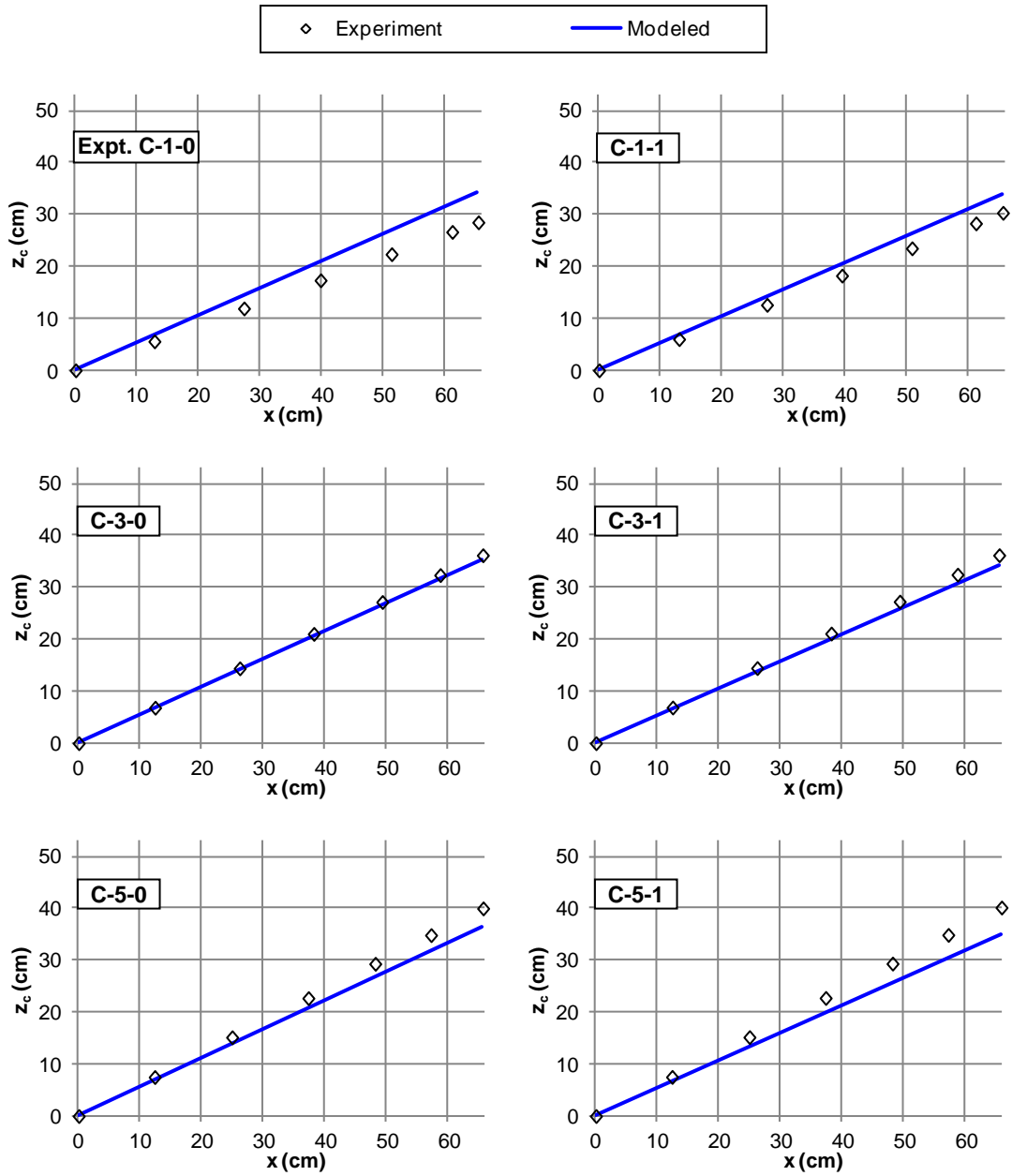


Figure 5-9. Comparison of measured bubble plume centerlines with modeled centerlines for the case of pure bubble plumes and the case of bubbly jets with small Q_w in the crossflow of 0.47 m/s

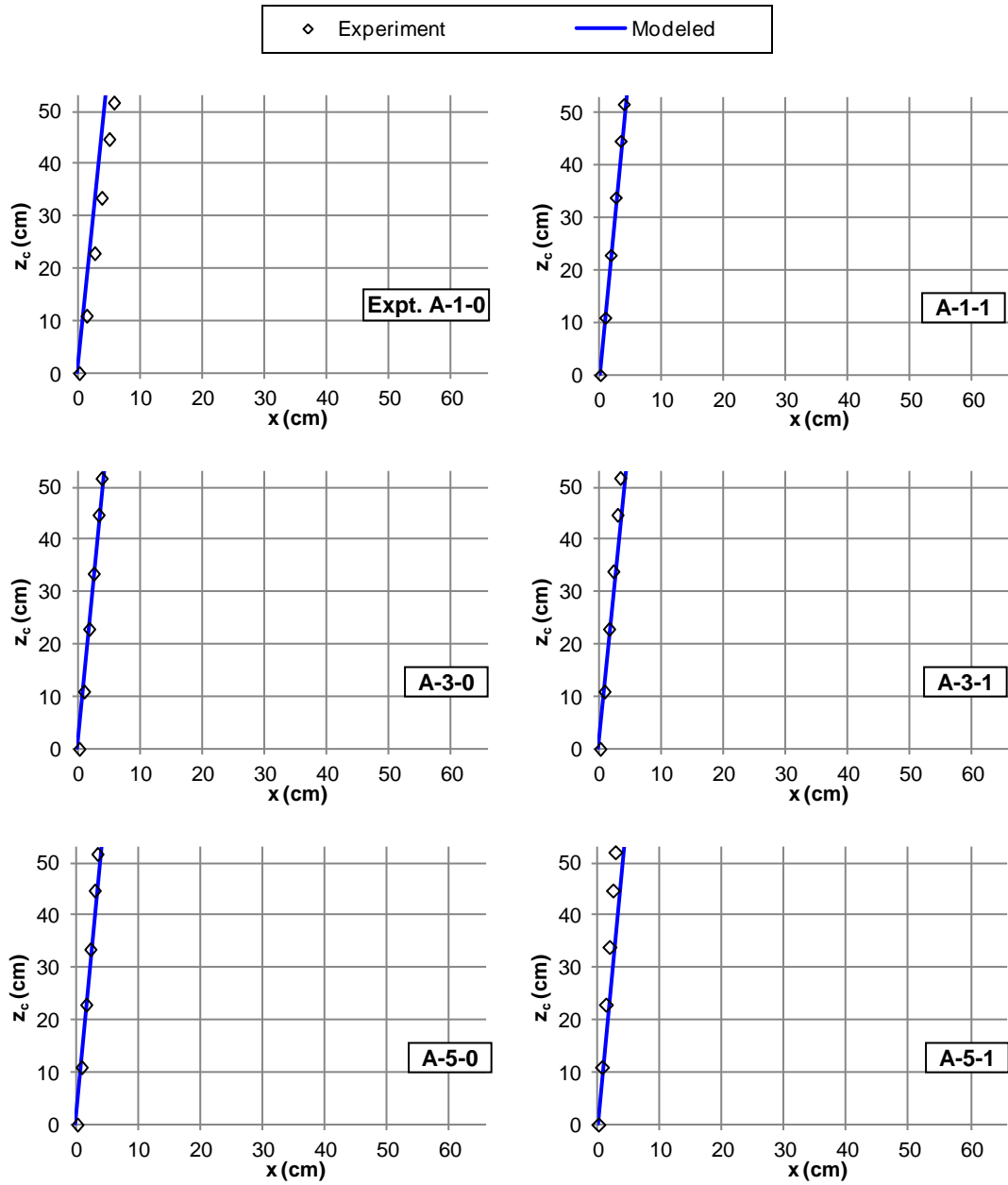


Figure 5-10. Comparison of measured bubble plume centerlines with modeled centerlines for the case of pure bubble plumes and the case of bubbly jets with small Q_w in the crossflow of 0.02 m/s

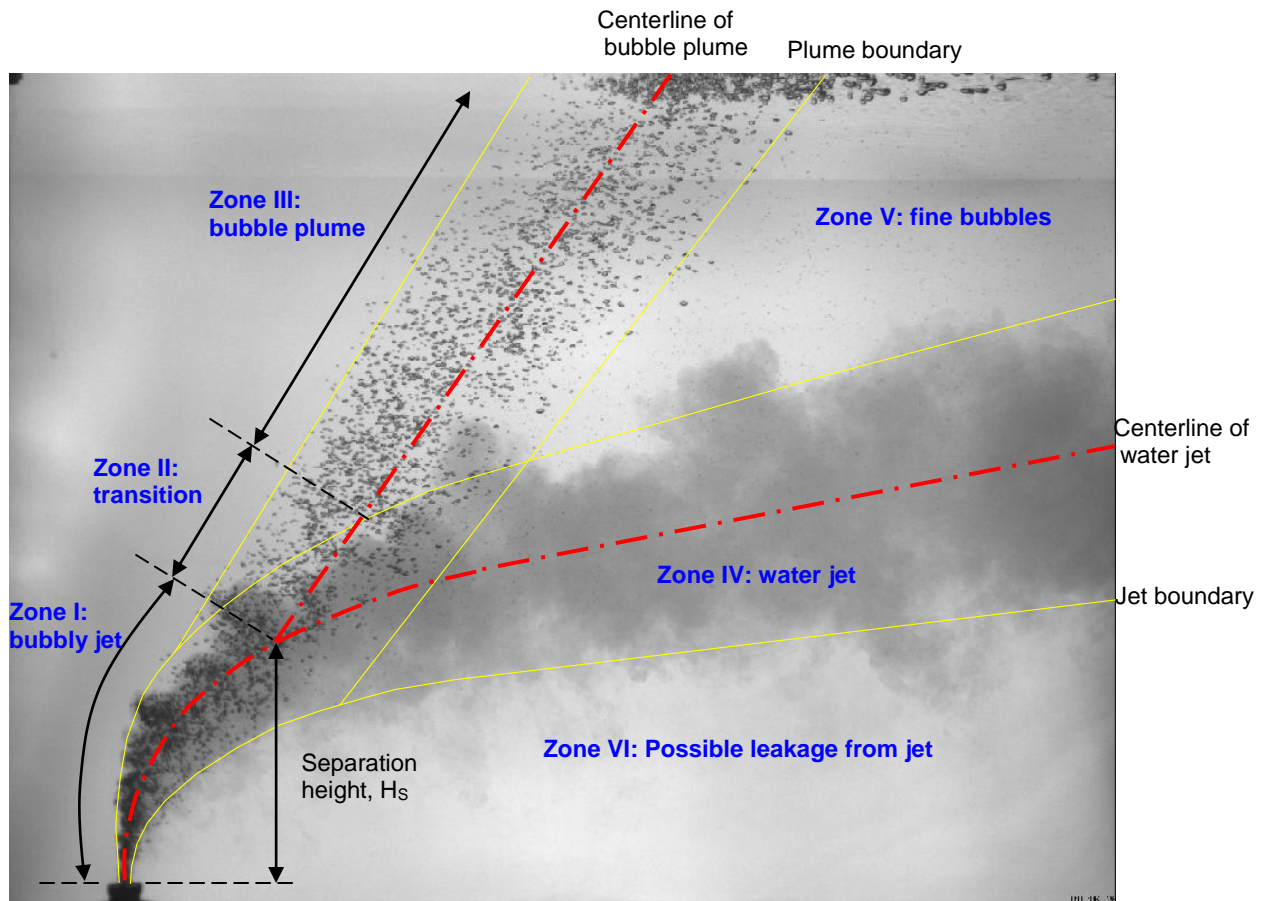


Figure 5-11. Division of six zones for the case of bubbly jets: I, bubbly jet zone where bubbles and water jet are well mixed; II, transition zone where bubble start separating from water jet; III, zone of separated bubble plume; IV, zone of separated water jet; V, a zone where rather tiny bubbles can be observed; VI, a zone where possible leakage from bubbly jet or water jet may occur. Definition of separation height, H_s , is also illustrated. Photo shown is for Experiment B-1-5.

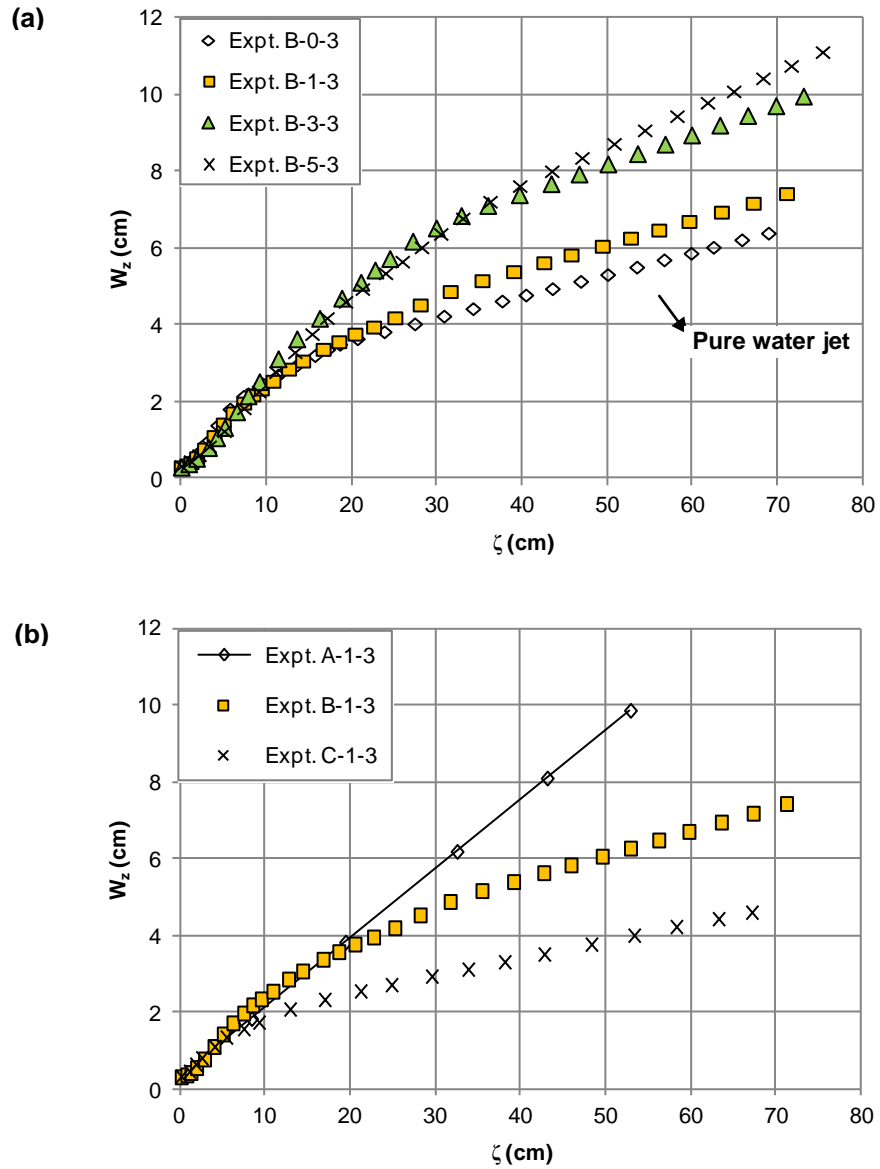


Figure 5-12. (a) Effect of the existence of bubbles on the water jet half-thickness W_z along the jet centerline ζ in the bubbly jet experiments with $Q_w = 3$ LPM and $U = 0.20$ m/s; (b) Effect of the strength of crossflow on W_z in the bubbly jet experiments with $Q_a = 1$ LPM and $Q_w = 3$ LPM

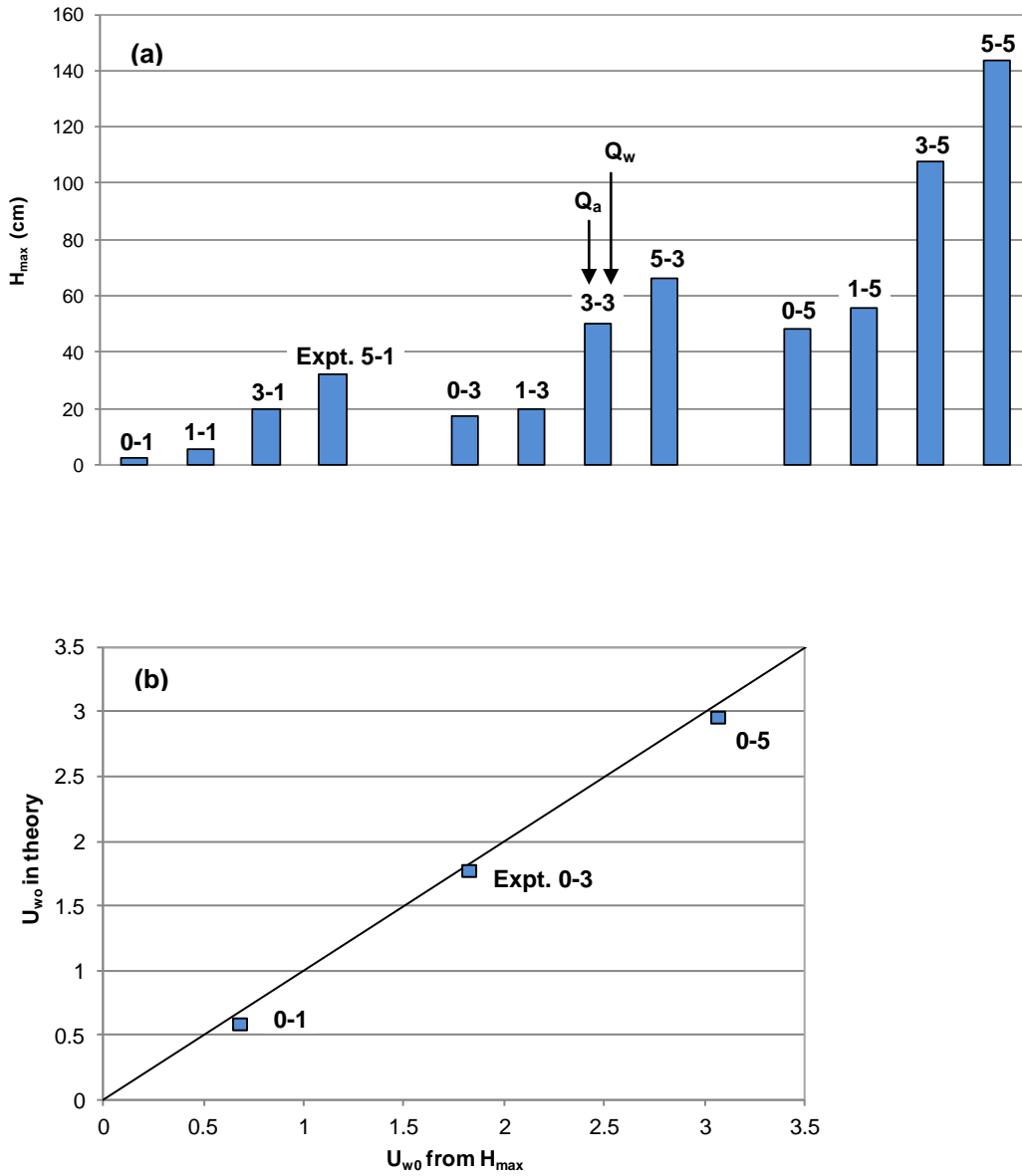


Figure 5-13. (a) Measurement result of max rise height of bubbly jets and pure water jets; (b) comparison of water velocities at the nozzle exit based on max rise height with theoretical values for the case of pure water jets

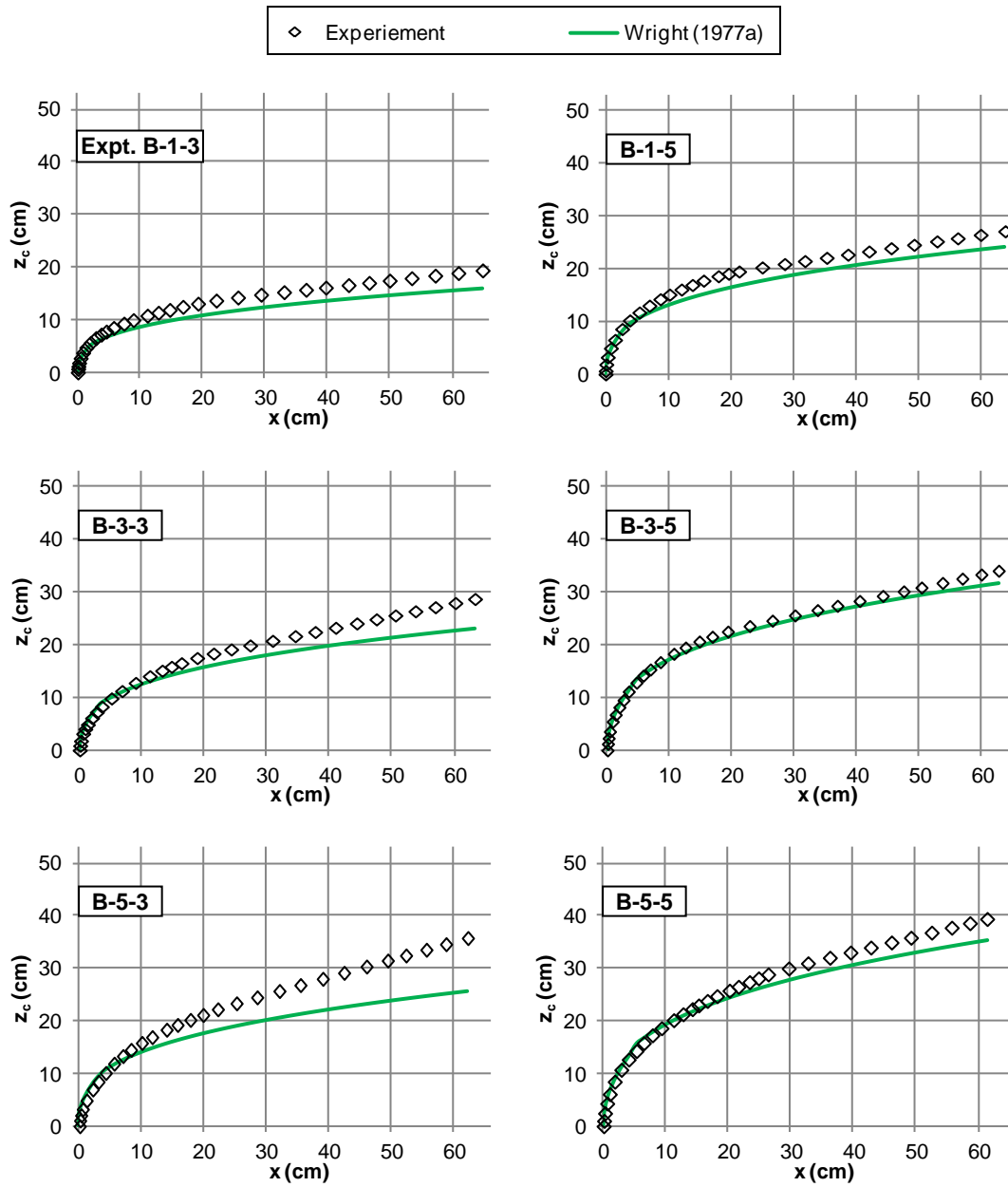


Figure 5-14. Comparison of measurement results of water jet centerlines with modeled centerlines for the case of bubbly jets in the crossflow of 0.20 m/s

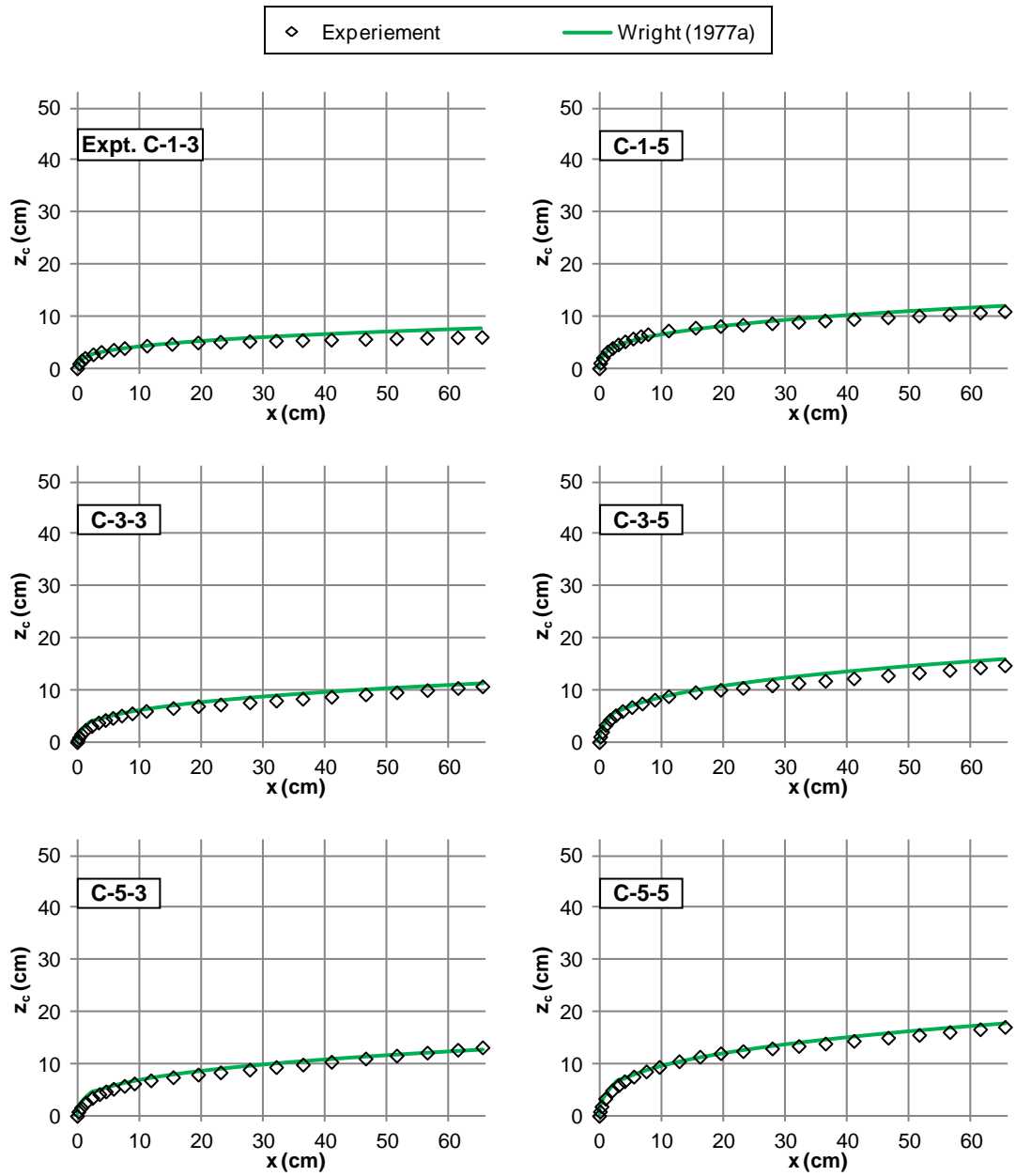


Figure 5-15. Comparison of measurement results of water jet centerlines with modeled centerlines for the case of bubbly jets in the crossflow of 0.47 m/s

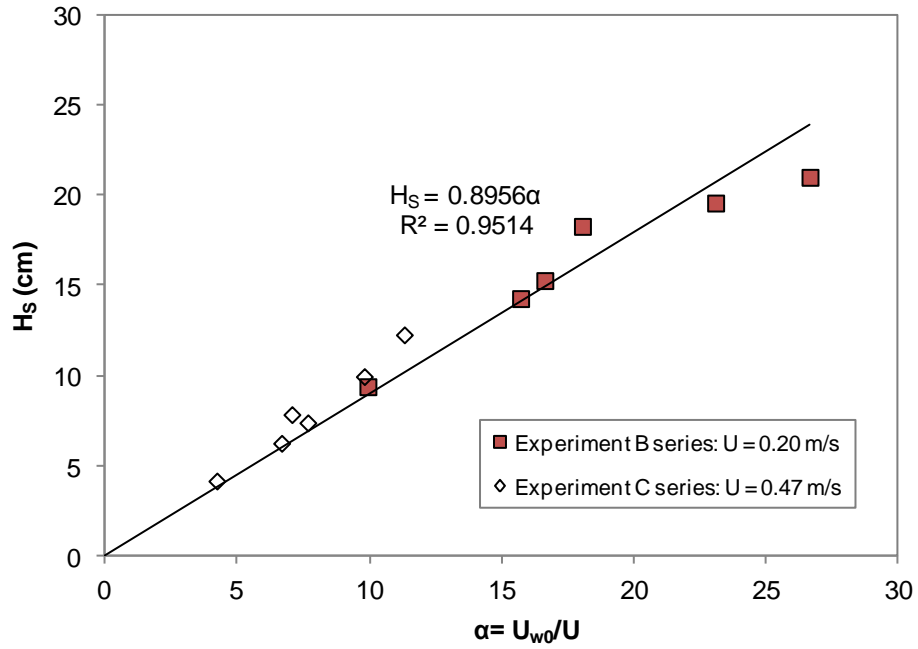


Figure 5-16. Relation of separation height, H_s , with α for bubbly jets

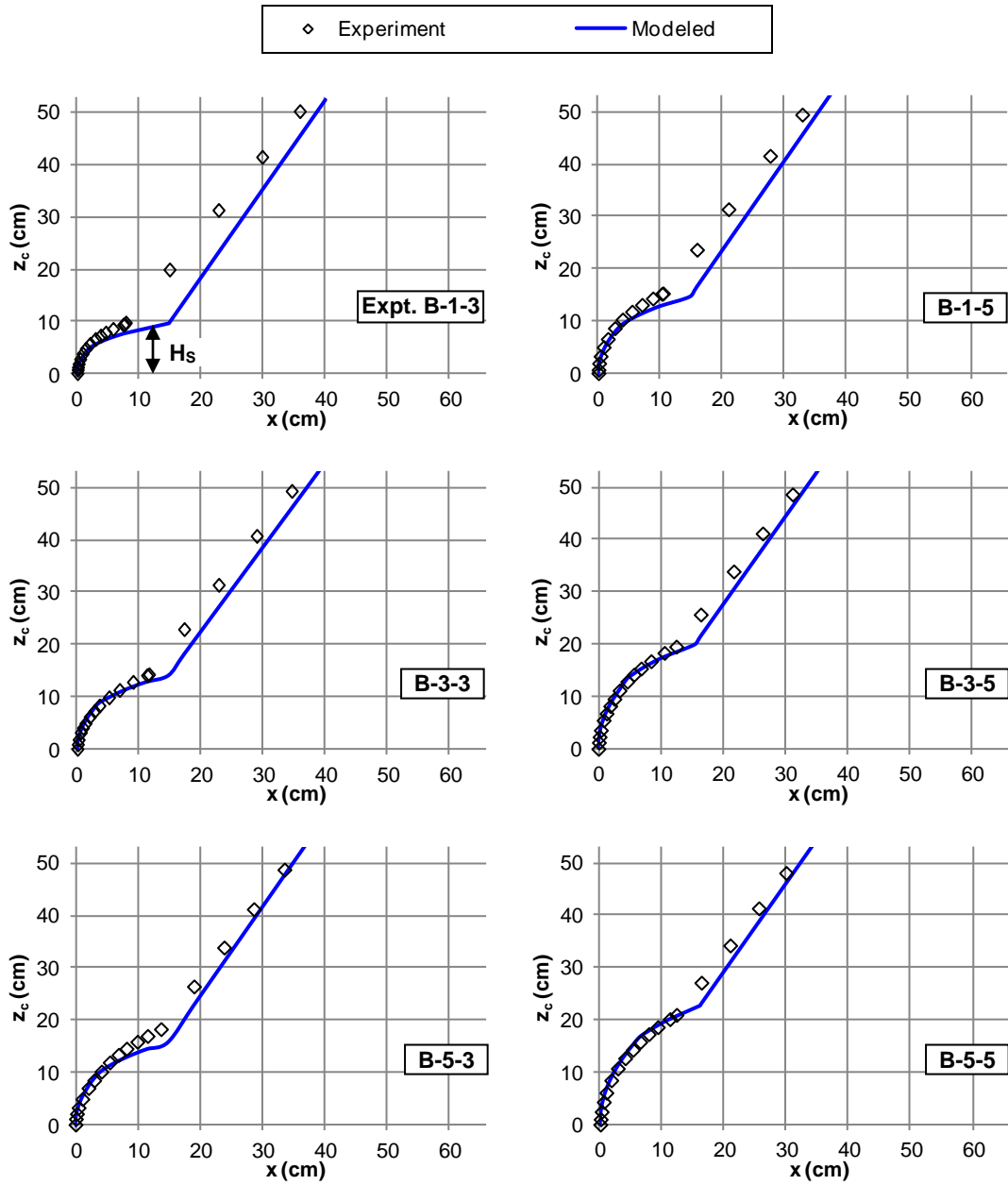


Figure 5-17. Comparison of measurement results of bubble plume centerlines with modeled centerlines for the case of bubbly jets in the crossflow of 0.20 m/s

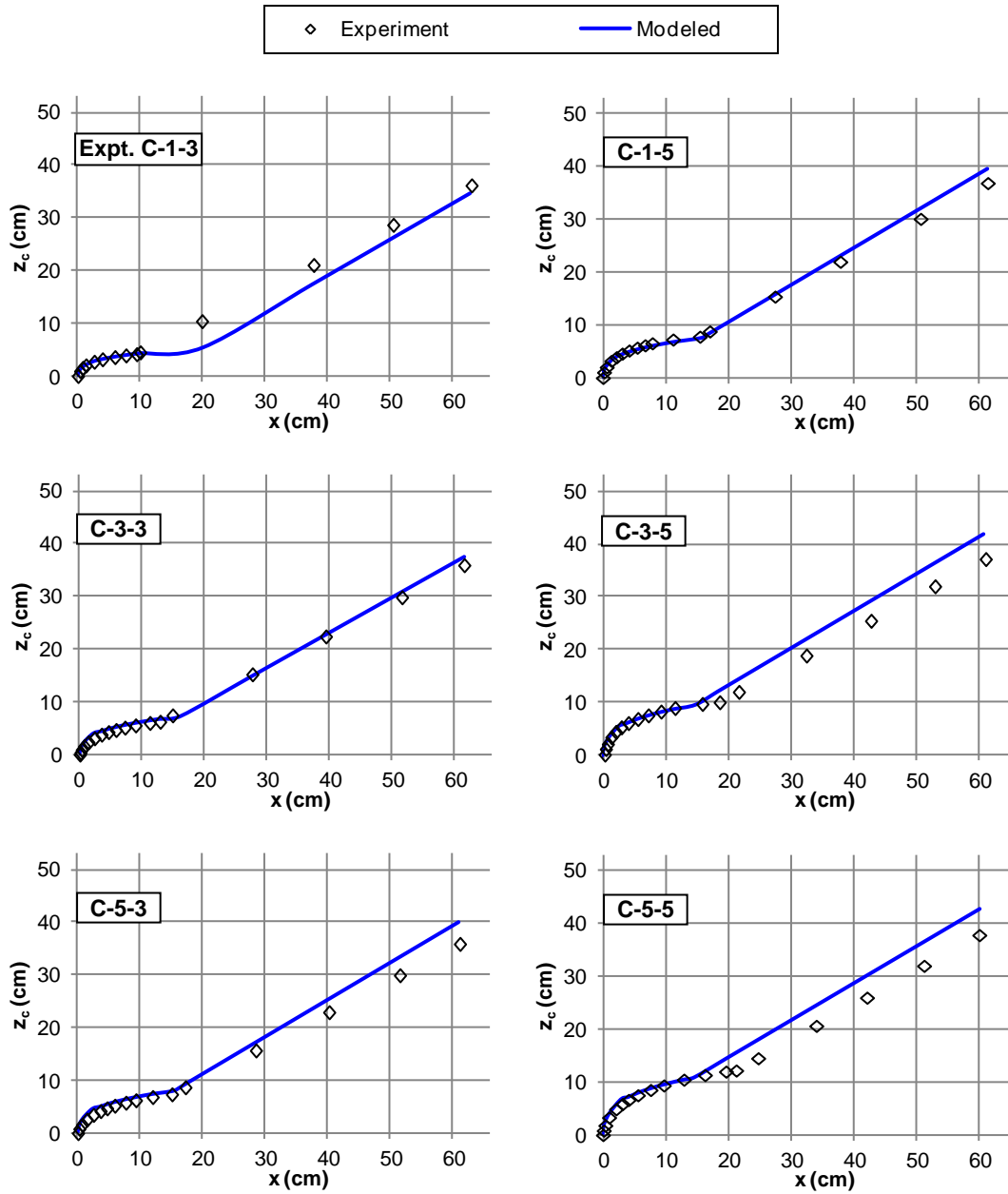


Figure 5-18. Comparison of measurement results of bubble plume centerlines with modeled centerlines for the case of bubbly jets in the crossflow of 0.47 m/s

Chapter 6

Measurements of Bubble Plumes and Bubbly Jets in a Crossflow^{*}

6.1 Introduction

The low dissolved oxygen (DO) problem has also been found to be widespread in ice-covered rivers throughout the arctic and sub-arctic regions of Russia, Alaska, and Canada (Whitfield and McNaughton 1986; Chambers 2000) when river discharge is low and ice cover prevents reaeration at the water surface. This problem is also frequently encountered in polluted water bodies worldwide. The Athabasca River, which is the concerned river in this study, is an important river in northern Alberta, Canada. It not only supplies water to Alberta's pulp and paper mills industry and Canada's oil sand industry and receives effluents from them, but also provides habitat for more than 30 species of fish. In winters, the river's DO has been reported to drop below the chronic guideline of 6.5 mg/L currently used in Alberta, as a result of industrial wastewater discharge and sediment oxygen demand at the river bottom (Lima Neto et al. 2007). Low DO level might severely affect the feeding rate, spawning, hatch and even the survival of fish and benthic macroinvertebrate species (Chambers 2000).

Lima Neto et al. (2007) reported a direct and low-cost remediation measure to increase the DO level in the Athabasca River: injecting pure oxygen or air through the existing effluent diffusers of the pulp and paper mills along the river. Two field oxygen

^{*} The content of this chapter has been edited and submitted as a journal manuscript: Zhang, W.M., and Zhu, D.Z. (2012). "Measurements of bubble plumes and bubbly jets in a crossflow." *J. Fluid Mech.*, submitted.

injection tests have been conducted and the results showed that the absorption rate of the injected oxygen into the river water could reach as high as 50%. The mixture of air (or gas oxygen)-water (effluent) injected via nozzles of the diffuser into the cross-flowing river water is essentially the problem of bubble plumes and bubbly jets in crossflow. A bubble plume is produced by the injection of a gas into a liquid usually via a nozzle or slot, while a bubbly jet is produced by the injection of a gas-liquid mixture into a liquid.

To improve the gas oxygen absorption rate, it is crucial to study the bubble properties in bubble plumes and bubbly jets such as bubble size and velocity. Previously, laboratory experiments have been conducted in stagnant water (see Lima Neto et al. 2008a,b,c,d; Lima Neto 2012). In this study, cross-flowing ambient flow is introduced in a large laboratory flume. By using a double-tip optical fiber probe system, this study provides systematic and detailed measurements on the evolution of bubble properties in bubble plumes and bubbly jets along their trajectories in a crossflow. The measurement results will be useful for the development and validation of computer models on multiphase jets and plumes. This study will improve the understanding on bubble plumes and bubbly jets in crossflow, and thus guide the activities such as artificial aeration and mixing in the environment where crossflow is present (e.g., in rivers).

6.2 Literature Review

In addition to the application of artificial aeration and mixing in low DO water bodies, bubble plumes and bubbly jets are also widely used in lake or reservoir destratification, heat exchanger and industrial reactors, bubble breakwaters, ice prevention in harbors, and assessing the impact of accidental blowout of sub-sea oil and gas wells. Because of the wide applications, bubble plumes and bubbly jets have been under active research

for the last several decades (Milgram 1983; Sun and Faeth 1986a,b; Wüest et al. 1992; Socolofsky and Adams 2002; Sahoo and Luketina 2003; Seol et al. 2007; Norman and Revankar 2011; Fox 2012; many others). However, most of the studies were conducted in stagnant water, and only two studies (i.e., Mannasseh et al. 1998; Socolofsky and Adams 2002) were found by the authors in crossflow while crossflow is typically present in many of applications mentioned above. In this section, studies in stagnant water will be first reviewed as they are the foundation for the studies in crossflow, followed by the limited studies in crossflow.

Compared with bubble plumes, bubbly jets were reported to be able to produce smaller bubbles without the use of porous airstone that is susceptible to clogging (Lima Neto et al. 2008b,d). Thus bubbly jets attract growing interests because of the higher gas transfer efficiency and lower construction and maintenance costs (Fonade et al. 2001; Lima Neto et al. 2008a,b,d). The property of a bubble plume or bubbly jet has been reported to be determined by numerous factors, including gas and liquid flow rates, nozzle types and sizes, injection directions (e.g., horizontal or vertical), ambient flow conditions, container sizes and geometries, liquid impurity and surfactants (Clift et al. 1978; Lima Neto et al. 2008a,b,c,d).

For a bubble plume or bubbly jet in stagnant water, some basic but important features reported in the literature are summarized as follows. First, within a short distance from the nozzle, bubble breakup/coalescence takes place that is rather complicated (Varley 1995). The breakup frequency and the size of resulting daughter bubbles have been reported by Martínez-Bazán et al. (1999a,b), and the breakup mechanisms and theoretical models have been reviewed by Liao and Lucas (2009). Beyond some distance where bubble diameter is smaller than a critical diameter (defined from the equivalence of turbulence stresses to surface tension forces), no

further breakup occurs and the probability distribution function remains frozen (Martínez-Bazán et al. 1999a). Second, the radial range of bubbles only occupy a fraction of a bubble plume or bubbly jet, and the ratio of the radius of the bubble core to the radius of the liquid jet is typically in the range of 0.4 - 1.0 (Milgram 1983; Lima Neto et al. 2008b; Lima Neto 2012). This ratio is expected to increase with the increasing value of plume (or jet) velocity relative to the bubble slip velocity (Milgram 1983). Third, the centerline of the bubble core usually exhibits periodic oscillation with regard to the nozzle centerline (also called the wandering motion) in both confined and unconfined setups (Milgram 1983; Lima Neto et al. 2008c). The oscillation in a frequency of 0.1 - 0.2 Hz that is not present in single-phase jets or plumes, is usually attributed to buoyancy driven instability strengthened by the walls, if any, and/or the coherent flow structure (Lima Neto et al. 2008c). Fourth, in the case of shallow ambient water, when a bubble plume or bubbly jet reaches the water surface, surface jet forms and re-circulating cells exist in both confined and unconfined setups (Fanneløp et al. 1991; Lima Neto et al. 2008c).

Fifth, inside the bubble core, bubbles rise due to buoyancy, and the rise velocity is higher than the liquid velocity. Bubble slip velocity, defined as the relative bubble velocity to the liquid velocity, is usually in the range of 0.2 - 0.8 m/s and mainly depends on bubble diameter (Milgram 1983; Simonnet et al. 2007; Lima Neto et al. 2008b; Lima Neto 2012). Smaller bubbles usually correspond to smaller bubble slip velocity (Sahoo and Luketina 2003; Lima Neto et al. 2008b). Bubble slip velocity in a bubble plume or bubble jet has been reported 2-6 times higher than the rise velocity of an isolated bubble with a similar diameter in stagnant water because of the drag reduction for the trailing bubbles in the wakes of the leading bubbles (Krishna et al. 1999; Ruzicka 2000; Lima Neto et al. 2008b). Sixth, the radial distributions of bubble

velocity and gas void fraction are usually assumed to be Gaussian in the models developed for bubble plumes or bubbly jets (Milgram 1983; Fanneløp et al. 1991; Wüest et al. 1992; Norman and Revankar 2011; Lima Neto 2012). The measurement results of Milgram (1983), Sun and Faeth (1986a,b) and Lima Neto et al. (2008b) confirmed the Gaussian distribution of bubble velocity, while the result of Seol et al. (2007) showed a distribution between Gaussian and top-hat for the bubble velocity. Stanley and Nikitopoulos (1996) stated that the bubble velocity distribution may not be Gaussian because bubble velocity non-linearly depends on bubble size and the size distribution may not be Gaussian. Their measurement on bubble velocity distribution was not Gaussian, but not dramatically different from it. The measurement of Lima Neto et al. (2008b,d) on gas void fraction approximately followed Gaussian.

In the bubble core, bubble size (diameter) is the key parameter that controls the mass transfer (dissolution) of the gas into the liquid. The mass transfer process can be expressed as (Mueller et al. 2002; Lima Neto et al. 2008a):

$$\frac{dC}{dt} = K_L a (C_s - C) \quad (6.1)$$

where K_L is the mass transfer coefficient or the liquid film coefficient; a is the gas-liquid interfacial area per unit volume or specific interfacial area; C_s is the saturation concentration of the dissolved gas in the liquid; and C is the current concentration of the dissolved gas. The two parameters of K_L and a are perhaps mostly controlled by bubble diameter (Sahoo and Luketina 2003; Lima Neto et al. 2008a). Motarjemi and Jameson (1978) reported for oxygen adsorption in water that K_L increased from 0.005 cm/s to the peak value of 0.05 cm/s when bubble diameter d_b increased from 0.2 mm to 2 mm, but further increase of d_b resulted in a slight decrease of K_L (or treated as a constant in Wüest et al. (1992)). Obviously, the specific interfacial area a decreases with the increase of d_b and with the expansion of a bubble plume or bubble jet. In addition,

bubble size determines bubble shape and rise velocity (Clift et al. 1978), and thus the residence time in the liquid that directly affect the amount of gas transferred. Generally, it appears that smaller bubbles promote the gas transfer process. To achieve smaller bubble diameter, single orifice nozzle with smaller nozzle size, multiple-orifice nozzle and porous airstone can be used as reported in Lima Neto et al. (2008a). Moreover, compared to bubble plumes, bubbly jets may produce bubbles with significantly smaller and more uniform sizes as a result of the breakup of large bubbles due to the mean velocity and turbulence of the injected liquid (Lima Neto et al. 2008b,d). Lima Neto et al. (2008b) proposed a criterion for the initiation of air-bubble breakup process in water: a nozzle Reynolds number based on the superficial water velocity is larger than 8,000, or a Weber number based on bubble slip velocity is larger than 25. The optimum bubble size for aeration and mixing has been studied by Motarjemi and Jameson (1978), Wüest et al. (1992), and Sahoo and Luketina (2003; 2006).

With the introduction of bubbles, the properties of plumes or jets may be changed compared to those of single-phase plumes or jets. First, the liquid velocity is enhanced, but its radial distribution remains unchanged. The increase of liquid velocity is because of the less area occupied by the liquid at the nozzle exit and of the possible enhancement of velocity due to bubble wakes. In the confined setups of Kumar et al. (1989) and Iguchi et al. (1997), only a slight increases of liquid velocity were observed, but 2-4 times increases were reported in a large tank by Lima Neto et al. (2008b,d). The experimental results of Sun and Faeth (1986a,b), Kumar et al. (1989), Iguchi et al. (1997), Seol et al. (2007), and Lima Neto et al. (2008b,d), confirmed the Gaussian distribution of liquid velocity at sections up to $72d$ where d is the nozzle diameter, with initial gas volume fraction at the nozzle up to 83% (100% for bubble plume). Second, the existence of bubbles modifies the turbulence level of the liquid phase. At present, no

confirmed conclusion can be made as to the turbulence is enhanced or suppressed because both the two possibilities has been reported (see the summaries of Kumar et al. 1989; Stanley and Nikitopoulos 1996; Rensen et al. 2005; Akhmetbekov et al. 2010). Perhaps the increase or decrease of turbulence relates to the relative size of bubbles compared to turbulent eddies (Kumar et al. 1989), and to different experimental setups and conditions such as different discrete and continuous phases used.

Third, bubbles increase the entrainment of the ambient liquid into bubble plumes or bubbly jets. Based on an experiment in a large tank, Lima Neto et al. (2008b) reported that at 43 cm above the nozzle, the liquid entrainment in bubbly (air-water) jets could be 1.0 - 4.5 times of that in pure water jets with the same water flow rates at the nozzle, and this ratio increased with initial gas volume fraction, and decreased with the nozzle Reynolds number. By using the “entrainment hypothesis” as in single-phase plumes or jets (Morton et al. 1956), the entrainment coefficient for bubble plumes and bubbly jets have been reported in the range of 0.04-0.15 (Milgram 1983; Fanneløp et al. 1991; Seol et al. 2007; Lima Neto et al. 2008b; Lima Neto 2012). Although this is a wide range, most studies reported an entrainment coefficient larger than those in single-phase circular jets or plumes, and the additional entrainment is usually attributed to the wake effect of bubbles. Some empirical relations have been proposed for the entrainment coefficient in bubble plumes or bubbly jets as a function of bubble Froude number (Milgram 1983), of bubble slip velocity, kinematic buoyancy flux and the height above the nozzle (Seol et al. 2007), and of a densimetric Froude number at the nozzle exit (Lima Neto 2012). Forth, the existence of bubbles may affect the spreading rates of bubble plumes or bubbly jets. The spreading rates have been reported to be 0.11-0.14 in the experiments of Lima Neto et al. 2008(b, c), which appears slightly

different from the spreading rate of close to 0.1 for single-phase circular jets or plumes (Rajaratnam 1976; Lee and Chu 2003).

For a bubble plume or bubbly jet in stagnant water, unlike a single-phase plume or jet, no simple and ready-to-use relations have been reported for the axial and radial distributions of bubble properties (e.g., void fraction) and liquid properties (e.g., liquid velocity). The most prevailing way to predict these distributions is the use of integral models, which are established based on modifying the classical integral models for single-phase plumes or jets. The works of Milgram (1983), Fanneløp et al. (1991), Wüest et al. (1992), Socolofsky et al. (2008), Lima Neto (2012) and others have shown some promising aspects of the integral models when compared to experimental results. The drawback of the integral models is that the equations need to be solved numerically, requiring certain mathematic skills. Computational fluid dynamics (CFD) models, widely-used in single-phase jets or plumes, have been also used in bubble plumes or bubbly jets. Among the early attempts in CFD models are Sun and Faeth (1986a,b) and in recent years, CFD modeling studies have been reported more and more frequently, such as direct numerical simulation (DNS) by Esmarelli and Tryggvason (1998; 1999), large eddy simulation (LES) by Dhotre et al. (2009) and Fox (2012) and others. Generally, the mechanisms related with bubbles are not well understood, including the bubble breakup/coalescence, shape change, oscillation, and rotation of bubble itself, the wake effect of bubbles, bubble-bubble interactions, bubble-continuous (liquid) phase interactions, and etc. More high quality measurements on bubble or liquid properties will definitely promote the development and validation of CFD models.

To measure bubble properties, non-intrusive and intrusive methods can be used. The most common non-intrusive method includes the use of photography technique for bubble number, size, void fraction and velocity (Kumar et al. 1989; Krishana et al.

1999), laser Doppler anemometer/velocimetry (LDA or LDV) for mean and fluctuating velocities of both bubbles and liquid phase (Sun and Faeth 1986a,b), and phase Doppler anemometer/velocimetry (PDA or PDV) for bubble size and velocity (Stanley and Nikitopoulos 1996). Other reported non-intrusive methods are the use of particle image velocimetry (PIV) and particle tracking velocimetry (PTV) with image processing technique for the velocity field of both bubbles and liquid phase (Seol et al. 2007), and planar fluorescence for bubble imaging (PFBI) for bubble size and velocity (Akhmetbekov et al. 2010), and others. The non-intrusive techniques can be only used for the case of low gas void fractions (typically a few percents). For the case of higher gas void fractions, intrusive method is much more reliable (Chanson 2002; Chang et al. 2003). The most common intrusive techniques are the use of the optical fiber probes (Boes and Hager 2003; Chang et al. 2003; Kiambi et al. 2003; Murzyn et al. 2005; Chaumat et al. 2005; Simonnet et al. 2007; Rojas and Loewen 2007; Lima Neto 2008a,b,c,d) and conductivity/resistivity probes (Chanson 2002). From these probes, local information at a measurement point can be obtained, including gas void fraction, bubble number, frequency, size, velocity and specific interfacial area. To obtain a whole-picture, measurement needs to be conducted at many points, which is time-consuming. To measure the liquid phase velocity, bubbles significantly adds the difficulty. The use of LDA (or LDV) appears to be the most widely used technique (Sun and Faeth 1986a,b; Kumar et al. 1989; Simonnet et al. 2007), and this technique has been reported by Simonnet et al. (2007) in a bubble plume with a local gas void fraction up to 35%. When gas void fraction is low (a few percents), mini propeller anemometers (Milgram 1983; Fanneløp et al. 1999; Lima Neto 2008a), PIV (Seol et al. 2007), and hot film anemometers (Rensen et al. 2005) have also been used to measure the liquid

velocity. A more complete review on the measurement techniques in gas-liquid flows can be found in Boyer et al. (2002).

Above is a brief review of the studies on bubble plumes and bubbly jets in stagnant ambient fluids. So far, rather limited studies have been reported in crossflow, although single-phase jets or plumes in crossflow have been reported by Rajaratnam (1976), Lee and Chu (2003) and others. Manasseh et al. (1998) observed air bubble trajectory in cross-flowing water, and reported that, for bubbles with a diameter of approximately 4 mm and bubbling rate of 44 Hz (numbers of bubbles per second) at the nozzle, bubble trajectory in plan view may become two sinusoidal paths or multiple paths, which appeared to depend on the crossflow velocity. In side view, bubble trajectory approximated a linear line in different crossflow velocities, but with a different angle to the crossflow velocity. Socolofsky and Adams (2002) reported laboratory experiments of multi-phase plumes produced by injecting air or a mixture of air and liquid (oil or alcohol) in uniform cross-flowing water. They observed the separation of dispersed phase (bubbles) from the continuous phase (entrained ambient fluid) or other dispersed phases (oil or alcohol) at certain height due to the buoyancy of the bubbles, and proposed an empirical relation for the separation height. Above this height, the trajectory of bubble column was found to generally follow a linear line, which was governed by the vector sum of bubble slip velocity and cross-flowing velocity. The separated continuous-phase plume behaved like a momentum jet, and the momentum was originated from the entrainment and acceleration of the multiphase plume before the separation. A similar separation of air bubble plumes from water jets has been also observed by Lima Neto et al. (2008d) in an experiment of horizontally injected bubbly jets in stagnant water.

From this literature review, it is clear that bubble plumes and bubbly jets are being actively studied in stagnant water. More studies are needed to further understand both bubble and liquid properties. Studies in crossflow are quite limited. To the authors' knowledge, no experimental study has been reported on the investigation of bubble properties in crossflow by using the techniques such as the optical fiber probes, which is the main focus of this study. In this study, at the crossflow of 0.20 m/s, more than 2,070 points at five sections ($20d$ - $100d$) were systematically measured on bubble properties by using a double tip optical fiber probe system for twelve bubble plumes and bubbly jets.

6.3 Experimental Setup and Procedure

6.3.1 Apparatus and Procedure

The experiments were conducted in a large tilting flume of 25 m \times 1.2 m \times 0.8 m (L \times W \times H) in the T. Blench Hydraulics Laboratory at the University of Alberta. The flume is made of glass and smooth fiberglass. Honeycomb flow straightener in the feed plenum is used to uniformly distribute water to the flume. The water depth in the flume can be controlled with a tailgate. The water is re-circulated by a pump between the flume and an underground sump of about 300 m³. In this study, the flume was kept at a slope of zero (horizontal), and was operated at a discharge of 155.8 ± 0.5 L/s and a water depth of 65 ± 0.1 cm, i.e., at a cross-sectional average velocity of approximately 0.20 m/s.

The experimental apparatus were built at about 14 m downstream of the flume entrance (see Fig. 6-1). A nozzle was set vertically in the middle of the flume transect. The nozzle exit, with a diameter of 6 mm, was 12 cm above the flume bed. This distance was determined from a preliminary Acoustic Doppler Velocimeter (ADV) test to exclude the effect of bed roughness and thus to have a more uniform vertical

distribution of ambient velocity in the measurement zone. The ADV test also showed that the side walls of the flume only had a significant effect on transverse distribution of ambient velocity within 20 cm from the each side wall, which is beyond the measurement zone (± 12.5 cm from the middle of the flume). Before exiting from the nozzle, air and water were completely mixed in a Venturi injector (Model 384, Mazzei Injector Corp.). The air was supplied from a gas line of the laboratory, and a pressure-regulating valve was used to keep the air at 1 atm and constant flow rates. The air and water discharges were controlled with rotameters. In this study, the air discharge Q_a was set to be 1, 3, and 5 Liters per minute (LPM), and the water discharge Q_w was 0, 1, 3, and 5 LPM. The fluctuations of the air discharge and water discharge were less than 2%.

To visualize the trajectories of bubbly jets, dye was injected into the water pipeline upstream of the water pump. Images of the trajectories were captured with a high resolution charge coupled device (CCD) camera (TM-1040 CL, Pulnix America Inc.), which was controlled by a computer frame grabber system (Streams 5, IO Industries Inc.). The frame rate was set to be 30 frames per second, and the exposure time 1/2000 seconds. To clearly capture images of individual bubbles, a 8-48 mm Pentax TV zoom lens was used. The background light was provided by 2×1000 watts halogen lamps and diffused in a softbox of 1.2 m × 0.9 m (L×H).

Bubble properties were measured by using a commercial double-tip optical fiber probe system (RBI Instruments Inc.). Similar RBI optical probe system have been used by Boes and Hager (2003), Kiambi et al. (2003), Murzyn et al. 2005, Chaumat et al. (2005), Simonnet et al. (2007) and Lima Neto et al. (2008a,b,d). The system consists of an optical probe, an electronic unit, an acquisition box, and user interface software. The principal of phase detection by the system is as follows: an optoelectronic module emits infrared light through fiber-optic cables to two sapphire tips of the probe; the sensitive

surface of the cone-shaped tip behaves as a Descartes prism, i.e., the emitted light is refracted when the tip is surrounded with liquid and reflected back when surrounded with gas; the reflected light is converted with a photo-sensitive diode to electronic signal, which is then amplified and detected through a threshold technique. From the two-state signal corresponding to air or water at each tip, bubble frequency (or number) f and gas void fraction α can be obtained. By cross-correlating the signals from the two tips, bubble traveling time from one tip to the other can be estimated, and bubble velocity u_b can be calculated because the distance between the tips is fixed. Bubble specific interfacial area, a , and bubble mean Sauter diameter, d_b , are calculated by the optical probe system, respectively, as:

$$a = 4f / u_b \quad (6.2)$$

$$d_b = 3\alpha u_b / 2f \quad (6.3)$$

In this study, the distance between the tips measured to be 1.17 ± 0.01 mm. The end of the tips was approximately $30 \mu\text{m}$. The sampling rate of the signals could reach up to 1 MHz. An oscilloscope (TDS 210, Tektronix Inc.) was used to visualize the electronic signals to ensure that the optical probe system worked properly during the experiments. The optical probe was positioned with a computer-controlled traverse system (NF90, Velmex Inc.) in the vertical and transverse directions, and positioned manually in the longitudinal direction. The positioning error of the traverse system was tested to be less than 0.1 mm, and the error in the longitudinal direction was estimated to be approximately 0.1-0.2 mm.

In this study, a total of 12 experimental scenarios were investigated (see Table 6-1), with initial gas volume fraction at the nozzle α_0 ranging from 0.17-1. The optical probe was adjusted to be aligned with the angle of a bubble plume based on the CCD images taken before the experiments. In each scenario, five cross-sections at distances

of $20d$, $40d$, $60d$, $80d$, and $100d$ along the centerline trajectory ζ of bubble plumes from the nozzle exit were selected for measurement, where d is the diameter at the nozzle exit. The first section was chosen to be $20d$ to try to avoid the complex bubble breakup/coalescence near the nozzle (Varley 1995; Martínez-Bazán et al. 1999a). At each section, measurements were conducted along a “cross” (see Fig. 6-1): first, measurements were taken in the η direction in the vertical plane parallel to the side walls in the middle of the flume, where η is perpendicular to the plume centerline trajectory ζ and points downwards; then, measurements were carried out in the transverse y direction along the point that had the peak value of void fraction in the η direction. For measurements in either the η or y direction, 12-21 points were selected within the bubble plume range. To have an overall understanding of the distribution of bubble properties at a whole cross-section, two cross-sections were measured at a mesh of $1\text{ cm} \times 1.25\text{ cm}$, that is, Section $80d$ in Expt. 3-0 (in this study, the experiment I.D. is composed of two numbers: the first and second numbers represent the air and water flow rates in the unit of LPM in the nozzle, i.e., Q_a and Q_w respectively) and Section $80d$ in Expt. 3-3. The two sections were selected for the cases of bubble plumes and bubbly jets, respectively, without any significant influence of the initial jet momentum and the free water surface in the flume.

In this study, a total of 2,070 points were measured with a measurement period of 3 minutes for each point. If the measurement values at a point appeared suspicious, measurement would be repeated. Thus a total of 2,425 times measurements were conducted. The 60 points that had peak gas void fractions measured in the η direction were also measured in the y direction at different times. On average, the relative differences between the two measurements at one location were only $-4.2 \pm 6.6\%$ for bubble numbers, $-4.7 \pm 6.6\%$ for void fraction, $0.6 \pm 3.9\%$ for bubble velocity, $-4.6 \pm 6.8\%$

for bubble interfacial area, and -0.13 ± 5.6 % for bubble diameter. This suggested a high repeatability of the experiments in this study. The differences mainly originated from the slight differences in the control of the flow discharge in the flume and air and water discharges at the nozzle each day, which is inevitable.

6.3.2 Calibration of the Optical Probe System

The optical probe system was calibrated in gas void fraction, bubble size and bubble velocity before the experiments. Based on Chang et al. (2003) and Lima Neto et al. (2008a), the calibration of gas void fraction was conducted in a PVC cylinder (see Fig. 6-2). Air from the laboratory gas line was diffused via a porous airstone, and the air flow rate was controlled with a rotameter. The global gas void fraction in the cylinder can be calculated to be $\alpha_{global} = h_0/(h_0+h_i)$, where h_0 is the water depth before air injection; and h_i is the increase of the water depth due to the existence of bubbles. The local void fraction α_{local} at the measurement point from the optical probe was assumed to be the same as the global void fraction because of the use of an airstone. Chang et al. (2003) further adjusted the value of α_{local} considering the change of hydrostatic pressure when bubbles rose. Because the relative influence of pressure change on α_{local} is less than a few percent and other complex factors might also affect the value of α_{local} , e.g., bubble breakup/coalescence, bubble wakes, bubble shape distortion when pierced by the tips of the optical probe, boundary effect of the cylinder and etc., the adjustment of α_{local} due to change of hydrostatic pressure was simply neglected in this calibration.

The comparison of gas void fractions measured with the optical probe with those from the bubble cylinder is shown in Fig. 6-3(a). Generally, the optical probe is rather accurate in terms of gas void fraction. In the testing range of gas void fraction $\alpha \leq 20\%$ (the maximum $\alpha = 17.2\%$ in this study), the optical probe underestimates on

average only by $-2.2 \pm 3.3\%$. The relative error level obtained in this study is consistent with the relative error of -3% reported by Chang et al. (2003) and -11% by Lima Neto et al. (2008a) both of whom used the same calibration method as in this study, -(6-14)% by Kiambi et al. (2003) who compared the optical probe measurement with image processing, and 12% by Simonnet et al. (2007) who compared the results from an optical probe with those from pressure probes. Notice that both the two tips of the optical probe can independently measure the gas void fraction, and the values in Fig. 6-3(a) and the following figures are from the first (lower) tip. In this study, the second (higher) tip was found to detect 0-30% fewer bubbles than the first one. This is a common problem in intrusive probes and is in agreement with the result of 24-32% fewer bubbles detected by the second tip in Kiambi et al. (2003) because of the interference of the first tip on bubble shapes and trajectories.

The calibration of bubble size and bubble velocity was performed in the flume (see Fig. 6-1) with a water depth of 65 cm and an ambient velocity of only 2 cm/s. The ambient flow was controlled to be as close to stagnant water as possible to avoid the effect of crossflow on bubble trajectories. Air of low flow rates was injected through the nozzle to produce dilute bubble plumes. Individual bubbles passing by the optical probes were captured by the CCD camera. When bubbles were dilute enough, each bubble pierced by the tips of the probe could be identified by comparing image recording time and signal recording time from the probe system; otherwise, some judgments might be required by analyzing previous and succeeding images. For the identified bubbles in the images, the equivalent bubble diameter (diameter of the sphere of equivalent projected area) and bubble velocity were determined and compared to those from the optical probe.

The calibration results of bubble diameter are shown in Fig. 6-3(b). From Fig. 6-3(b), in the testing range of $d_b = 2-12$ mm, the optical probe system underestimates bubble diameter on average by 26.6%, which is similar to the 12-27% difference obtained by Chaumat et al. (2005) and the 10% difference by Lima Neto (2008a). The large difference between the probe measurement and image processing is caused by the assumption used in Eq. (6.3): bubbles rise rectilinearly and are spherical. This assumption is only approximately valid when bubbles are small. From Fig. 6-3(b), at a bubble diameter of 2.3 mm, the probe measurement only differs 3% compared to that from the image processing. Larger bubbles tend to be ellipsoidal and the following equation has been used to account for the non-sphericity of bubbles (Moursali et al. 1995; Simonnet et al. 2007):

$$d_b = \chi^{2/3} 3\alpha u_b / 2f \quad (6.4)$$

where χ is the major to minor axis ratio. In this study, the χ value was found to be 1.1 for $d_b = 2.3$ mm, and 1.5-2 for $d_b = 4-12$ mm. With the correction in Eq. (6.4), for large bubbles, measured bubble diameters only differs approximately 6% from the image processing, much smaller than the 27% difference before the correction as shown in Fig. 6-3(b).

From the calibration, in this study, if the bubble diameter measured from the optical probe system $d_b \leq 4$ mm, the measurement value were used directly; however, if $d_b > 4$ mm, Eq. (6.4) was used to correct the d_b values. To simply the correction, an average value of $\chi = 1.78$ was used, close to the value of $\chi = 1.67$ for bubbles in a similar range of 4-10 mm in Simonnet et al. (2007). The constant χ value would produce a diameter difference of less than 7% between the probe measurement and image processing.

Fig. 6-3(c) shows the calibration results of bubble velocity. In the testing range of $u_b = 0-0.6$ m/s, the optical probe system overestimated the bubble velocity on average by 9%, compared to the velocity obtained from image processing. The present result is similar to the calibration results of 5% overestimation reported in Kiambi et al. (2003), 5-6% difference in Chang et al. (2003), 10-30% overestimation in Chaumat et al. (2005), approximately 15% uncertainty in Simonnet et al. (2007), and 29% overestimation in Lima Neto (2008a).

6.4 Results and Analysis

Photos of the bubble plumes or bubbly jets in all the 12 experimental conditions are shown in Fig. 6-4. As can be clearly observed, bubble properties (at least bubble size and shape) of pure bubble plumes ($Q_w = 0$ LPM) are close to those of bubbly jets with small Q_w (1 LPM), and bubble properties of bubbly jets with large Q_w (3 or 5 LPM) are close to each other. The bubble size in the first case is much larger than that in the second case, which will be analyzed later.

For a bubble plume, the trajectory approximates a quasi-line, as observed in Manasseh et al. (1998) and Socolofsky and Adams (2002). The quasi-linear trajectory is controlled by the vector sum of ambient crossflow and bubble rise velocity (Socolofsky and Adams 2002). For a bubbly jet, it is clear that near the nozzle, its trajectory is vertically upward because the initial jet momentum is dominant over the strength of crossflow; away from the nozzle ($10d-20d$), there is a short transition region where the bubbly jet trajectory is bent over by the crossflow as the jet momentum decays along the trajectory; further away from the nozzle (beyond $20d$), the trajectory of bubble column is close to quasi-linear, similar to the trajectory of a bubble plume, suggesting that the residue of jet momentum is no longer important. An interesting phenomenon for a

bubbly jet in crossflow is the separation of the discrete phase (bubbles) from the continuous phase (water jet) (see Fig. 6-4) as reported by Socolofsky and Adams (2002), which is caused by the buoyancy of the discrete phase. The trajectories of pure water jets, bubble plumes and bubbly jets at an ambient velocity of 0.20 m/s in this study, as well as at other two ambient velocities (0.02 and 0.47 m/s) were studied systematically in Chapter 5.

Chapter 6 focuses the measurement results from the optical probe system at the five Sections (20d - 100d as shown in Fig. 6-4) along the trajectory of the 12 bubble plumes and bubbly jets. A typical example of time series of gas void fraction and bubble velocity obtained from the optical probe system is present in Fig. 6-5. From Fig. 6-5, a measurement period of 3 minutes is sufficient to produce reliable time-averaged values. This period is within the measurement period of 1-5 minutes for similar optical probes in Chang et al. (2003), Chaumat et al. (2005) and Lima Neto et al. (2008a,b,d). An example of bubble size distribution at a measurement point is shown in Fig. 6-6. As shown, the size distribution resembles lognormal curve, close to those reported by Varley (1995) and Lima Neto et al. (2008a,b,d) for bubble plumes or bubbly jets in stagnant water. Moreover from Fig. 6-6, with the increase of water discharge at the nozzle, both bubble diameter and its range decrease, which are also similar to those found in Lima Neto et al. (2008a,b,d). The change of bubble diameter with water discharge can be also seen clearly in Table 6-1.

6.4.1 Gas Void Fraction

The measurement results of gas void fraction, α , in the η and y directions are shown in Figs. 6-7 and 6-8, respectively. At one location, measurements might be conducted more than once, and all the measurement results are shown in the figures to reflect the

level of data fluctuation. The measurement results are then non-dimensionalized and fitted with the Gaussian distribution by using the method of least squares, as shown in Figs. 6-9 and 6-10:

$$\alpha/\alpha_{\max} = \exp\left[-0.693(\eta/b_t)^2\right] \quad \text{or} \quad \alpha/\alpha_{\max} = \exp\left[-0.693(y/b_w)^2\right] \quad (6.5)$$

where α_{\max} is the maximum gas void fraction; b_t and b_w are half-thickness (in the η direction) and half-width (in the y direction) of a bubble plume or bubbly jet, respectively. The half-thickness or half-width here is defined similarly as in single-phase jets or plumes (Rajaratnam 1976): the location where $\alpha/\alpha_{\max} = 50\%$. Note that in Figs. 6-7, 6-8 and the following figures, the location of the centerline trajectory of a bubble plume or bubbly jet, i.e., $\eta = 0$ and $y = 0$, was determined (for $\eta = 0$) or adjusted (for $y = 0$, typically a few millimeters adjustment from the physical location of half of the flume width) from fitting the measurement results of α with the Gaussian distribution. The adjustment for $y = 0$ was done because jets from the nozzle would be inclined at an angle of approximate 1.3° from the middle of the flume to the right bank (looking downstream) due to the accuracy in the nozzle configuration.

Fig. 6-7 or 6-8 shows that with the increase of traveling distance from the nozzle, the peak value of α becomes smaller and the distribution of α becomes wider, similar to the concentration evolution in single-phase jets or plumes (Rajaratnam 1976; Lee and Chu 2003). Note that at Section 100d in several experiments such as Expts 5-0, 5-1, 5-3 and 5-5, measurements stopped at locations close to the water surface. Due to the hindering effect of water surface on the escape of bubbles into air, the values of α at these points may appear higher than the values without the water surface effect.

The experimental results indicate that α value increases with the increase of Q_a , while it decreases with the increase of Q_w . With the increase of Q_a , e.g., from Expt. 1-0 to Expt. 3-0 and further to Expt. 5-0, both bubble frequency and bubble size increases

(see Figs. 6-11 and 6-16), resulting α_{\max} value at Section 20*d* increases from 8.4% to 14.6% and further to 17.2%. With the increase of Q_w , large bubbles will break into smaller bubbles due to the mean water velocity and turbulence of the water jet (Lima Neto et al. 2008b,d). Although the total number of bubbles increases, bubbles are also diffused more widely (see Figs. 6-8 and 6-20), thus the local change of bubble frequency might be small (see Fig. 6-11). Overall, bubble size decreases significantly while the change of bubble frequency is small, thus α value decreases. At Section 20*d* in particular, with a larger Q_w , bubble frequency might increase significantly (see Expts. 3-3 and 3-5 in Fig. 6-11) because the length of potential core increases with the ratio of jet exit velocity to ambient velocity in crossflow (Rajaratnam 1976). Thus at Section 20*d*, although bubble diameter decreases, α might still be comparable to that with smaller Q_w (see Expts. 3-3 and 3-5 in Fig. 6-7). It is interesting to note that with the increase of Q_w , the gaps of α among Sections 40*d*, 60*d*, 80*d*, and 100*d* become smaller. This indicates that the water discharge at the nozzle helps bubbles get diffused wider and reach a stable state faster.

By comparing Figs. 6-7 with 6-8, it can be observed that at $Q_w = 0$ or 1 LPM, the spreading range of α is larger in the η direction than that in the y direction (also see Fig. 6-20). This is because for a bubble plume or bubbly jet with small Q_w , buoyancy exerts additional force on bubbles to spread wider in the η direction, while no such forces exist in the y direction. On the contrary, for a bubbly jet with $Q_w = 3$ or 5 LPM, the spreading range is smaller in the η direction than that in the y direction (also see Fig. 6-20). The comparison of the spreading range of gas void fraction in the η direction and that in the y direction can be also clearly seen from Fig. 6-31.

As shown in Figs. 6-9 and 6-10, the distribution of α generally follows the Gaussian distribution at different sections in both the η and y directions in all the

experiments. The present Gaussian distribution in crossflow is similar to the approximated Gaussian distribution of α for bubbly jets in stagnant water reported by Lima Neto et al. (2008b,d), suggesting no obvious effect of crossflow on the distribution of α . The present results are also similar to the approximated Gaussian distribution of time-averaged concentration in single-phase jets in crossflow reported by Smith and Mungal (1998) and Lee and Chu (2003). And the reason for such similarity might be that the value of α in the present study is low, less than 18% and mostly in the range of 0.5-10%.

From Fig. 6-10, it is interesting to point out that at $Q_w = 3$ or 5 LPM, the measurement points in the y direction appear to be slightly flatter than the Gaussian distribution, and the points near the plume centerline are more close to the top-hat distribution. The flatter distribution in the y direction at a larger value of Q_w perhaps is related to the fact that at a larger Q_w , the separation of bubble column from water jet is lagged (see Fig. 6-4) and thus the suppressing effect of crossflow on the spread of bubbly jets in the η direction is more obvious (e.g., see Expts. 3-1 and 3-3 in Fig. 6-7), resulting in a wider spread of bubbly jets in the y direction (see Figs. 6-8 and 6-20). Similar wider spread in the y direction has been also reported in single-phase jets in crossflow (Lee and Chu 2003).

6.4.2 Bubble Frequency

The measurement results of bubble frequency, f , in the η and y directions are shown in Figs. 6-11 and 6-12. Similar as for gas void fraction, the distribution of f generally follows the Gaussian distribution in both the η and y directions. Also similarly, in the y direction, Fig. 6-12 shows the distribution of f follows a distribution between the Gaussian and top-hat in the experiments with $Q_w = 3$ or 5 LPM.

With the increase of Q_a , f increases as expected. For instance, from Expt. 1-0 to Expt. 3-0 and further to Expt. 5-0, the maximum value of f at Section 20d increases from 7.3 Hz to 12.5 Hz and further to 13.6 Hz. While with the increase of Q_w , more bubbles are produced due to the breakup of large bubbles; meanwhile, the spread of a bubbly jet is enhanced; as a result f might increase (e.g., see Expts. 3-1 and 3-3 in Fig. 6-11), or decrease or be comparable as before (e.g., see Expts. 3-0 and 3-1). At Section 20d, with the increase of Q_w , f increases significantly and reaches a value of up to 80 Hz (i.e., 14,400 bubbles detected in 3 minutes) in Expt. 5-5. Comparing Fig. 6-11 with Fig. 6-12, the same conclusion can be drawn on the spread of bubble plumes or bubbly jets as that from gas void fraction: at $Q_w = 0$ or 1 LPM, the spreading range is larger in the η direction than that in the y direction; however, at $Q_w = 3$ or 5 LPM, just to the contrary.

6.4.3 Bubble Velocity

In the η direction: The measurement results of bubble velocity, u_b , in the η direction are shown in Fig. 6-13. Note that for the measurement results of u_b (Figs. 6-13 and 6-15) and bubble diameter d_b (Figs. 6-16 and 6-17), the data points with gas void fraction of $\alpha < 0.05\%$ (i.e., usually the number of bubbles detected within 3 minutes < 20 -30) were discarded and not shown in the figures. This ensures the statistical meaning of the data, because both u_b and d_b relies on the statistics of the signals obtained from the two tips of the optical probe. Even the data with $\alpha < 0.05\%$ have been filtered, some data fluctuations could be still observed at the edge of a bubble plume or bubbly jet in these figures.

In all the 12 experiments, as shown in Fig. 6-13, the distribution of u_b no longer follows the Gaussian distribution in the η direction, which is rather different from that of gas void fraction (Fig. 6-7). The present result in the η direction in crossflow is also

different from the results in stagnant water where Milgram (1983), Sun and Faeth (1986a,b) and Lima Neto et al. (2008b) measured the Gaussian distributions of u_b , Stanley and Nikitopoulos (1996) reported a distribution not dramatically different from the Gaussian, and Seol et al. (2007) found a distribution between the Gaussian and the top-hat. This suggests the important effect of crossflow on bubble velocity. Fig. 6-13 shows that u_b in the upstream side ($-\eta$ direction; see Fig. 6-1) is generally smaller than that in the downstream side ($+\eta$ direction). This interesting phenomenon is related with the distribution of d_b , the wake effect of bubbles, and the separation of bubbles from water jets.

For pure bubble plumes or bubbly jets with small Q_w (1 LPM), the peak values of d_b appear in the downstream side (see Fig. 6-16), which is in accordance with the location of peak values of u_b . Further examination of Figs. 6-13 and 6-16 reveals that: the difference of u_b between the upstream and downstream sides is much more obvious than that for d_b (e.g., see Sections 20*d* and 40*d* in Expt. 3-0); and at Sections 80*d* and 100*d*, d_b is comparable or even larger in the upstream side, which is contrary to the trend for u_b . Larger value of u_b in the downstream side might be further explained by the bubble wake effect.

For the case of pure bubble plumes and bubbly jets with $Q_w = 1$ LPM, Fig. 6-14 shows a typical example of possible wake effect of preceding bubbles on a single trailing bubble. The images show that: when a single trailing bubble is close to some leading bubbles, first the trailing bubble aligns itself behind the leading bubbles; then the bubble gets elongated and sucked into the wakes of leading bubbles. A very similar process has been reported by Krishna et al. (1999) who studied bubble wake effect of large gas bubbles in water. They also reported an acceleration process as the trailing bubble approached the leading bubble, which is confirmed here in Fig. 6-14(b) - Fig. 6-

14(d). Due to the acceleration, the trailing bubble finally coalesces into the leading bubbles, and rises slower as a whole afterwards, as shown in Fig. 6-14(d) - Fig. 6-14(e), because bubbles become flat and thus the drag increases. The acceleration - deceleration process shown in Fig. 6-14(b) - Fig. 6-14(e) can be noticed even with naked eyes during the experiments. Further examination suggests that this process is in accordance with the larger bubble velocity in the downstream side and smaller velocity in the upstream side. As will be discussed later (Fig. 6-33 - Fig. 6-35), bubble wake effect is significant in the experiments where bubbles are larger (pure bubble plumes or bubbly jets with $Q_w = 1$ LPM), while it is relatively weak in the experiments where bubbles are much smaller (bubbly jets with $Q_w = 3$ or 5 LPM).

For the case of bubbly jets with $Q_w = 3$ or 5 LPM, the distribution of u_b is mainly affected by the jet initial momentum and the separation of bubbles from water jets. Expt. 3-5 or 5-5 in Fig. 6-13 is a typical example to show the evolution of u_b in a bubbly jet. Near the nozzle where the jet remaining momentum is still dominant over the crossflow, u_b follows the Gaussian distribution as in a single-phase jet. However, with the increase of the traveling distance from the nozzle, the jet momentum attenuates and bubbles start to separate from the water jet (Fig. 6-4). In this separation process, bubbles in the downstream side are still in the water jet, while bubbles in the upstream side have completely separated from the water jet, resulting in larger values of u_b in the downstream side because u_b actually contains the water jet velocity. By comparing Fig. 6-4 with Fig. 6-13, it can be found that: the gradual shift of the centerline (peak value location) of the distribution of u_b to the downstream side is in accordance with the gradual separation of bubbles from the water jet. Once the separation is complete, u_b reaches a terminal velocity of approximately 0.4 m/s along the bubble column centerline in all the 12 experiments. The terminal rise velocity of bubbles will be discussed later in

Fig. 6-33 - Fig. 6-35. In Expt. 1-3 or 3-3, the Gaussian distribution of u_b is expected to occur at a location lower than the first measurement location (Section 20d).

Overall, with the increase of Q_a , u_b increases; but the increase might not be obvious if the Q_a has already reached a certain value because further increase in Q_a increases both buoyancy and drag forces of bubbles. For example, the maximum value of u_b increases from 0.48 m/s in Expt. 1-0 to 0.74 m/s in Expt. 3-0, and it only further increases to 0.83 m/s in Expt. 5-0. With the increase in Q_w , u_b may (see Expts 3-3 and 3-5) or may not (see Expts 3-1 and 3-3) increase. This depends on the balance between the increase of u_b due to the increase of initial momentum of the water jet, and the decrease of u_b due to the decrease of d_b caused by bubble breakup induced by the water jet.

In the y direction: The measurement results of u_b distribution in the y direction are shown in Fig. 6-15. In all the experiments, the distribution is generally symmetric and follows the Gaussian distribution, which is quite different from that in the η direction. The Gaussian distribution agrees with the results of bubble plumes or bubbly jets in stagnant water (Milgram 1983; Sun and Faeth 1986a,b; Lima Neto et al. 2008b). The symmetry of u_b is because that every point in the y direction is equally affected by the bubble wakes in the upstream side or by the separation of bubbles from the water jets. Notice that the measurement of u_b in Fig. 6-15 was conducted at $\eta = 0$ (see Fig. 6-1), and thus its peak values are usually smaller than the peak values in Fig. 6-13.

As indicated from the comparison of Fig. 6-15 with Fig. 6-17, in a bubble plume, it appears that the distribution of u_b in the y direction is mostly affected by bubble size; while in a bubbly jet, the distribution is also affected by the initial jet momentum. Moreover, comparison of Fig. 6-13 with Fig. 6-15 also suggests that: in a bubbly jet, u_b reaches terminal velocities in the y direction faster than that in the η direction (e.g., see Expt. 3-3 and 3-5) because of the wider spread of a bubbly jet in the

y direction as suggested from the distribution of gas void fraction in Figs. 6-7 and 6-8 (see also Fig. 6-20).

6.4.4 Bubble Diameter

In the η direction: The measurement results of the distribution of bubble diameter, d_b , in the η direction are shown in Fig. 6-16. As only $d_b > 4$ mm was adjusted for bubble non-sphericity, it may appear a sudden jump of bubble diameter near $d_b = 4$ mm in Fig. 6-16 (e.g., at Section 20d in Expts. 1-0 and 1-1). At Section 100d in Expt. 5-3, the large value of d_b in the upstream side is because the measurement location is close to the water surface, as stated previously.

The experimental results show that Q_a and Q_w have the most important impact on d_b . Generally, with an increase of Q_a , d_b increases (e.g., see Expts. 1-0 and 3-0 in Fig. 6-16), while with an increase of Q_w , d_b decreases (e.g., see Expts. 3-1 and 3-3). Of course, such increase or decrease of d_b might be slight if Q_a or Q_w has already reached a certain value (e.g., see Expts. 3-3 and 3-5). In this study, the maximum d_b was around 20 mm in Expt. 5-0, and the minimum d_b was 1.5 - 2 mm in Expt. 1-5. By comparing the experiments with $Q_w = 1$ LPM and those with $Q_w = 3$ LPM, it appears that there might exist a critical value of Q_w between 1 LPM and 3 LPM, which is able to obviously break large bubbles ($d_b = 10 - 20$ mm) into much smaller ones ($d_b = 2 - 4$ mm). The criterion to produce small bubbles will be discussed later in Fig. 6-29(b).

As shown in Fig. 6-16, it is interesting to note that bubble size becomes smaller with the traveling distance from the nozzle. This suggests that bubbles become flatter when bubbles rise because of the hydrostatic pressure of the ambient water on bubbles' leading surface even though the pressure decreases slightly during the rise of bubbles. The flattening of bubbles indicates the increase of drag force of bubbles and the drag

force will eventually reach an equivalent value with buoyancy force, resulting in bubbles rising in uniform motion (as seen from the terminal velocity in Fig. 6-13).

For a bubble plume or bubbly jet with small Q_w (1 LPM), Expt. 3-0 or 5-0 in Fig. 6-16 is a typical example to show the evolution of d_b in the η direction. The larger d_b in the downstream side at Section 20*d* is consistent with the observation from the CCD images. This is related to that bubbles exiting from the nozzle is tall and slim in shape and it is easier for larger bubbles to be flushed to the downstream side because of the larger contact area with the crossflow. Meanwhile, the mean flow and turbulence of the crossflow may break the bubbles that are directly contacted with crossflow in the upstream side into smaller ones. With the increase of traveling distance from the nozzle, larger bubbles tend to migrate from the downstream side to the upstream side because of the buoyancy of large bubbles, while smaller bubbles tend to move to the downstream side (see Sections 80*d* and 100*d* in Expt. 3-0). Similar “fractionation” effect of crossflow on bubbles of different sizes was also observed by Socolofsky and Adams (2002).

For a bubbly jet, Expt. 3-5 or 5-5 in Fig. 6-16 presents a typical example to show the evolution of d_b . It is clear that the initial jet momentum also affect the evolution. When Q_w is large enough (5 LPM), the jet mean velocity and turbulence directly break large bubbles into smaller ones (see Section 20*d* in Expt. 5-5) and such breakup is strongest in the jet centerline where the velocity is maximum (see Fig. 6-13). Then, large amount of smaller bubbles coalesce and thus d_b increases (See Section 40*d* in Expt. 3-5). Afterwards, d_b decreases because of the flattening of bubbles when bubbles rise as stated previously. Finally, d_b is approximately uniform in the η direction if Q_w is large enough (See Sections 80*d* and 100*d* in Expt. 3-5). However, if Q_w is not large enough (3 LPM), d_b finally appears larger in the downstream side than in the

upstream side (see Sections 80*d* and 100*d* in Expt. 1-3, 3-3 and 5-3), contrary to the trend in a bubble plume. Smaller d_b in the upstream side in Expt. 3-3 (and Expts. 1-3 and 5-3) is in accordance with the CCD images and with the longer tail in the upstream side in the distribution of gas void fraction (see Fig. 6-7). This is probably related with the relative strength of crossflow, water jet and buoyancy of bubbles. In Expts. 1-3, 3-3 and 5-3, d_b at Section 20*d* is not the minimum probably because that Q_w is not large enough to directly produce bubbles small enough as in Expt. 5-5; d_b reaches the minimum at Section 40*d* perhaps because of the continuous breakup of bubbles exerted by the water jet.

In the y direction: The measurement results of the distribution of d_b in the y direction are shown in Fig. 6-17. For bubble plumes and bubbly jets with $Q_w = 1$ LPM, although there might be some data fluctuation at the plume edge due to small number of bubbles detected within the measurement period, generally the distribution of d_b follows the Gaussian distribution in all the experiments. This distribution is rather different from the asymmetric distribution in the η direction. The symmetric distribution of d_b in the y direction is because of the symmetric effects of bubble wakes and separation of bubbles from the water jets in the y direction, as stated previously.

For bubbly jets with $Q_w = 3$ and 5 LPM, the distribution of d_b in the y direction is also affected by the initial jet momentum as in the η direction. At Section 20*d*, the distribution approximates an inverted Gaussian distribution (e.g., see Expt. 3-5 or 5-5). In the experiments with $Q_w = 3$ LPM, it appears that Q_w is not large enough to make d_b smallest at once; while in the experiments with $Q_w = 5$ LPM, d_b becomes minimum at Section 20*d*. In a bubbly jet, as suggested from the comparison of Fig. 6-17 with Fig. 6-16, there appears a trend that d_b becomes uniform after some distance from the nozzle can be realized faster in the y direction than that in the η direction.

6.4.5 Specific Interfacial Area

The measurement results of the distribution of specific interfacial area, a , in the η and y directions are shown in Figs. 6-18 and 6-19. Similarly as for gas void fraction or bubble frequency, the distribution of a generally follows the Gaussian distribution in all the 12 experiments. And also similarly, for bubbly jets with $Q_w = 3$ or 5 LPM, the distribution of a may follow the Gaussian at Section 20d, but beyond Section 20d, it appears to follow a distribution between the Gaussian and the top-hat.

From Eq. (6.2), a is affected by both bubble frequency f and bubble velocity u_b . Because the data range for f (generally 0 - 20, see Fig. 6-11) is much larger than that for u_b (generally 0.3 - 0.8 m/s, see Fig. 6-13), the distribution of a is mainly affected by the distribution of f . This explains the similarity between the distributions of a with f (see Figs. 6-18 and 6-19, with comparison to Figs. 6-11 and 6-12). At Section 20d in the experiments with $Q_w = 5$ LPM, because of the large value of u_b there, the distribution of a is also affected by the distribution of u_b , which explains the difference between the peak values of a in the experiments with $Q_w = 5$ LPM and that in the experiments with $Q_w = 0 - 3$ LPM (see Fig. 6-18) is not as obvious as the difference for the peak value of f (see Fig. 6-11).

6.4.6 Cross-sectional Distribution

Above, the measurement results of bubble properties are reported only in one direction, either the η or y direction. In order to have an overall view, measurements were also conducted with a measurement mesh of 1 cm \times 1.25 cm at the whole sections of 80d in Expts. 3-0 and 3-3. For each experiment, at least 200 points were measured with non-zero data (in the bubble zone). The distribution of gas void fraction α is shown in Fig. 6-

20, where the widely-used plume boundary defined as the location corresponding to $5\% \alpha_{max}$ is also presented.

From Fig. 6-20, the shape of the distribution of α in a bubble plume is significantly different from that in a bubbly jet. In a bubble plume, the shape is close to an ellipse, with the axis in the η direction slightly longer than that in the y direction. The reason for the major axis in the η direction is that the buoyancy makes large bubbles spread wider in that direction as shown in Fig. 6-4. While in a bubbly jet, the distribution of α appears in a kidney shape. The kidney shape is similar to that in a single-phase jet or plume in crossflow, which is caused by the two counter-rotating vortices developed in the bent-over region of a jet or plume in crossflow (Smith and Mungal 1998; Lee and Chu 2003). At Section 80*d* in Expt. 3-3, the bubble column has already separated from the water jet (see Fig. 6-4), and the kidney shape is expected to inherit from the bubbly jet before the separation. The wider transverse range of the kidney shape clearly explains the wider distribution of α in the y direction than the Gaussian distribution, as stated earlier. It is interesting to note that the symmetric distribution of α with respect to the plane of $y = 0$ in a bubble plume, but not in a bubbly jet. The slight asymmetry of α in a bubbly jet is similar to the slight asymmetry of concentration distribution in single-phase jets in crossflow reported by Smith and Mungal (1998).

The distributions of bubble frequency, bubble velocity, bubble diameter, and specific interfacial area at Section 80*d* in Expts 3-0 and 3-3 are shown in Fig. 6-21 - Fig. 6-24. Their general ellipse or kidney shapes are similar to that of α in Fig. 6-20 as expected, however the inner distributions may be rather different. By comparing Figs. 6-21 and 6-24 with Fig. 6-20, the inner distributions of bubble frequency and bubble specific interfacial area for either a bubble plume or a bubbly jet are very similar to that

of α . But the inner distributions of bubble velocity and bubble diameter are rather different from that of α . Fig. 6-22 shows that in a bubble plume, bubble velocity u_b is largest near the centerline of the flume (i.e., $y = 0$) and in the downstream side (i.e., $\eta > 0$) of the cross-section; while in a bubbly jet, u_b is more uniform and only slightly larger in the downstream side. Fig. 6-23 shows that in a bubble plume, bubble diameter is larger in the upstream side; while in a bubbly jet, it is more uniform and slightly larger in the downstream side. These findings are in accordance with those reported previously in the η or y direction.

6.5 Discussions

6.5.1 Properties along the Centerlines of Bubble Plumes and Bubbly Jets

Bubble properties along the centerlines of bubble plumes and bubbly jets are shown in Fig. 6-25 - Fig. 6-30. Fig. 6-25(a) presents the change of dimensional gas void fraction α along the centerline trajectories ζ/d . From Fig. 6-25(a), α generally decreases with the increase of ζ/d due to the spread of a bubble plume or bubbly jet in both the η and y directions. Meanwhile from Fig. 6-25(a), in pure bubble plumes or bubbly jets with small Q_w (1 LPM), there appears a trend that the decreasing of α slows down with the increase of ζ/d ; and in bubbly jets with large Q_w (3 or 5 LPM), this trend can be clearly demonstrated by the fact that α will reach a terminal stable value at $\zeta/d = 40 - 60$. There should exist a terminal value of α for either a bubble plume or bubbly jet because bubbles are expected not to diffuse unlimitedly or freely as dye (or pollutants) in the ambient water. In case of bubbly jets with large Q_w (3 or 5 LPM), the water jets quickly diffuses bubbles to a certain range, which explains why α reaches the terminal value faster in this case than that in the case of bubble plumes or bubbly jets with small Q_w (in which the jet effect is limited due to the small jet initial momentum). After bubble

separation from the water jets, turbulent diffusion of the ambient water is not strong enough to obviously diffuse bubbles further to a larger range, which is supported by the observation that the thickness of bubble column does not obviously increase after the bubble separation as shown in the CCD images in Fig. 6-4. In fact, the locations where α reaches the terminal value, $\xi/d = 40 - 60$, approximates the separation locations of bubbles from the water jets as can be seen from the comparison of Fig. 6-25(a) with Fig. 6-4.

In Fig. 6-25(b), the case of bubbly jets with large Q_w (3 or 5 LPM) is non-dimensionalized, as this case has small bubbles that are the interest for artificial aeration. The following equation is used to describe the trend of α along the centerlines of bubbly jets with large Q_w :

$$\alpha/\alpha_t = 2.70(\xi/H_S)^{-1.51} \quad \text{for } \xi/H_S \leq 2 \quad \text{with } R^2 = 0.94 \quad (6.6)$$

where α_t is the terminal value of α ; H_S is the separation height of bubbles from the water jets (defined as the vertical height of the intersection of water jet centerline with bubble column centerline ξ); and R is the correlation coefficient. From Fig. 6-25(b), Eq. (6.6) fits α nicely before α reaches the terminal value at $\xi/H_S = 2$; and afterwards, $\alpha = \alpha_t$. It is interesting to note that: in this study, $\xi/H_S = 2$ is the critical point for α reaching the terminal value. Whether this is experiment-specific or not needs more experiments.

To further understand the change of α with centerline trajectory ξ/d , Expt. 5-5 is selected as an example and its experimental result is compared with the modeling result of a single-phase jet in crossflow by using CORMIX1 in Fig. 6-26(a). CORMIX is the US Environmental Protection Agency's approved software that is widely used for modeling jets or plumes discharged into the ambient water. In Fig. 6-26(a), the single-phase jet is assigned with an initial concentration $C_0 = \alpha_0$ and initial jet exit velocity $U_0 = U_{w0}$ as in Expt. 5-5. Note that, here, U_{w0} is based on the maximum rise height of a

bubbly jet injected in air (i.e., method III in Table 6-1; this method is preferable than the other two methods, for details, Chapter 5). As shown in Fig. 6-26(a), the experimental result is generally close to the modeling result in the study range of $\zeta/d \leq 100$. For $\zeta/d \leq 60$, the measurement result of α is slightly smaller than the modeling result, because CORMIX1 assumes equal spread of single-phase jet in either η or y direction in crossflow while in reality jet in crossflow spreads faster in the y direction (Rajaratnam 1978; Lee and Chu 2003). For $\zeta/d \geq 80$, the measurement result is larger than the modeling result because the limited spread of bubble range after bubble separation as discussed earlier.

Fig. 6-27 presents the change of bubble velocity along the centerline of a bubble plume or bubbly jet. Similarly as α , u_b decreases along ζ/d until it reaches a terminal stable velocity of 0.35-0.50 m/s in the centerline (ζ) direction. In Expts 1-0 and 1-1, the terminal velocity has been reached even at $\zeta/d = 20$. The terminal velocity is reached once the buoyancy force of a bubble is equivalent to the drag force. And the terminal velocity mainly depends on bubble diameter, which will be discussed further in Fig. 6-33. For the Expt. 5-5, the experimental result of u_b is compared with the modeling result of single-phase jet centerline velocity in Fig. 6-26(b). As seen from Fig. 6-26(b), the experimental result is generally close to the modeling result. At $\zeta/d = 20$, the u_b value is smaller than the single-phase jet velocity because some of the jet energy is dissipated in breaking bubbles near the nozzle and diffusing bubbles away from the nozzle. Beyond $\zeta/d \geq 60$, u_b reaches a terminal value while the single-phase jet velocity continues to decay, which explains the experimental result is larger than the modeling result at $\zeta/d \geq 60$. Fig. 6-28 shows the change of bubble frequency along the centerlines of bubble plumes or bubbly jets. As shown, f decreases with ζ/d before reaching a terminal value, similar to that of α . It also appears that f reaches its terminal value faster than α .

Fig. 6-29(a) presents the change of bubble diameter along the centerline of a bubble plume or bubbly jet. The decreasing trend of d_b with ξ/d only appears in Expts 3-0, 3-1, 5-0 and 5-1, in which bubbles are large near the injection location and potentially experience bubble breakups afterwards. Roughly three ranges of d_b can be detected in Fig. 6-29(a): 2-4 mm, 8-10 mm, and 11-17 mm. The present results of d_b are plotted with a nozzle Reynolds number Re based on nozzle diameter and the superficial water velocity at the nozzle (Method I in Table 6-1) in Fig. 6-29(b), together with the results of Lima Neto et al. (2008b) for bubbly jets in stagnant water. From Fig. 6-29(b), the present results in crossflow are close to that in stagnant water, suggesting that the present strength of crossflow (0.20 m/s) has negligible effect on changing d_b . Lima Neto et al. (2008b) proposed that a simple criterion for the breakup of larger bubbles into smaller ones: Re based on superficial water velocity at nozzle should be larger than 8,000. From Fig. 6-29, this criterion proposed in stagnant water is still valid for bubbly jets in crossflow. Fig. 6-30 presents the change of specific interfacial area along the centerlines, which is similar to the change of bubble frequency in Fig. 6-24 and the similarity can be explained from Eq. (6.2).

6.5.2 Spreading Rates of Bubble Plumes and Bubbly Jets

Based on the Gaussian distribution of gas void fraction (Figs. 6-9 and 6-10), spreads of bubble plumes or bubbly jets are examined in all 12 experiments and the results are shown as examples in Fig. 6-31. Note that in Fig. 6-31, the half-thicknesses and half-widths at the nozzle exit location are also presented, assuming that they are equal to half of the nozzle diameter, i.e., $b_t/d = 0.5$ and $b_w/d = 0.5$. As can be seen from Fig. 6-31, the spread of a pure bubble plume is quite different from that of a bubbly jet. In the case of a pure bubble plume, the spread can be approximated as a single straight line; while in

the case of a bubbly jet, the spread needs to be described with two straight lines. The joint of the two straight lines approximately reflect the location where bubbles separate from the water jet (see Figs. 6-31 and 6-4). Moreover, in the case of pure bubble plumes and bubbly jets with small Q_w (1 LPM), the half-thickness b_t is larger than the half-width b_w at the same location; while in the case of a bubbly jet with large Q_w (3 or 5 LPM), b_w is larger, as already shown in Fig. 6-20. From the spreading results of all the 12 experiments, the sectional distributions of gas void fraction in Fig. 6-20 are representative for the cases of pure bubble plumes and bubbly jets, respectively.

In the case of pure bubble plumes, the spreading rates (the slope of fitted straight line) of half-thickness b_t and half-width b_w are found to be 0.05-0.08 and 0.04-0.05, respectively, both of which are smaller than the typical spreading rate of approximately 0.10 for single-phase jets or plumes in stagnant water (Rajaratnam 1976; Lee and Chu 2003). The spreading rate of b_t increases with the increase of Q_a , which is in accordance with the larger vertical range of air bubbles as shown in Expt. 5-0 in Fig. 6-4. Such trend also applies for the spreading rate of b_w , but not as obvious as for b_t .

In the case of bubbly jets with small Q_w (1 LPM), two straight lines are used to fit the experimental results before and after the separation location approximately at $\zeta/d = 20$. Within $\zeta/d = 20$, the spreading rates of b_t and b_w are found to be 0.08-0.13 and 0.07-0.11, which are close to each other and close to that of single-phase jets or plumes in stagnant water. Beyond $\zeta/d = 20$, both the spreading rates of b_t and b_w are in the range of 0.03-0.05, which are similar to the spreading rates of 0.06 in the case of bubbly jets with small Q_w in stagnant water reported by Lima Neto et al. (2008b). Note that in Lima Neto et al. (2008b), the definition of b_t or b_w was defined as the location where the gas void fraction was 37% (e^{-1}) of its maximum value, and thus their b_t or b_w value and spreading rate should be 1.2 times of those in this study.

In the case of bubbly jets with large Q_w (3 or 5 LPM), again two straight lines are needed to fit the experimental results. Within the separation location, the spreading rates of b_t and b_w are found to be 0.10 and 0.14-0.21, respectively. Before the separation, bubbles are well mixed with the water jets (see Fig. 6-4) and thus the spreading rate of b_t is measured to be exactly the same as that in single-phase jets. The spreading rate of b_t in this study is also close to the spreading rate of 0.10 (also the definition of 37% for jet half-width or half-thickness was used) in the case of bubbly jets with large Q_w in stagnant water reported by Lima Neto et al. (2008b). The larger spreading rate of b_w is due to the formation of two counter-rotating vortices in the transverse direction for jets in crossflow (also see Fig. 6-20). The larger spreading rate of b_w compared to b_t is different from the case of bubbly jets in stagnant water where the jet spreading is symmetrical. Beyond the separation location, the spreading rates of b_t and b_w are found to be 0.01-0.02 and 0.02-0.07, respectively. Note that the negative spreading rate of -0.01 obtained for b_t in Expt. 3-5 possibly arises from experimental errors. After the separation, the spreading rates of b_t and b_w are much smaller compared to those before the separation. The small spreading rate of b_t agrees with the observation in the CCD images in Fig. 6-4 that bubble plume thickness does not increase obviously after bubble separation from the water jets.

6.5.3 Conservation of Air Flow Rate

In this study, the background air concentration in the ambient water is expected to be close to its saturation concentration because of the continuous recirculation (each half an hour) of the water between the sump and the flume that is about 3 m above the sump water surface. Moreover, the contact time of injected air bubbles with the ambient water

is short, less than 1.3 seconds. Therefore, the injected air flow rate via the nozzle is expected to conserve during the rise of bubbles.

At a downstream section, the air flow rate can be calculated with the following formula:

$$Q_a = \int_{-\infty}^{+\infty} \int_{-\infty}^{+\infty} U_b \alpha d\eta dy \quad (6.7)$$

$$\alpha = \alpha_{\max} \exp[-0.693(\eta/b_t)^2] \exp[-0.693(y/b_w)^2] \quad (6.8)$$

where Eq. (6.8) is based on the Gaussian distribution of α in both the η and y directions (see Figs. 6-9 and 6-10). In the experiments of bubbly jets with large Q_w (3 or 5 LPM), bubble velocity U_b can be well assumed to follow the top-hat distribution (approximately 0.4 m/s in the ζ direction, see Figs. 6-13 and 6-15) at Sections 80*d* and 100*d* after the separation of bubbles with the water jets. For these sections, analytical solution to Eq. (6.7) can be obtained by integrating and by using the definition of error function:

$$Q_a = 1.44\pi U_b \alpha_{\max} b_t b_w \quad (6.9)$$

The integration results are shown in Fig. 6-32 and compared with the injected air flow rates at the nozzle.

Fig. 6-32 shows that: the air flow rates from integration are generally close to the injected rates. On average, the integrated value of Q_a is $(12.9 \pm 11.1)\%$ smaller than the injected value. The discrepancy mainly originates from the assumption of Gaussian distribution of α in the y direction, which in fact is a distribution between Gaussian and top-hat as stated previously. Another reason for the smaller integrated value of Q_a might be the fact that: rather tiny bubbles, with diameters in the magnitude of 0.1 mm, were observed downstream of bubbly jets, but cannot be detected by the optical probe. The smaller integrated value of Q_a could be also because of the dissolution of injected air into the water. Of course, measurement errors in U_b (9%) and α (2%) could be another

error source. Moreover, error could also originate from the fact that the measurements in the η and y direction were conducted in two different days, when the controls in the ambient flow, air discharge and water discharge were inevitably slightly different. Overall, the conservation of air flow rate, to a large extent, suggests that the reliability of the measurement results from the optical probe.

6.5.4 Bubble Slip Velocity

Bubble slip velocity, U_s , also called terminal rise velocity, refers to the bubble velocity U_b relative to the bubble-induced water velocity U_{bw} in the vertical direction inside a bubble plume:

$$U_s = (U_b - U_{bw}) \sin \theta \quad (6.10)$$

where θ is the angle of centerline ζ with respect to the ambient water velocity. For each experimental condition in this study, θ was measured from the processing of 10 images (for details, see Chapter 5). Since traditional methods, such as ADV and PIV, are not able to measure U_{bw} because of the existence of bubbles, U_{bw} is first assumed to be small in this study. The results of $U_s = U_b \times \sin \theta$ versus bubble diameter d_b are shown in Fig. 6-33, where U_b uses the measurement results at Section $100d$. In Fig. 6-33, the classic relation of U_s versus d_b for single isolated air bubbles in stagnant water at 20 °C (the same temperature in this study) reported by Clift et al. (1978) are also presented, together with the experimental results of bubbly jets in stagnant water reported by Lima Neto et al. (2008b)

As can be seen in Fig. 6-33, the present results of U_s without the consideration of U_{bw} lie between the relations reported by Clift et al. (1978) and Lima Neto et al. (2008b). For the case of bubbly jets with large Q_w (3 or 5 LPM), the present results are generally close to that of Clift et al. (1978). With the increase of Q_a (i.e., larger and

more bubbles), such as in Expts. 5-3 and 5-5, the present results are slightly larger than that of Clift et al. (1978). On the other hand, for the case of pure bubble plumes and bubbly jets with small Q_w (1 LPM), the present results are obviously larger than that of Clift et al. (1978), and the difference becomes larger with the increase of Q_a .

The importance of U_{bw} is then examined from dye stripe experiments as shown in Fig. 6-34. In these experiments, dye stripes, used as tracer to track the vertical movement of the ambient water inside bubbles, were released with negligible initial momentum upstream of bubble plumes or bubbly jets. From the dye stripe experiments, it can be confirmed that U_{bw} is important in the case of large bubbles (bubble plumes and bubbly jet with small Q_w), while it is small in the case of small bubbles (bubbly jets with large Q_w). Also as seen from Expt. 3-0 in Fig. 6-34, it appears that U_{bw} is primarily caused by passage of large bubbles and secondarily by bubble wakes.

In the case of bubble plumes and bubbly jet with small Q_w , as shown in the modeling of bubble plume centerline ζ in Chapter 5, the centerline angle θ from images is rather close to the angle determined from the ambient velocity U and U_S from Clift et al. (1978), i.e., $\arctan(U_S/U)$, but it is obviously smaller than the angle determined from U and u_b from the optical probe, i.e., $\arcsin(U/u_b)$. This again confirms the important existence of U_{bw} in this case. This also indicates that the difference between the present results of U_S and that of Clift et al. (1978) in Fig. 6-33, ΔU_S , possibly reflects the value of U_{bw} in the vertical direction, $U_{bw,v}$. Fig. 6-35 presents the comparison between ΔU_S and $U_{bw,v}$, where $U_{bw,v}$ is estimated from the centerline movement of dye stripes. As shown, the general difference between ΔU_S and $U_{bw,v}$ is only $(-11.9 \pm 12.3)\%$. Fig. 6-35 confirms that: if U_{bw} is considered, the present results of U_S are generally close to that of single isolated bubbles reported by Clift et al. (1978). The present results of U_S in crossflow are smaller than that of Lima Neto et al. (2008b) in stagnant water, possibly

because that in crossflow, bubble wakes are flushed downstream and thus have a less effect on U_{bw} , while in stagnant water trailing bubbles are directly in the wakes of preceding bubbles.

6.5.5 Aeration Potential and Bubble Size Recommended for Artificial Aeration

Bubble size might be the most important parameter that needs to be considered in the design and operation of an aeration system, as it directly affects the mass transfer coefficient K_L , specific interfacial area a and bubble slip velocity U_s (thus the residence time) (Lima Neto et al. 2008a). In addition, the air flow rate Q_a also affects the aeration efficiency by affecting the value of specific interfacial area a (see Fig. 6-18). In order to have a direct judgment in the aeration ability of each experiment, aeration potential, defined as in Eq. (6.11), was calculated at Section 80d.

$$\int_{-\infty}^{+\infty} \int_{-\infty}^{+\infty} K_L a d\eta dy = 1.44\pi K_L a_{\max} b_l b_w \quad (6.11)$$

where the distribution of a was assumed to be Gaussian in both the η and y directions (see Figs. 6-18 and 6-19), and for simplicity, its half-thickness or half-width was assumed to be the same as that for gas void fraction; a_{\max} was the maximum value of a measured at Section 80d; and K_L was assumed to be constant (0.04 cm/s) for $d_b > 1.3$ mm according to Wüest et al. (1992). The calculation results are shown in Fig. 6-36. Obviously, smaller value of bubble diameter (e.g., see Expts. 5-3 and 5-5 in Table 6-1 and Fig. 6-36) and larger value of air flow rate (e.g., see Expts. 3-5 and 5-5 in Fig. 6-36) are more favorable for artificial aeration. The use of large Q_w (3 or 5 LPM) to produce bubbles of small d_b (2-3 mm) can increase by several times the aeration ability of the setup (e.g., see Expts. 5-0 and 5-5 in Fig. 6-36).

As to the optimum bubble diameter d_b for efficient artificial aeration, Motarjemi and Jameson (1978) recommended d_b in the range of 0.3 - 1 mm, although K_L reached

its peak value at $d_b \approx 2$ mm. This range is much smaller than the typical diameter of 2 - 5 mm used in aeration of effluents and natural waters (Sahoo and Luketina 2003) since there appears no easy or cheap way to produce such tiny bubbles in large quantities (Motarjemi and Jameson 1978; Sahoo and Luketina 2006). In practice, Wiest et al. (1992) recommended d_b of 1.6 - 2 mm for efficient oxygenation in a deep stratified lake, and d_b of about 20 mm for artificial mixing. Considering both mechanical efficiency and oxygen dissolution efficiency, Sahoo and Luketina (2003) suggested d_b of close to 2 mm for oxygen transfer from air bubbles into the water of a linearly stratified reservoir.

According to Sarimeseli and Kelbaliyev (2004), for air bubbles in water, the maximum stable bubble diameter depends mainly on the energy dissipation rate per unit mass (turbulence level). From the present experiments, it is rather easy to break bubbles with $d_b > 10$ mm into bubbles with d_b in the range of 2-3 mm (see Table 6-1) as long as providing certain turbulence level ($Re > 8,000$ based on superficial water velocity at the nozzle exit, see Fig. 6-29(b)). However, it appears relatively difficult to further break bubbles into those with $d_b < 2$ mm by further increasing turbulence level (see Expts. 1-3 and 1-5, 3-3 and 3-5, 5-3 and 5-5 in Table 6-1). Similar statement was also made by Sahoo and Luketina (2006). Further increase of turbulence level might be able to produce tiny bubbles with $d_b = 1-2$ mm or even smaller (speculated from Section 20d in Expt. 5-5 in Fig. 6-16), however, these bubbles are expected to coalesce at some distance away from the nozzle where the turbulence level is not as strong as that near the nozzle.

In the present study, the minimum stable bubble diameter measured at sufficient distance away from the nozzle is 1.8 mm, which occurs in the Expt. 1-5 with the experimental condition of $Re > 8,000$ and the smallest ratio of Q_a/Q_w . This size is quite comparable to the smallest bubble sizes obtained in Lima Neto et al. (2008 b,d) who

used a similar setup as the present in a large tank (Table 6-2). This suggests that the effect of the present crossflow is relatively small compared to that of bubbly jet turbulence. Other relevant studies in the literature are also listed in Table 6-2. In the study of Martínez-bazán et al. (1999a), tiny bubbles with $d_b = 0.5-1$ mm were produced due to the large Re and the small value of Q_a (thus less probability of coalescence among bubbles away from the nozzle). The use of needle nozzles for air injection and grid for enhancing turbulence might also make bubble size smaller. The studies of Stanley & Nikitopoulos (1996) and Kumar et al. (1989) provide a general idea of bubble size, although their results were obtained near the nozzle exit. From Table 6-2, it may be inferred that: to produce bubbles in large quantities with large value of Q_a , the minimum stable bubble diameter can be controlled approximately 2 mm. Thus, bubbles of 2 mm, at this stage, are recommended for the practical activities of artificial aeration.

6.6 Summaries and Conclusions

In Chapter 6, bubble properties in bubble plumes and bubbly jets in a crossflow of 0.20 m/s were studied by using a calibrated double-tip optical probe system. A total of 12 bubble plumes and bubbly jets were produced by injecting different combination of air and water flows via a single-orifice nozzle. For each of the 12 experiments, measurements were conducted in both the η and y directions (see Fig. 6-1) at 5 sections, i.e., Sections $20d$, $40d$, $60d$, $80d$ and $100d$ where d is the nozzle diameter. To have an overall view, the whole section of $80d$ was also measured in detail in two experiments. Totally, 2,070 points were measured, with each one measured for 3 minutes. This study probably is the first one that reports detailed measurements on bubble properties for bubble plumes and bubbly jets in crossflow. Thus, this study will improve the understanding on bubble plumes and bubbly jets in crossflow, and enhance their

practical applications such as in artificial aeration and mixing in the environment where crossflow is present (e.g., in rivers and oceans). This study also provides valuable data for the development and calibration of computational fluid dynamics models on air-water two-phase flows. The main conclusions from this study are as follows:

- (1) In general, the 12 experiments can be divided into two cases, the case of pure bubble plumes and bubbly jets with small water discharge at the nozzle Q_w (1 LPM) that has large and irregular bubbles; and the case of bubbly jets with large Q_w (3 or 5 LPM) that has small and uniform bubbles. A more general criterion to have the second case is that: the nozzle Reynolds number based on superficial water velocity at the nozzle, Re , should be larger than 8,000. This criterion proposed for bubbly jets in stagnant water by Lima Neto et al. (2008b) is still valid for bubbly jets in crossflow.
- (2) The distributions of gas void fraction, bubble frequency and specific interfacial area are found to generally follow the Gaussian distribution in both the η and y directions. Particularly, in the case of bubbly jets with large Q_w (3 or 5 LPM; or $Re > 8,000$), their distribution in the y direction is between the Gaussian and the top-hat distributions.
- (3) The distribution of bubble velocity is found not symmetrical in the η direction and bubble velocity in the downstream side is larger, which is related with the bubble wake effect in a bubble plume and separation of bubbles from water jet in a bubbly jet. However, its distribution in the y direction is found to be a symmetrical Gaussian. The distribution of bubble diameter is found rather complex, and is affected primarily by air and water discharges at the nozzle and the distance from the nozzle.

- (4) The detailed cross-sectional measurements show a shape of ellipse for a bubble plume, with the axis in the η direction slightly longer than that in the y direction; while it is a kidney shape for a bubbly jet, which is similar to that for a single-phase jet or plume in crossflow.
- (5) Overall, bubble property values decay with the increase of bubble plume centerline trajectory until they reach a terminal and stable value. An empirical relation is proposed for gas void fraction.
- (6) In the case of pure bubble plumes, the spreading rates of half-thickness and half-width (defined as 50% of the centerline gas void fraction) are found to be 0.05-0.08 and 0.04-0.05, respectively, both smaller than that of simple jets or plumes. In the case of bubbly jets, the spreading rates are close to that of single-phase jets in crossflow before the separation of bubbles from the water jets; after the separation, they become obviously smaller. The air flow rates were calculated to be conserved.
- (7) In the case of pure bubble plumes and bubbly jets with small Q_w (1 LPM or $Re \leq 8,000$), bubble induced water velocity inside bubble plumes is important and cannot be neglected; while, in the case of bubbly jets with large Q_w (3 or 5 LPM or $Re > 8,000$), it is negligible. The present results on bubble slip velocity is close to that of single isolated bubbles in stagnant water, rather than that of bubbly jets in stagnant water. Aeration potential of each of the 12 experiments was calculated and bubbles of $d_b \approx 2$ mm are recommended for artificial aeration in practice.

References

- Akhmetbekov, Y. K., Alekseenko, S. V., Dulin, V. M., Markovich, D. M., and Pervunin, K. S. (2010). "Planar fluorescence for round bubble imaging and its application for the study of an axisymmetric two-phase jet." *Exp. Fluids*, 48(4), 615-629.

- Boes, R. M., and Hager, W. H. (2003). "Two-phase flow characteristics of stepped spillways." *J. Hydraul. Eng.*, 129(9), 661–670.
- Boyer, C., Duquenne, A. M., and Wild, G. (2002). "Measuring techniques in gas-liquid and gas-liquid-solid reactors." *Chem. Eng. Sci.*, 57(16), 3185-3215.
- Chambers, P. A., Brown, S., Culp, J. M., Lowell, R. B., and Pietroniro, A. (2000). "Dissolved oxygen decline in ice-covered rivers of northern Alberta and its effects on aquatic biota." *J. Aquatic Ecosystem Stress and Recovery*, 8(1), 27-38.
- Chang, K. A., Lim, H. J., and Su, C. B. (2003). "Fiber optic reflectometer for velocity and fraction ratio measurements in multiphase flows." *Rev. Sci. Instrum.*, 74(7), 3559-3565.
- Chanson, H. (2002). "Air-water flow measurements with intrusive, phase-detection probes: Can we improve their interpretation?." *J. Hydraul. Eng.*, 128(3), 252-255.
- Chaumat, H., Billet-Duquenne, A. M., Augier, F., Mathieu, C., and Delmas, H. (2005). "Application of the double optic probe technique to distorted tumbling bubbles in aqueous or organic liquid." *Chem. Eng. Sci.*, 60(22), 6134-6145.
- Clift, R., Grace, J. R., and Weber, M. E. (1978). *Bubbles, drops and particles*, Academic, New York.
- Dhotre, M.T., Nicenoa, B., Smith, B.L., and Simiano, M. (2009). "Large-eddy simulation (LES) of the large scale of bubble plume." *Chem. Eng. Sci.*, 64(11), 2692-2704.
- Esmaeeli, A., and Tryggvason, G. (1998). "Direct numerical simulation of bubbly flows. Part 1. Low Reynolds number arrays." *J. Fluid Mech.*, 377, 313-345.
- Esmaeeli, A., and Tryggvason, G. (1999). "Direct numerical simulation of bubbly flows. Part 2. Moderate Reynolds number arrays." *J. Fluid Mech.*, 385, 325-358.
- Fanneløp, T. K., Hirschberg, S., and Küffer, J. (1991). "Surface current and recirculating cells generated by bubble curtains and jets." *J. Fluid Mech.*, 229, 629-657.
- Fonade, C., Doubrovine, N., Maranges, C., and Morchain, J. (2001). "Influence of a transverse flowrate on the oxygen transfer performance in heterogeneous aeration: Case of hydro-ejectors." *Water Res.*, 35(14), 3429-3435.
- Fox, R. (2012). "Large-eddy-simulation tools for multiphase flows." *Annu. Rev. Fluid Mech.*, 44:47-76.
- Herringe, R.A., Davis, M.R. (1976). "Structural development of gas-liquid mixture flows." *J. Fluid Mech.* 73, 97-123.

- Hodgson, J. E., Rajaratnam, N. (1992). "An experimental study of jet dilution in crossflows." *Can. J. Civ. Eng.*, 19,733-743.
- Iguchi, M., Okita, K., Nakatani, T., and Kasai, N. (1997). "Structure of turbulent round bubbling jet generated by premixed gas and liquid injection." *Int. J. Multiphase Flow*, 23, 249-262.
- Kiambi, S. L., Duquenne, A. M., Dupont, J. B., Colin, C., Risso, F., and Delmas, H. (2003). "Measurements of bubble characteristics: Comparison between double optical probe and imaging." *Can. J. Chem. Eng.*, 81(3-4), 764-770.
- Krishna, R., Urseanu, M. I., van Baten, J. M., and Ellenberger, J. (1999). "Rise velocity of a swarm of large gas bubbles in liquids." *Chem. Eng. Sci.*, 54(2), 171-183.
- Kumar, S., Nikitopoulos, D. N., and Michaelides, E. E. (1989). "Effect of bubbles on the turbulence near the exit of a liquid jet." *Exp. Fluids*, 7(7), 487-494.
- Lee, J. H. W., and Chu, V. H. (2003). *Turbulent jets and plumes – a Lagrangian approach*. Kluwer Academic publisher, Norwell, Massachusetts, USA.
- Liao, Y., and Lucas, D. (2009). "A literature review of theoretical models for drop and bubble breakup in turbulent dispersions." *Chem. Eng. Sci.*, 64(15), 3389-3406.
- Lima Neto, I. E. (2012). "Modeling the liquid volume flux in bubbly jets using a simple integral approach." *J. Hydraul. Eng.*, 138(2), 210-215.
- Lima Neto, I. E., Zhu, D. Z., Rajaratnam, N., Yu T., Spafford., M., and McEachern, P. (2007). "Dissolved oxygen downstream of an effluent outfall in an ice-cover river: natural and artificial aeration." *J. Environ. Eng.*, 133 (11), 1051-1060.
- Lima Neto, I. E., Zhu, D. Z. and Rajaratnam, N. (2008a). "Air injection in water with different nozzles." *J. Environ. Eng.*, 134 (4), 283-294.
- Lima Neto, I. E., Zhu, D. Z. and Rajaratnam, N. (2008b). "Bubbly jets in stagnant water." *Int. J. Multiphase Flow*, 34 (12), 1130-1141.
- Lima Neto, I. E., Zhu, D. Z. and Rajaratnam, N. (2008c). "Effect of tank size and geometry on the flow induced by circular bubble plumes and water jets." *J. Hydraul. Eng.*, 134 (6), 833-842.
- Lima Neto, I. E., Zhu, D. Z. and Rajaratnam, N. (2008d). "Horizontal injection of gas-liquid mixtures in a water tank." *J. Hydraul. Eng.*, 134 (12), 1722-1731.
- Manasseh, R., Yoshida, S., and Kajio, N. (1998). "Bubble Trajectory Bifurcations in Crossflow." 13th Australasian Fluid Mechanics Conference, Monash University, Melbourne, Australia.

- Mart ínez-Bazán, C., Montañés, J. L., Lasheras, J. C. (1999a). "On the breakup of an air bubble injected into a fully developed turbulent flow. Part 1. Breakup frequency." *J. Fluid Mech.*, 401, 157-182.
- Mart ínez-Bazán, C., Montañés, J. L., Lasheras, J. C. (1999b). "On the breakup of an air bubble injected into a fully developed turbulent flow. Part 2. Size pdf of the resulting daughter bubbles." *J. Fluid Mech.*, 401, 183-207.
- Milenkovic, R., Sigg B., and Yadigaroglu, G. (2005). "Study of periodically excited bubbly jets by PIV and double optical sensors." *Int. J. Heat Fluid Flow*, 26(6), 922-930.
- Milgram, J.H. (1983). "Mean flow in round bubble plumes." *J. Fluid Mech.*, 133, 345-376.
- Morton, B.R., Taylor, G.I., and Turner, J.S. (1956). "Turbulent gravitational convection from maintained and instantaneous sources." Proceedings of the Royal Society of London, Series A, 234(1196),1-23.
- Motarjemi, M., and Jameson, G. J. (1978). "Mass transfer from very small bubbles - The optimum bubble size for aeration." *Chem. Eng. Sci.*, 33(11), 1415-1423.
- Moursali, E., Mari é, J.L., and Bataille, J. (1995). "An upward turbulent bubbly boundary layer along a vertical flat plate." *Int. J. Multiphase Flow*, 21(1), 107-117.
- Mueller, J. A., Boyle, W. C., and Pöpel, H. J. (2002). *Aeration: Principles and practice*, CRC, New York.
- Murzyn, F., Mouaze, D., and Chaplin, J. R. (2005). "Optical fibre probe measurements of bubbly flow in hydraulic jumps." *Int. J. Multiphase Flow*, 31(1), 141-154.
- Norman, T. L., and Revankar, S. T. (2011). "Buoyant jet and two-phase jet-plume modeling for application to large water pools." *Nucl. Eng. Des.*, 241(5), 1667-1700.
- Rajaratnam, N. 1976. *Turbulent jets*. Elsevier Scientific, Amsterdam, The Netherlands.
- Rensen, J., Luther, S., and Lohse, D. (2005). "The effect of bubbles on developed turbulence." *J. Fluid Mech.*, 538, 153-187.
- Rojas, G., and Loewen, M. (2007). "Fiber-optic probe measurements of void fraction and bubble size distributions beneath breaking waves." *Exp. Fluids*, 43(6), 895-906.
- Ruzicka, M. C. (2000). "On bubbles rising in line." *Int. J. Multiphase Flow*, 26(7), 1141-1181.
- Sahoo, G. B., and Luketina, D. (2003). "Modeling of bubble plume design and oxygen transfer for reservoir restoration." *Water Res.*, 37(2), 393-401.

- Sahoo, G. B., and Luketina, D. (2006). "Response of a tropical reservoir to bubbler destratification." *J. Environ. Eng.*, 132(7), 736-746.
- Sarimeseli, A., and Kelbaliyev, G. (2004). "Modeling of the break-up of deformable particles in developed turbulent flow." *Chem. Eng. Sci.*, 59(6), 1233-1240.
- Seol, D. G., Bhaumik, T., Bergmann, C., and Socolofsky, S. A. (2007). "Particle image velocimetry measurements of the mean flow characteristics in a bubble plume." *J. Eng. Mech.*, 133(6), 665-676.
- Simonnet, M., Gentric, C., Olmos, E., Midoux, N. (2007). "Experimental determination of the drag coefficient in a swarm of bubbles." *Chem. Eng. Sci.*, 62, 858-866.
- Smith, S.H., and Mungal, M.G. (1998). "Mixing, structure and scaling of the jet in crossflow." *J. Fluid Mech.*, 357, 83-122.
- Socolofsky, S. A., and Adams, E. E. (2002). "Multi-phase plumes in uniform and stratified crossflow." *J. Hydraul. Res.*, 40(6), 661-672.
- Socolofsky, S. A., Bhaumik, T., and Seol, D. G. (2008). "Double-plume integral models for near-field mixing in multiphase plumes." *J. Hydraul. Eng.*, 134(6), 772-783.
- Stanley, K. N., and Nikitopoulos, D. E. (1996). "Bubble measurements in a gas-liquid jet." *Chem. Eng. Comm.*, 143(1), 1-22.
- Sun, T. Y., and Faeth, G. M. (1986a). "Structure of turbulent bubbly jets. I: Methods and centerline properties." *Int. J. Multiphase Flow*, 12(1), 99-114.
- Sun, T. Y., and Faeth, G. M. (1986b). "Structure of turbulent bubbly jets. II: Phase property profiles." *Int. J. Multiphase Flow*, 12(1), 115-126.
- Varley, J. (1995). "Submerged gas-liquid jets: Bubble size prediction." *Chem. Eng. Sci.*, 50(5), 901-905.
- Whitfield, P.H., and McNaughton, B. (1986). "Dissolved-oxygen depressions under ice cover in two Yukon rivers." *Water Resour. Res.*, 22 (12), 1675-1679.
- Wüest, A., Brooks, N. H., and Imboden, D. M. (1992). "Bubble plume modeling for lake restoration." *Water Resour. Res.*, 28(12), 3235-3250.

Table 6-1. Experimental Conditions for Bubble Plumes and Bubbly Jets in the Crossflow of 0.20 m/s

| Experiment I.D. | Q _a (LPM) | Q _w (LPM) | α ₀ | d _b ^{**} (mm) | Method I [*] | | Method II [*] | | Method III [*] | |
|--------------------|-------------------------|-------------------------|----------------|--------------------------------------|--------------------------|--------|--------------------------|--------|--------------------------|--------|
| | | | | | U _{w0} (m/s) | Re | U _{w0} (m/s) | Re | U _{w0} (m/s) | Re |
| 1-0 | 1 | 0 | 1.00 | 8.31 | 0 | 0 | 0 | 0 | 0 | 0 |
| 1-1 | 1 | 1 | 0.50 | 7.74 | 0.59 | 3,537 | 1.18 | 7,074 | 1.01 | 6,089 |
| 1-3 | 1 | 3 | 0.25 | 2.02 | 1.77 | 10,610 | 2.36 | 14,147 | 1.98 | 11,871 |
| 1-5 | 1 | 5 | 0.17 | 1.77 | 2.95 | 17,684 | 3.54 | 21,221 | 3.31 | 19,879 |
| 3-0 | 3 | 0 | 1.00 | 9.46 | 0 | 0 | 0 | 0 | 0 | 0 |
| 3-1 | 3 | 1 | 0.75 | 8.77 | 0.59 | 3,537 | 2.36 | 14,147 | 1.95 | 11,721 |
| 3-3 | 3 | 3 | 0.50 | 2.44 | 1.77 | 10,610 | 3.54 | 21,221 | 3.13 | 18,783 |
| 3-5 | 3 | 5 | 0.38 | 2.11 | 2.95 | 17,684 | 4.72 | 28,294 | 4.60 | 27,613 |
| 5-0 | 5 | 0 | 1.00 | 10.93 | 0 | 0 | 0 | 0 | 0 | 0 |
| 5-1 | 5 | 1 | 0.83 | 9.05 | 0.59 | 3,537 | 3.54 | 21,221 | 2.50 | 15,022 |
| 5-3 | 5 | 3 | 0.63 | 2.79 | 1.77 | 10,610 | 4.72 | 28,294 | 3.60 | 21,583 |
| 5-5 | 5 | 5 | 0.50 | 2.19 | 2.95 | 17,684 | 5.89 | 35,368 | 5.31 | 31,887 |

Note: ^{*} Method I uses the concept of superficial water velocity at the nozzle: $U_{w0} = 4Q_w/\pi d^2$;

Method II considers the initial gas volume fraction: $U_{w0} = 4Q_w/[(1-C_0)\pi d^2]$;

Method III is based on the maximum rise height H_{max} : $U_{w0} = (2g H_{max})^{1/2}$;

^{**} Mean bubble diameter based on measurement at Section 80d in both η and y directions.

Table 6-2 Summary of minimum mean bubble diameter in experiments of air-water bubbly jets discharged via nozzles in water

| Study | Setup | Q _a (LPM) | Q _w (LPM) | Nozzle Diameter d (mm) | U _{w0} ² (m/s) | Re ³ (10 ³) | Min. Mean d _b (mm) |
|--|---------------------------------|-------------------------|-------------------------|---|---------------------------------------|---------------------------------------|--|
| Present ¹ | Large flume (with crossflow) | 1 | 3 | 6 | 1.77 | 10.6 | 2 |
| | | 1 | 5 | 6 | 2.95 | 17.7 | 1.8 |
| Lima Neto et al. (2008b) ¹ | Large tank | 0.4 | 5 | 6 | 2.95 | 17.7 | 1.7 |
| | | 1 | 5 | 6 | 2.95 | 17.7 | 2.1 |
| | | 0.4 | 7 | 9 | 1.83 | 16.5 | 2 |
| | | 1 | 7 | 6 | 4.13 | 24.8 | 1.8 |
| Lima Neto et al. (2008d) ¹ | Large tank | 1 | 7 | 6 | 4.13 | 24.8 | 1.8 |
| Milenkovic et al. (2005) | Large tank | 4.15 | 122.15 | d _{water} = 90; d _{air} = 3.4 (39 needle nozzles) | 0.32 | 28.8 | 2 |
| Mart ínez-baz án et al. (1999a) | Large tank | 0.065- 0.072 | 1.8-7.2 | Effective d _{water} = 1.5-3; d _{air} = 0.4-1.2 (1 needle nozzle) | 17 | 26-51 | 0.5-1(1.4-2 near the air nozzle exit) |
| Iguchi et al. (1997) | Confined column | 0.06-2.4 | 2.52- 4.98 | 5 | 2.14- 4.23 | 10.7- 21.2 | 2 (1-3) |
| Stanley & Nikitopoulos (1996) | Large tank | 0.03 | 6.35 | 12.7 | 0.84 | 10.7 | 1.5-2.4 near the nozzle exit |
| Kumar et al. (1989) | Confined tank | 0.06- | 2.75- | d _{water} = 12.5 (with grid); | 0.37- | 4.6-9.1 | 0.6-2 near the nozzle exit |
| | | 0.64 | 5.33 | d _{air} = 0.5 (3 needle nozzles) | 0.73 | | |

Note: ¹ only several sets of the experiments that produced smallest bubbles are present;

² superficial water velocity at the nozzle exit;

³ based on superficial water velocity and nozzle diameter.

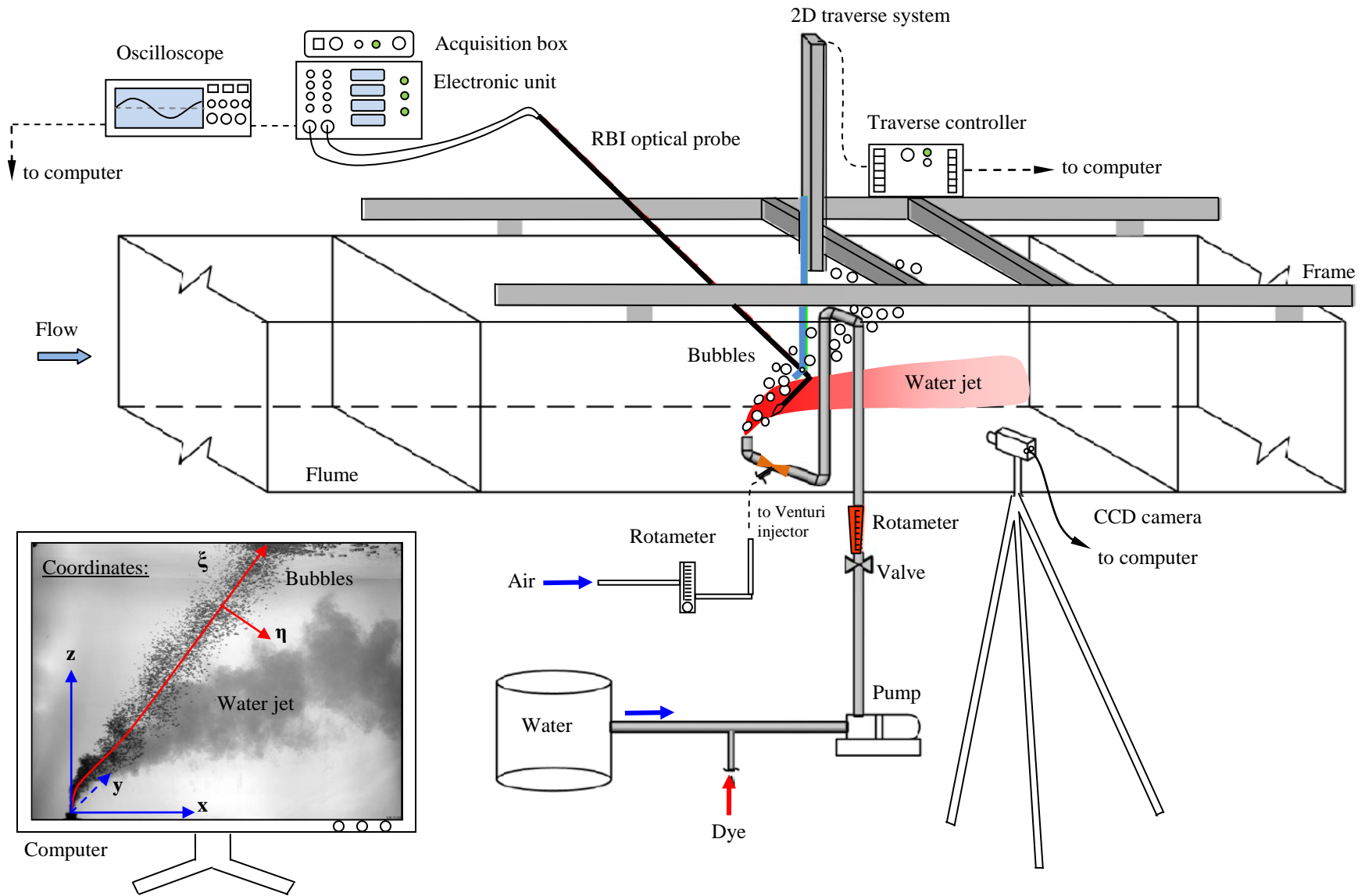


Figure 6-1. Schematic of experimental setup in a flume of 25 m × 1.2 m × 0.8 m (L × W × H)

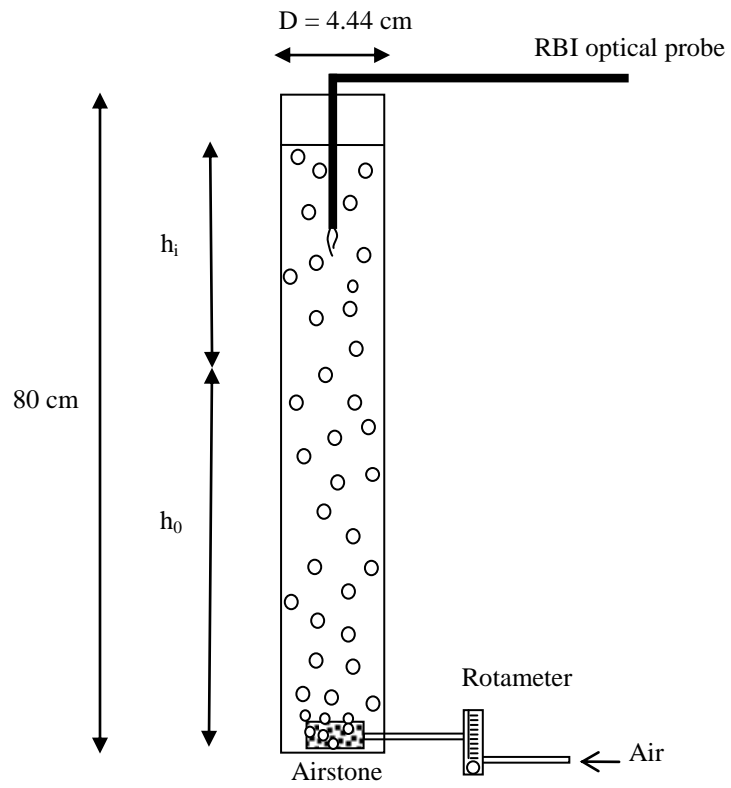


Figure 6-2. Cylinder used to calibrate gas void fraction measurement by using the optical probe

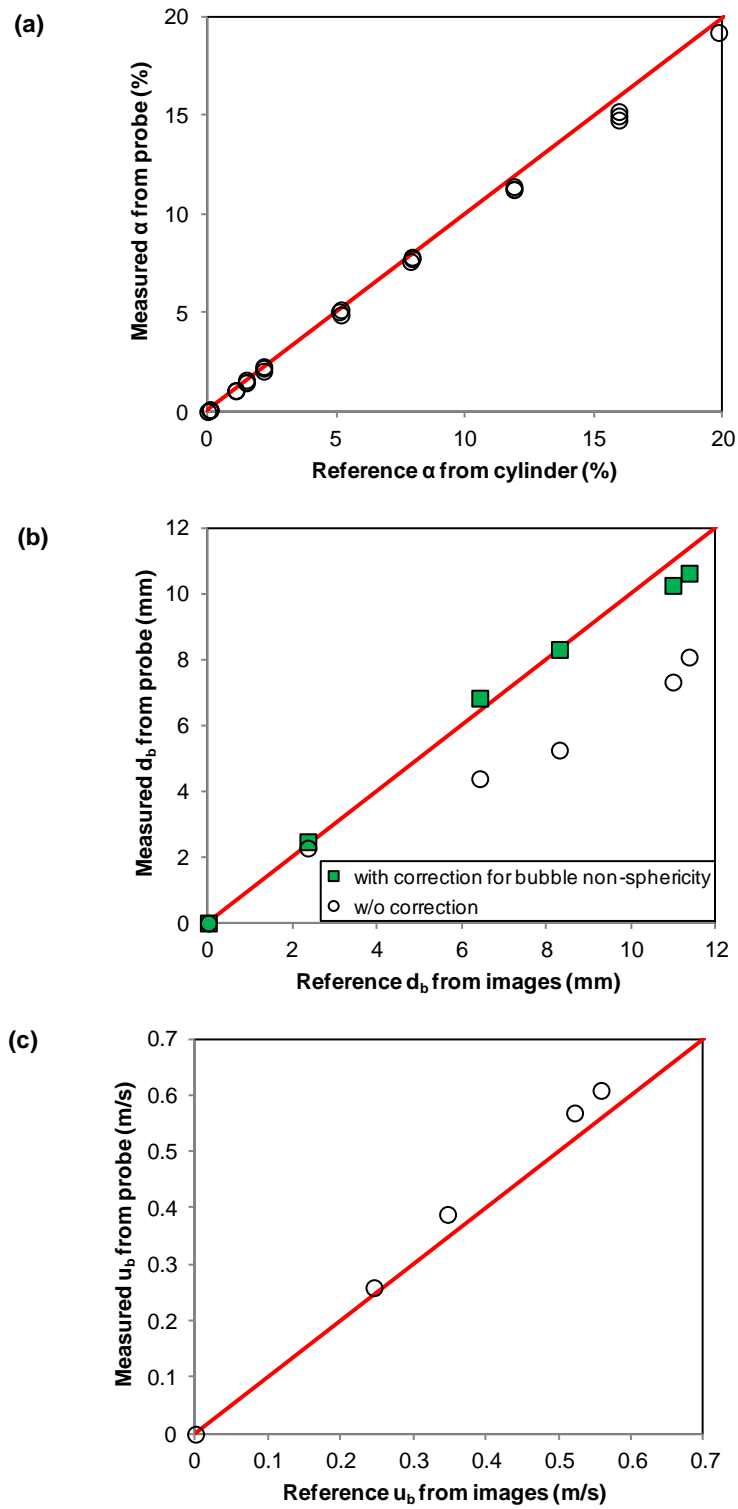


Figure 6-3. Calibration of the optical probe on (a) void fraction, (b) bubble diameter, and (c) bubble velocity

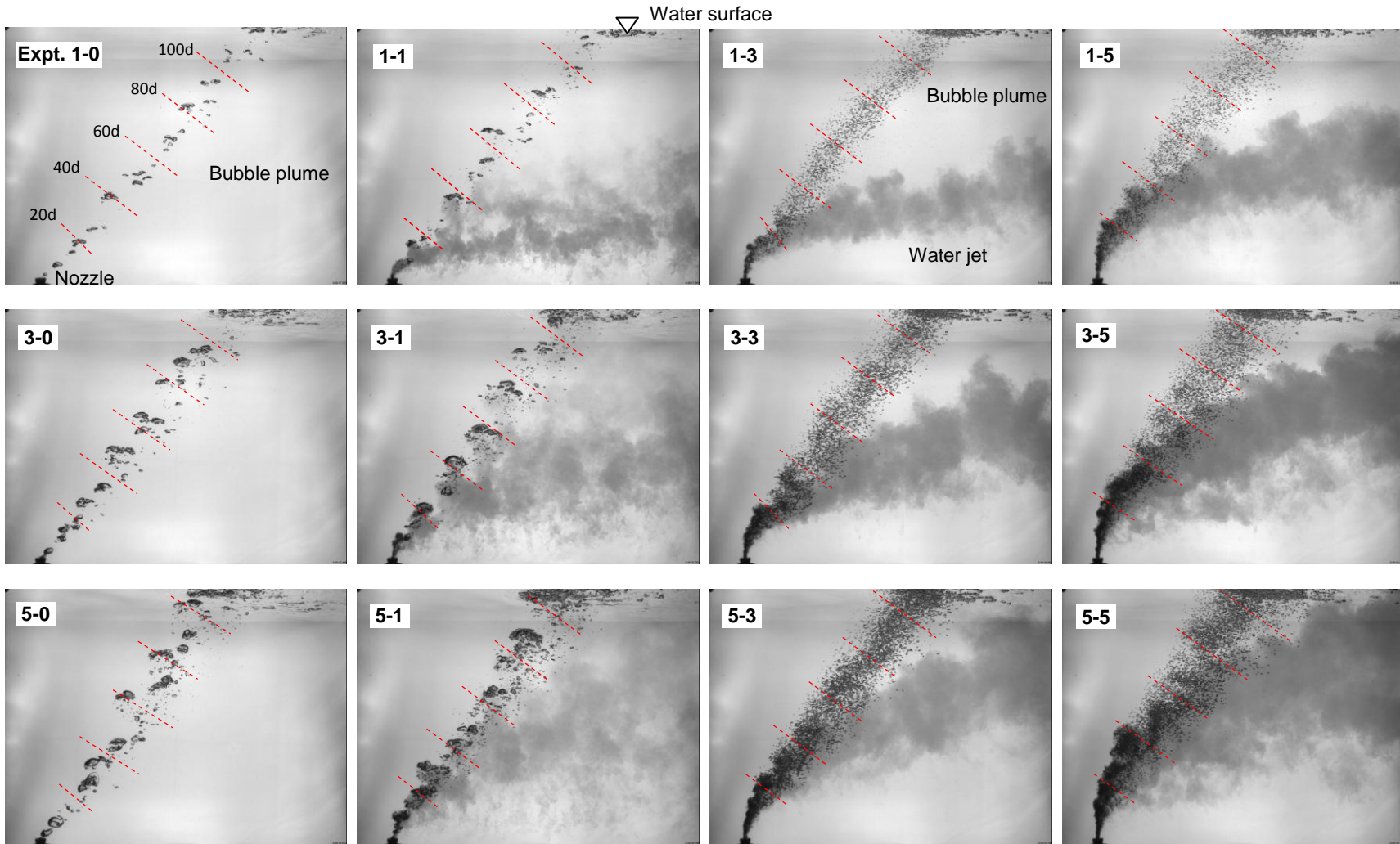


Figure 6-4. Photos of bubble plumes or bubbly jets in 12 experimental conditions; side view, photo size: $73.7 \times 55.0 \text{ cm}^2$; the first and second numbers in the experiment scenarios represent the gas and water discharges at the nozzle exit (unit: LPM), respectively, and the same way will be used in all the following figures

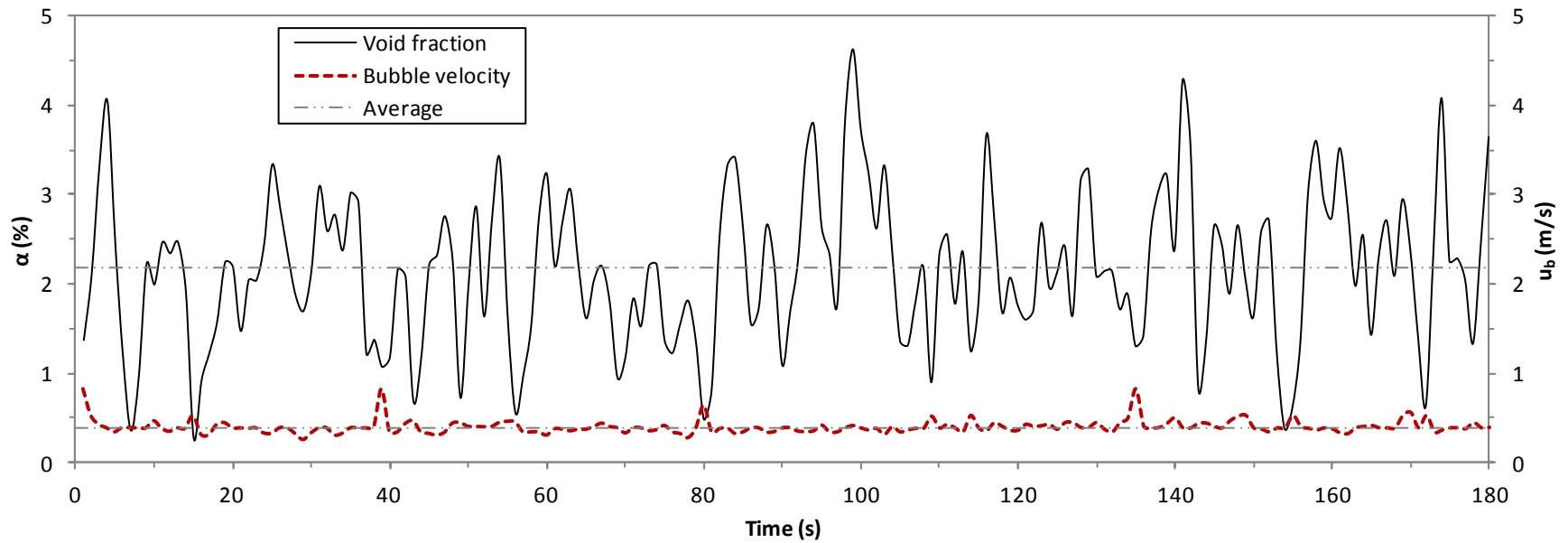


Figure 6-5. Typical time series of gas void fraction and bubble velocity obtained from the optical probe system; time series using moving average, with time step of 1 second and averaging window size of 2 seconds; measurement taken near the bubbly jet centerline ($\eta = -0.14$ cm, $y = 0.35$ cm) at Section 80d in Experiment 3-3.

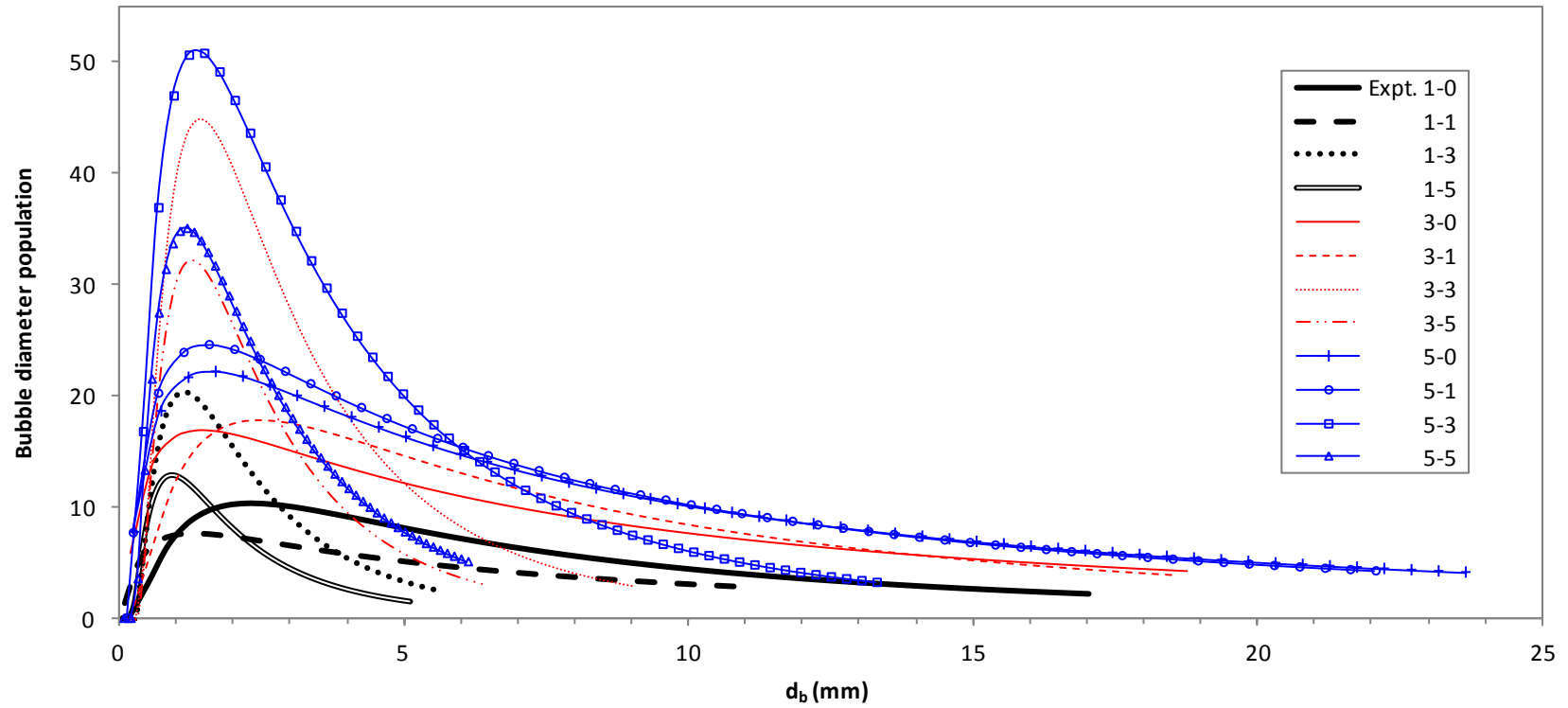


Figure 6-6. Typical bubble size distribution measured at the bubble plume centerline at Section 80d in each experiment; data were directly obtained from the optical probe system, without adjustment for bubble non-sphericity, to exclude the change of size distribution due to the adjustment

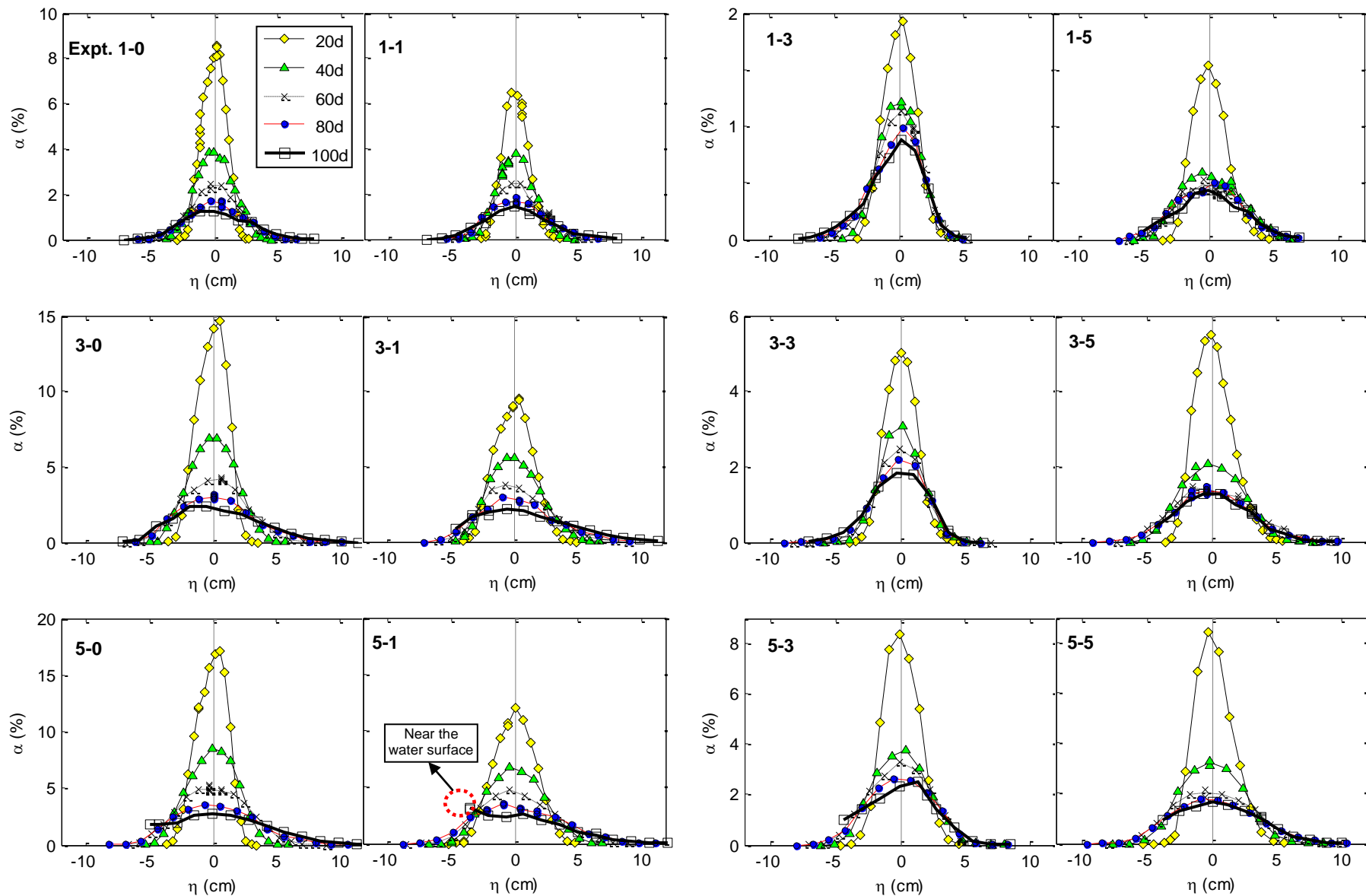


Figure 6-7. Distribution of gas void fraction in the η direction

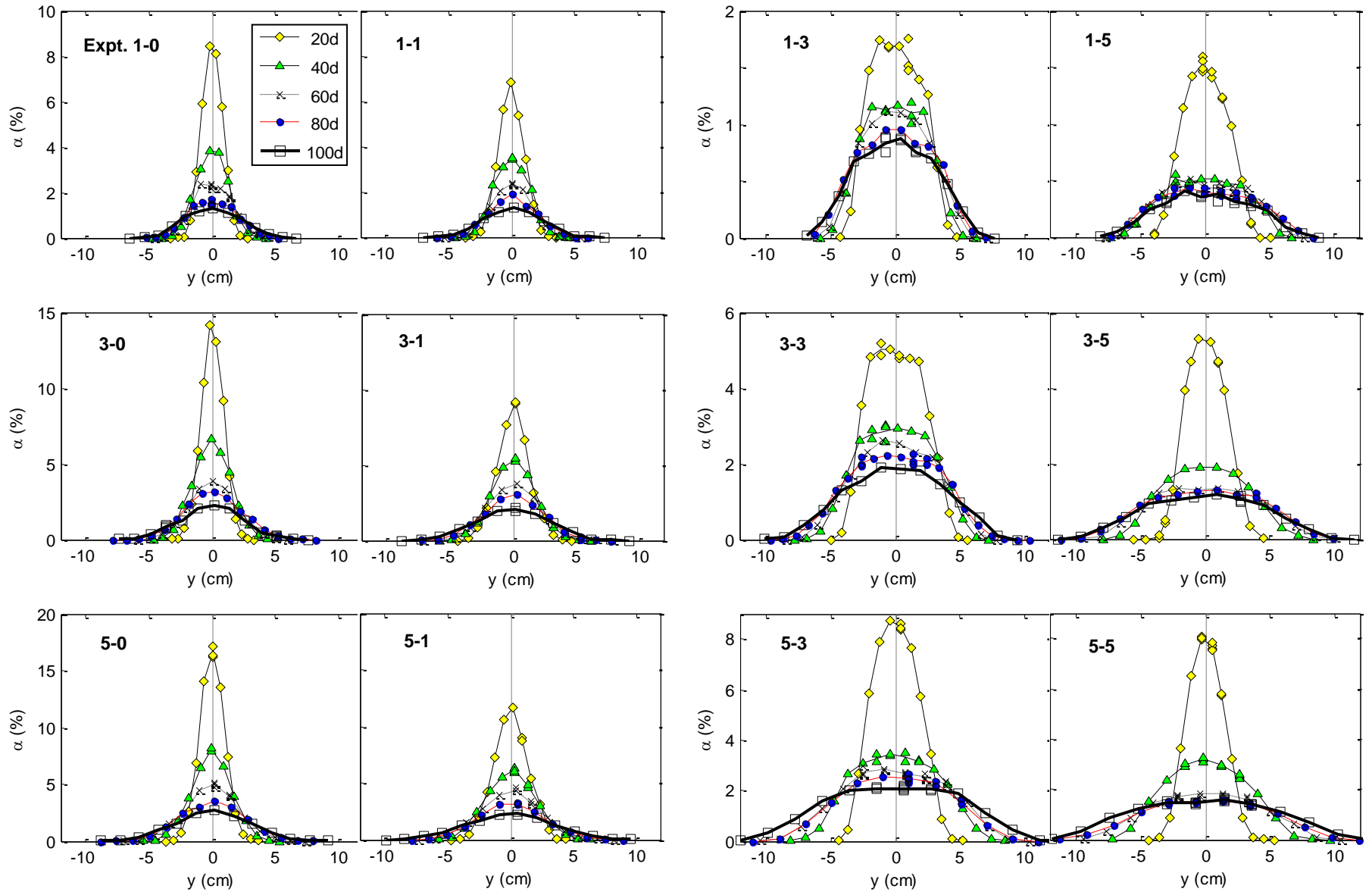


Figure 6-8. Distribution of gas void fraction in the y direction

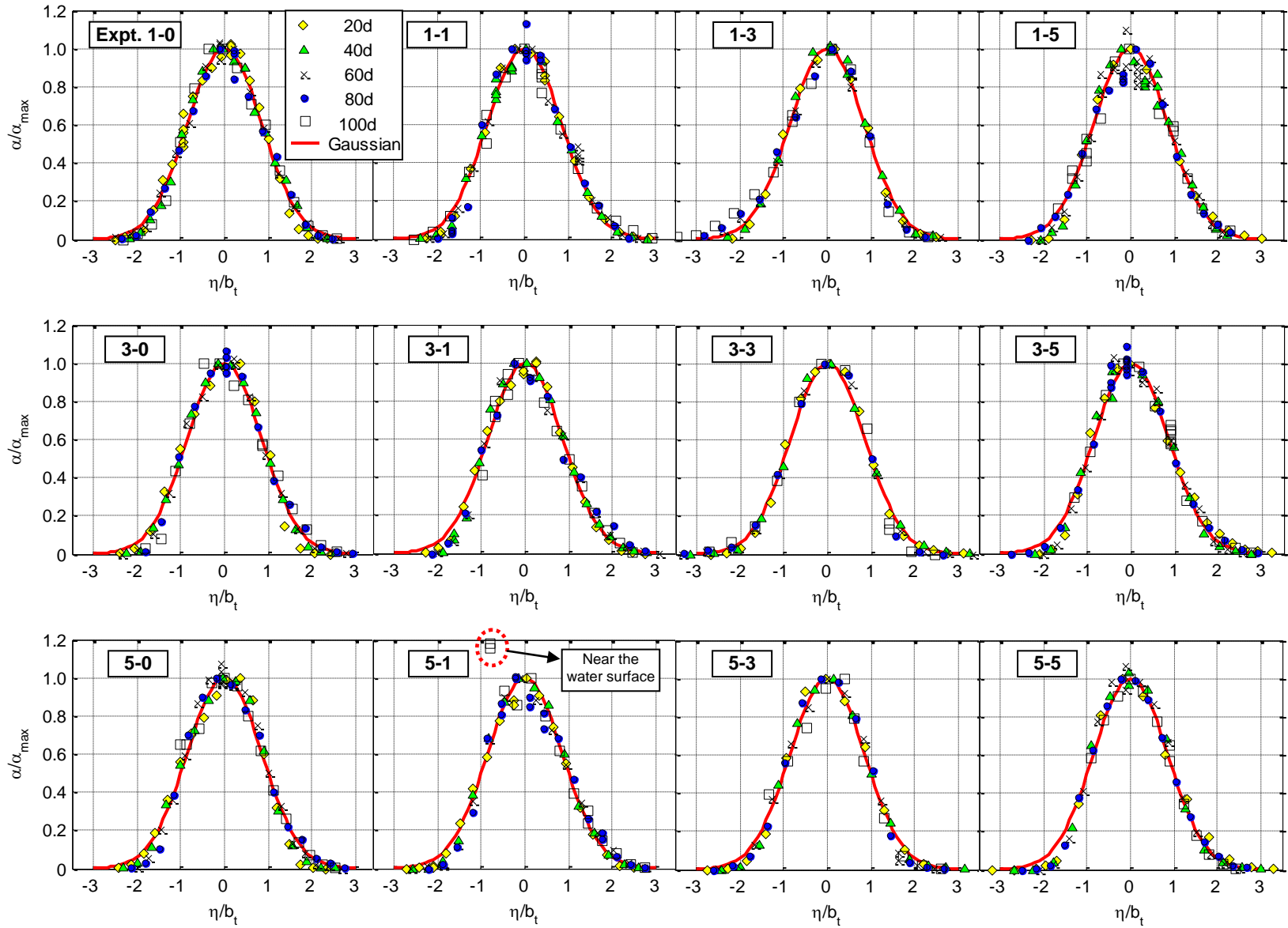


Figure 6-9. Distribution of dimensionless gas void fraction in the η direction

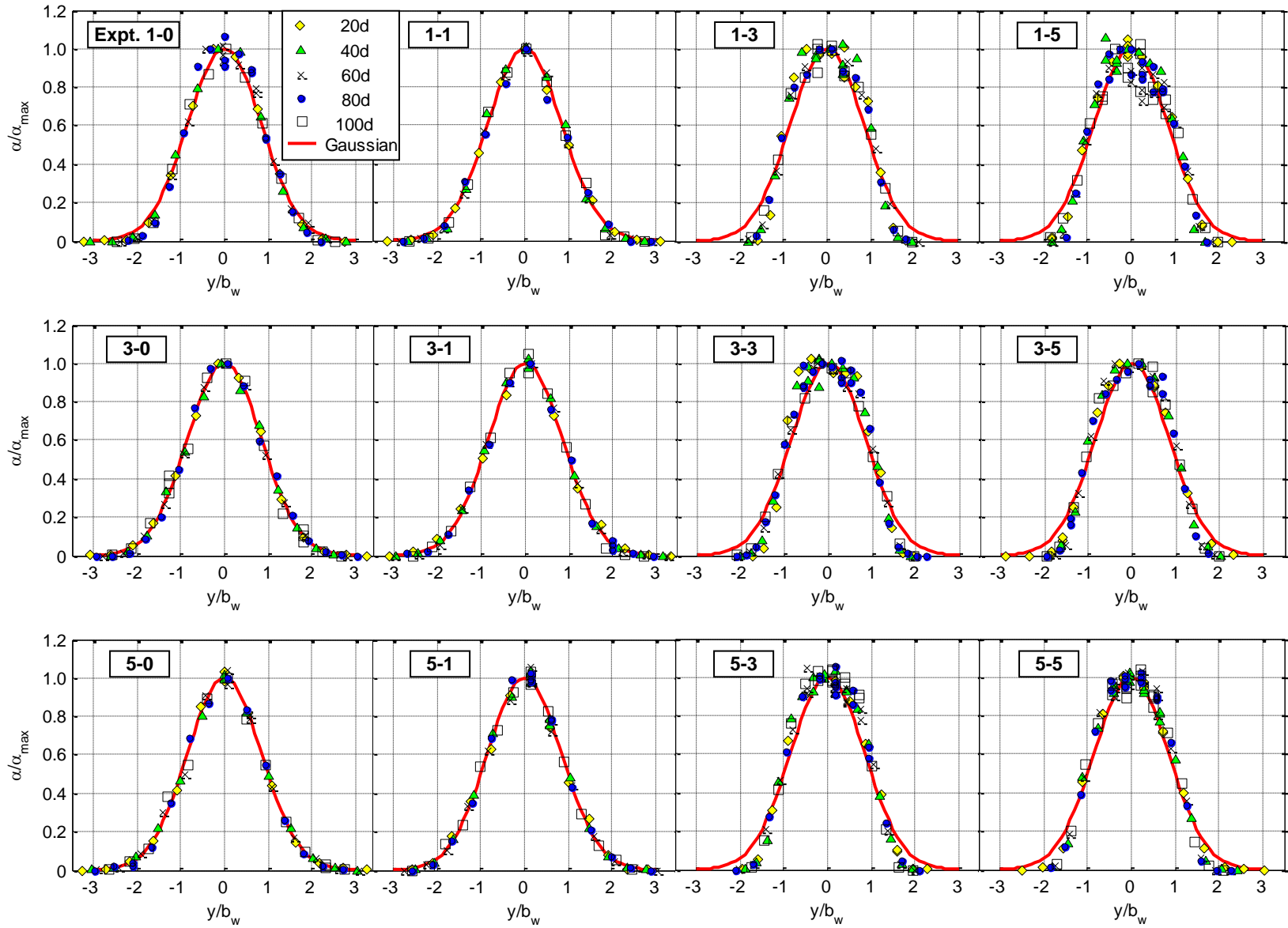


Figure 6-10. Distribution of dimensionless gas void fraction in the y direction

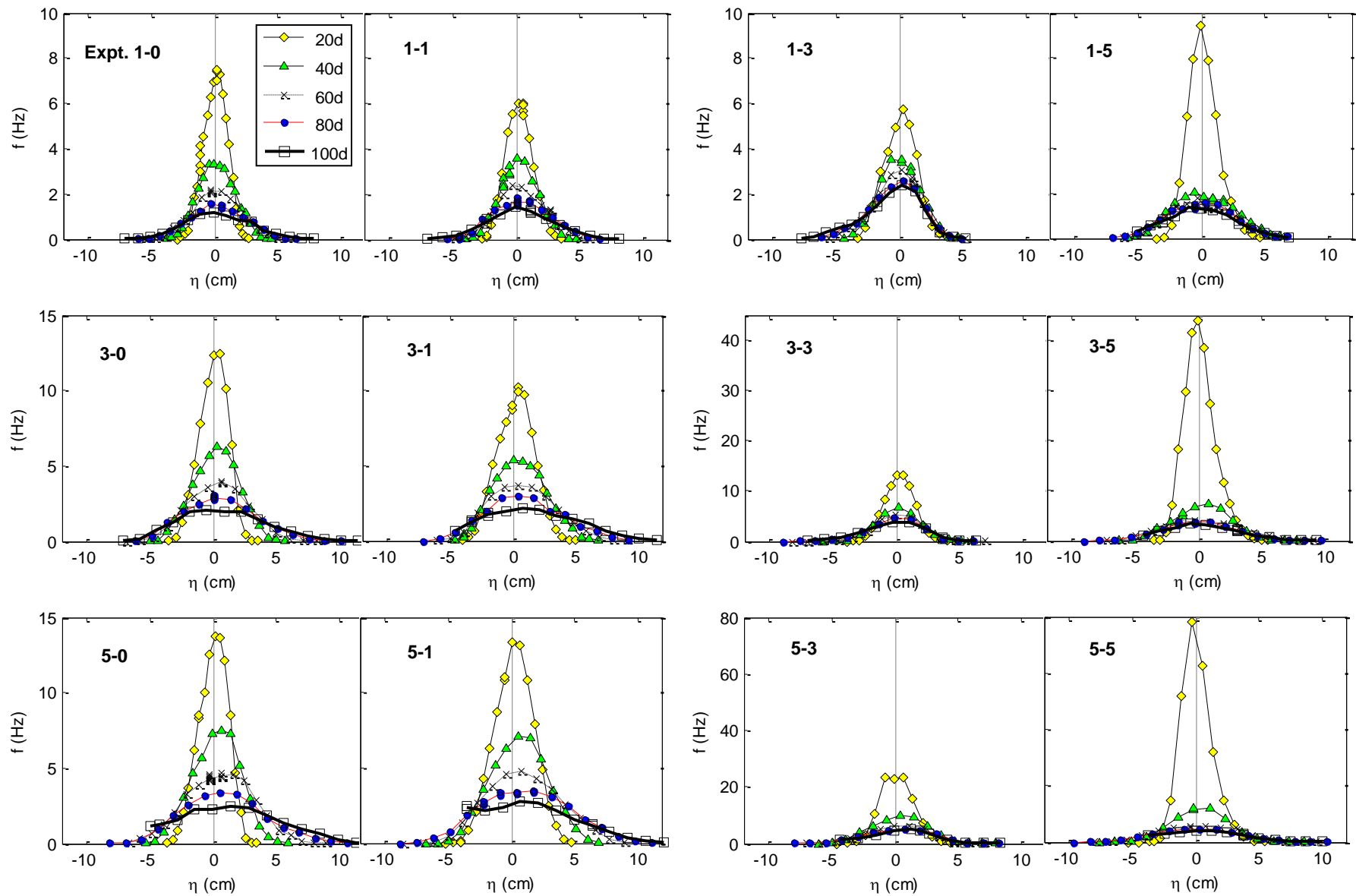


Figure 6-11. Distribution of bubble frequency in the η direction

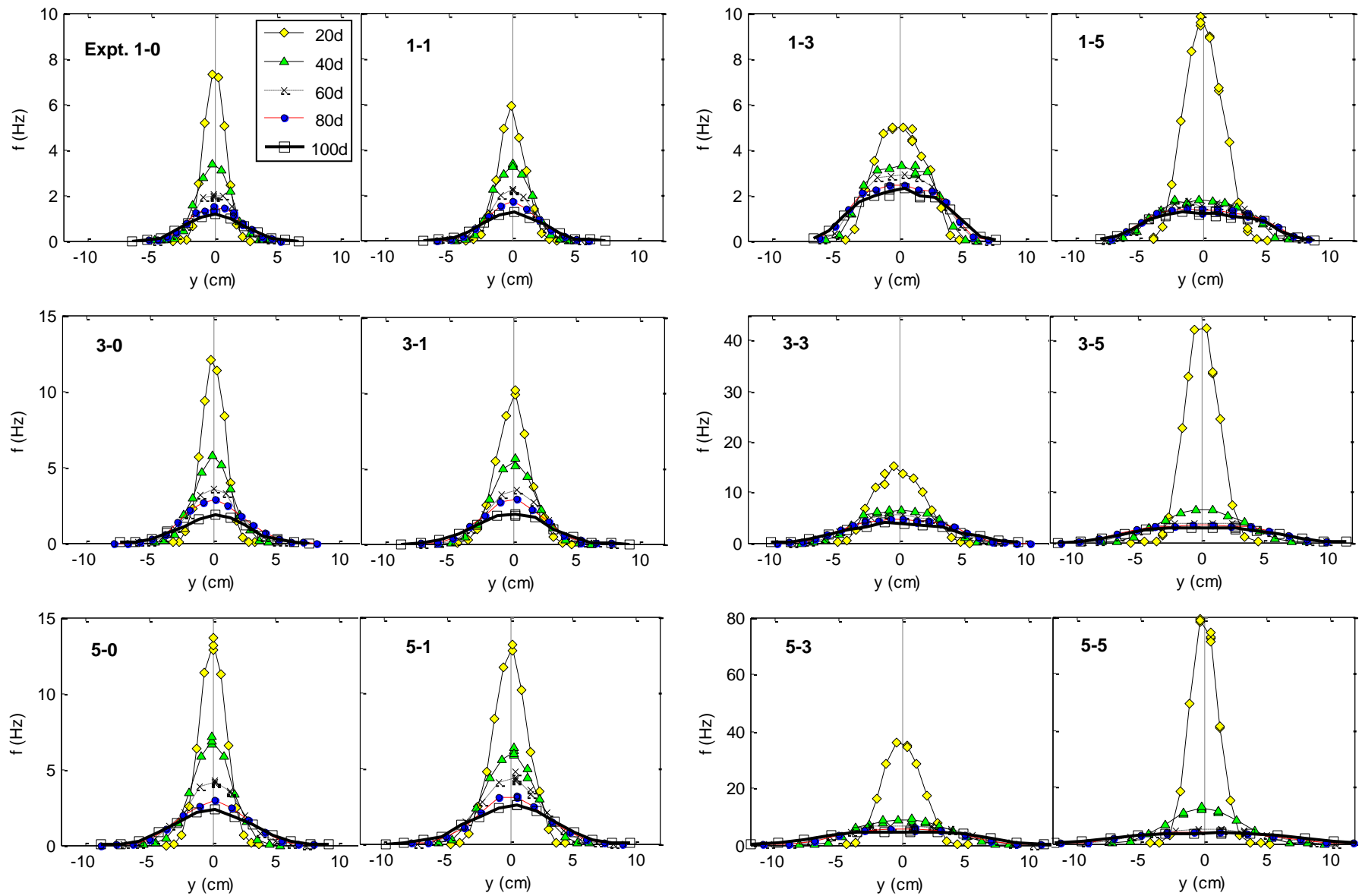


Figure 6-12. Distribution of bubble frequency in the y direction

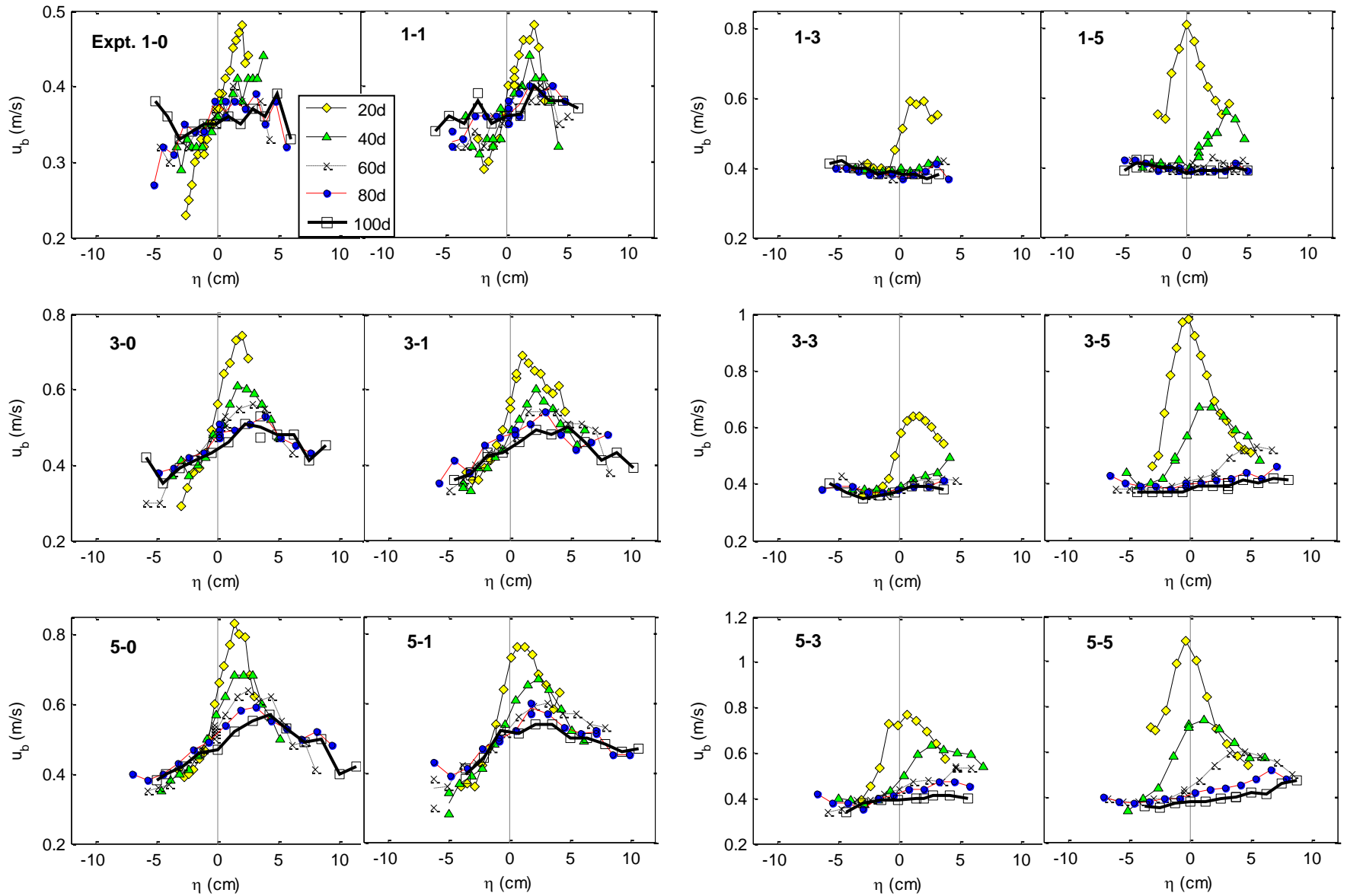


Figure 6-13. Distribution of bubble velocity in the η direction

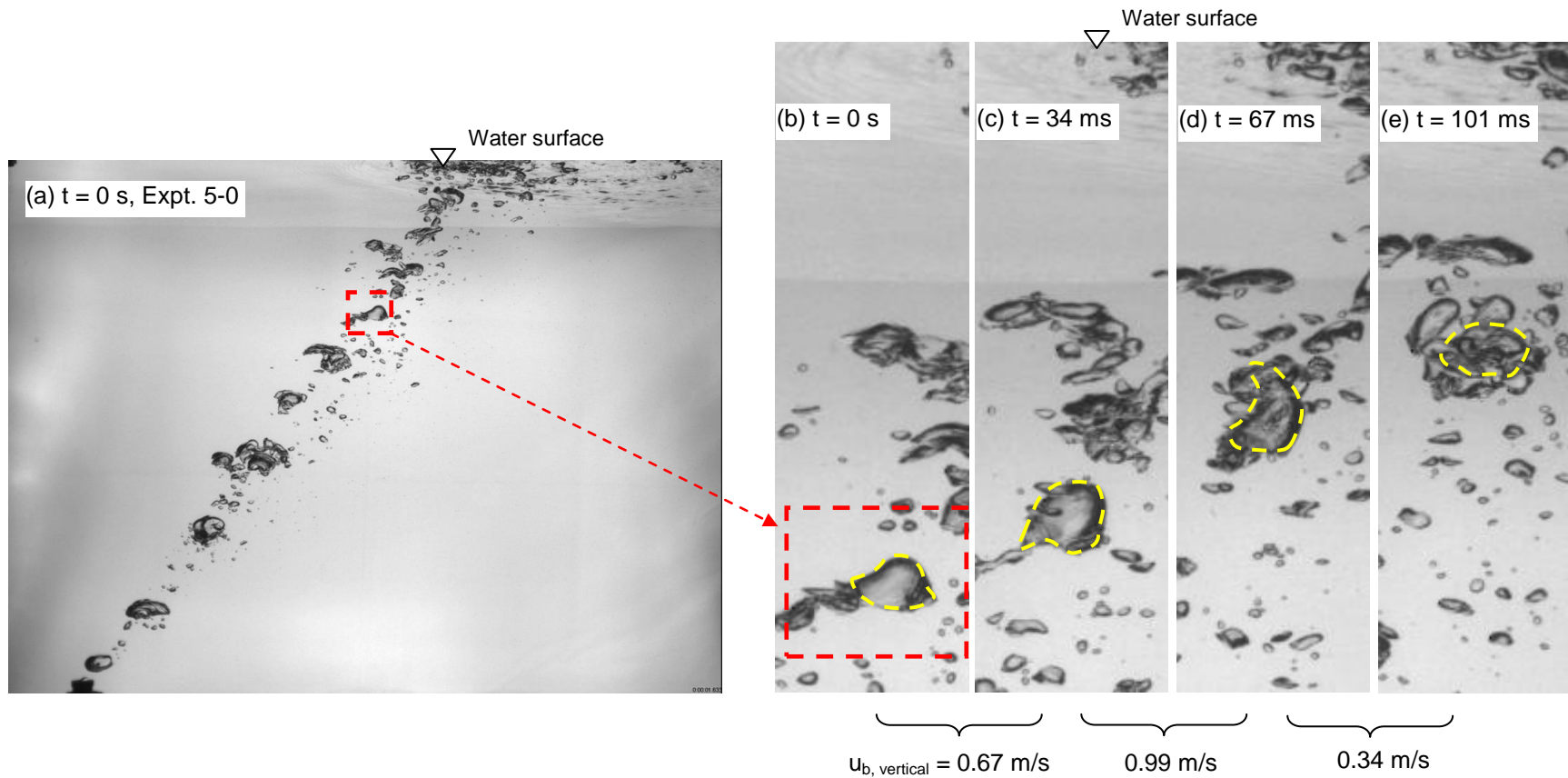


Figure 6-14. Possible effect of bubble wakes on a single bubble in Expt. 5-0; although tracking the same bubble may not appear direct in part of the images in Fig. (b)-(e), it is more direct by comparing the whole images; bubble velocities are based on the vertical locations of the front of the bubble, i.e. vertical interfacial velocities, and the interfacial velocity is used in the RBI optical probe system (Kiambi et al. 2003); image size in (a): $73.7 \times 55.0 \text{ cm}^2$ and in (b)-(e): $5.5 \times 18.8 \text{ cm}^2$

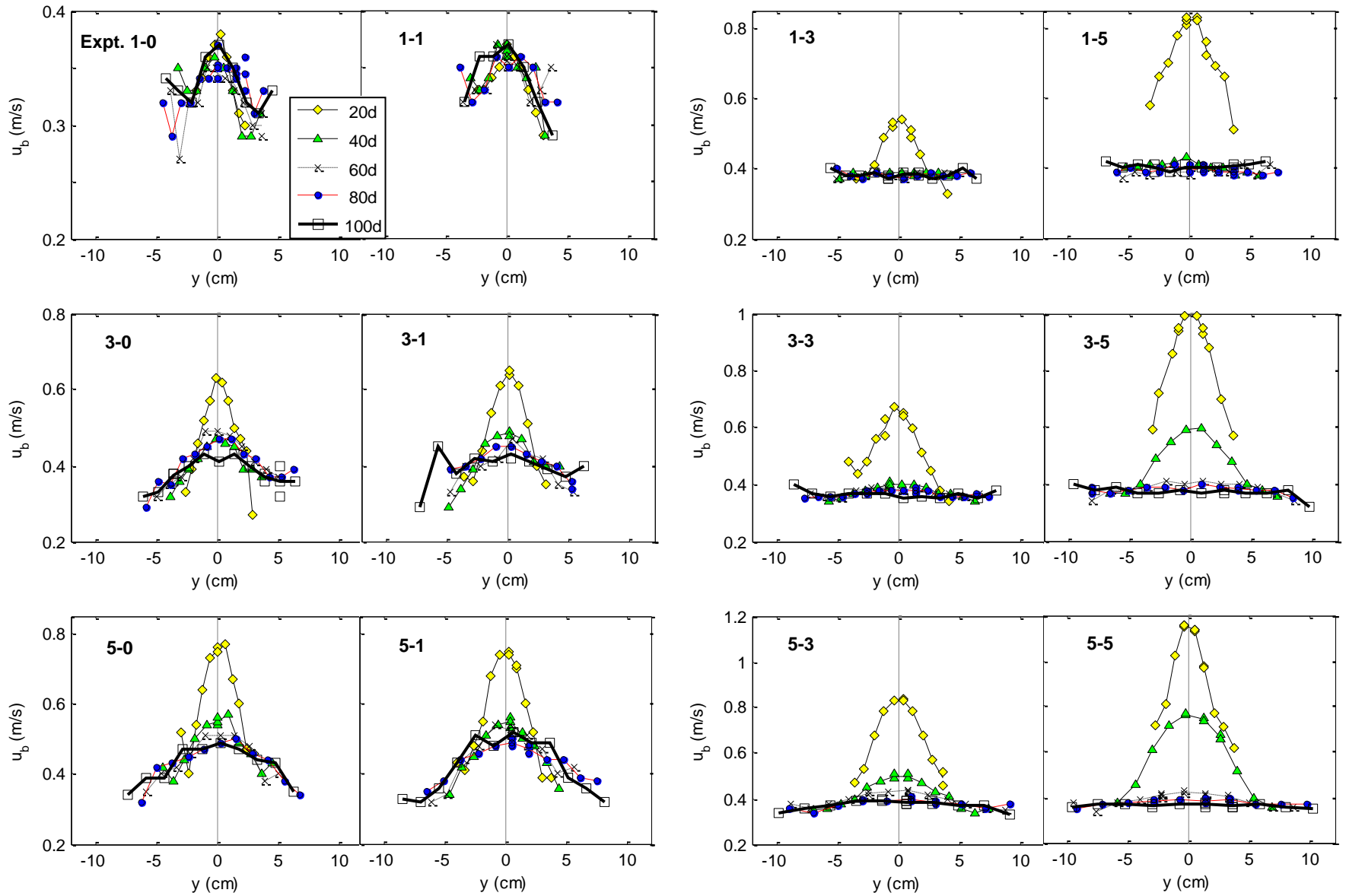


Figure 6-15. Distribution of bubble velocity in the y direction

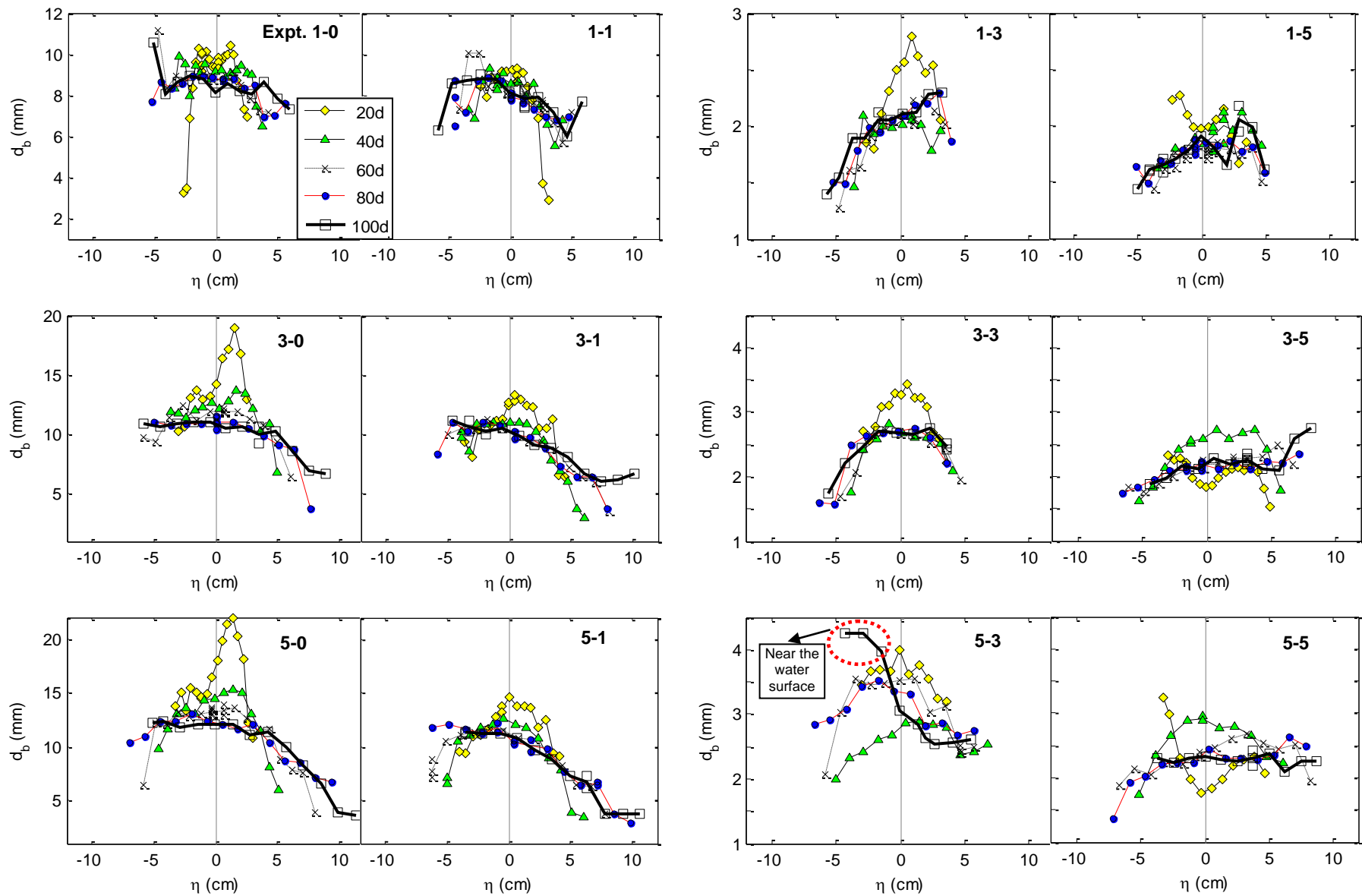


Figure 6-16. Distribution of bubble diameter in the η direction

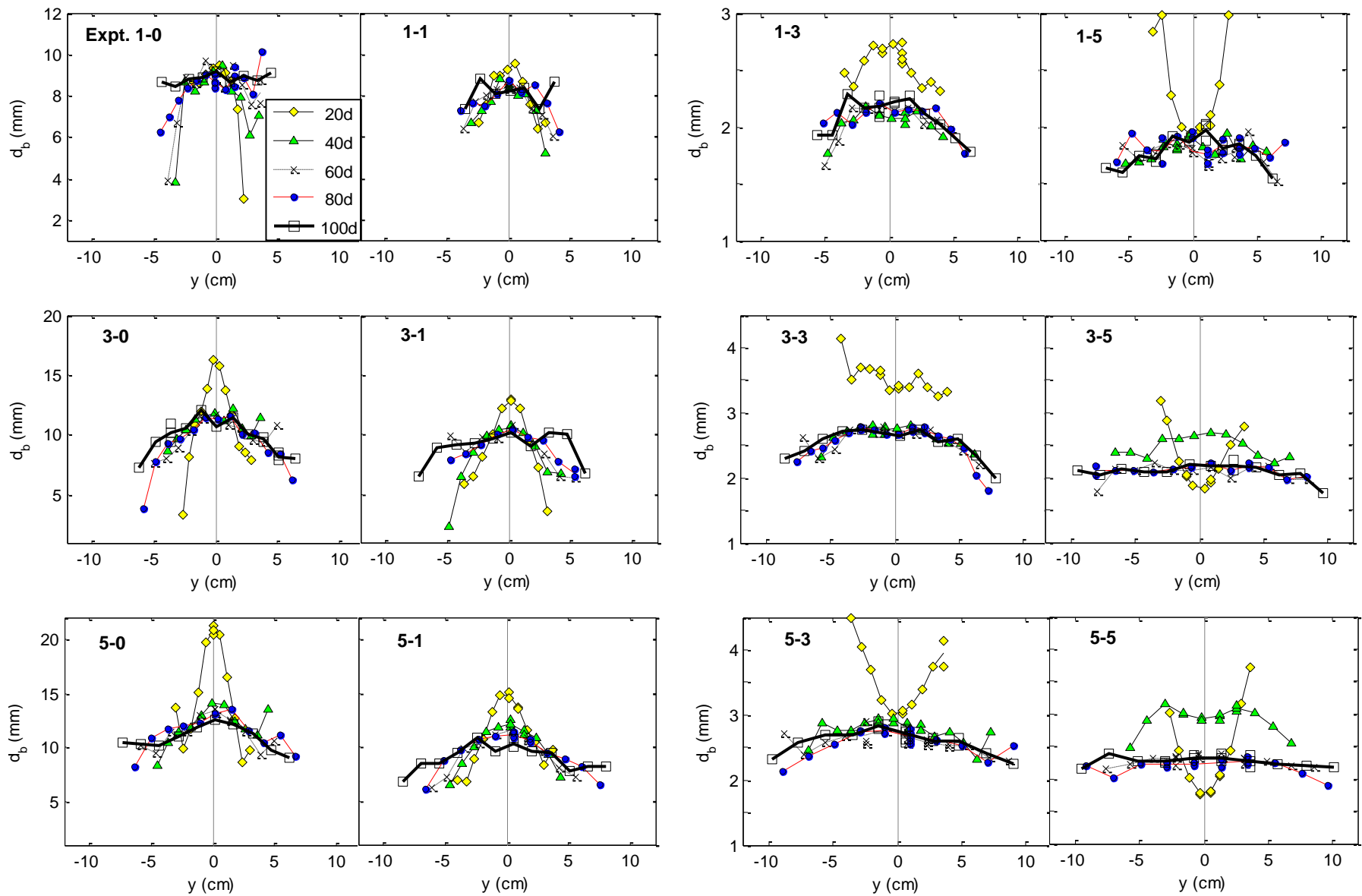


Figure 6-17. Distribution of bubble diameter in the y direction

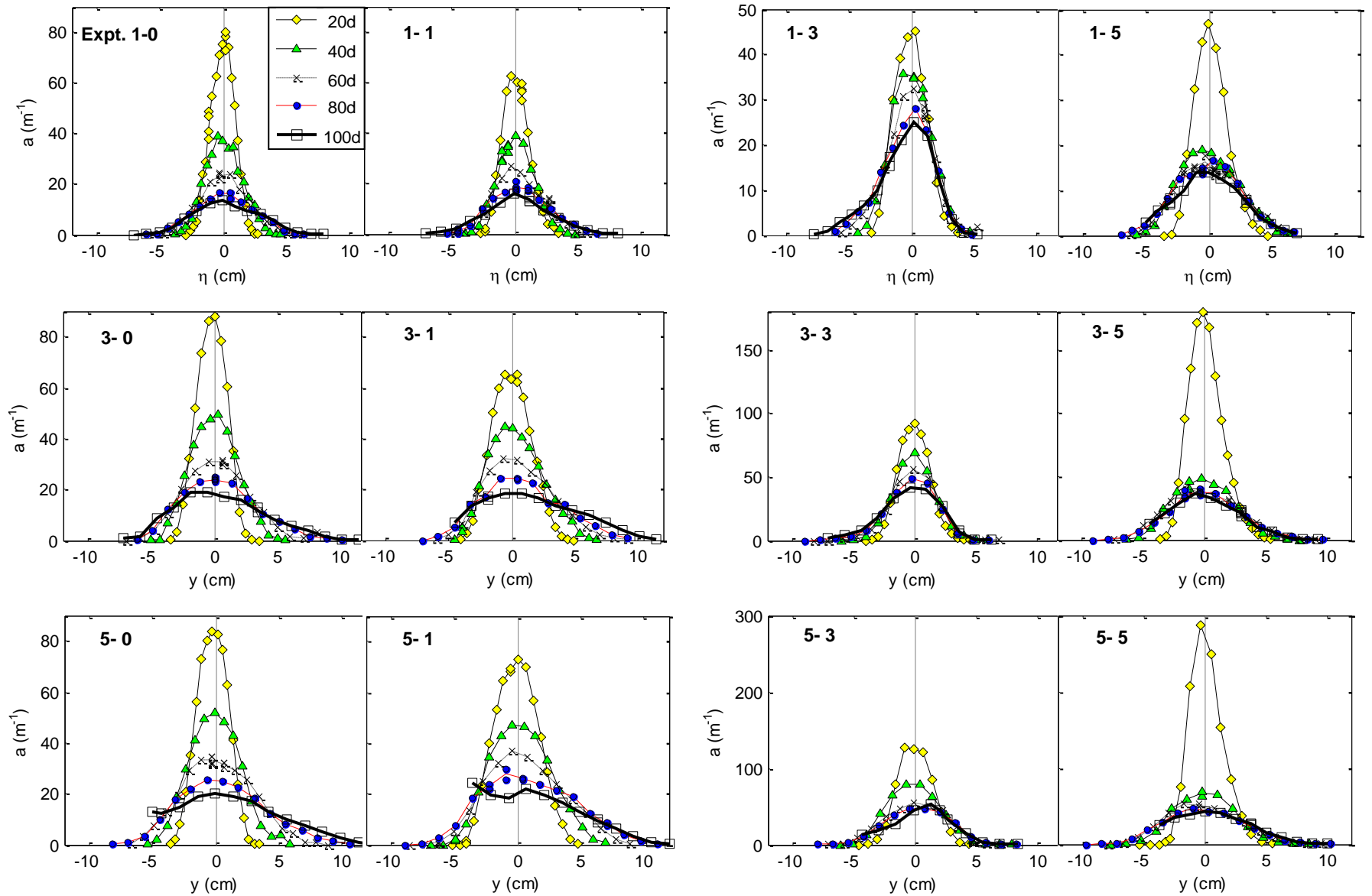


Figure 6-18. Distribution of specific interfacial area in the η direction

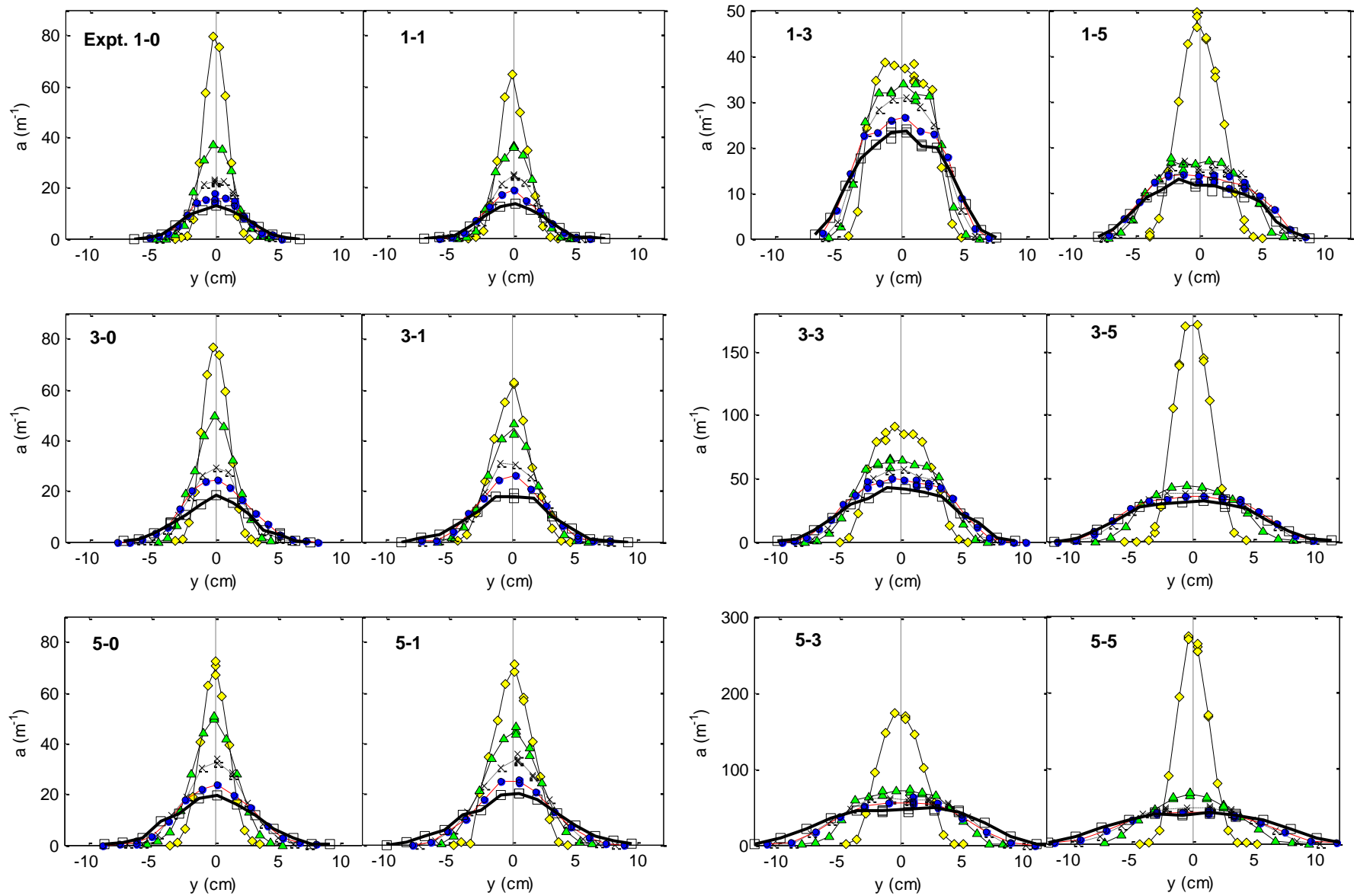


Figure 6-19. Distribution of specific interfacial area in the y direction

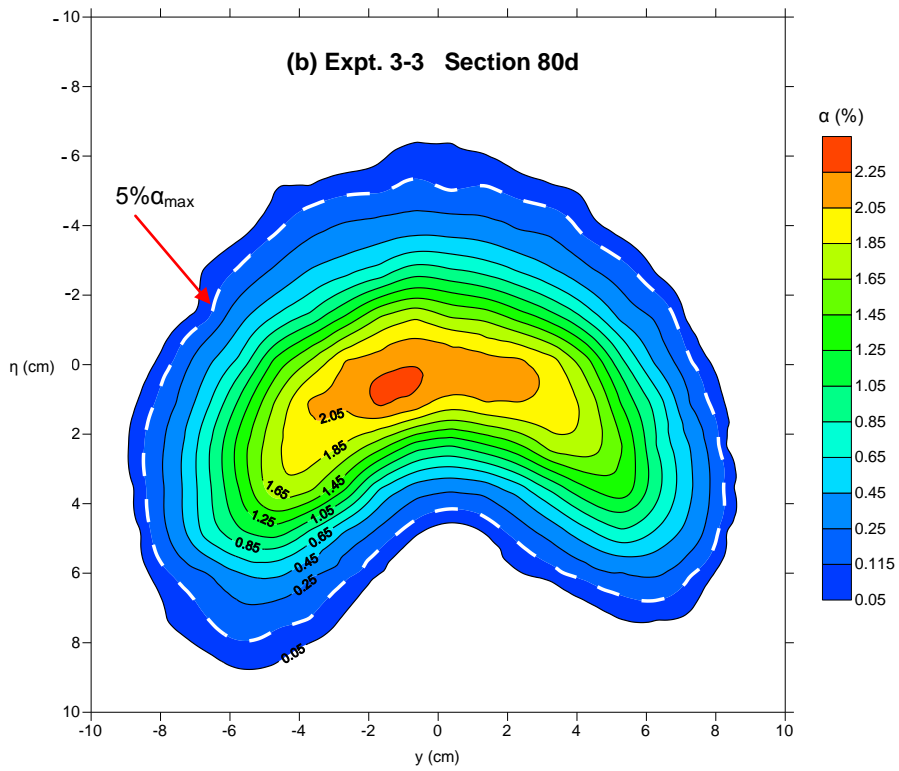
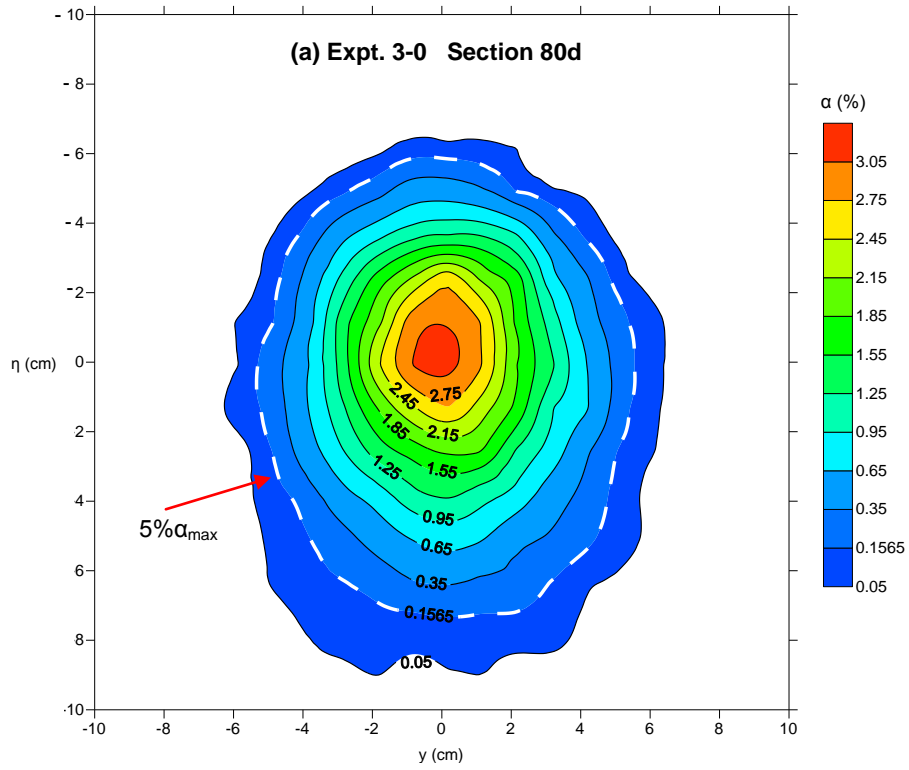


Figure 6-20. Distribution of void fraction at Section 80d in (a) experiment 3-0 and (b) experiment 3-3, with a measurement mesh of $1 \times 1.25 \text{ cm}^2$

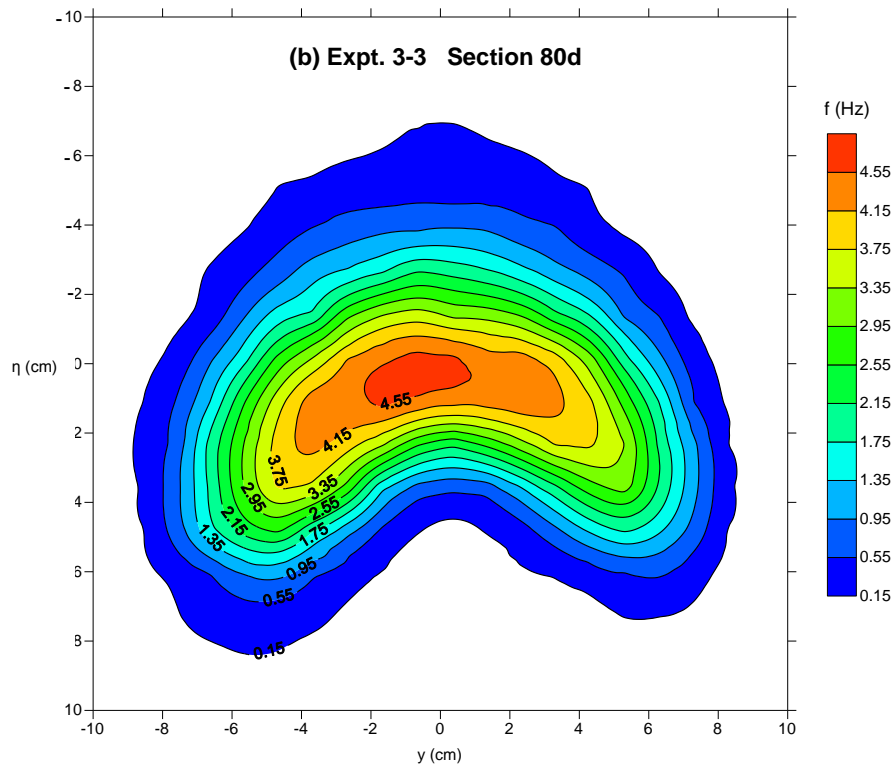
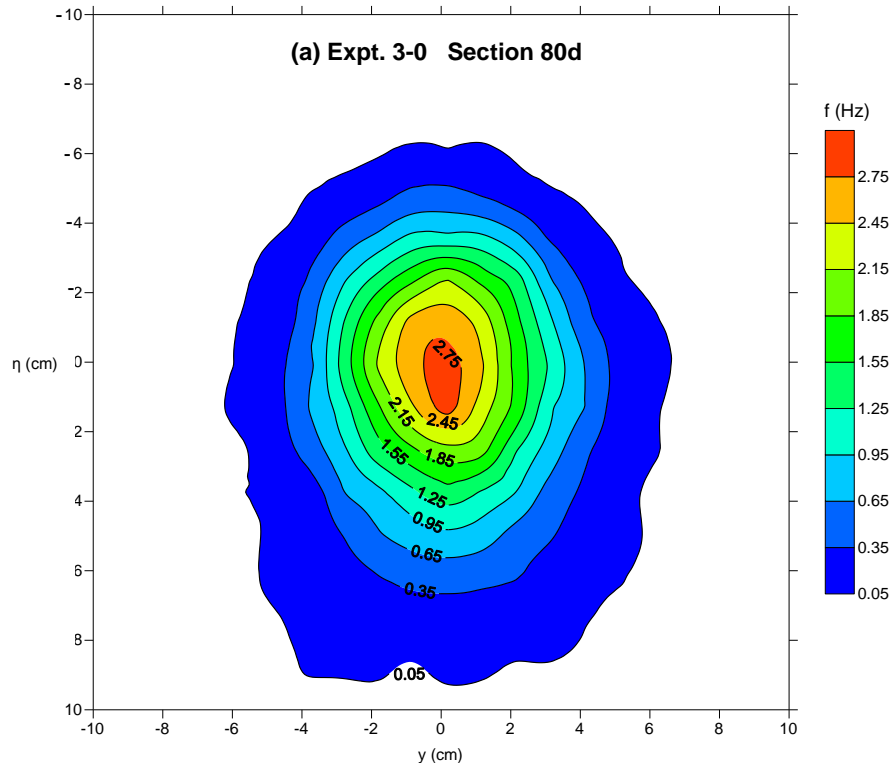


Figure 6-21. Distribution of bubble frequency at Section 80d in (a) experiment 3-0 and (b) experiment 3-3, with a measurement mesh of $1 \times 1.25 \text{ cm}^2$

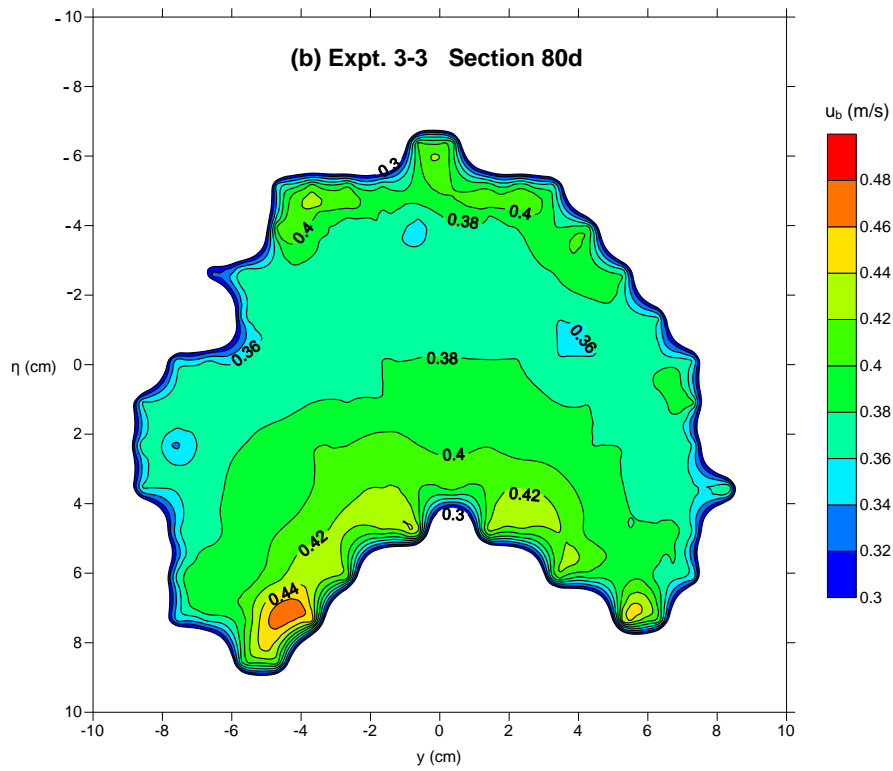
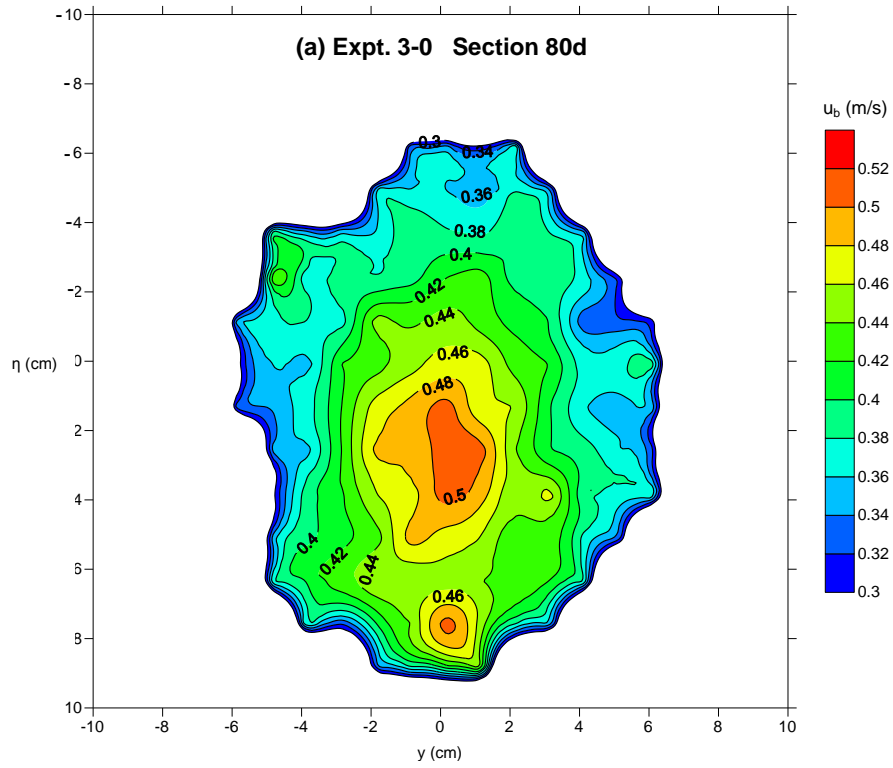


Figure 6-22. Distribution of bubble velocity at Section 80d in (a) experiment 3-0 and (b) experiment 3-3, with a measurement mesh of $1 \times 1.25 \text{ cm}^2$

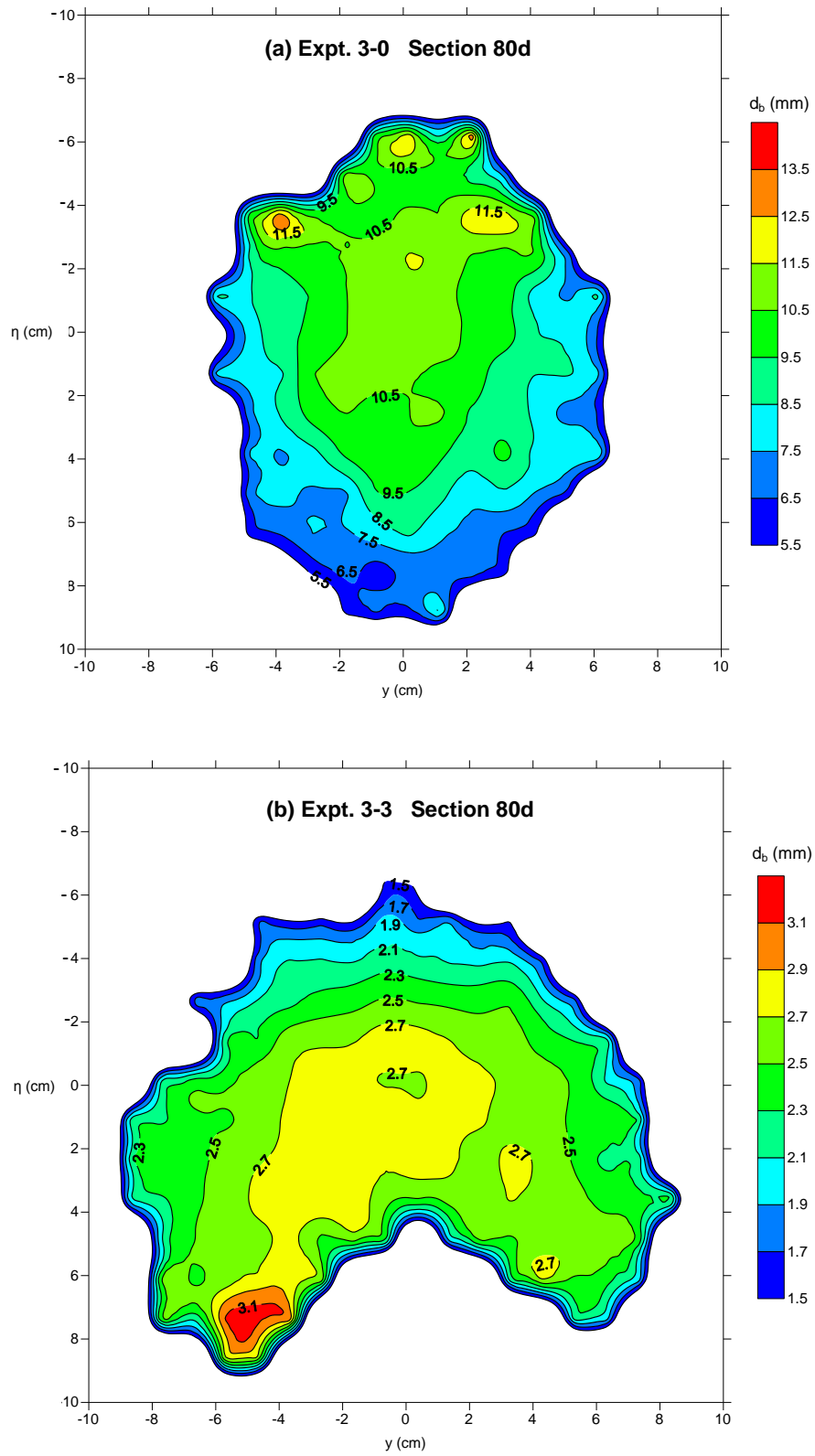


Figure 6-23. Distribution of bubble diameter at Section 80d in (a) experiment 3-0 and (b) experiment 3-3, with a measurement mesh of $1 \times 1.25 \text{ cm}^2$

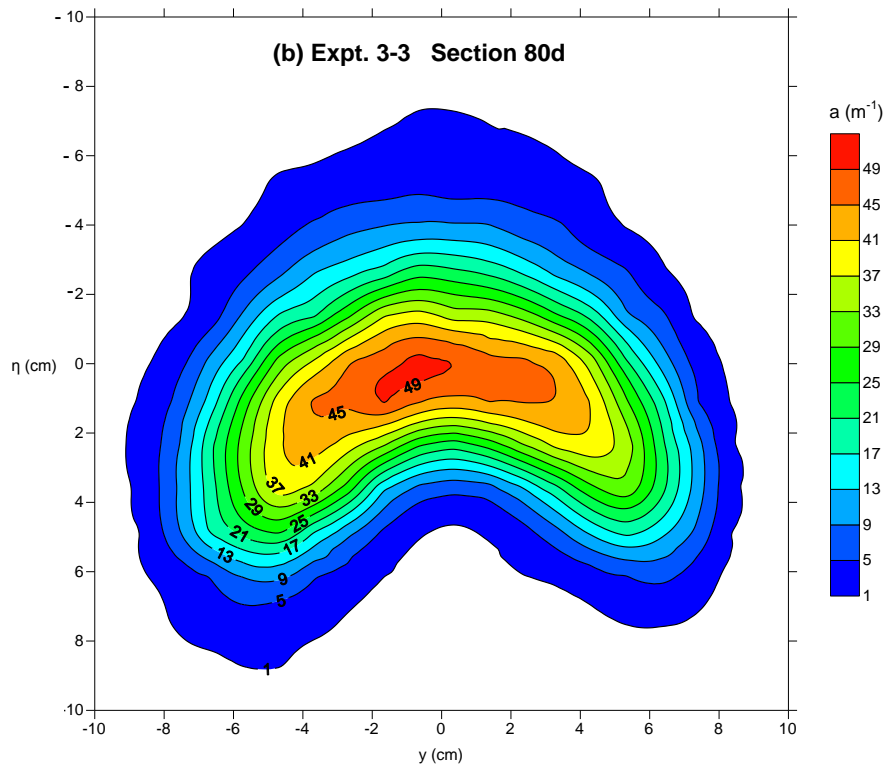
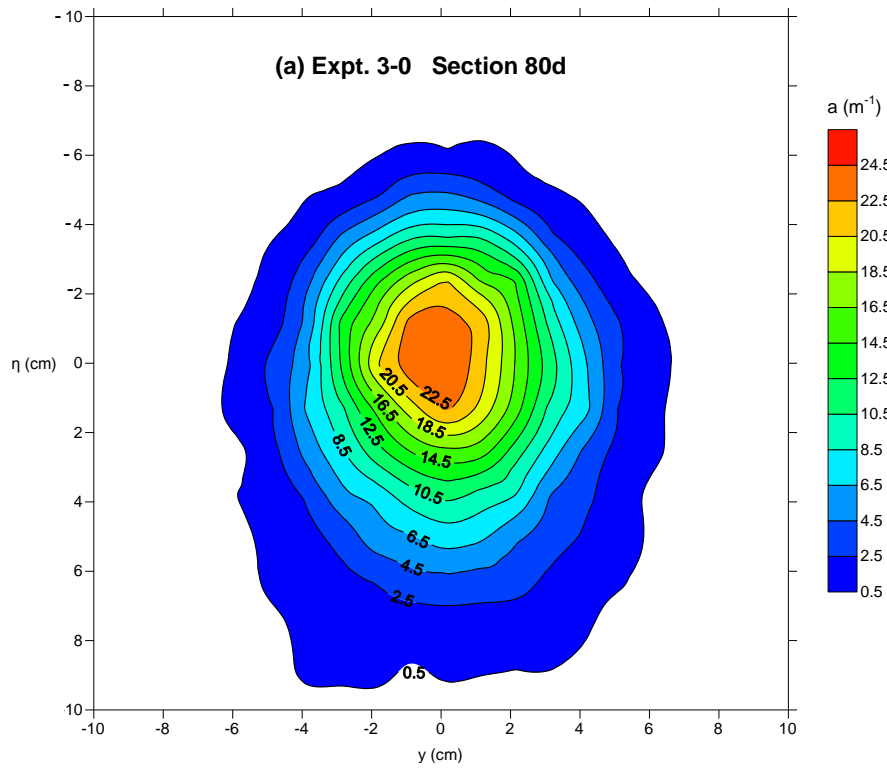


Figure 6-24. Distribution of bubble specific interfacial area at Section 80d in (a) experiment 3-0 and (b) experiment 3-3, with a measurement mesh of $1 \times 1.25 \text{ cm}^2$

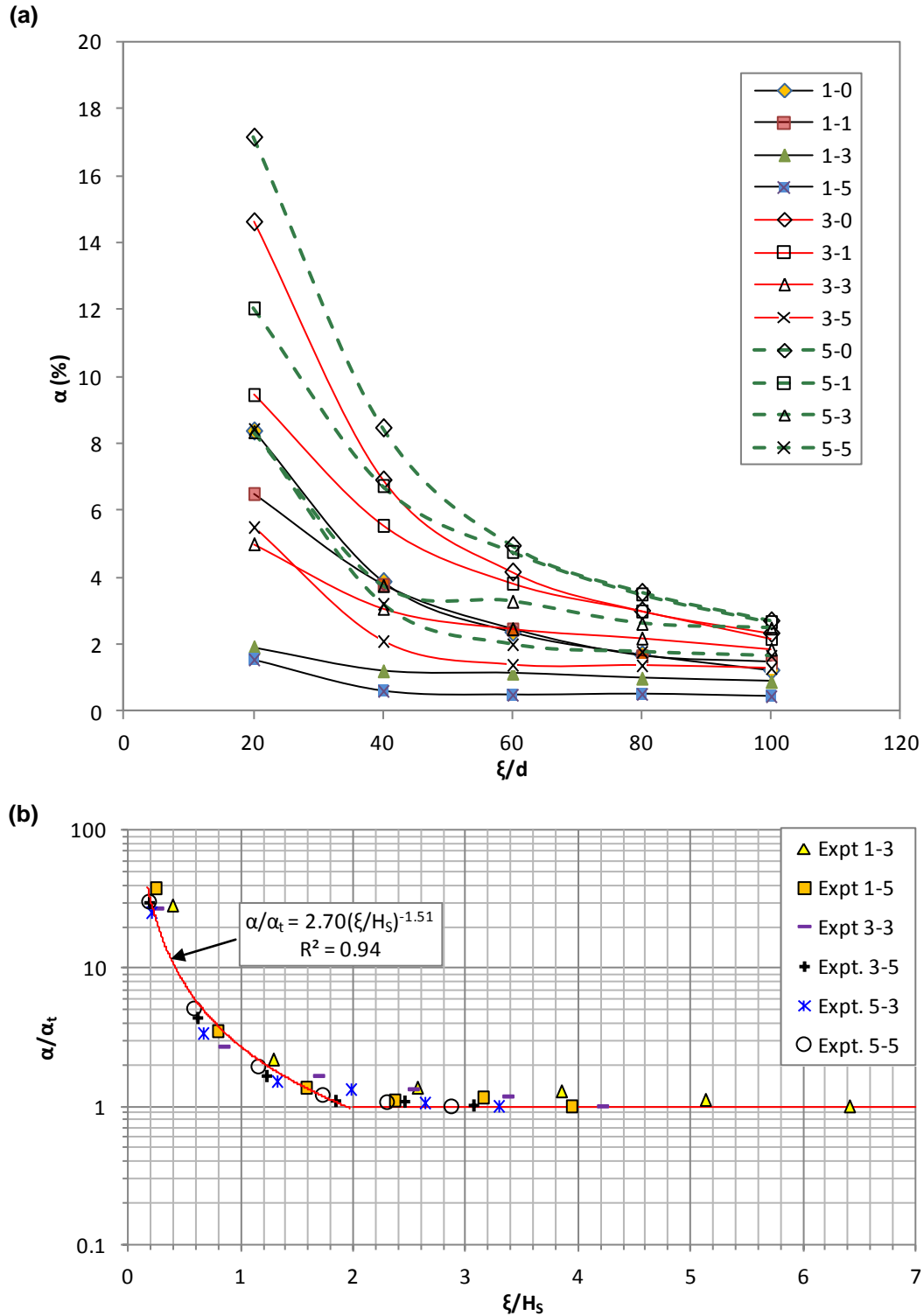


Figure 6-25. Change of (a) dimensional gas void fraction along the centerlines of bubble plumes or bubbly jets; and (b) dimensionless gas void fraction along the centerlines of bubbly jets with $Q_w = 3$ or 5 LPM ($Re > 8,000$)

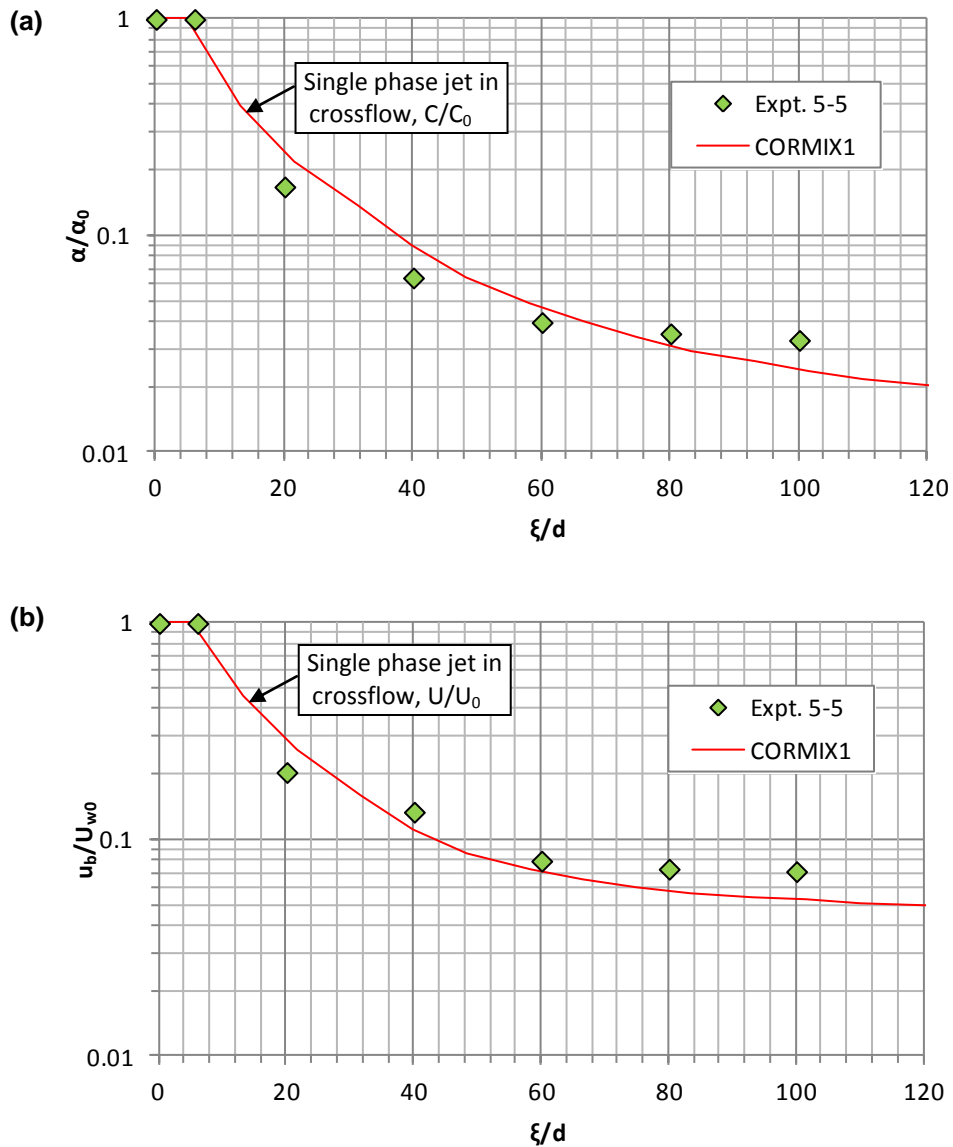


Figure 6-26. Comparison between the experimental result of Expt. 5-5 and the modeling result from CORMIX1 for a single-phase jet in crossflow that has initial concentration $C_0 = \alpha_0$ and initial velocity $U_0 = U_{w0}$ (using Method III in Table 1) as in Expt. 5-5, (a) dimensionless centerline gas void fraction or concentration and (b) dimensionless centerline bubble velocity or jet velocity

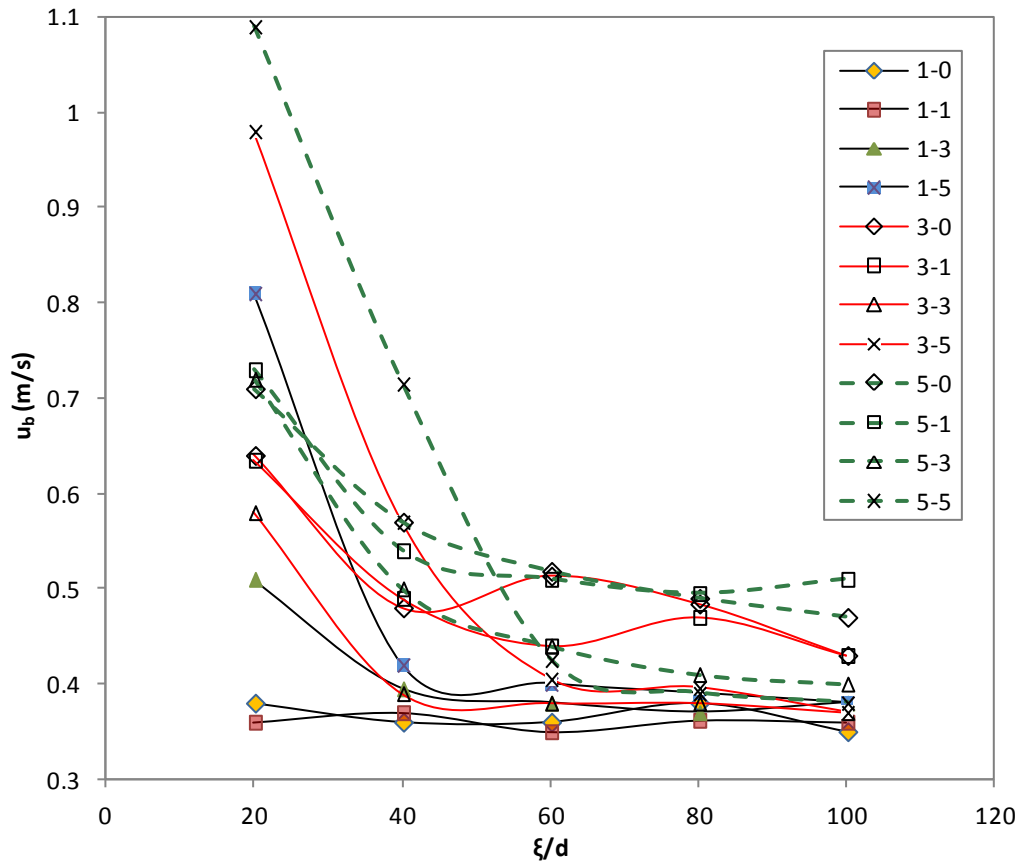


Figure 6-27. Change of bubble velocity along the centerlines of bubble plumes or bubbly jets

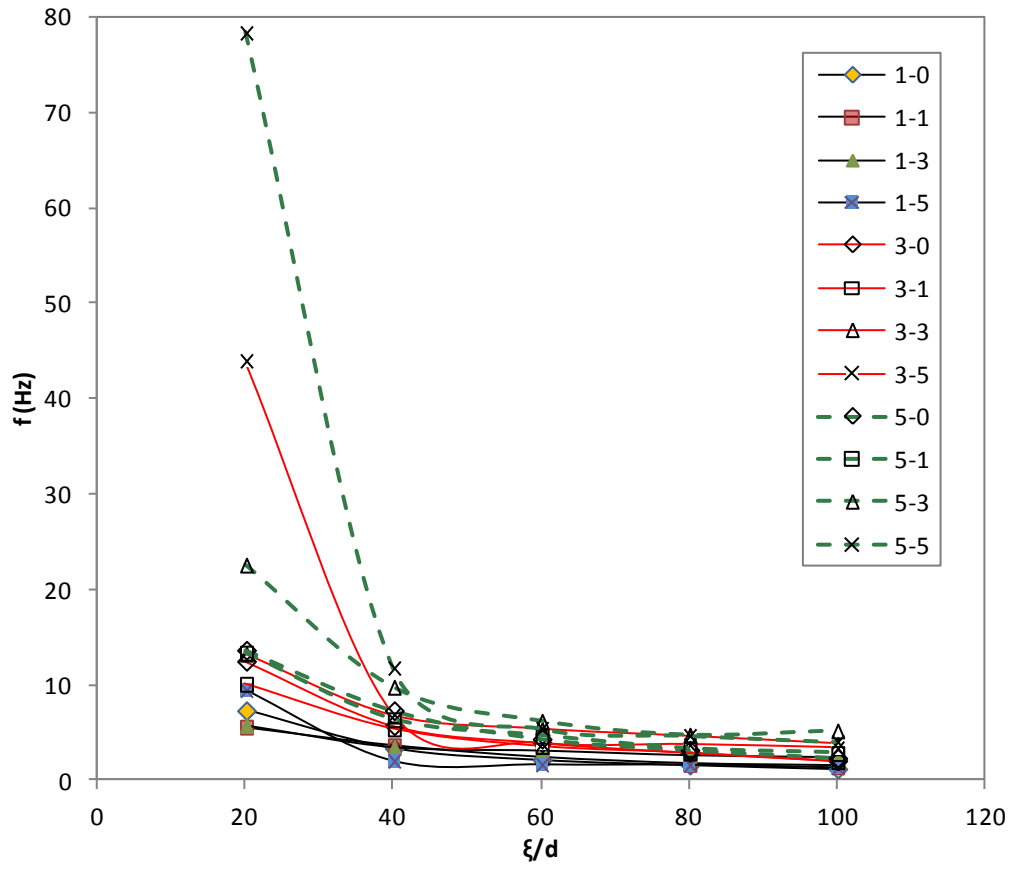


Figure 6-28. Change of bubble frequency along the centerlines of bubble plumes or bubbly jets

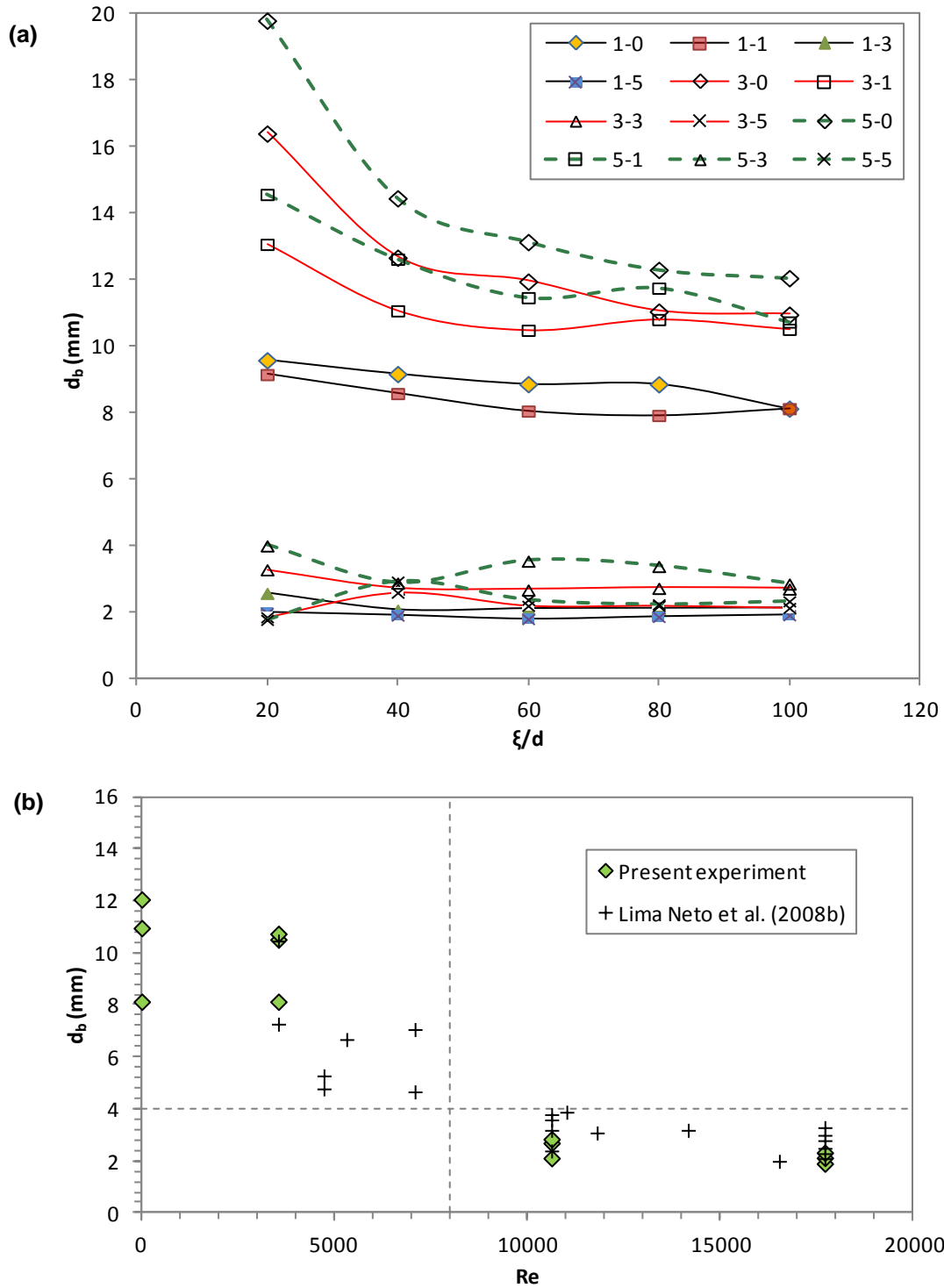


Figure 6-29. (a) Change of bubble diameter along the centerlines of bubble plumes or bubbly jets; (b) change of bubble diameter at the centerlines at Section $100d$ with Reynolds number based on superficial water velocity at the nozzle exit

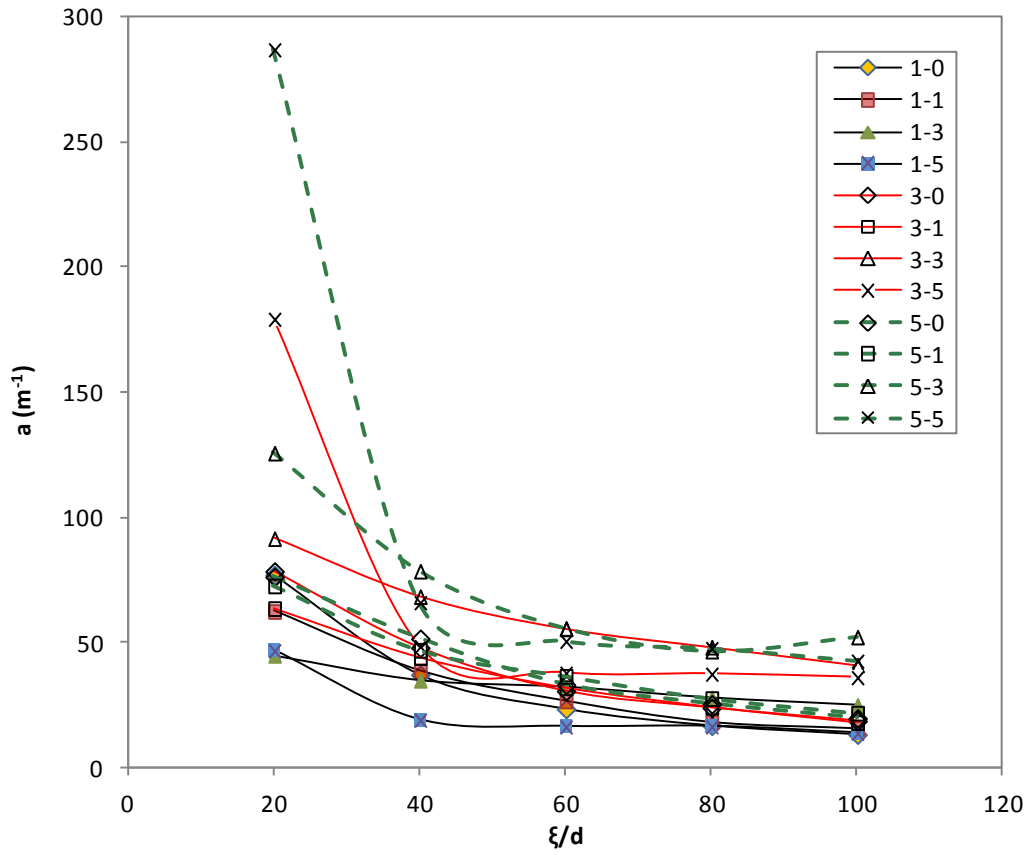


Figure 6-30. Change of specific interfacial area along the centerlines of bubble plumes or bubbly jet

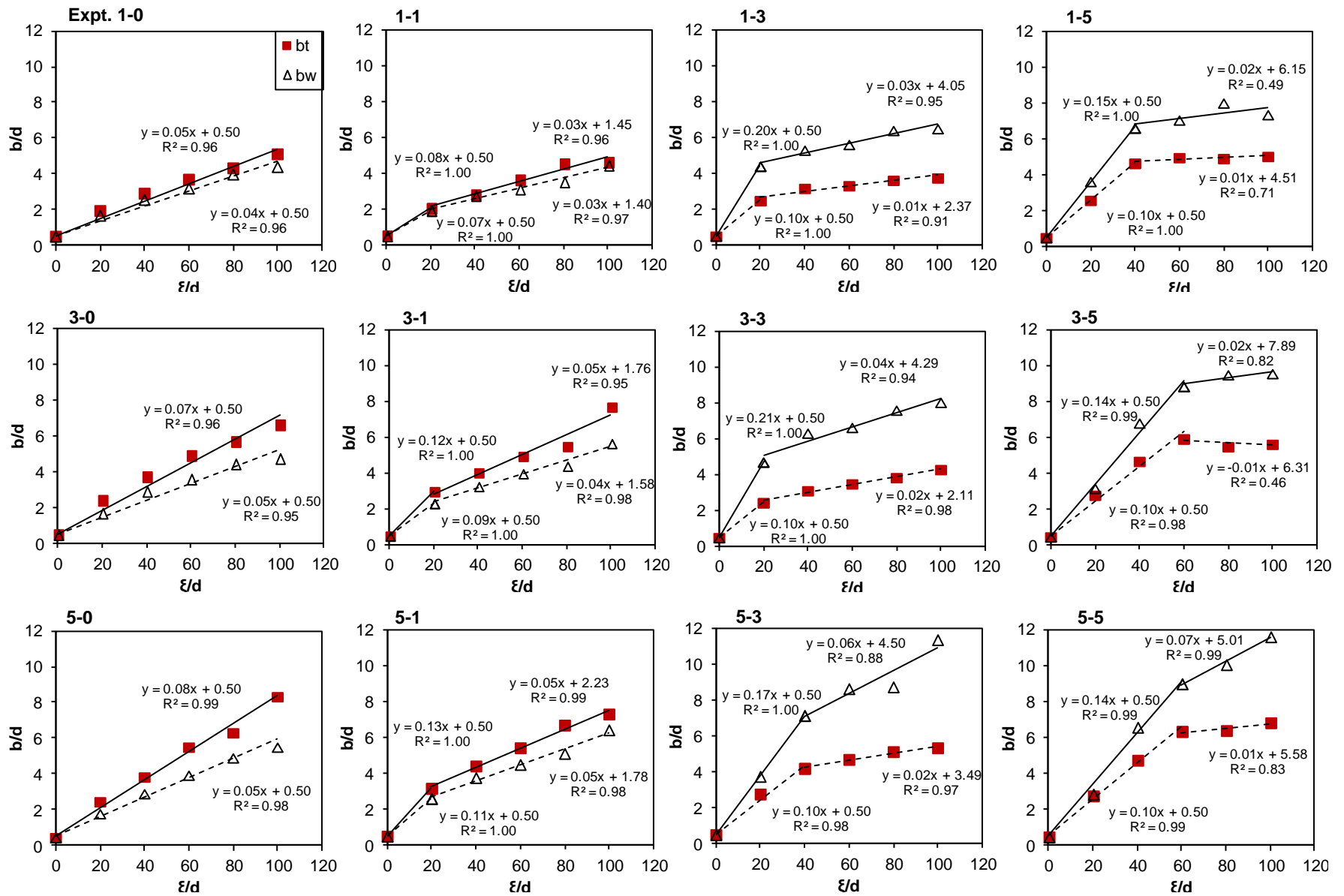


Figure 6-31. Spreads of the bubble plumes or bubbly jets in all the 12 experiments

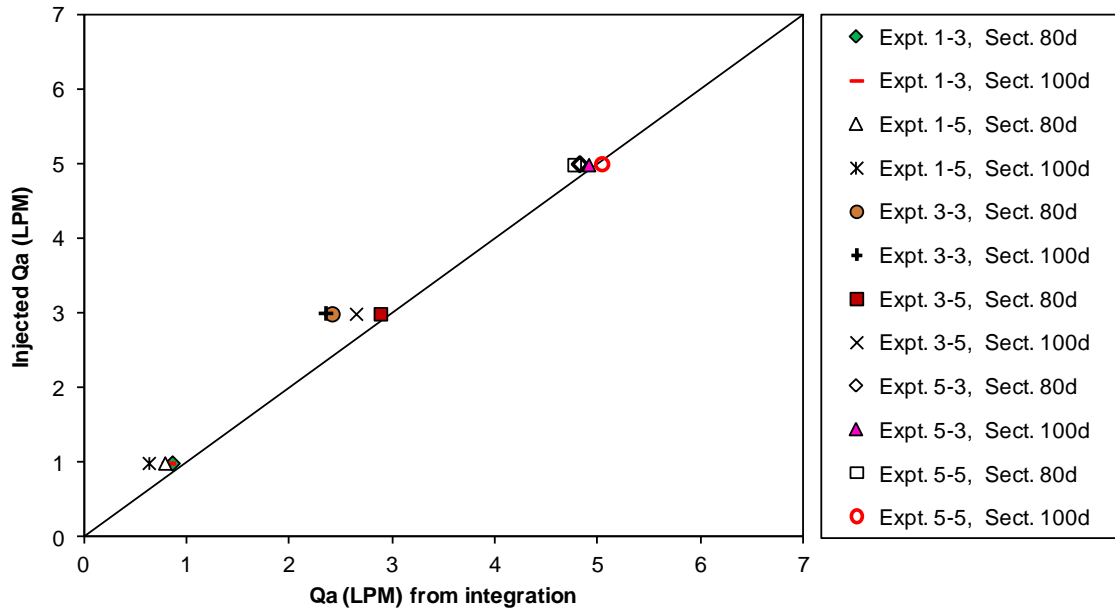


Figure 6-32. Comparison of air flow rates at Sections 80d and 100d from integration of Eq. (6.7) with their injected rates in the experiments of bubbly jets

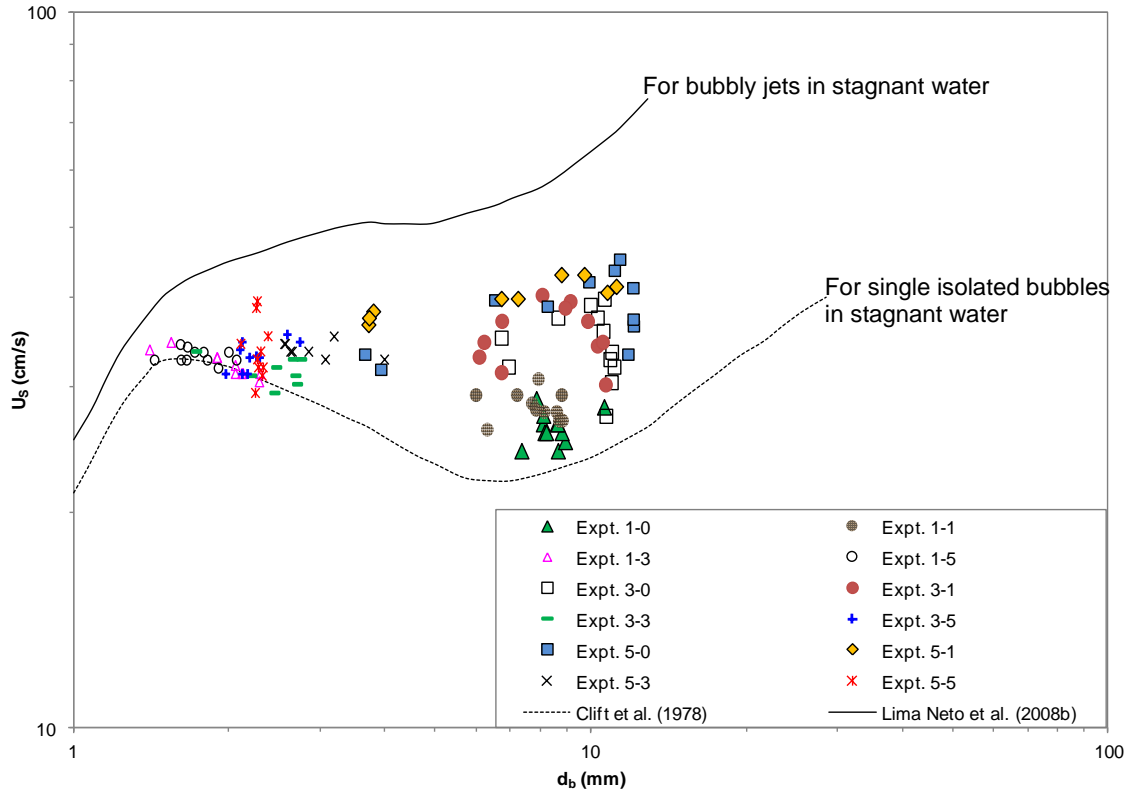


Figure 6-33. Relation of bubble slip velocity with bubble diameter for bubble plumes and bubbly jets in crossflow, without the consideration of bubble-induced water velocities inside bubble plumes

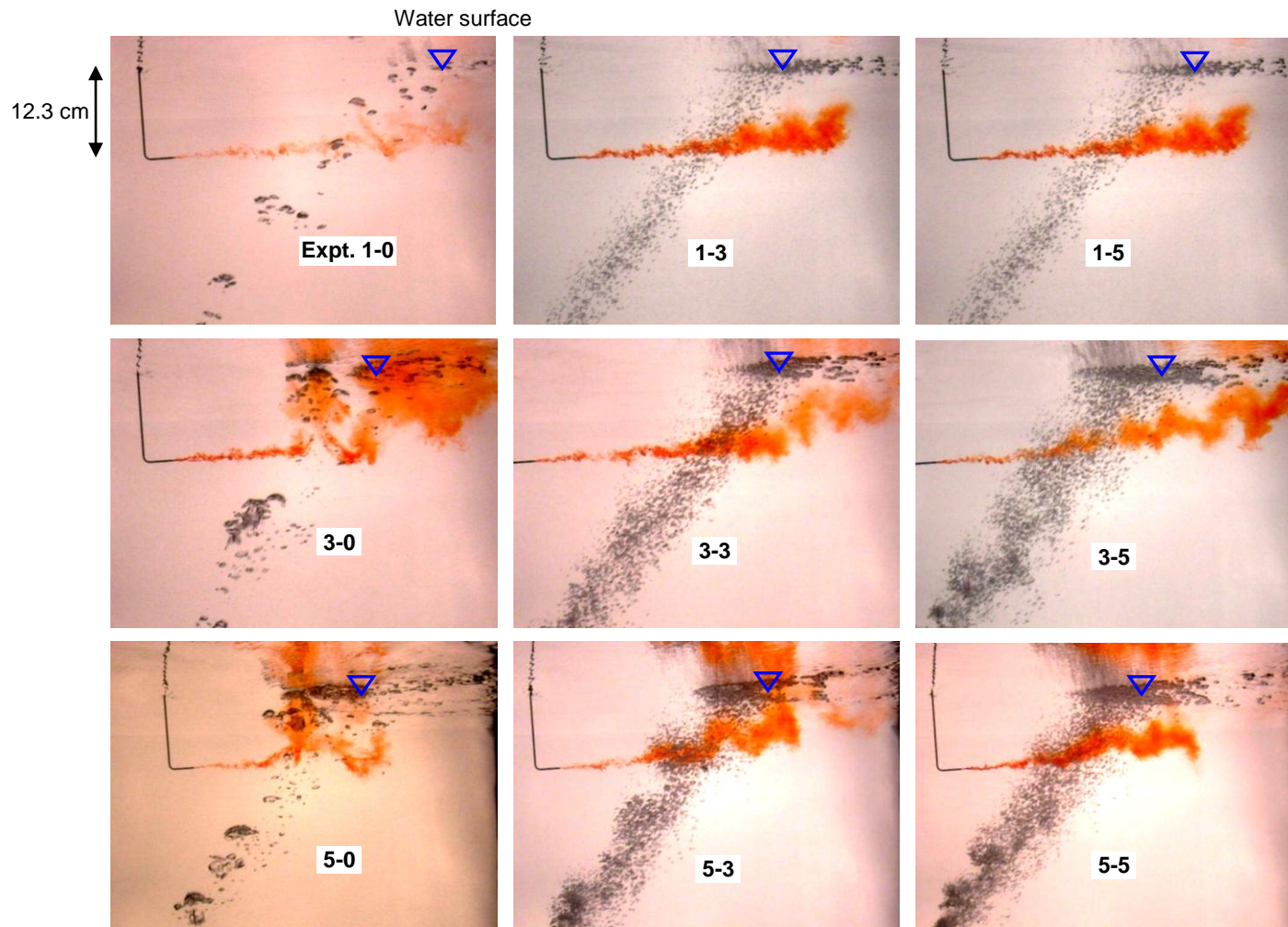


Figure 6-34. Dye stripe experiments to show the strengths of bubble-induced water velocities inside bubble plumes

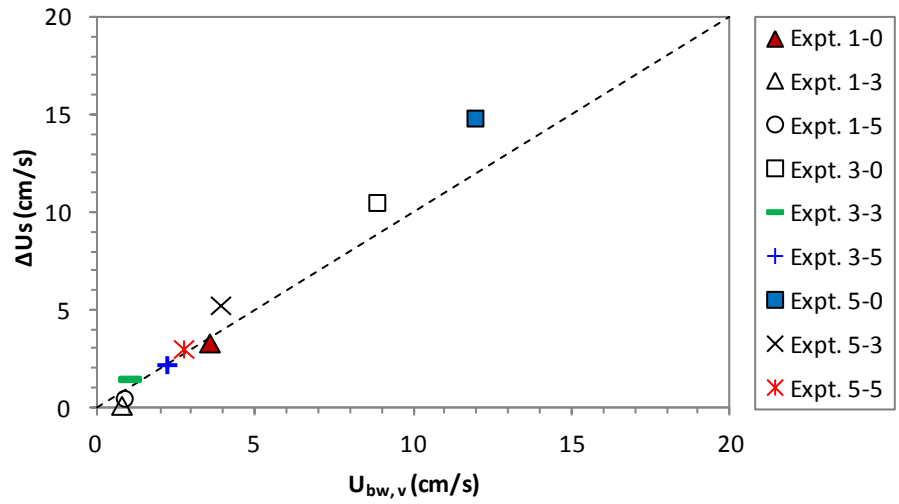


Figure 6-35. Comparison of average difference of bubble slip velocity from the present measurement and that from Clift et al. (1978) in Fig. 6-33, ΔU_s , with bubble induced water velocity in the vertical direction $U_{bw,v}$ estimated from videos of dye stripe experiments

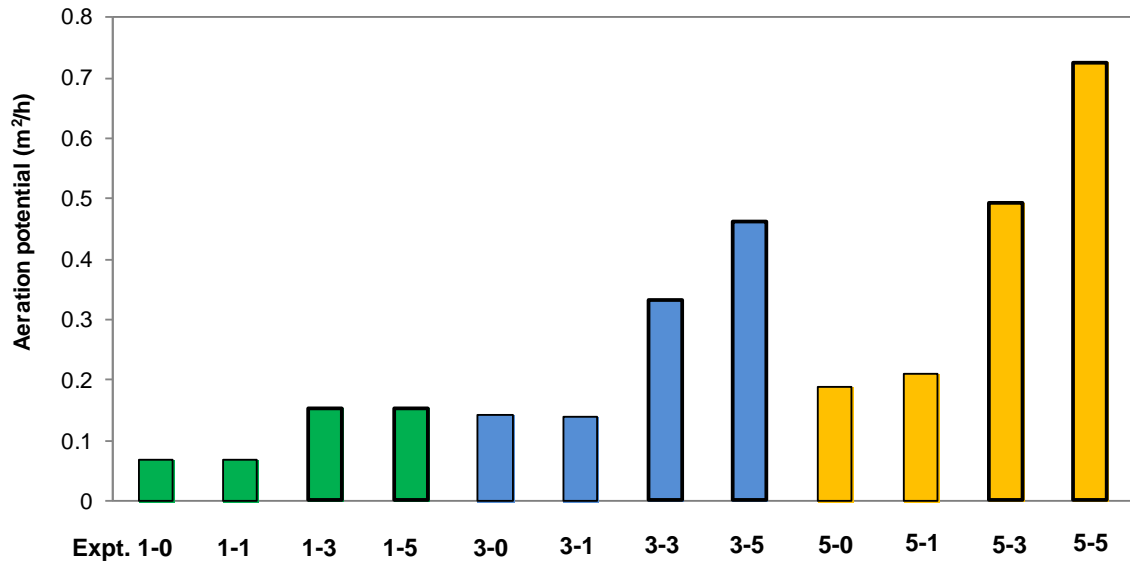


Figure 6-36. Aeration potential ($\int_{-\infty}^{+\infty} \int_{-\infty}^{+\infty} K_L a d\eta dy$) at Section 80d in each experiment

Chapter 7

General Conclusions and Recommendations for Future Research

7.1 General Conclusions

This thesis studied two important aspects related with air/oxygen injection through existing effluent diffusers to improve DO levels in rivers: effluent mixing; and bubbly jets in crossflow. Detailed conclusions can be found in each of the preceding five chapters. More general conclusions are summarized as follows:

- In Chapter 2, based on a comprehensive literature review, it was found that all varieties of jets and plumes except simple jets and plumes are still currently under active studies.
- In Chapter 3, based on a field dye test, it was found that the near-field mixing of effluents discharged from a multiport diffuser into a shallow river will in sequence experience four zones: the free jet zone, the jet surface impingement zone, the merging zone, and the vertical mixing zone. The current knowledge in the second and third zones is limited.
- In Chapter 4, it was found that the variation of river discharge has a significant (linear positive correlation) impact on dimensional transverse mixing coefficient in a fixed river reach, but not on the dimensionless coefficient. Ice cover tends to reduce the dimensionless transverse mixing coefficient.
- In Chapter 5, it was found that the general behaviors of bubble plumes and bubbly jets in crossflows are strongly affected by the air and water flow rates at

the nozzle and by the strength of crossflow. Large bubbles are more preferable for artificial mixing, while small bubbles are better for artificial aeration.

- In Chapter 6, for bubble plumes and bubbly jets in crossflow, it was found that the Gaussian distribution generally can well describe the distributions of gas void fraction, bubble frequency and specific interfacial area. The distributions of bubble velocity and bubble diameter are more complex. The spreading rate of bubble plumes decreases after the separation of bubbles from bubbly jets. Bubble induced water velocity is substantial in bubble plumes with large bubbles, while it is small in bubbly jets with small bubbles. Bubble slip velocity is close to that of single isolated bubbles in stagnant water.

7.2 Recommendations for Future Research

Overall, this thesis contributes to the knowledge of the performance of multiport diffuser, river mixing, artificial aeration and mixing in crossflow. There are still many aspects left to continue research in these broad areas. The followings are recommended for future research:

On Effluent Mixing in Rivers:

- Experimental studies on the jet merging and jet impingement at the water surface; and their Computational Fluid Dynamics (CFD) modeling;
- Application of CFD modeling for the near-field mixing downstream of an outfall or multiport diffuser;
- Field measurements on the helical motion (secondary flow) in a river, and relate it with transverse mixing coefficient;

- Continue the endeavor to try to establish a more accurate and widely-accepted empirical formula for transverse mixing coefficient, which might include parameters on both river hydrodynamics and morphodynamic features.

On Bubble Plumes and Bubbly Jets in Crossflow

- Experimental studies on the effect of different nozzle types and sizes in crossflow, e.g., multiport diffusers;
- Experimental studies on the effect of crossflow strength on the distributions of bubble properties;
- Experimental studies on the effect of water depth and ice cover on bubble properties;
- Experimental investigation of the effect of bubbles on the turbulence of water jets for the case of bubbly jets;
- Experimental studies on direct measurements of dissolved oxygen with bubble properties;
- Experimental studies in stratified ambient crossflow;
- Experimental studies with the introduction of solid particles, i.e., gas-liquid-solid multiphase jets and plumes;
- Developments and calibration of CFD models on two-phase or multiphase jets and plumes with and without crossflow.